Advances in crystallography

Laurent Guérin

To cite this version:

Laurent Guérin. Advances in crystallography. Cristallography. Université de Rennes, 2024. tel-04729441

HAL Id: tel-04729441
https://hal.science/tel-04729441v1

Submitted on 10 Oct 2024

ADVANCES IN CRYSTALLOGRAPHY

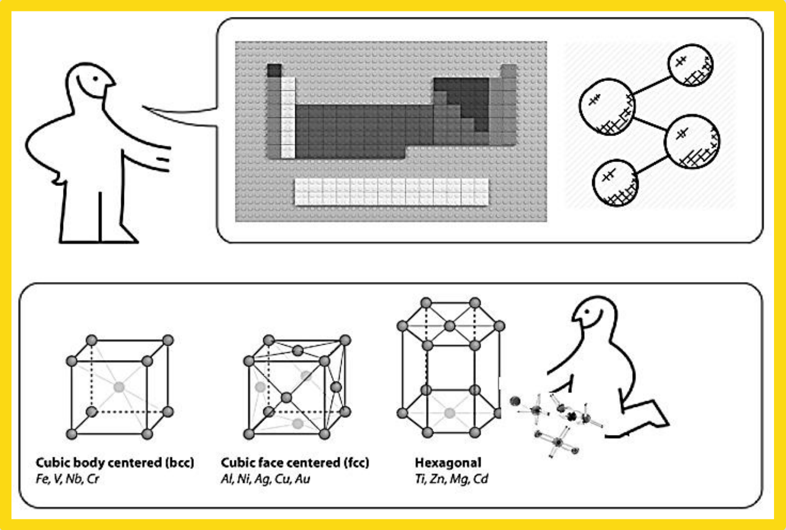

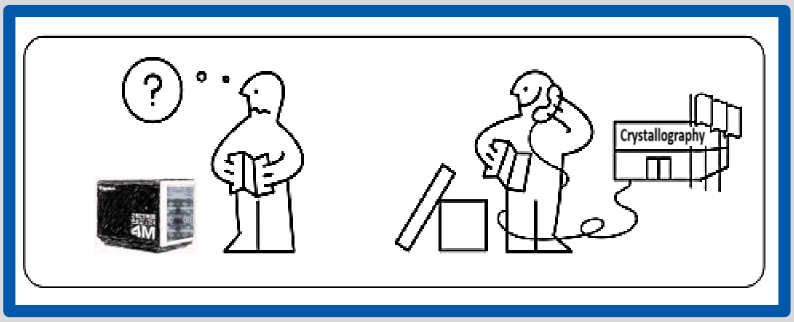

Laurent Guérin

Habilitation à diriger des recherches

Date et lieu de soutenance : 05 Juin 2024 – Université de Tokyo

Composition du Jury :

Marc Fourmigué	PRESIDENT
Pascale Launois	RAPPORTEUR
Philippe Guionneau	RAPPORTEUR
Hiroshi Kitagawa	RAPPORTEUR
Maciej Lorenc	EXAMINATEUR

HDR préparée au sein des Laboratoires :
DYNACOM, IRL2015, CNRS, Université de Rennes – Université de Tokyo
Institut de Physique de Rennes UMR-CNRS – Université de Rennes

Keywords

Advanced materials, Advanced data interpretation, Aperiodic order, Analytical analysis of diffraction, Correlated disorder, Crystallography, Cutting-edge experiment, Data analysis, Diffraction techniques, Diffuse scattering, Innovative methodologies, Materials science, Molecular materials, ΔPDF analysis, Phase transition, Photoinduced phenomena, Single crystal, Structural dynamics, Superspace crystallography, Synchrotron facilities, Total scattering method, TR-segmented method, Ultrafast crystallography, X-ray crystallography

Abstract

In this manuscript, we investigate the forefront of crystallography, exploring novel methodologies and cutting-edge experimental techniques. The integration of advanced techniques, such as ultrafast crystallography and time resolved diffuse scattering, revolutionizes our ability to look at dynamic processes at the atomic level. We investigate a range of materials, from aperiodic systems to correlated disorder systems, pushing the boundaries of crystallographic study. The advancements in data analysis streamline the interpretation of complex crystal structures. Our research unveils key findings in aperiodic disorder, photoinduced phase transitions, and correlated disorder. We discuss the implications of our work in materials science, emphasizing the potential for applications in designing new materials. This manuscript represents a comprehensive exploration of crystallography's latest frontiers, offering insights into materials' structural dynamics and paving the way for future advancements in the field.

Acknowledgements

Je tiens à remercier les membres de mon jury. C'était un plaisir et un honneur. Je remercie Marc Fourmigué, directeur de recherche CNRS à l'ISCR à l'Université de Rennes pour avoir présidé mon jury d'HDR, Pascale Launois, directrice de recherche CNRS au LPS, Université de Paris Sud, Philippe Guionneau, professeur des universités à l'ICMCB à l'Université de Bordeaux et Hiroshi Kitagawa, professeur des universités à l'Université de Kyoto d'avoir rapporté mon manuscrit d'HDR (malgré sa longueur) et Maciej Lorenc, directeur de recherche CNRS à l'Institut de Physique de Rennes, Université de Rennes pour avoir été examinateur lors de ma soutenance. Les discussions avec les rapporteurs et la discussion finale lors de ma soutenance ont été un réel plaisir. Je referai pas cela tous les jours mais j'en garde un excellent souvenir. Je pense et j'espère que nous nous reverrons et auront l'occasion de discuter et peut être travailler ensemble sur les sujets qui nous passionnent.

Je remercie mes collègues et amis avec qui j'ai travaillé ces 20 dernières années. J'ai appris tellement grâce à vous. Merci à Eric pour ton soutien lors de ma thèse et ces dernières années. Merci à Céline, Philippe et Bertrand, on a formé pendant quelques années la dream team apériodique. C'était vraiment fun.

Preface

Writing my HDR was much more fun that I thought.

Embarking on the journey of composing this manuscript has been an exciting and, at times, challenging experience. As the pages unfolded, it became apparent that the task demanded more time and thinking than initially envisioned. The process was undeniably enjoyable, pushing the boundaries of my understanding and provoking new ideas to work with crystallography.

This manuscript, while conceived as a habilitation à diriger des recherches, has taken on a character of its own. It has evolved into more than a documentation of my scientific results; rather, it has assumed the form, I hope, of a comprehensive textbook on crystallography.

One of the challenges faced during the writing process was the inclination to draw examples solely from my own research. This self-imposed limitation, inherent to the nature of a habilitation manuscript, occasionally led to moments of frustration. The desire to incorporate a broader spectrum of examples from the extensive literature was palpable.

While this manuscript primarily revolves around my specific research journey, I envision future expansions. The aim is to enrich the content with a diverse array of examples gleaned from the broader scientific literature.

In essence, this manuscript is a snapshot of a moment in my scientific career. May it serve not only as a text to evaluate my work and hopefully to award me my habiliation but also as a resource that sparks curiosity and deepens understanding in the fascinating field of crystallography.

In order to facilitate the evaluation of the HDR, I consider that the pages with grey background color are the essential parts of the HDR: the introduction, small resume of each chapter, conclusion and the scientific project.

Laurent Guérin

Contents

Introduction

Crystallography, the science of figuring out how atoms arrange themselves in crystals, has experienced significant progress, enhancing our grasp of materials and their characteristics. This area has gone through substantial changes, all thanks to cutting-edge technologies and innovative approaches. In recent times, the use of advanced technologies has completely transformed crystallography. X-ray crystallography has undergone improvements in both resolution and speed, empowering researchers to explore molecular structures with unparalleled precision. The upgrades of synchrotron radiation facilities as well as X-ray free electron laser have notably boosted the efficiency of data collection, facilitating the study of more complex samples.

The creation of innovative diffraction techniques has expanded the reach of crystallography. Serial crystallography, for example, allows scientists to determine the structure of nanocrystals. Ultrafast crystallography has unveiled novel insights into dynamic atomic-scale processes. Capable of capturing snapshots of molecular changes within femtoseconds, this technique sheds light on ultrafast phenomena like photoinduced phase transitions and electronic excitations.

Progress in data analysis tools has streamlined the process of crystallographic data treatment. The utilization of machine learning algorithms has become increasingly prevalent, simplifying the decoding of intricate crystal structures and minimizing the time and expertise required for manual analysis.

Crystallography has evolved significantly, not just in decoding well-organized structures but in venturing into more complex organization. Recent advances in concept of superspace crystallography has allowed the exploration of aperiodic structures, structures that lack translation symmetry. Crystallography is also tackling correlated disorder, deciphering the intricate interactions between atoms. In this context, the arrangement is not a chaotic randomness but a blend of order and disorder.

In this manuscript, we embark on a four-chapter journey, from the foundations to the frontiers of crystallography, from its basic principles to more advanced concept and techniques that allow us to understand the real and complex structure of materials and how they evolve when they transform.

The "Basics of Crystallography” is where we start. This first chapter is a crash course on how scientists use X-rays to figure out the structure of materials. It dives into the fundamentals. This basic crystallography method exposes the fundamental relationships between Bragg peaks' intensities and the underlying average atomic structures of crystals, setting the stage for the more complex structure analysis. It presents all the mathematical foundation of diffraction by a perfect crystal as well as some clever algorithms that have transformed crystallography from a laborious task into an efficient process, enabling the automatic solution of crystal structures within few minutes.

The second chapter "Aperiodic Order and Superspace Crystallography" explores a world where crystals don't play by the rules—they're not arranged in periodic patterns. The very definition of crystals undergoes a paradigm shift as we encounter incommensurate modulated structures, incommensurate composites, and quasicrystals. Previously considered forbidden symmetries now find expression in these unconventional crystal structures. Superspace crystallography, a concept introduced by De Wolff, extends our understanding into higher-dimensional spaces, restoring translational symmetry.

Transitioning to the third chapter, "Correlated Disorder and Diffuse Scattering," we confront the imperfections inherent in materials. Much like examining a painting up close, we discover that materials possess a certain disorder, introducing a layer of complexity atop their ordered structures. The disorder observed isn't chaotic; it shows correlations. Understanding correlated disorder becomes essential to understand material properties. In this chapter, we dive into canonical examples, and presents from the theoretical and experimental point of view the analysis of the diffuse scattering. As diffuse scattering emerges from the more and more sensitive detectors, we explore advanced analysis techniques, including the 3D-ΔPDF method. This technique, enables the analysis of local correlations in three dimensions. Through scientific cases, we show the power of this method in revealing the correlation in the disorder.

Lastly, the fourth chapter presents the advances in crystallography to study how structure evolves under light irradiation. When light interacts with certain materials, it sets off a chain reaction involving numerous atoms and electrons. This domino effect unfolds in cooperative molecular materials, where a single photon can induce a cascade of structural changes leading to a macroscopic-scale excited domain. It manifests across different length scales and timescales. This chapter shows the diverse manifestations of photoinduced processes, ranging from ultrashort-lived transitions to those with lifetimes extending from minutes to hours. Sophisticated experimental methods, such as femtosecond time-resolved diffraction, become our tools of analysis capturing the dynamic changes in crystal lattice structures in real-time. We present the different limitations and the different advances in the field with the development of the serial crystallography and time resolved electron diffraction and the use of more advanced concept such as superspace and diffuse scattering to study precursor phenomena of photoinduced phase transitions.

In our conclusion, we try to push the limit of crystallography in analyzing the total scattering pattern, envisioning a future where the combined analysis of diffuse scattering and the diffraction pattern becomes standard for understanding material transformations.

Because of the length of the manuscript, each chapter has at its beginning, a short resume that I call “Essentials” that is self-consisting, sets the context, presents the important results and outlines my research works. The reader interested in the essentials can deep dive in the chapter for a complete and lengthy explanation of the different concepts.

Essentials of Basics of Crystallography

The introduction chapter is intended to give a quick review of the basics of crystallography presenting all the equations relevant for the other chapters and the methods to study phase transition. Spin transition is presented to showcase the power of crystallography study.

Diffraction from a perfect crystal

The total scattered amplitude as the function of $\boldsymbol{q}$ the scattering wave vector is equal to:

$$A(\boldsymbol{q}) = \mathfrak{F}\{\rho_{crystal}(\boldsymbol{r})\} = S(\boldsymbol{q}) \times F(\boldsymbol{q})$$

With $S(\boldsymbol{q}) \neq 0$ only when $\mathbf{q} = \boldsymbol{G_{hkl}}$ is a reciprocal vector

And the structure factor

$$F(\boldsymbol{G_{hkl}}) = F_{hkl} = \sum_j f_j(\boldsymbol{G_{hkl}})\, e^{i2\pi(hx_j + ky_j + lz_j)}$$

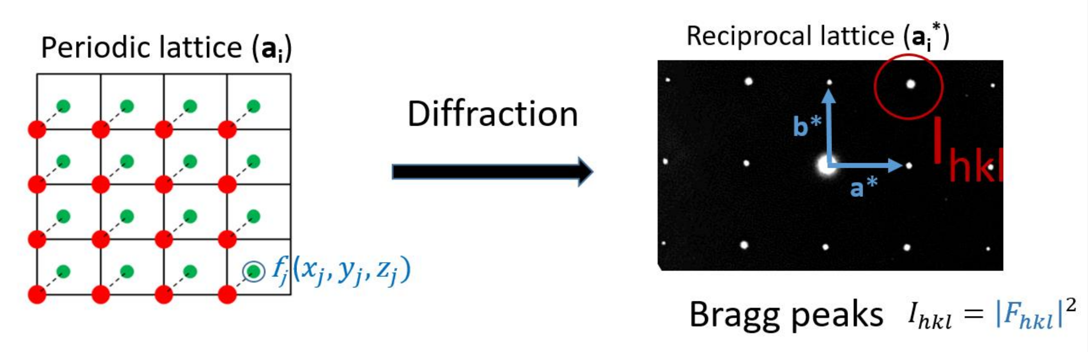

Figure 0-1: From crystal to diffraction image

Structure determination is the process of finding the position and the nature of the atoms within a unit cell by analyzing the Bragg peaks intensity and the structure factor.

$\rho(\boldsymbol{r}) = \mathfrak{F}^{-1}\{F(\boldsymbol{q})\}$ can be obtained using different algorithms. Charge flipping algorithm requires only diffracted intensities for structure determination. The four-step process involves inverse Fourier transformation, charge flipping of negative peaks, Fourier transformation of the new density, and replacement of amplitudes with experimental values. Iterative until convergence, the algorithm yields an accurate electron density representation based solely on experimental structure amplitudes.

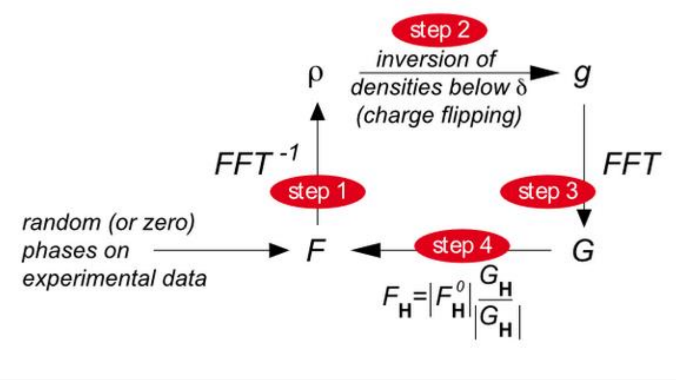

Figure 0-2 : the charge flipping algorithm

Crystallography study of Phase transition

Diffraction is wonderful tool to study phase transition. The different signatures and their relation with a phase transition are the following:

- Peak shift and cell parameters
- Bragg reflection condition and group-subgroup relationships
- Superstructure Bragg peaks and symmetry breaking
- diffuse scattering and pretransitionnal phenomena
- Structure determination and structure analysis.

A case study: spin crossover systems

SCO involves the alteration of the electronic configuration in a transition metal compound, shifting between high spin (HS) and low spin (LS) states due to external factors like temperature, pressure, light, magnetic and electric fields.

The substantial structural changes at both intra and intermolecular levels can be precisely studied through X-ray diffraction and represent distinctive signatures of the spin transition.

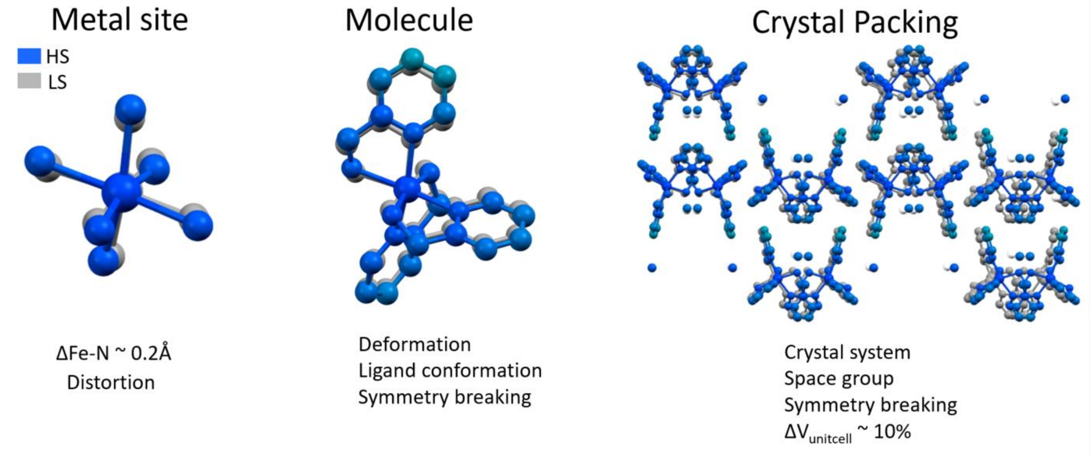

Figure 0-3 : atomic structure of the metal site, the molecule and the crystal packing for the low spin state (grey) and the high spin state (blue). The low to high state transition is associated to distortion of the metal site, deformation of ligands, symmetry breaking, change of crystal system and space group and unit cell expansion.

The [Fe (2-pic)$_3$]Cl$_2$ EtOH belongs to the class of materials undergoing a transition from a diamagnetic Low Spin state (LS, S = 0) to a paramagnetic High Spin state (HS, S = 2) under the influence of temperature.

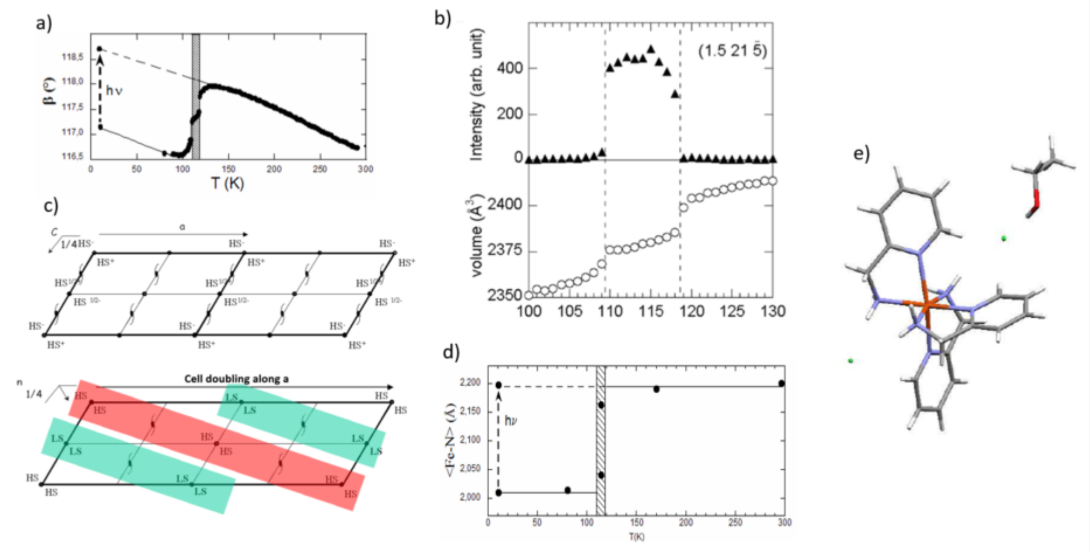

Figure 0-4 : (a) Evolution of lattice parameters as a function of temperature (b) New Bragg peaks appear in the intermediate phase, characteristic of symmetry breaking (c) group-subgroup relationship (d) structure analysis (e) Structure of [Fe(2-pic)3]Cl2 EtOH

- Cell parameters

Figure 0-4 (a) shows two phase transitions from the low spin (LS) low temperature phase to an intermediate (IS) phase at 109K and from the IS to the high spin high temperature phase at 117K.

- Group-subgroup relationship and superstructure Bragg peaks

The volume doubles in the intermediate phase. (Figure 0-4 (b)) This doubling of the lattice is associated with the loss of symmetry elements and results in the appearance of superstrucure Bragg peaks in the intermediate phase. In the intermediate phase (IS), the symmetry breaking associated with the lattice doubling leads to the loss of other elements (inversion centers and 2_1 axes). (Figure 0-4 (c))

- Structure analysis of the intermediate phase (Figure 0-4 (d-e))

The resolution of the crystal structure of the LS and HS phase shows a change of the distance Fe-N in the LS and HS states due to the spin transition. IP phase reveals that every other site is populated by HS and LS molecules, as indicated by the Fe-N bond lengths at each site. This symmetry breaking corresponds to a long-range ordering of planes composed of entirely LS molecules and planes composed of entirely HS molecules.

- Symmetry breaking and order parameter

The symmetry breaking associated with the doubling of the lattice along the a direction, corresponding to a transition at the BZ edge, necessitates the presence of an order parameter in addition of the totally symmetric average HS fraction γHS order parameter. This parameter describes the ordering of HS/LS species in the intermediate phase. The square root of the intensity of the superstructure peaks (h+1/2 k l) associated with the lattice doubling is proportional to the order parameter η and is 0 in the HS and LS phases.

This chapter presented how we can use the different techniques in crystallography to study phase transition. We applied the tools to the case of SCO materials. This crystallography methods are very general and employed in many laboratories all over the world. In the next chapter, we will explore more advanced concepts in crystallography.

This chapter is based on the following papers:

L. Guérin, N. Huby, E. Collet, L. Toupet, H. Cailleau, and K. Tanaka, Structural Investigation of the Photoinduced Spin Transition in the Three States Molecular System [Fe(2-Pic)3]Cl2EtOH, ***J. Phys.: Conf. Ser***. 21, 136 (2005).

N. Huby, **L. Guérin**, E. Collet, L. Toupet, J.-C. Ameline, H. Cailleau, T. Roisnel, T. Tayagaki, and K. Tanaka, Photoinduced Spin Transition Probed by X-Ray Diffraction, ***Phys. Rev. B*** 69, (2004).

E. Trzop, D. Zhang, L. Piñeiro-Lopez, F. J. Valverde-Muñoz, M. Carmen Muñoz, L. Palatinus, **L. Guérin**, H. Cailleau, J. A. Real, and E. Collet, Inside Back Cover: First Step Towards a Devil's Staircase in Spin-Crossover Materials, ***Angewandte Chemie International Edition*** 55, 1 (2016).

Concepts presented in the chapter 1 were used in the following works :

Laurent Guérin*, Elzbieta Trzop, Tadahiko Ishikawa, Shinya Koshihara ,Takashi Yamamoto, Bertrand Toudic, Reizo Kato*, Frustrated competitive forces in the Et2Me2Sb[Pd(dmit)2]2 molecular conductor, **Physical Review B** 108, 134104 (2023).

Céline Mariette,Philippe Rabiller,**Laurent Guérin**, Claude Ecolivet ,Ilya Frantsuzov, Bo Wang, Shane M. Nichols, Philippe Bourges, Alexei Bosak, Yu-Sheng Chen, Mark D. Hollingsworth, Bertrand Toudic, **Physical Review B** 106, 134109 (2022).

L. Guérin*, T. Yoshida*, E. Zatterin, A. Simonov, D. Chernyshov, H. Iguchi, B. Toudic, S. Takaishi, and M. Yamashita, Elucidating 2D Charge-Density-Wave Atomic Structure in an MX–Chain by the 3D-ΔPair Distribution Function Method, ***ChemPhysChem*** 23 (2022).

H. Ichikawa, S. Nozawa, T. Sato, A. Tomita, K. Ichiyanagi, M. Chollet, **L. Guérin**, N. Dean, A. Cavalleri, S. Adachi, T. Arima, H. Sawa, Y. Ogimoto, M. Nakamura, R. Tamaki, K. Miyano, and S. Koshihara, Transient Photoinduced 'Hidden' Phase in a Manganite, ***Nature Material*** 10, 101 (2011)

L. Guérin, D. Glijer, N. Moisan, M. Lorenc, M. B.-L. Cointe, E. Collet, H. Cailleau, A. Ota, G. Saito, X. Shao, H. Yamochi, M. Chollet, K. Onda, T. Ishikawa, and S. Koshihara, Phase Transition in (EDO-TTF)2PF6: Domain Growth in the Thermal Hysteresis and Ultra-Fast Photoinduced Effects, ***J. Phys.: Conf. Ser.*** 21, 149 (2005).

Chapter 1: Basics of Crystallography

The introduction chapter is intended to give a quick review of the basics of crystallography. Basics doesn’t refer by any means to simple. It refers to the old and very efficient way to do crystallography and represents the vast majority of studies on crystals. It is based on the relation between the intensities of Bragg peaks and the structure of crystal at the atomic level. Despite this relation is not straightforward, scientists during the last century invent very powerful algorithms that allow us, actual scientists, to solve structure in a matter of minutes. Because these Bragg peaks characterize the structure of the material, they are commonly named structure Bragg Peaks. Their presence and position sign the symmetry of the crystal and are a very valuable probe to detect phase transition when we change the external conditions (temperature, pressure, light…). Because it is a so efficient probe, it is used in many laboratories and large scale facilities all the over the world. The recent scientific progress on sources and detectors unlocked the possibilities to perform full data collection on tens of crystals in a day. To illustrate the power of crystallography, I will use the example of spin transition system compounds. The spin transition illustrates a change between two electronic spin states. The capacity of an electron to move from one stable electronic state to another stable in a manner that can be both reversed and detected is what makes these molecular systems attractive within the field of molecular electronics. For crystallography, they are nice systems as they show clear signature of phase transition with change of symmetry, volume and large change in the structure. As I worked during my scientific career mostly with X-rays, I will presents the basic theory within the scope of X-ray diffraction although most of the concepts and equations are completely valid for electrons and neutrons.

1.1 BASIC THEORY OF DIFFRACTION

I assume that readers know the (old) definition of the crystal based on the periodic repetition of atoms and the basic principle of diffraction of X-ray on matter. The expressions derive here assume that we place ourselves in the kinematic approach of the diffusion of X-rays by a distribution of electrons in a sample which will be assumed to have infinite volume to simplify the calculations. The phenomena link to absorption and the geometry of the experiments will be neglected (polarization, Lorentz factor). We place ourselves in the so-called Fraunhofer regime, that is to say that we consider a source of radiation, non-polarized, strongly monochromatic, illuminating homogeneously in a parallel beam the entire sample made up of independent point scatterers. The scattered intensity is collected by a detector located at a large distance (relative to its dimensions) from both the sample and the source. I recall that in this condition, the total scattered amplitude as the function of $\boldsymbol{q} = \boldsymbol{k_f}\text{-}\boldsymbol{k_i}$ where $\boldsymbol{q}$, $\boldsymbol{k_f}$ and $\boldsymbol{k_i}$ are the scattering, final and initial wave vector respectively is equal to:

$$A(\boldsymbol{q}) = \int_V d^3\boldsymbol{r}\rho(\boldsymbol{r})e^{i\boldsymbol{q}\cdot\mathbf{r}}$$

The total scattered amplitude in space as a function of $\boldsymbol{q}$ is thus the product of the electronic density $\rho(\boldsymbol{r})$ and the phase difference $e^{i\boldsymbol{q}\cdot\mathbf{r}}$, where $\mathbf{r}$ is the position vector of the region of electronic density integrated over the whole scattering volume V. This corresponds to the Fourier transform of the electron density of the whole crystal:

$$A(\boldsymbol{q}) = \mathfrak{F}\{\rho_{crystal}(\boldsymbol{r})\}$$

Diffraction from a perfect crystal

The fact that crystal is a periodic structure in the three dimension of space is a property that simplifies tremendously the calculation of the scattered amplitude. Instead of dealing with an electron density of 10^{23} atoms, we can easily describe the crystal as a 3D lattice decorated with few atoms (few could mean thousands of atoms thanks to the advent of powerful sources and highly sensitive detectors).

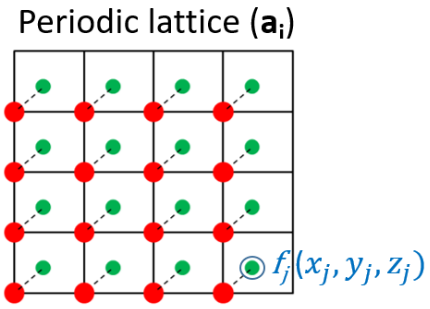

Figure 1-1 : a crystal composed of a periodic lattice defined by ($\mathbf{a}_i$) vectors and a motif with atoms f_j at position (x_j,y_j,z_j)

Let’s consider a perfect lattice with basic vector (**a**$_i$) with i=1,2,3. Atoms are located at position (x_j, y_j, z_j) in the unit cell (Figure 1-1).

Crystal as a convolution product

The first thing to show is that the electron density of crystal $\rho_{crystal}(\boldsymbol{r})$ can be expressed as the convolution of electron density of the unit cell $\rho(\boldsymbol{r})$ and the lattice distribution $L(\boldsymbol{r})$.

For simplicity, I do the calculation for 1D crystal of periodicity a and show that:

$$\rho_{crystal} = L(r) \otimes \rho\,(r)$$

The electron density of the whole crystal $\rho_{crystal}$ is a simple sum of the electron density of the unit cell $\rho(r)$:

$$\rho_{crystal} = \textstyle\sum_u \rho(r-ua)$$

and the lattice distribution is a Dirac comb of periodicity a:

$$L(r) = \sum_u \delta(r-ua)$$

each comb corresponding to the position of the node of the lattice in the real space (Figure 1-2).

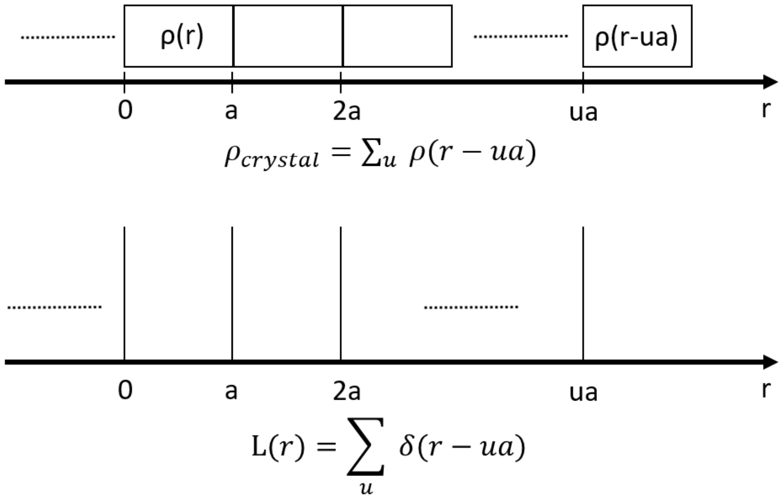

Figure 1-2 : Electron density of a 1D crystal of periodicity a defined by the lattice distribution.

We can calculate $L(r) \otimes \rho\,(r)$ using the mathematical description of the lattice and the electron density.

$$L(r) \otimes \rho(r)$$

Using the definition of the convolution product,

$$= \int \sum_{u} \delta(s - ua)\rho(r - s)ds$$

$$= \sum_{u} \int \delta(s - ua)\rho(r - s)ds$$

$$p = s - ua \ and \ dp = ds$$

$$= \sum_{n} \int \delta(p)\rho(r - p - ua)dp$$

Using the property of the delta function,

$$= \sum_{u} \rho(r - ua)$$

$$= \rho_{crystal}$$

Scattering amplitude from crystal

We can now easily calculate the scattering amplitude of the whole crystal

$$A(\boldsymbol{q}) = \mathfrak{F}\{\rho_{crystal}(\boldsymbol{r})\}$$

$$A(\boldsymbol{q}) = \mathfrak{F}\{L(r) \otimes \rho(r)\} = \mathfrak{F}\{L(r)\} \times \mathfrak{F}\{ \rho(r)\} = S(\boldsymbol{q}) \times F(\boldsymbol{q})$$

The amplitude $A(\boldsymbol{q})$ is the simple multiplication of two terms $S(\boldsymbol{q})$ and $F(\boldsymbol{q})$.

Form factor $S(\boldsymbol{q})$

The first term $S(\boldsymbol{q}) = \mathfrak{F}\{L(r)\}$ is known as the form factor and can be expressed using a Dirac comb in the **q** space:

$$S(\boldsymbol{q}) = \mathfrak{F}\{L(r)\} = \int L(r)e^{iq\cdot r}dr$$

$$= \int \sum_{u} \delta(r - ua)e^{iqr}dr$$

$$= \sum_{u} \int \delta(r - ua)e^{iqr}dr$$

$$with \, p = r - ua \ and \ dp = dr$$

$$= \sum_{u} \int \delta(p)e^{iq(p+ua)}dp$$

Using the property of the delta function and the Poisson summation formula,

$$= \sum_{u} e^{iqua} = \frac{2\pi}{a} \sum_{h} \delta\left(q - h\frac{2\pi}{a}\right)$$

The reciprocal lattice

The form factor corresponds in the **q** space to a Dirac Comb of $\frac{2\pi}{a}$ periodicity (Figure 1-3), each comb corresponding to the position of the node of a lattice in the reciprocal space. In the three dimensional space, it defines what is known as the **reciprocal lattice** with basic vectors (**a$_i$***), i=1,2,3.

The reciprocal lattice vectors are related to the real lattice (**a$_i$**) by the set of equations $\boldsymbol{a_i}.\boldsymbol{a_j^*} = 2\pi\delta_{ij}$.

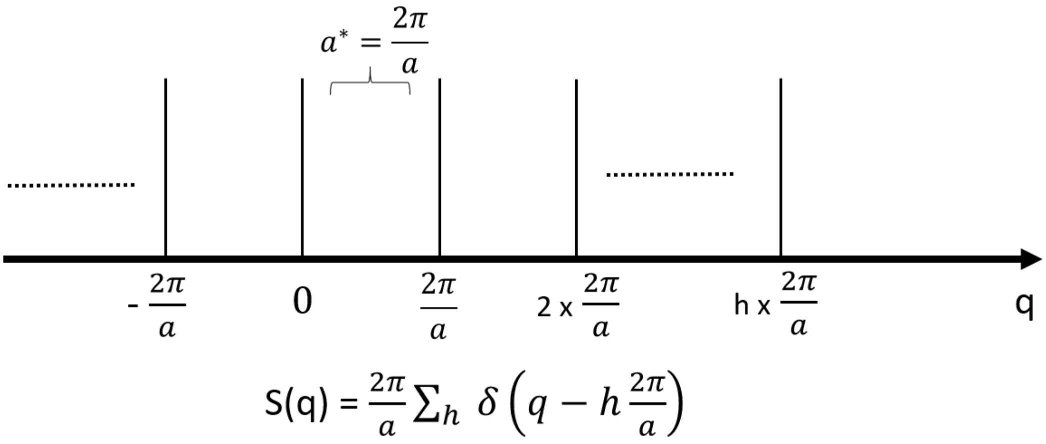

Figure 1-3 : the reciprocal lattice distribution of periodicity a*.

An important observation is that the S(q) is different from zero only when **q** is equal to a reciprocal lattice vector $\mathbf{q} = \boldsymbol{G_{hkl}} = h\boldsymbol{a_1^*} + k\boldsymbol{a_2^*} + l\boldsymbol{a_3^*}$ and therefore the scattering amplitude $A(\boldsymbol{q})$ is non zero only for $\mathbf{q} = \boldsymbol{G_{hkl}}$. This is the Laue condition. Experimentally, that means that we collect intensities on the detector only for well-defined **q** vectors that correspond to nodes of the reciprocal lattice: the Bragg peaks. By collecting a sufficient amount of Bragg peaks, the reciprocal and the real lattice can be measured with a very high precision (hundredth of an angstrom in the real space).

Structure factor $F(\boldsymbol{q})$

The second term $F(\boldsymbol{q}) = \mathfrak{F}\{\rho(r)\}$ is the structure factor. The calculation of the Fourier transform considering j atoms at the $\boldsymbol{r_j} = x_j\boldsymbol{a_1} + y_j\boldsymbol{a_2} + z_j\boldsymbol{a_3}$ position in the unit cell gives:

$F(\boldsymbol{q}) = \sum_j f_j(\boldsymbol{q})\, e^{i\boldsymbol{q}\cdot\boldsymbol{r_j}}$ where $f_j(\boldsymbol{q})$ is the atomic form factor of the jth atom

In the Laue condition $\mathbf{q} = \boldsymbol{G_{hkl}}$ and using the definition of the reciprocal space,

$$F(\boldsymbol{G_{hkl}}) = F_{hkl} = \sum_j f_j(\boldsymbol{G_{hkl}})\, e^{i2\pi(hx_j+ky_j+lz_j)}$$

The intensity measured at the detector I_{hkl} is, in these conditions, proportional to the time average of the square of the module of the structure factor: $I_{hkl} = |\langle F_{hkl}\rangle|^2$ (Figure 1-4).

The structure factor is named this way because it is constituted of atomic form factors f_j which defines the nature of the atoms present in the unit cell and phase factor $e^{i2\pi(hx_j+ky_j+lz_j)}$ depending on the position of the atom within the unit cell. The associated Bragg Peaks are named structure Bragg peaks as their position, their presence and their intensity depend on the geometry and the structure of the unit cell.

The property of periodicity which allows to describe the electron density of the whole crystal as $\rho_{crystal} = L(\boldsymbol{r}) \otimes \rho\,(\boldsymbol{r})$ was essential to relate the intensity of Bragg peaks to the structure of the crystal. In the case of aperiodic materials that by definition are not defined by a three dimensional periodic lattice, we will introduce new periodicities in a higher dimensional space known as superspace of 3+d dimensions that will allow us to describe the aperiodic order. By using the same concepts presented for the three dimensional space in the superspace, we will define a superspace reciprocal lattice that will give rise to additional Bragg peaks called satellite Bragg peaks. Their intensity can be linked to the structure of the aperiodic order. If this concept of superspace is a little bit confusing right now, it will become clearer in the chapter 2 where the superspace crystallography will be presented. The important point to remember is that periodic lattice gives rise to Bragg peaks that can be described with the reciprocal lattice and their intensity depends of the structure the unit cell.

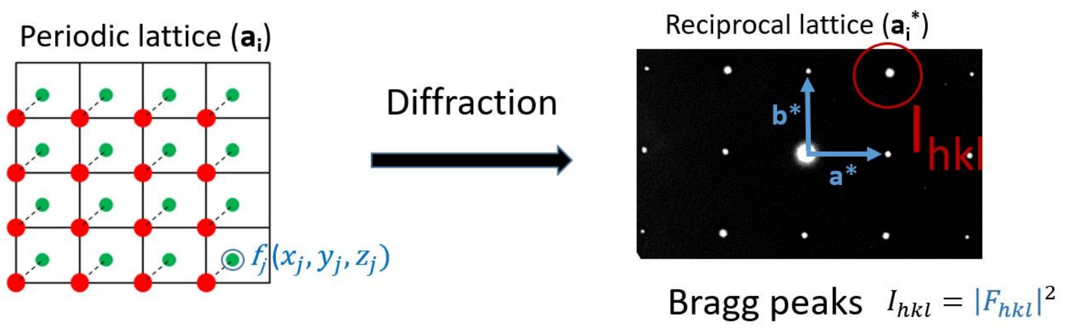

Figure 1-4 : real and reciprocal space.

1.2 STRUCTURE DETERMINATION

Structure determination is the process of finding the position and the nature of the atoms within a unit cell. In other words, that means to be able from the measurements of intensities of Bragg peaks to determine the structure factor.

We showed in the previous section that $F(\boldsymbol{q}) = \mathfrak{F}\{\rho(r)\}$ so it is just a matter of inverted this equation. Mathematically it is very simple using the inverse Fourier transform:

$$\rho(\boldsymbol{r}) = \mathfrak{F}^{-1}\{F(\boldsymbol{q})\}$$

Because F_{hkl} is a complex number, we can rewrite F_{hkl} like this:

$$F_{hkl} = \sum_j f_j\, e^{i2\pi(hx_j+ky_j+lz_j)} = |F_{hkl}|e^{i\varphi(hkl)}$$

And calculate the inverse Fourier transform :

$$\rho(xyz) = \mathfrak{F}^{-1}\{F_{hkl}\} = \frac{1}{V}\sum_{hkl} |F_{hkl}|\, e^{i\varphi(hkl)} e^{-i2\pi(hx+ky+lz)}$$

The function $\rho(xyz)$ is known as the electron density map (Figure 1-5). Peaks in the maps correspond to maximum of electron densities and therefore to the position of the atoms within the unit cell. The amount of electrons within a limited volume at that position characterizes the nature of the atom. This is what crystallographers called the structure.

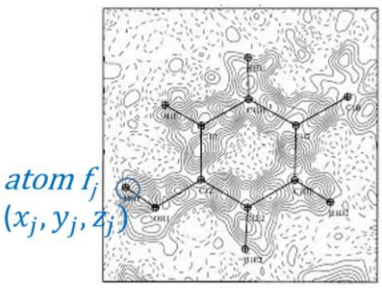

Figure 1-5 : “The structure”

The problem is that the process of inverse Fourier transform is not that simple because the intensities that are collected $I_{hkl} = |\langle F_{hkl} \rangle|^2$ are only one part of the structure factor, the phase $\varphi(hkl)$ is completely unknown and cannot be determined directly from a diffraction experiment. This is the (in)famous “phase problem”.

How not to deal with the phase problem

One way and very old way to avoid the phase problem is just to ignore it. This is a very common way to deal with a problem in general. It is done by ignoring the phase and by taking the inverse Fourier transform of $|\langle F_{hkl} \rangle|$. This gives the autocorrelation function of the electron density in the unit cell and is referred as the Patterson map or in the case of completely order system, the Pair Distribution Function (PDF). Despite it is possible by inspecting the Patterson to recover the periodicity of the crystal, it is not possible to tell the position of the atoms in the unit cell. Only information about interatomic vectors are available through the analysis of the PDF. Many methods exist in crystallography to guess and refine such information in order to obtain a crystallographic model which matches well with the experimental data and circumvents the phase problem. This Patterson method has been mostly abandoned since the discovery of very powerful algorithm that recover the phases. Nevertheless, we will see in the chapter 3 that it can be a valuable tool to describe correlated disorder in crystals. I will present the theory of PDF and some simple example in chapter 3.

How to deal with the phase problem

Solution came in 1955 with the invention of **the direct methods** by Hauptman and Karle for which they were awarded the 1985 Nobel Prize in Chemistry. The Nobel Prize citation was “for their outstanding achievements in the development of direct methods for the determination of crystal structures”. The methods generally exploit constraints or statistical correlations between the phases of different Fourier components that result from the fact that the scattering density must be a positive real number.

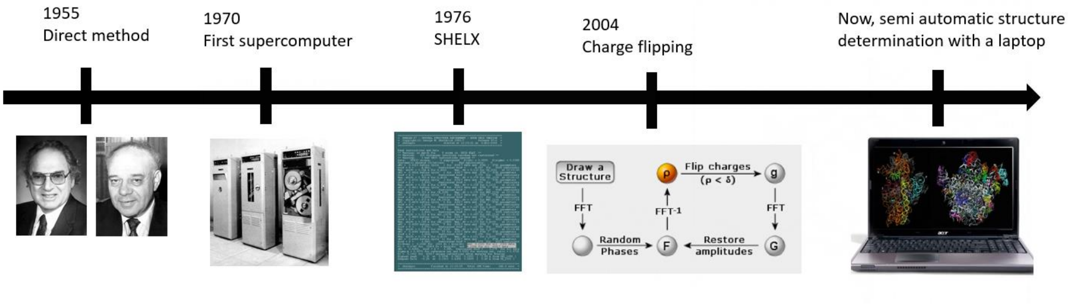

Figure 1-6 : evolution in crystal structure determination

Several packages implement the direct methods and the most famous one is SHELX with a first version in 1976. Another more recent phase retrieval algorithm is the **charge flipping algorithm** (CFA). This algorithm was proposed by G. Oszlányi & A. Sütó [1]. This algorithm does not requires any a priori information other than the diffracted intensities. It consists of four steps indicated in the Figure 1-7 below:

1. Calculate the inverse Fourier transform of the structure factors. The resulting electron density $\rho(x)$ has positive and negative peaks due to the wrong phases.

2. The negative peaks (up to a small limit δ) are set positive (charge flipping) and a new electron density function is established.

3. The Fourier transform of this new density is calculated.

4. The phases of the new structure factors are kept but the amplitudes of the structure factors are replaced by the experimental ones.

This procedure continues in a loop with step 1 to 4 until a converging solution is found. The final result should indicate the proper electron density of the structure based on the experimental structure amplitudes.

For more detailed explanation of CFA, I invite the reader to read the article “the charge-flipping algorithm in crystallography” by Lukas Palatinus in Acta Cryst B published in 2013 [2]. He discussed among other things the competitiveness with state-of-the-art software and methods and concluded that the choice of the method is a matter of taste, habits, the ease of use … In my research, one of the main advantage of the CFA is that it can be applied in arbitrary dimensions, allowing the solution of ordinary periodic structures as well as modulated structures and quasicrystals. I will discuss the CFA applied to aperiodic system in chapter 2.

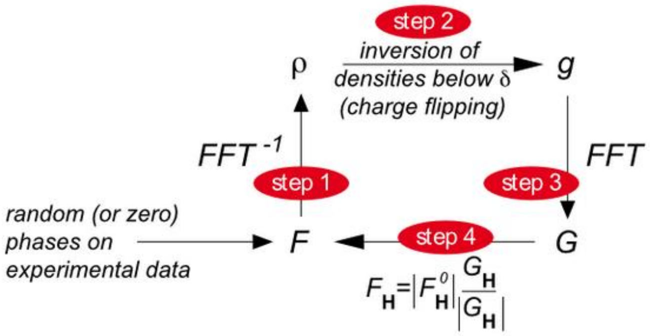

Figure 1-7 : the charge flipping algorithm

Thanks to this algorithm and their integration to popular software, structure determination is now a very common task for crystallographers. Some of my colleagues can solve structure in less 10 minutes, I’ve seen also diffractometer software solving structures on the fly. The bottleneck of this technique is the ability of the chemists to synthesize and grow good quality and relatively large single crystals. The only thing that I know is that growing crystals is the work of artists and my feeling (and my lack of knowledge) doesn’t differ when I look at a crystal or at a painted masterpiece.

1.3 CRYSTALLOGRAPHY STUDY OF PHASE TRANSITION

When we change the external conditions, some crystals undergo a phase transition. Although phase transition often refers to solid/liquid/gas transition, in solids, phase transition means a change of the structure without changing is chemical composition. They are classified into two primary groups :

First-order phase transitions involve a latent heat. During these transitions, a system either absorbs or releases a fixed (usually substantial) amount of energy per unit volume. Throughout this process, the system's temperature remains constant as heat is added. These changes involve abrupt shifts in volume, enthalpy, and entropy resulting from alterations in the way the crystals are packed. Although this transition requires symmetry breaking to qualify as a first-order transition, the position of the atoms shift from one structure to another must happen in a coordinated manner, and these displacements should be small. Examples are the phase transition from the ice to water or Ferro to paramagnetic in iron.

Second-order phase transitions, also known as "continuous phase transitions," exhibit distinct characteristics. They are marked by a divergent susceptibility, an infinite correlation length, and a power-law decay of correlations near the critical point. Famous examples of second-order phase transitions include the ferromagnetic transition, superconducting transition (with Type-I superconductors displaying a second-order transition at zero external field, and Type-II superconductors having second-order transitions in various states), and the superfluid transition. Lev Landau formulated a phenomenological theory for second-order phase transitions : second order phase transitions occur when a new state of reduced symmetry develops continuously from the disordered (high temperature) phase. The ordered phase has a lower symmetry and implies a phenomenon of spontaneously symmetry breaking. He introduced also the concept of **order parameter** which is a measure of the degree of order across the boundaries in a phase transition system; it normally ranges between zero in the high temperature phase and nonzero in the other. One way to describe a phase transition is therefore to understand what is or are the order parameters and measure them. Order parameters may be a symmetry breaking order parameter associated to a change of symmetry in the system or a totally symmetric order parameter that is usually associated to a local transformation like a change of electronic or magnetic state of a molecule.

Diffraction is wonderful tool to study phase transition because we can have access to the geometry of lattice, the symmetry in the structure and the local structure of the molecule.

1.3.1 Cell parameters and lattice determination

The position of the Bragg peaks which are defined by $S(\boldsymbol{q})$ are related to the lattice through the calculation of $L(\boldsymbol{r}) = \mathfrak{F}^{-1}\{S(\boldsymbol{q})\}$. This is easily compute and is a basic exercise for undergraduate students. The determination of the lattice parameters allows to classify the crystal in one of the seven crystal system (cubic, quadratic…). By measuring the position of the Bragg peaks function of a change of external parameters such as temperature, we can follow the dependence of the cell parameters and observe phase transitions.

1.3.2 Crystal symmetry

We can show that symmetry elements in the lattice such as unit cell centering or glide planes induce systematic absences, i.e Bragg peaks that are systematically absent :

Exemple of C centering

$$F(\boldsymbol{G_{hkl}}) = F_{hkl} = \sum_j f_j(\boldsymbol{G_{hkl}})\, e^{i2\pi(hx_j+ky_j+lz_j)}$$

$$F_{hkl} = f\, e^{i2\pi(hx+ky+lz)} + f\, e^{i2\pi(h(x+\frac{1}{2})+k(y+\frac{1}{2})+lz)}$$

$$F_{hk0} = f\, e^{i2\pi(hx+ky)}(1+e^{i\pi(h+k)})$$

$$F_{hk0} = f\, e^{i2\pi(hx+ky)}(1+(-1)^{(h+k)})$$

$$F_{hk0} = 0, \text{if h + k odd}$$

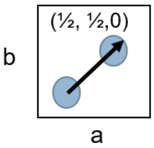

2 identical atoms at (x,y,z) and (x+½, y+½,z)

In order to characterize the symmetry of a crystal, we have to look for those systematic absences. The best way to do it is to look directly at the diffraction images. Most of the modern software for diffraction analysis provide an algorithm to reconstruct – unwarp diffraction images of a given reciprocal plane. It is straightforward to observe systematic absences condition with bare eyes. (Figure 1-8)

The observation of the symmetries of the crystal allows the determination of the space group. Three dimensional periodic crystals can be classified within the 230 possible **space group** at 3 dimension. We will see in the chapter 2 that we can do the same procedure to classify aperiodic crystals within the superspace group classification.

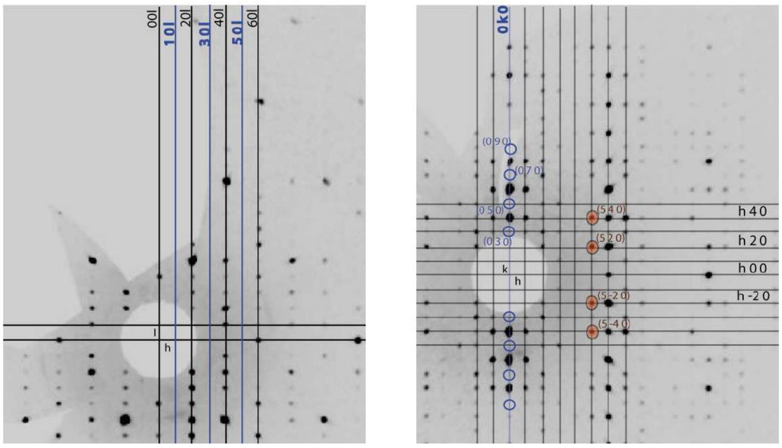

Figure 1-8 : reconstructed diffraction pattern of TMTTF-Mellitate at 120K showing systematic absences ((blue circle) of the type (h odd, k, l) in the (h0l) plane (left) and type (0, k odd, 0) in the (hk0) plane (right). The associated symmetry elements are a a-glide plane perpendicular to the b axis and a 2_1 screw axis along the b axis (J. Rio, L.Guérin, unpublished data).

I have the feeling that the step of space group determination is often overlooked by many of my colleagues. The reason is that it exists algorithm that automatically search for systematic absences after the data reduction, directly by looking at integrated intensities in the hkl file. Yes, this works most of the times but I can also tell that I have seen numerous error. Because the structure determination for the direct methods and the structure refinement rely on the symmetry of the system, it is very important to define the space group with confidence. Note that surprisingly, symmetry is not required for CFA and symmetry constrained CFA is even less efficient [2].

1.3.3 Group-subgroup relationships

Another interest of defining the space group of each phase is due to the fact that, in the case of structural phase transition associated with a loss of symmetry element, the space group of the low symmetry phase is related to the space group of the high symmetry phase by a group-subgroup relationship. Some significant applications include [3]:

1. Establishing clear and concise structural connections between different crystal structure types by constructing family trees of group-subgroup relationships
2. Solving issues related to twinned crystals and antiphase domains.
3. Investigating changes in structures and physical properties that occur during phase transitions, with applications of Landau theory. Various references, including Aizu, Aroyo & Perez-Mato, Birman, Cracknell, Howard & Stokes, Igartua et al., Izyumov & Syromyatnikov, Landau & Lifshitz, Lyubarskii, Salje, Stokes & Hatch, and Toledo have explored these aspects (see references in [3])

The use of crystallographic group-subgroup relationships has proven to be a valuable tool to study phase transition. It can be extend to aperiodic materials as presented in chapter 2.

1.3.4 Symmetry breaking and superstructure Bragg peaks

When a phase transition is accompanied with a symmetry breaking, additional Bragg peaks appears which sign the apparition of an higher order phase. They are called superstructure Bragg peaks. Their intensity is related to the value of symmetry breaking order parameter in each phase. In the high symmetry disordered phase, the order parameter is null and the superstructure Bragg peaks are absent. In the low symmetry phase, symmetry breaking occurs, **superstructure Bragg peaks** appear and their intensity can be related to the order parameter as follows for the case of a simple order-disorder transition on one site:

For this calculation, we consider a crystal constituted of a molecule that can be in two different states A and B with an associated molecular structure factor F_A and F_B. In the high symmetry phase, all sites are in the A state. In the low symmetry phase, one site every two site along the a axis can switch to the B state so that ABABABA long range order appears (Figure 1-9). The symmetry breaking associated with the doubling of unit cell along the direction *a*, which corresponds to a transition at the Brillouin zone border, imposes the presence of the symmetry breaking order parameter η. It describes the ordering of A/B species in the low symmetry phase.

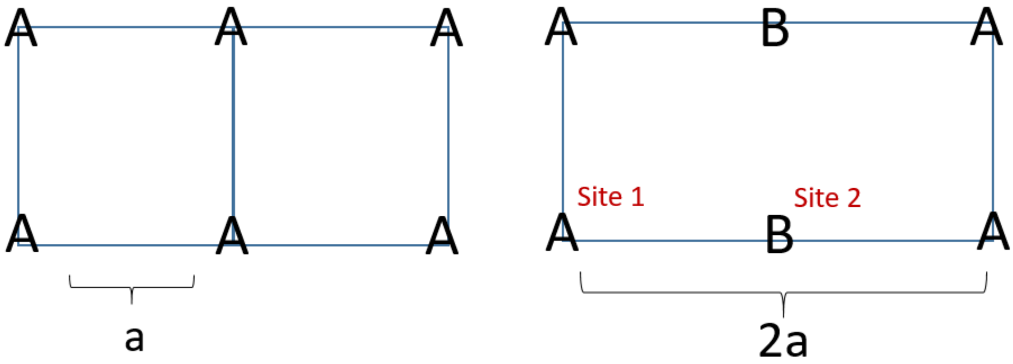

Figure 1-9: high and low symmetry phase with two sites occupied by species A and B.

We introduce this order parameter η that defines the A species population of the two non-equivalent sites (1 and 2)

$\eta = \gamma_A^1 - \gamma_A^2$, where γ_A^1 and γ_A^2 are the proportion of A on site 1 and 2 respectively.

The structure factor in the intermediate phase can be separated into two terms for the two sites not equivalent by symmetry. If F_A and F_B are the structural factors respectively of A and B molecules, the mean structure factor in the double unit cell is :

$$< \mathrm{F(hkl)} >= \gamma_A^1 \mathrm{F_A} + (1 - \gamma_A^1)\mathrm{F_B} + [\gamma_A^2 \mathrm{F_A} + (1 - \gamma_A^2)\mathrm{F_B}]\mathrm{exp}(-\mathrm{i}\pi \mathrm{h})$$

For h odd,

$$< \mathrm{F(hkl)} \geq [\gamma_A^1 - \gamma_A^2] \times (\mathrm{F_A} - \mathrm{F_B}) = \eta \times (\mathrm{F_A} - \mathrm{F_B})$$

The h odd condition of the double unit cell corresponds to the condition (h+1/2, k, l) and defines the superstructure Bragg peaks. In the high symmetry phase, all sites are in the A state, therefore η is null and the superstructure Bragg peaks associated to the symmetry breaking are absent. In the low symmetry phase, the square root of the intensity of the superstructure lines (h+1/2 k l) associated with the cell doubling is proportional to the order parameter η.

Measuring the intensity of the superstructure Bragg peaks permits the measurement of the symmetry breaking order parameter. This is a very common technique when we want to study phase transition in crystal. We will see numerous examples in this manuscript.

1.3.5 Pretransitionnal phenomena and diffuse scattering

Critical phenomena occur near the phase transition. In a very naïve way, we can describe the apparition of the low symmetry phase as the formation of local domains with a finite size that fluctuate within the high symmetry phase. In the phenomenological approach of Ginzburg-Landau, the fluctuation are taken into account by introducing an order parameter that varies spatially. Near the critical point, fluctuations of the order parameter correspond to the apparition of a local order defined by correlation length. In the reciprocal space, this local order will give rise to diffuse scattering. The analysis of the diffuse scattering will be presented in the chapter 3.

1.3.6 Structure analysis

Solving the structure of both phases is another way to analyze the phase transition. In the case of molecular materials for instance, changes of electronic or magnetic state of a molecule are often accompanied by a reorganization of the material at the molecular level with change of bond length, torsion, bending… Most of the diffraction measurements are performed with sub angstrom resolution and allow the measurement with a very high precision of distances and angles between atoms or bonds that can be used to define electronic states of a molecule.

The analysis of diffracted pattern from crystals is a wonderful tool to study phase transition and its associated changes of functionality. Phase transition can be followed looking directly at the diffraction pattern and spotting change of positions of Bragg peaks or apparition of superstructure Bragg peaks. The symmetry can be analyzed through group-subgroup relationships, order parameters measured with the intensity of Bragg peaks, change of electronic state or spin spate through the analysis of bond length or bond angles. Diffraction measurements give so rich results.

1.4 ADVANCES IN EXPERIMENTAL TECHNIQUES

During the last 20 years of my research work, I took part in or witnessed the improvement of experimental X-ray diffraction techniques to obtain the best quality data, with the highest resolution in the shortest amount of time. The adage a picture is worth a thousand words is popularly attributed to Confucius, but according to Wikipedia was born much more recently: "It is believed that the modern use of the phrase stems from an article by Fred R. Barnard in an advertising trade journal, in 1921, promoting the use of images in advertisements".

So let me show you three pictures that we obtained on a crystal of Alkane-urea crystal that will for sure advertise the improvement of the quality of data in just 10 years (Figure 1-10).

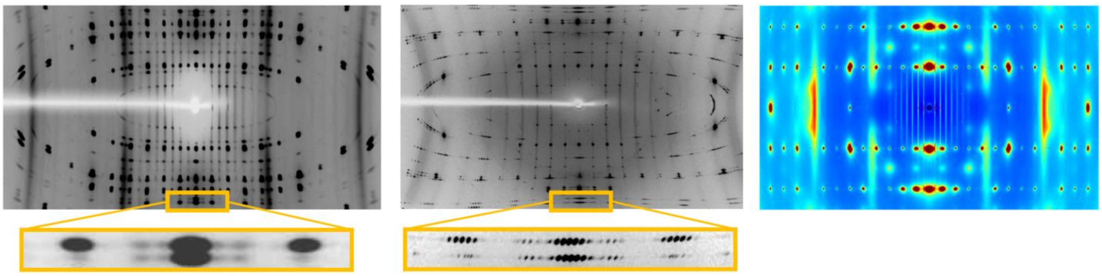

Figure 1-10 : oscillation image of nonadecane/urea single crystal at 100K. left : molybdenum source, 30s exposure, image plate. Middle : copper source, 30s exposure, image plate detector. Right : ESRF synchrotron source, 1s exposure, Pilatus single photon detector.

The first two images were obtained around 2010 at the Institut de Physique de Rennes during the commissioning of our new diffractometer system. At that time, we installed and commissioned a new diffractometer with the purpose to study aperiodic materials. We needed very high resolution, very high flux and very good signal/noise ratio in order to observe weak satellites peaks and diffuse scattering. The solution we selected was the Cu rotating anode as source and an image plate as detector. We can clearly see the improvement of the resolution on the enlarged images of the structure Bragg peak and the satellites Bragg peaks. In the case of the low resolution, it is impossible to observe and/or define the position of the satellites Bragg peaks as they are merged within the structure Bragg peak whereas with the Cu source, Bragg peaks are clearly defined and we can use this kind of image to characterize the aperiodicity in the alkane-urea system. The last image was obtained in 2016 at the ID29 beamline of the ESRF. The synchrotron source from an U21 undulator at 15keV was monochromatized using a silicon (111) and the diffracted pattern was recorded using the Pilatus 6M single photon counting detector. In other words, the diffracted pattern was obtained using one of the best X-ray source in the world on one of the best detector in the world. I think this image is astonishing and beautiful. It shows with a precision and clarity almost every type of scattering signals we can get from a crystal : structure Bragg peaks, satellites, thermal diffuse scattering, diffuse scattering from 1st kind disorder, 2nd kind disorder and pretransitionnal diffused scattering. The combination of having a very reliable and high resolution diffractometer at home to perform day to day analysis and the campaign at large scale facility such as ESRF, SOLEIL, APS, ALS, ISIS was very fruitful as we will see later.

The development of software and automated diffractometer permits even non specialized scientists to determine simple structure in a routine manner. This is a very important result of the work of the crystallographers of the last century. We can now consider that the structure determination from X-ray diffraction is a standard characterization tool available for the solid state scientist. In the meantime, the application of the most recent techniques in diffraction allows the investigation of more and more complicated problem. Pour crystallinity or very small sample can be studied as well as sample under extreme condition like high pressure or intense pulsed laser light. As single photon detector or intense X-ray source are becoming more and more available to the crystallographer, it is becoming complicated to ignore very weak satellites or diffuse scattering and discard them in the discussion of the structure-property relationship. Some of the properties of the system originate from disorders in the system or from aperiodic orders. For example, the analysis of all the kind of scattering shown in Figure 1-10 was necessary to understand the physics of alkane-urea. I, my colleagues from the group and other independent team in the world developed tools, software and techniques to analysis “out of the Bragg” signals. We will learn the methods in the chapter 2 and 3.

Additionally to the development of analysis tools, I’ve spent hours and hours at the beginning of my scientific journey at constructing and operating beamlines. Building a beamline from scratch is a very interesting project on its own and the presentation of this work deserve to be done as it represents 5 years of my career but it is out of the scope of this topic. I will present briefly in the chapter 4 the research I developed as a beamline scientist at the Photon Factory synchrotron, Japan and the ESRF synchrotron, France.

1.5 A CASE STUDY : SPIN CROSSOVER SYSTEMS

In the spirit of the article “Crystallography and spin crossover. A view of Breathing materials” by Pr. P. Guionneau [4] or “Spin-crossover materials: Getting the most from x-ray crystallography” by Dr. S. Pillet [5], I will use our crystallography studies of spin crossover systems (SCO) as a case study on how crystallography tools presented in 1.3 can be applied to evidence, characterize and interpret phase transitions in materials and reveal the relation between the change of the structure and the change of properties.

SCO involves the alteration of the electronic configuration in a transition metal compound, shifting between high spin (HS) and low spin (LS) states due to external factors like temperature, pressure, light, magnetic and electric fields. This transition induces changes in the material's magnetic, optical, and structural properties. The interplay between the material's inherent properties and external conditions has been extensively explored over the past three decades, revealing a complex phenomenon [6,7].

The SCO is evident in first-row transition metal elements with electronic configurations from d^4 to d^7. In octahedral iron(II) complexes for instance, the SCO is associated to the electronic configuration shift from a paramagnetic high-spin (HS) state (S = 2) to a diamagnetic low-spin (LS) state (S = 0). In the ground state, the distribution of electrons in the e_g and t_{2g} orbitals depends on the strength of the ligand field and electronic repulsion. When the ligand field is strong, the energy difference between e_g and t_{2g} prevails over the electronic repulsion between electrons per orbital, resulting in the Low Spin (LS) state. The orbitals are filled in a manner that minimizes the total spin (S=0, diamagnetic state). On the other hand, when the ligand field is weak, electrons occupy the orbitals following Hund's rule, maximizing the total spin (S=2, paramagnetic state), leading to the High Spin (HS) state.

These materials often exhibit photo-switchable properties and undergo photoinduced phase transitions between different spin states, known as the Light-Induced Excited Spin-State Trapping (LIESST) effect [8].

The phase transition is typically depicted by the evolution of the High Spin fraction (γHS), i.e., the percentage of species in the High Spin state, as a function of temperature. In accordance with theoretical models (thermodynamics and Ising model), the variation of this parameter is associated with interactions between molecules. In solids, depending on the strength of molecular interactions, the transition curve can be gradual (weak interactions) or abrupt, resulting from long-range cooperative interactions (Figure 1-11) [9,10].

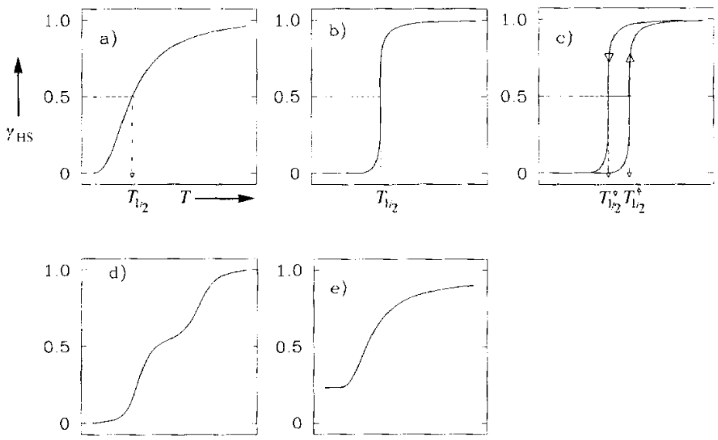

Figure 1-11 : possible types of phase transition in SCO: a) Gradual transition b) First-order transition (abrupt): The phase shift is discontinuous and covers only a few kelvins. Strong interactions between molecules in the High Spin state accelerate the transition. c) Transition with wide hysteresis. d) Two-step. e) Partial transition. (figure from [9])

The structural modifications induced by the spin conversion primarily involve the metal-ligand distances. Figure 1-12 schematically represents the expansion of the coordination sphere that consistently accompanies the Low Spin (LS) to High Spin (HS) transition in the case of Fe(II). In the High Spin state, initially vacant non-bonding e_g orbitals become populated. The lobes of these orbitals, directed towards the coordinated elements, then repel the ligands. This process contributes to the expansion of the metal coordination sphere during the LS to HS transition. At the intramolecular level, this process is primarily assessed by the average metal-ligand distance, which increases during the LS to HS transition. The structural resolution of Fe(II) complexes coordinated with nitrogen ligands (commonly encountered) has demonstrated a significant variation in this length between the two states, approximately 0.2 Å (10%). At the intermolecular level, this results in an increase in the volume of the crystal lattice. The SCO phenomenon initiates at the metal center and then spreads throughout the solid material across various scales, influencing structural ordering up to the macroscopic level.

The substantial structural changes at both intra and intermolecular levels, associated with elastic interactions between molecules, can be precisely studied through X-ray diffraction and represent distinctive signatures of the spin transition.

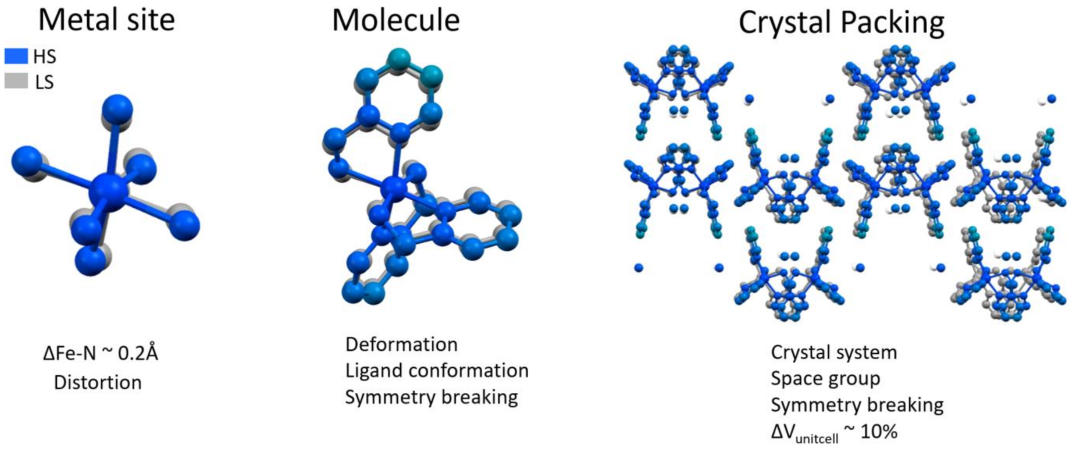

Figure 1-12 : : atomic structure of the metal site, the molecule and the crystal packing for the low spin state (grey) and the high spin state (blue). The low to high state transition is associated to distortion of the metal site, deformation of ligands, symmetry breaking, change of crystal system and space group and unit cell expansion (adapted from [4])

1.5.1 First case : HS/LS ordering in $[Fe(2\text{-}pic)_3]Cl_2$ EtOH

The $[Fe(2\text{-}pic)_3]Cl_2EtOH$ belongs to the class of materials undergoing a transition from a diamagnetic Low Spin state (LS, S = 0) to a paramagnetic High Spin state (HS, S = 2) under the influence of temperature, pressure, and magnetic field. The Fe^{2+} ion and six nitrogen atoms from the three 2-pic molecules (2-aminomethyl-pyridine) form a metal-ligand ensemble. Each constituent is connected to three others through hydrogen bonds. The transition between the HS and LS states occurs in two steps, with a plateau observed during the temperature evolution of the fraction γ_{HS} (Figure 1-13). The aim now is to investigate the intermediate phase using crystallography. [11,12]

Let’s recall the tool we have to study phase transition using crystallography :

1. Cell parameters and lattice determination
2. Crystal symmetry
3. Group-subgroup relationships

4. Symmetry breaking and superstructure Bragg peaks
5. Pretransitionnal phenomena and diffuse scattering
6. Structure analysis

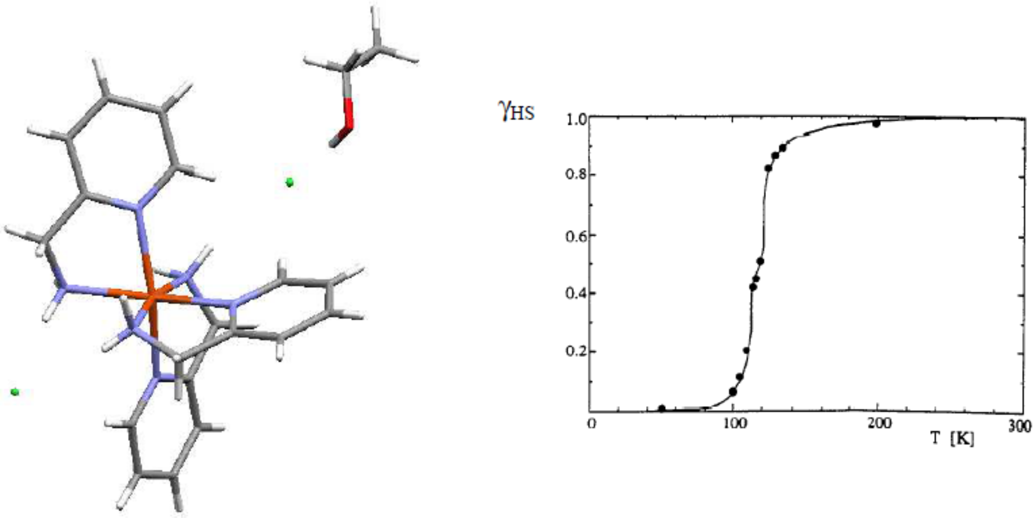

Figure 1-13 : Structure of [Fe(2-pic)$_3$]Cl$_2$EtOH (left). Transition curve (right) determined from magnetic measurements.

Cell parameters and lattice determination

Figure 1-14 shows the evolution of the cell parameters with the temperature. We can see clearly two abrupt changes of the cell parameters at 109K and 117K. They signed two phase transitions from the low spin (LS) low temperature phase to an intermediate (IS) phase at 109K and from the IS to the high spin high temperature phase at 117K. The crystal system in the three phases is monoclinic. As expected, the volume of the unit cell changes around 3% from LS to HS.

Crystal symmetry

Analysis of the diffraction pattern and systematic extinctions in LS and HS shows the presence of 2_1 screw axis along the b axis and a c-glide plane perpendicular to the b axis. The space group is $P2_1/c$ for both phases.

Group-subgroup relationship and superstructure Bragg peaks

The lattice parameter a, and consequently the volume, doubles in the intermediate phase (Figure 1-15). This doubling of the lattice is associated with the loss of symmetry elements and results in the appearance of superstrucure Bragg peaks in the intermediate phase. All Bragg peaks (h+1/2 k l) are indexed in the lattice of the LS phase (space group P21/c) and HS phase (P21/c).

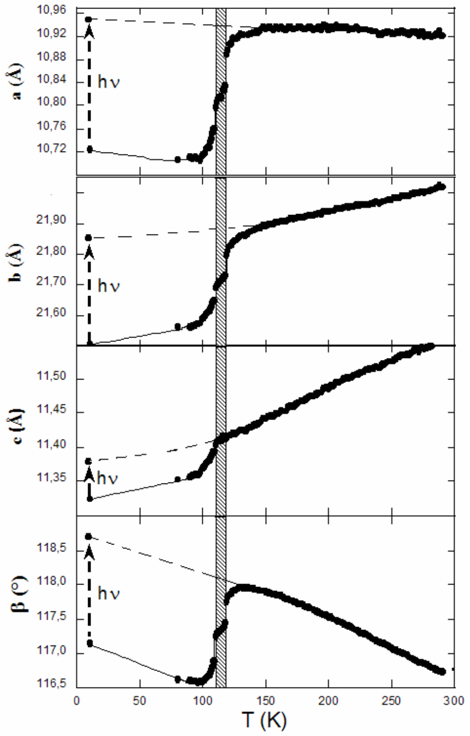

Figure 1-14 : Evolution of lattice parameters as a function of temperature. Two discontinuities delineating the intermediate phase appear at T1 = 109 K and T2 = 117 K and are characteristic of two first-order transitions between the HS phase and the intermediate phase, and the intermediate phase and the BS phase. The lattice parameter is doubled in the intermediate phase, but this doubling is not represented for the sake of clarity.

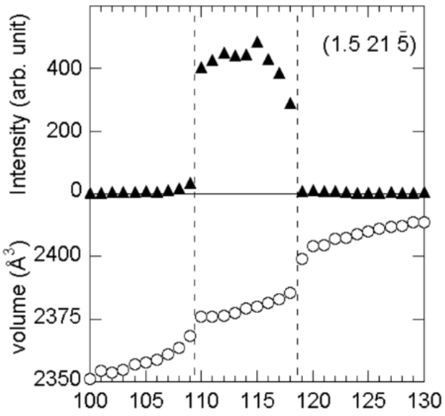

Figure 1-15 : Temperature dependence of the volume (bottom) and the Bragg peak (1.5 21 –5) indexed in the P21/c space group. New Bragg peaks appear in the intermediate phase, characteristic of symmetry breaking, and the volume is doubled (not shown in the figure).

In the intermediate phase (IS), the symmetry breaking associated with the lattice doubling leads to the loss of other elements (inversion centers and 2_1 axes) (Figure 1-16). The space group is $P2_1/n$.

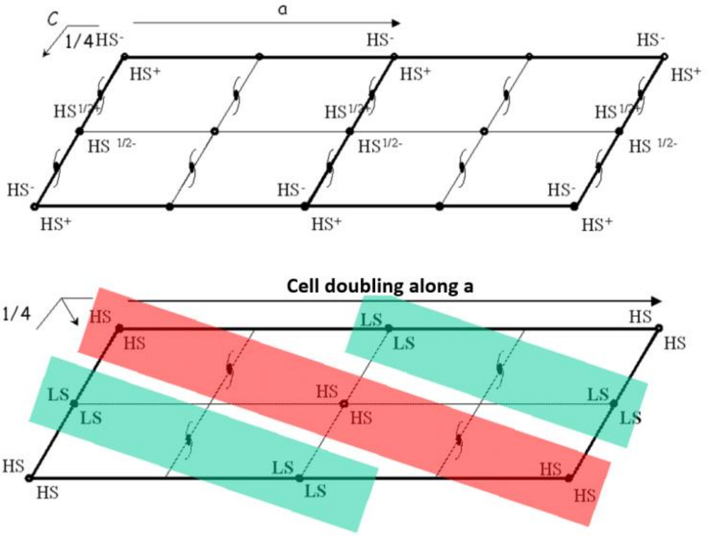

Figure 1-16 : Representation of the space group of the HS and BS phases (top) and the intermediate phase (bottom). The lattice doubling has resulted in a change from the $P2_1/c$ space group to the $P2_1/n$ space group. Ordering of HS and BS planes is induced by symmetry.

The restoration of these symmetry elements in the LS phase corresponds to a re-entrant phase, where the symmetry of the HS phase reappears in the LS phase but differs from that in the intermediate phase.

Structure analysis of the intermediate phase

The resolution of the crystal structure of the LS and HS phase shows as expected a change of the distance Fe-N in the LS and HS states (Figure 1-17) of around 0.2 Å.

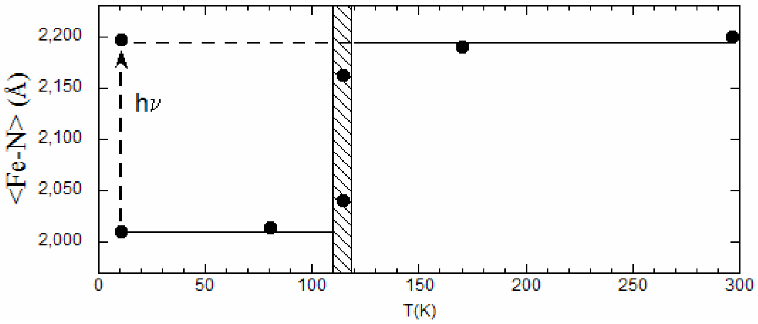

Figure 1-17 ; Temperature dependence of the Fe-N bond length. The bond length for the two non-equivalent ferrous sites is characteristic of the coexistence of an HS state and a BS state in the intermediate phase (striped zone).

IP phase reveals that every other site is populated by HS and LS molecules, as indicated by the Fe-N bond lengths at each site. This implies that the Fe-equivalent sites by symmetry in the HS or LS phase are no longer equivalent in the intermediate phase. This symmetry breaking corresponds to a long-range ordering of planes composed of entirely LS molecules and planes composed of entirely HS molecules.

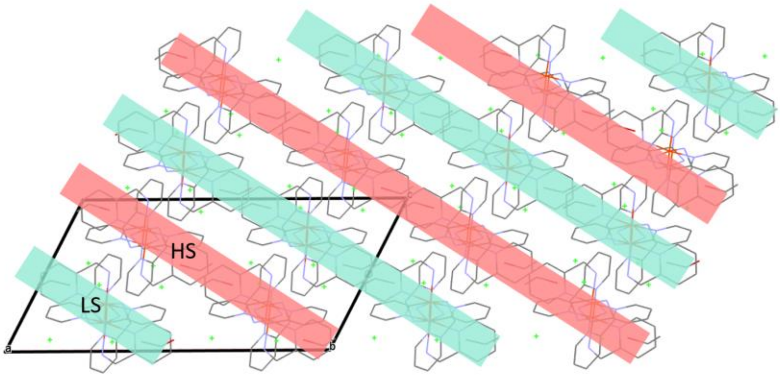

Figure 1-18 : Structure of the intermediate phase. The symmetry breaking in the intermediate phase induces a long-range ordering of HS and LS planes.:

As shown in Figure 1-18, the resolution of the structure of the intermediate phase reveals that every other Fe site is in the LS or HS state. The arrangement of these sites occurs in the form of successive planes entirely composed of LS or HS states. Chernyshov et al. [13] measured that the population of HS species on a site is 0.85. In our study [12], we did not observe disorder on sites where 100% of the molecules occupying site 1 or 2 are in the HS or BS state, respectively. Therefore, the crystal structure consists mainly of HS and LS stripes alternating in a HS-LS-HS-LS sequence which can be described as a spin-state concentration wave (SSCW).

Symmetry breaking and order parameter

The symmetry breaking associated with the doubling of the lattice along the a direction, corresponding to a transition at the BZ edge, necessitates the presence of a symmetry breaking order parameter in addition of the totally symmetric average HS fraction γHS order parameter. This parameter describes the ordering of HS/LS species in the intermediate phase. Following what we did in 1.3.4, we introduce the order parameter η, which defines the population of HS species on the two non-equivalent sites (1 and 2) by symmetry in the ordered intermediate phase. $\eta = \gamma_{HS}^{1} - \gamma_{HS}^{2}$, where γ_{HS}^{1} and γ_{HS}^{2} are the proportion of HS molecules on site 1 and 2 respectively. The square root of the intensity of the superstructure peaks (h+1/2 k l) associated with the lattice doubling is therefore proportional to the order parameter η and is 0 in the HS and LS phases (Figure 1-19). Since no disorder was observed on the sites, the maximum value that η takes in the intermediate phase is 1, corresponding to an occupation of 100% of HS and LS molecules on sites 1 and 2, respectively.

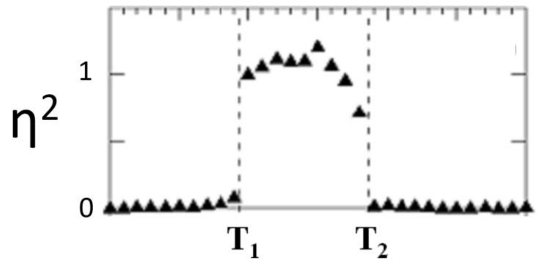

Figure 1-19 : Temperature dependence of the square of the order parameter η associated with the

1.5.2 Case 2 : Stair case like conversion and multistep transition in $\{Fe[(Hg(SCN)_3)_2](4,4'\text{-bipy})_2\}_n$

In a paper published in 2016 in Angewandte Chemie [14], we reported a bimetallic 2D coordination polymer $\{Fe[(Hg(SCN)_3)_2](4,4'\text{-bipy})_2\}_n$ that exhibits a thermal high-spin (HS) low-spin (LS) staircase-like conversion characterized by a multi-step dependence of the HS molar fraction γHS. Between the fully HS (γHS=1) and LS (γHS=0) phases, two steps associated with different ordering appear in terms of spin-state concentration waves (SSCW).

Evolution of the χT product (χ=magnetic susceptibility, T temperature) was used to characterize the conversion of γHS against T, as shown in Figure 1-20. Above about 180 K, χT value is consistent with a fully Fe^{II} HS (γHS=1) phase. Below about 95 K, χT is indicative of a fully Fe^{II} LS phase (γHS=0). Furthermore, the γHS versus T plot shows two other steps in addition to the HS and LS phases. One in the 108–125 K interval, where γHS=0.5, and one in the 96–108 K interval around γHS=0.34. Single-crystal X-ray diffraction data have been recorded for different temperature in order two characterize the two steps using our crystallographic tools presented in 1.3. Similar to the first case of $[Fe(2\text{-pic})_3]Cl_2EtOH$, by looking at the change of the unit cell parameters and volume, we evidenced the three phase transitions in agreement with the magnetic susceptibility measurement.

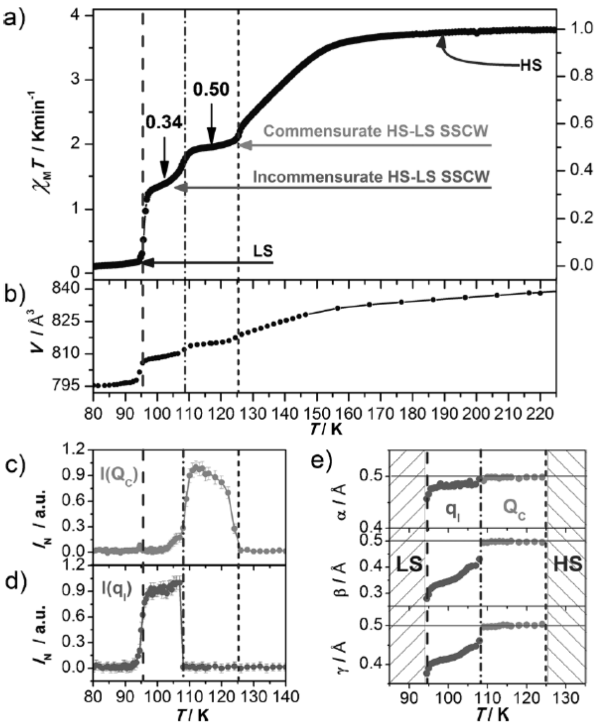

Figure 1-20 : a) Temperature dependence of χT, scaled to γHS b) Unit cell volume given in the (a,b,c) cell of the HS and LS phases. c) Intensity of superstructure, indexed Qc = ½ a*+ ½ b*+ ½ c* d) Intensity of the satellite reflections, indexed q_i = αa*+βb*+γc*. e) Evolution of the coordinates a, b, and γ of Qc and q_i.

The first plateau γHS=0.5

The crystallography analysis of the step γHS=0.5 is exactly similar to what we already presented for the first case. A symmetry breaking occurs on the 108–125 K plateau, which corresponds to a doubling along (a+b+c) and is characterized by the appearance of superstructure Bragg peaks at **Qc** = ½ **a***+ ½ **b***+ ½ **c*.** The intensity of the Bragg peaks is dependent on temperature (Figure 1-20-c) indicating that this phase is surrounded by two first-order phase transitions around 125 and 108 K, in agreement with magnetic data. The intensity of the superstructure Bragg peaks are related to the order parameter η^c which defines the population of HS species on the two non-equivalent sites (1 and 2). The structural refinement at 117 K in the doubled cell reveals two different iron sites: site 1 is mainly LS, and site 2 is mainly HS. We estimated γHS=0.05 on site 1 and γHS=0.95 on site 2. Therefore, the crystal structure consists mainly of HS and LS stripes alternating in a HS-LS-HS-LS sequence along **Qc**, which can be described as a spin-state concentration wave (SSCW) and is commensurate with the initial (a,b,c) lattice (Figure 1-21). This spatial modulation of γHS, translating through the modulation of Fe_N, is schematically represented by a wave in Figure 1-21, and is related to the modulation of the probability that crystalline sites in **r** will be HS:

$$\gamma_{\mathrm{HS}}(\mathrm{r}) = \gamma_{\mathrm{HS}} + (\eta^c/2)\cos(\boldsymbol{Q}_c\boldsymbol{r})$$

The amplitude of the wave is η^c=0.9, which is related to the probability of HS state population by sites 1 or 2.

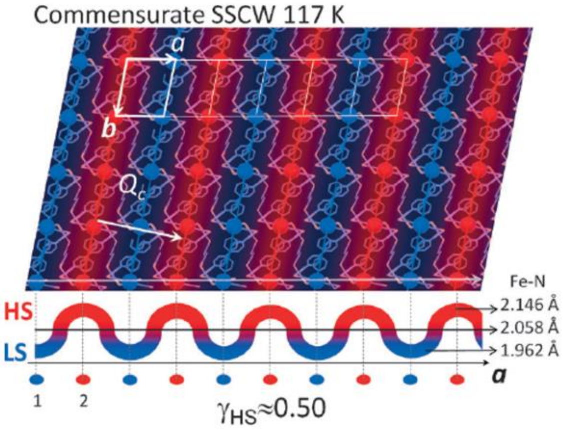

Figure 1-21 : Striped structure sliced in the (a,b) plane of the SSCW forming along Qc. It is commensurate with the (a,b,c) lattice (white) and made of mainly LS (blue, Fe_N=1.962) and HS (red, Fe_N=2.146) sites alternating in the LS-HS-LS-HS sequence around Fe_N=2.058 (γHS=0.5).

The second plateau γHS ≈ 0.34

Another step is observed at γHS≈0.34, which is close to 1/3. The nature of the order on this step is compelling. Analysis of the diffraction pattern showed that the symmetry breaking on the 96–108 K step does not correspond to a unit cell tripling. Different types of Bragg peaks appear, which cannot be indexed with the three vectors basis of the reciprocal lattice. A fourth vector $\mathbf{q_i}$ is required for indexing the scattering vector Q of the peaks, where :

$$\boldsymbol{Q} = \mathrm{h}\boldsymbol{a}^* + \mathrm{k}\boldsymbol{b}^* + \mathrm{l}\boldsymbol{c}^* + \mathrm{m}\boldsymbol{q}_i$$

and $\boldsymbol{q}_i = \alpha\boldsymbol{a}^* + \beta\boldsymbol{b}^* + \gamma\boldsymbol{c}^*$.

At 102 K, α=0.48, β=0.35, and γ=0.42 cannot be expressed as simple rational numbers. Because Bragg peaks are the signature of a long range order, the additional Bragg peaks signs the apparition of long rang order which has a different (and irrational) period than the 3d periodic structure defined by the **a**, **b** and **c** lattice vectors. The structure is therefore no longer 3D periodic. It is an aperiodic structure and we called this kind of aperiodic order, an incommensurately modulated structure. In this study, we used the 4D superspace crystallography and revealed a SSCW incommensurate with the 3d periodic lattice corresponding to a HS-LS sequence incommensurate with the molecular lattice.

How does the superspace crystallography works and how can we define aperiodic order ? This is the topic of the next chapter.

Essentials of aperiodic order and superspace crystallography

Aperiodic crystals are defined as crystalline structures exhibiting long-range order but lacking translational symmetry. They fall into three categories : Incommensurate modulated structures, aperiodic composites and quasicrystals. The concept of **superspace crystallography** was introduced by de Wolff, Janner and Janssen to restore the lost translational symmetry. The Bragg reflections of aperiodic crystals can be indexed using integers by extending the three reciprocal basis vectors with one or more additional vectors, as described by:

$$\mathbf{Q} = \sum_{i=1}^{3+d} h_i \mathbf{a}_i^*$$

where **Q** is the scattering vector of the Bragg reflection, d is the number of additional periodicities, h_i are integer Miller indices, and $\mathbf{a}_i^*$ are reciprocal basis vectors.

In this chapter 2, we present how the superspace crystallography is used to analyze the aperiodic order.

SUPERSPACE CRYSTALLOGRAPHY APPLIED TO INCOMMENSURATE MODULATED CRYSTALS

A modulated incommensurate crystal can be seen as a perturbation of a periodic tridimensional lattice by a modulation which period is in an incommensurate ratio with the periodicity of the mean lattice. Modulation functions can be described as wave functions, defined by a wave vector **q** that determines the direction and wavelength of the wave.

$\boldsymbol{q} = \alpha\boldsymbol{a}^* + \beta\boldsymbol{b}^* + \gamma\boldsymbol{c}^*$, where α, β and γ cannot be expressed as simple rational numbers.

The vectors of the reciprocal space are written: $\mathbf{Q} = h\,\mathbf{a_1^*} + k\,\mathbf{a_2^*} + l\,\mathbf{a_3^*} + m\,\mathbf{q}$

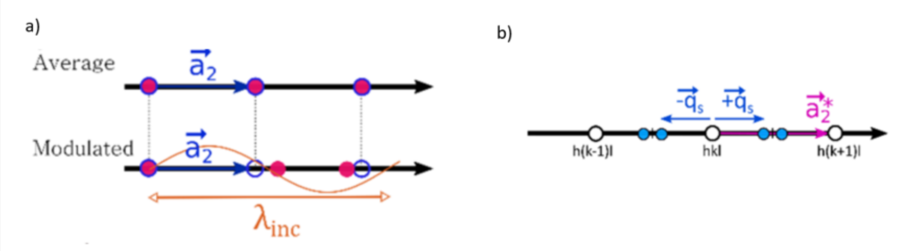

Figure 0-1 : (a) representation in the physical space of dimension 1, where the orange curve corresponds to the amplitude of the longitudinal incommensurate displacement along the axis; blue and pink circles are respectively the mean and the incommensurate positions (b) satellites Bragg peaks (blue circle) appears at positions +/- m**q** apart from the main Bragg peaks (white circle)

Superspace description of 1D incommensurate crystal

In order to recover the periodicity, we introduce a perpendicular direction to the physical space. This new dimension is what we call the superspace. We draw along the internal direction of the crystallographic superspace, the incommensurate modulation function. This defines a superspace cell where atoms are no more points in space but are defined by atomic modulation functions.

Diffraction from 1D incommensurate crystal – reciprocal superspace

The Bragg peaks positions are obtained by a projection of the reciprocal nodes of the associated reciprocal superspace cell on the physical reciprocal space. In the reciprocal space, one can define two types of Bragg peaks, the Bragg peaks (hkl0) also called main reflections, associated to the mean structure and the satellites (hklm) with m≠0 associated to the modulation.

Structure determination and analysis

In the case of a four dimensional superspace group, solving the structure means determining the atomic modulation function of all the atoms of the mean three dimensional unit cell as function of the period along the fourth dimension. Dual-space methods like charge flipping algorithm do not impose restrictions on the form of the reconstructed scattering density, allowing for a direct generalization to superspace. The implementation of the CFA in the Superflip program available in JANA software, allowing the direct solution of structures in superspace, has elevated charge flipping to a preferred method for the ab initio solution of complex incommensurately modulated structures and quasicrystals.

An incommensurate modulated phase in $Et_2Me_2Sb[Pd(dmit)_2]_2$ molecular conductors

$Et_2Me_2Sb[Pd(dmit)_2]_2$ crystal structure is composed of alternately stacked anion layers consisting of $Pd(dmit)_2$ and insulating cation layers. The phase transition from the monoclinic high symmetry phase C2/c to the incommensurate one is marked by a continuous increase of the intensity of the satellite Bragg peaks. The structure of $Et_2Me_2Sb[Pd(dmit)_2]_2$ within its incommensurate phase was refined in a (3+1)-dimensional superspace using JANA and SUPERFLIP Programs. As shown in Figure 0-2, strong modulation of the structure of the dimer as well as the cation can be observed: The position of the Sb atom ΔSb is strongly modulated in the incommensurate phase. The torsion angle Ψ between the two ethyl groups in the Et_2Me_2Sb cation shows also a wide range of modulation. This is not observed for the intermolecular distance $d_{Pd\text{-}Pd}$ between the two $Pd(dmit)_2$ units forming the dimer. Generally, an incommensurate phase arises from a frustration between competitive forces. The structural analysis of the incommensurate phase showed that the competition among the steric effect, the magnetic frustration, and the CS state leads to the emergence of the incommensurate modulation.

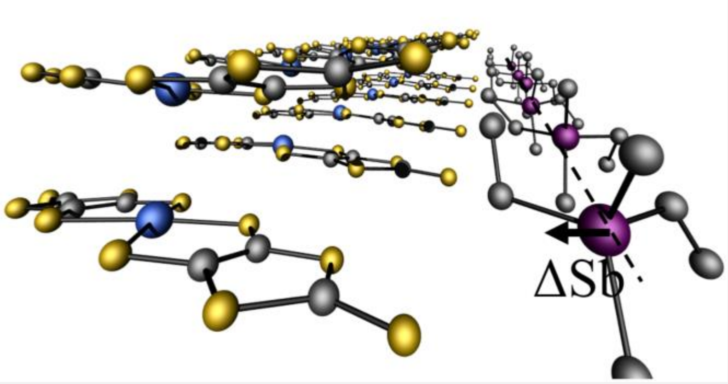

Figure 0-2 : incommensurate structure view from the real space. The Sb atom shows a displacement modulation.

SUPERSPACE APPROACH TO *n*-ALKANE – UREA APERIODIC COMPOSITES

Incommensurate composite crystals are based on two, interpenetrating lattice periodic structures that are mutually incommensurate. Because of the incommensurability, each subsystem attains an incommensurately modulated structure, where the other subsystems act as incommensurate external potentials for the subsystem under consideration.

Alkane-urea composites, formed by the intergrowth of urea ($CO(NH_2)_2$) and alkane (C_nH_{2n+2}) molecules, represent supramolecular compounds with intricate crystal structures. The crystallographic directions of the two subsystems perpendicular to the channels are commensurable. Urea molecules strictly confine alkane molecules, forming a composite crystal consisting of two subsystems with cell parameters along the channel direction generally in irrational ratio. Conventionally, the c-axis of the lattice is taken along this incommensurability direction, denoting c_h as the host urea lattice parameter, c_g as the guest alkane lattice parameter, and $\gamma = c_h/c_g$ as the ratio of the two lengths. By changing the alkane guest, one can modify the periodicity of the guest sublattice C_g and therefore change the incommensurability ratio $\gamma = c_h/c_g$.

For intergrowth nanotubular structures that have a single incommensurate direction $\boldsymbol{c}$, a four-dimensional (4D) superspace description gives the positions of all of the Bragg peaks :

$$\boldsymbol{Q}_{hklm} = h\boldsymbol{a}^* + \boldsymbol{kb}^* + l\boldsymbol{c_h}^* + m\boldsymbol{c}_g{}^*,$$

where $\boldsymbol{a}*$, $\boldsymbol{b}*$, $\boldsymbol{c_h*}$, and $\boldsymbol{c_g*}$ are the conventional reciprocal unit cell vectors. Four indices (h, k, l, and m) are needed to describe the four different types of structure Bragg peaks:

(hk 00) , (hk l 0), (hk 0m), and (hk lm), with l and m different from zero, correspond to the common, host, guest, and satellite Bragg peaks, respectively.

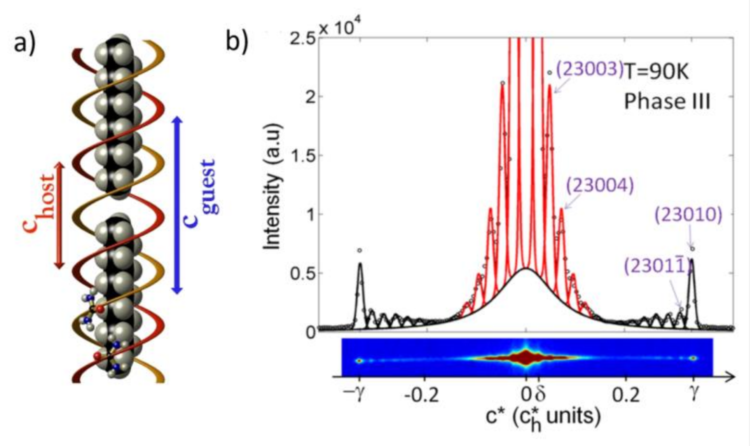

Figure 0-3: (a) Alkane-urea composites, (b) Typical diffraction pattern of alkane-urea composites showing Bragg peaks with 5 indices

.

Long-range modulation of a composite crystal in a five-dimensional superspace

The *n*-tetracosane⁄urea [n-$C_{24}H_{50}$⁄urea] is an aperiodic composite characterized by a misfit parameter very close to a rational number at ambient conditions: $\gamma=c_h/c_g = 0.3335$. The n-tetracosane/urea composite exhibits two phase transitions from 90K to 300K. In order to describe the superstructure Bragg peaks that appear in the low temperature phase, a fifth, independent reciprocal vector must be introduced. This yields the following expression for the set of vectors $\mathbf{Q}_{hklmn}$, which give the positions of the whole set of Bragg peaks in this phase:

$$\boldsymbol{Q}_{hklmn} = h\boldsymbol{a}^{*} + \boldsymbol{kb}^{*} + l\boldsymbol{c}_{\boldsymbol{h}}{}^{*} + m\boldsymbol{c}_{g}{}^{*} + n\,\boldsymbol{c}_{\boldsymbol{m}}{}^{*}$$

Contrary to the high temperature phase of rank 4, full characterization of the diffraction pattern of this lowest temperature phase therefore requires five independent parameters (*h*, *k*, *l*, *m*, and *n*).

The wavelength of the modulation along the channel axis, deduced from the parameter c_m, is on the order of 425 Å in real space. This corresponds to an exceptionally large period, approximately 40 times the pitch of the urea helix. This study demonstrates that, instead of seeking a commensurate lock-in solution, this inclusion compound create an additional modulation with a very long period to satisfy the interaction between the two sub-networks.

Phase transitions within crystals that are aperiodic by construction

We spent many years to study the phase diagrams of n-alkane/urea composite systems, from short guest like heptane (n=7) to very long guests like tetracosane (n=24). When cooling from room temperature, the phase transitions in these composite crystals reveal three main characteristics :

Solidification with lock-in or monoclinic ordering : The first corresponds to a transition towards monoclinic symmetry, particularly observed in compounds featuring short-chain guests (n = 7, 8, 11, 12), which exhibit a greater translational degree of freedom along the channels.

Ferroelastic transition : The second group of compounds undergo phase transitions that maintain the four dimensions of crystallographic superspace, corresponding to shifts from the hexagonal superspace group $P6_122(00\gamma)$ to the orthorhombic $P2_12_12_1(00\gamma)$.

Transition within the superspace : Particularly intriguing is the third group, which experiences an increase in the dimension of the crystallographic superspace from 4 to 5 (n = 15, 16, 18, 19, 21, 24).

An important results is that each phase transition in the n-alkane/urea superspace sequence of phase tree follows the group-subgroup irrespective of the change in rank and therefore we can extend the Landau Theory of phase transition to the superspace.

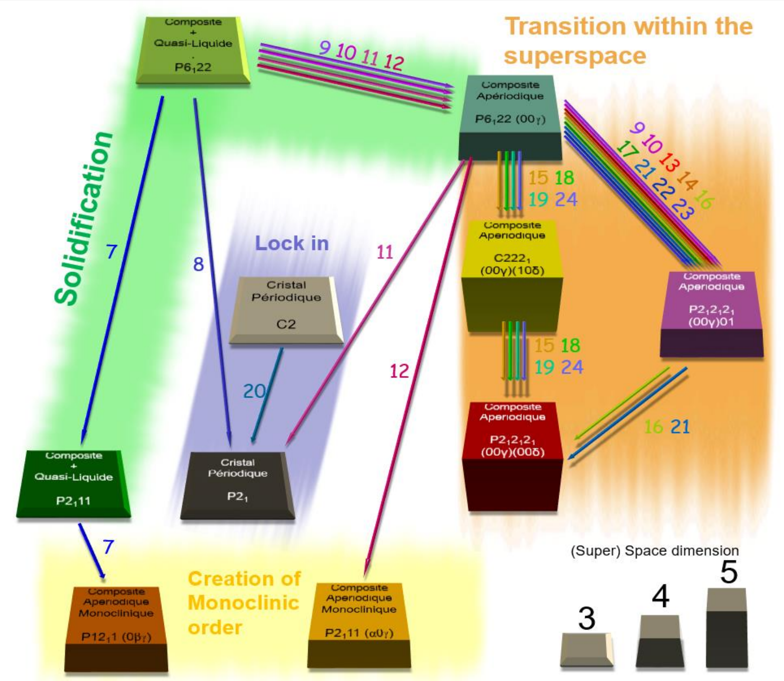

Figure 0-4 : The n-alkane/urea superspace sequence of phase

The use of superspace crystallography allows to recover the lost periodicity by embedding the 3d aperiodic crystal into 3+d superspace periodic space. Because of the recovered periodicity, diffraction patterns are comprised of sharp Bragg peaks allowing the crystallographer to apply the usual tools presented in the first chapter to the case of superspace.

The chapter 2 is based on the following papers :

Laurent Guérin*, Elzbieta Trzop, Tadahiko Ishikawa, Shinya Koshihara ,Takashi Yamamoto, Bertrand Toudic, Reizo Kato*, Frustrated competitive forces in the Et2Me2Sb[Pd(dmit)2]2 molecular conductor, **Physical Review B** 108, 134104 (2023).

Céline Mariette,Philippe Rabiller,**Laurent Guérin**, Claude Ecolivet ,Ilya Frantsuzov, Bo Wang, Shane M. Nichols, Philippe Bourges, Alexei Bosak, Yu-Sheng Chen, Mark D. Hollingsworth, Bertrand Toudic, **Physical Review B** 106, 134109 (2022).

Céline Mariette, **Laurent Guérin**, Philippe Rabiller, Yu-Sheng Chen, Alexei Bosak, et al.. The creation of modulated monoclinic aperiodic composites in n-alkane/urea compounds. ***Zeitschrift für Kristallographie***, 2015, 230 (1), pp.5--11.

Kamil K. Kolincio, Ramzy Daou, Olivier Perez, **Laurent Guérin**, Pierre Fertey, et al.. Giant Nernst effect in the incommensurate charge density wave state of P4W12O44. ***Physical Review B***, 2016, 94 (24), pp.241118

Laurent Guérin, Céline Mariette, Philippe Rabiller, Michael Huard, Sylvain Ravy, et al.. Long-range modulation in a five-dimensional crystallographic superspace. ***Physical Review B*** , 2015, 91 (18), pp.184101.

E. Trzop, D. Zhang, L. Piñeiro-Lopez, F. J. Valverde-Muñoz, M. Carmen Muñoz, L. Palatinus, **L. Guérin**, H. Cailleau, J. A. Real, and E. Collet, Inside Back Cover: First Step Towards a Devil's Staircase in Spin-Crossover Materials, ***Angewandte Chemie International Edition*** 55, 1 (2016).

Concepts presented in the chapter 2 were used in the following works :

A. Simonov, P. Rabiller, C. Mariette, **L. Guérin**, A. Bosak, A. Popov, and B. Toudic, Short-Range Order in the Quasiliquid Phases of Alkane Substructures within Aperiodic Urea Inclusion Crystals, **Physical Review B** 106, 054206 (2022).

Céline Mariette*, **Laurent Guérin***, Philippe Rabiller, Christophe Odin, Mariana Verezhak, et al.. High spatial resolution studies of phase transitions within organic aperiodic crystals. ***Physical Review B***, American Physical Society, 2020, 101 (18)

B. Toudic, **Laurent Guérin**, C. Mariette, I. Frantsuzov, P. Rabiller, et al.. Comment on Couzi et al. (2018): a phenomenological model for structural transitions in incommensurate alkane/urea inclusion compounds. ***Royal Society Open Science***, The Royal Society, 2019, 6 (8), pp.182073.

C. Ecolivet, M. Verezhak, Céline Mariette, **Laurent Guérin**, P. Rabiller, et al.. Phonons in an aperiodic alkane/urea composite crystal studied by inelastic x-ray scattering. ***Physical Review B***, 2018, 98 (22), pp.224308+.

Céline Mariette, Philippe Rabiller, **Laurent Guérin**, Bertrand Toudic. Crystallography and dynamics in superspace. ***EPJ Web of Conferences***, 2017, 155

C. Mariette, Ilya Frantsuzov, Bo Wang, **Laurent Guérin**, P. Rabiller, et al.. Frustrated pretransitional phenomena in aperiodic composites. ***Physical Review B***, 2016, 94 (18).

S. Zerdane, C. Mariette, G. J. McIntyre, M.-H. Lemée-Cailleau, P. Rabiller, **L. Guérin**, J. C. Ameline, and B. Toudic, Neutron Laue and X-Ray Diffraction Study of a New Crystallographic Superspace Phase In Nonadecane–Urea, ***Acta Crystallographica Section B***, 71, 293 (2015).

M. Huard, Bertrand Toudic, Philippe Rabiller, Claude Ecolivet, **Laurent Guérin**, et al.. Confined linear molecules inside an aperiodic supramolecular crystal: The sequence of superspace phases in n-hexadecane/urea. ***Journal of Chemical Physics***, 2011, 135 (20), pp.204505.

Bertrand Toudic, Ronan Lefort, Claude Ecolivet, **Laurent Guérin**, Roland Currat, et al.. Mixed acoustic phonons and phase modes in an aperiodic composite crystal. ***Physical Review Letters***, 2011, 107 (20), pp.205502.

Chapter 2: Aperiodic order and superspace crystallography

Periodic crystals are assemblies of atoms which possess long-range translational symmetry. Atoms are arranged according to a lattice in the unit cell, and the structure of the whole crystal can be constructed as a periodic repetition of the unit cell along three linearly independent directions. Aperiodic crystals are defined as crystalline structures exhibiting long-range order but lacking translational symmetry.

Aperiodic compounds fall into three categories (Figure 2-1):

1. Incommensurate modulated structures.
2. Incommensurate composites resulting from the intergrowth of two networks, with at least one of the ratios between their lattice parameters being irrational.
3. Quasicrystals which has caused a significant upheaval in the crystallographic community by revealing the possibility of symmetries previously considered forbidden in 3D space.

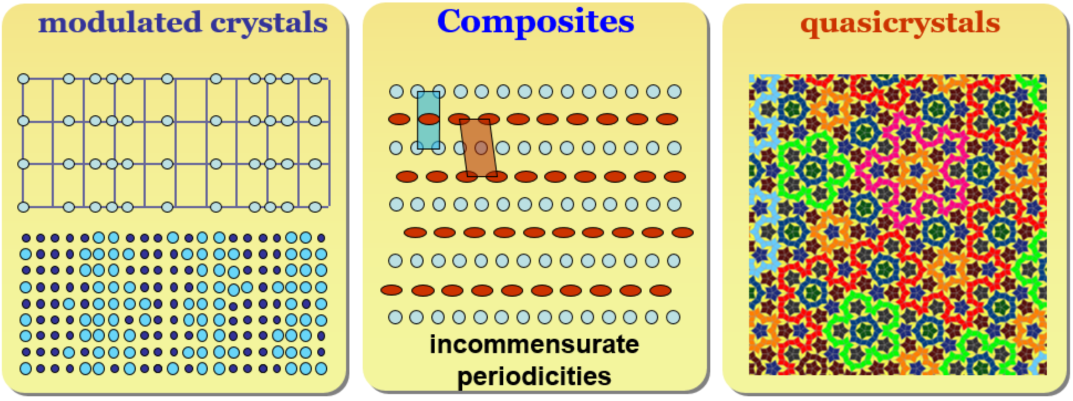

Figure 2-1 : The three distinct types of aperiodic crystals: (g) incommensurate modulated structures, (c) aperiodic composites composed of two incommensurate networks, and (d) quasicrystals exhibiting symmetries prohibited by translational symmetry.

One consequence of long-range order is that the diffraction patterns comprise of sharp Bragg reflections. Prior to 1991, crystals were defined based on the principle of translational symmetry until the International Union of Crystallography revised the crystal definition. It is now defined as a compound whose diffraction pattern is essentially discrete, composed of Bragg peaks. To restore the lost translational symmetry, it becomes necessary to increase the dimensionality of the system. This is the concept of **superspace crystallography** introduced by de Wolff, Janner and Janssen [15]. The Bragg reflections of aperiodic crystals can be reindexed using integers by extending the three reciprocal basis vectors with one or more additional vectors, as described by:

$$\mathbf{Q} = \sum_{i=1}^{3+d} h_i \mathbf{a}_i^*$$

where **Q** is the scattering vector of the Bragg reflection, d is the number of additional periodicities, h_i are integer Miller indices, and $\mathbf{a}_i^*$ are reciprocal basis vectors. One can observe that the Bragg reflections can be interpreted as the projection of the nodes of a reciprocal lattice in a (3 + d)-dimensional space, referred to as superspace. The reciprocal basis vectors $\mathbf{a}_i^*$ represent the projections of the basis vectors $\mathbf{a}_{si}^*$ of a reciprocal lattice in (3 + d) superspace. The direct lattice of this reciprocal lattice subsequently establishes a periodic atomic structure in superspace. In such a way, superspace crystallography allows the recovery of the translation symmetry which is absent in the physical space of dimension 3. The existence of periodicity in these higher dimensional space of dimension n= 3 + d permits a generalization of the standard crystallography. The reciprocal space, dual space of the superspace of dimension *n* is also of rang *n.* Similar to the 3d periodic case, the whole set of symmetry operations form a space group that is referred as superspace group of rank 3+d.

In this chapter 2, I will define the different categories of aperiodic material and present how we can use superspace crystallography to describe the aperiodic order and how we can use superspace crystallography to analyze the diffraction pattern of aperiodic materials. We will see that it is a generalization of the basic crystallography concepts to study 3d periodic lattice and phase transition presented in the chapter 1 to a lattice of (3+d) dimension in superspace. To illustrate those concepts, I will use scientific cases that I and my colleagues of the group worked on the last ten years.

2.1 SUPERSPACE CRYSTALLOGRAPHY APPLIED TO INCOMMENSURATE MODULATED CRYSTALS

A modulated incommensurate crystal can be seen as a perturbation of a periodic tridimensional lattice by a modulation which period is in an incommensurate ratio with the periodicity of the mean lattice [16–19]. Modulation functions can be described as wave functions, defined by a wave vector **q** that determines the direction and wavelength of the wave. The components of **q** are specified relative to the basis vectors of the reciprocal lattice of the basic structure in accordance with :

$\boldsymbol{q} = \alpha\boldsymbol{a}^{*} + \beta\boldsymbol{b}^{*} + \gamma\boldsymbol{c}^{*}$, where α, β and γ cannot be expressed as simple rational numbers.

An example of incommensurate displacive modulation is illustrated in the following Figure 2-2 for a two-dimensional system. Atomic displacements in the superstructure can exhibit both longitudinal and transverse components.

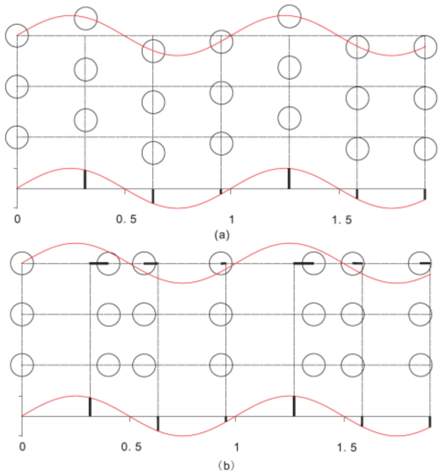

Figure 2-2 : : a two-dimensional incommensurate modulated crystal structure with transverse (a) and longitudinal (b) variations. Atoms, represented by circles, deviate from their regular lattice positions by varying amounts indicated by the bold bars. Numeric labels indicate the periods of the modulation waves. (From Li Liang, PhD thesis [20])

The vectors of the reciprocal space are written: $\mathbf{Q} = h\,\mathbf{a_1^*} + k\,\mathbf{a_2^*} + l\,\mathbf{a_3^*} + m\,\mathbf{q}$

In the reciprocal space, one can define two types of Bragg peaks, the Bragg peaks (hkl0) also called main reflections, associated to the mean structure and the satellites (hklm) with m≠0 associated to the modulation.

2.1.1 Superspace description of 1D incommensurate crystal

For simplicity, let us consider a chain of atoms of period a, modulated in position longitudinally in the direction a_2 by a sinusoidal function $A\sin(qy+\phi)$ where $q=\frac{2\pi}{\lambda}$, λ/a_2 is irrational, A is the amplitude of the modulation and ϕ the phase of the modulation taken equal to zero for sake of clarity (Figure 2-3). By introducing a perpendicular direction to the physical space, we draw along the internal direction of the crystallographic superspace, the incommensurate modulation function. This defines a superspace cell characterized by the $\mathbf{a_{s2}}$, $\mathbf{a_{s4}}$ basic vectors. The atom is no more a point but is defined by this **atomic modulation function** (orange curve). The real position of the atoms represented by pink circles in the physical space is obtained by a one-dimensional cut of the periodic superspace.

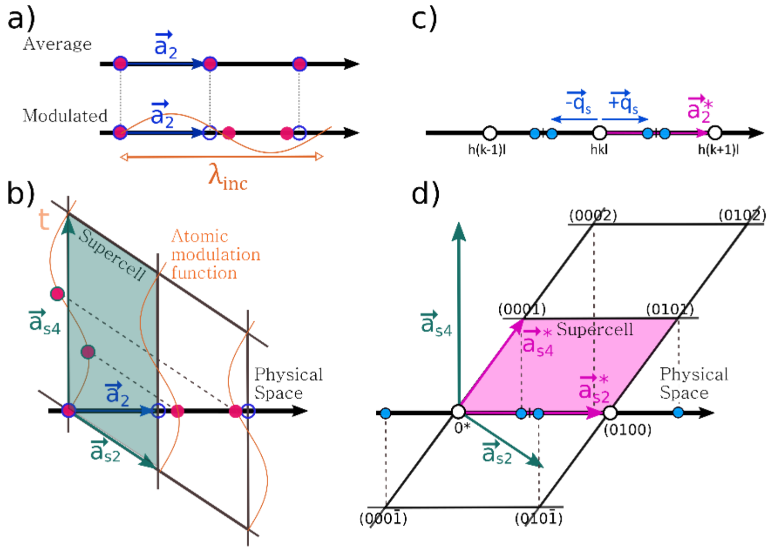

Figure 2-3 : left, schematic representation of an incommensurate phase in the real space : a) representation in the physical space of dimension 3, where the orange curve corresponds to the amplitude of the longitudinal incommensurate displacement along the axis; blue and pink circles are respectively the mean and the incommensurate positions b) in the superespace representation of dimension 3+1 the supercell in green is periodic, the orange curve represents the atomic modulation function along the internal dimension $\mathbf{a_{s4}}$ of the superspace. The actual positions of the atoms in pink circles are given by a horizontal cut. Right, schematic representation in the reciprocal space: a) satellites Bragg peaks (blue circle) appears at positions +/- m**q** apart from the main Bragg peaks (white circle); d) in the superspace representation, the reciprocal superspace of dimension 3+1 in pink is periodic, the actual Bragg positions are obtained by a projection of the reciprocal nodes on the physical reciprocal space of dimension 3.

2.1.2 Diffraction from 1D incommensurate crystal – reciprocal superspace

The associated reciprocal space is obtained by generalizing the expression $\boldsymbol{G}.\boldsymbol{T} = 2\pi$, $\boldsymbol{a_{si}}.\boldsymbol{a_{sj}^{*}} = 2\pi\delta_{ij}$, with i, j = 1, *4*. One can easily represent the periodic reciprocal superspace with their associated **as*** reciprocal vectors. In this simple case of an incommensurate modulation characterized by a single vector of modulation in 1d crystal, the dimension of the superspace group is two, characterized by the two reciprocal vectors $\mathbf{as_2}^*$ and $\mathbf{as_4*}$. Notice that in the construction of the reciprocal superspace $\mathbf{a_2*}$ and **q** are not necessarily the $\mathbf{as_2}^*$ and $\mathbf{as_4*}$ basis vectors of the reciprocal superspace.

The actual Bragg positions are obtained by a projection of the reciprocal nodes on the physical reciprocal space of dimension 1 (Figure 2-3). The diffraction pattern along the $\mathbf{a_2*}$ direction shows the two kind of Bragg peaks, the main (hkl0) reflection and the (hklm) satellites reflection at position m**q** from the main peaks. Only order 1 satellite are represented.

The computation of intensities for satellite peaks with indices (h k l m), where m is non-zero, can be carried out in straightforward cases. Considering a sinusoidal displacive modulation as described above, the position of the j^th^ atom in the l^th^ unit cell is expressed as:

$$\boldsymbol{U}_j^l = \boldsymbol{R_l} + \boldsymbol{r}_j + \boldsymbol{A}\sin\left(\boldsymbol{q}\cdot\boldsymbol{R_l} + \varphi_j\right)$$

With a following structure factor :

$$F(\boldsymbol{Q}) = \sum_{j,l} f_j e^{i\boldsymbol{q}\cdot U_j^l} = \sum_{j,l} f_j e^{i\boldsymbol{Q}\cdot(\boldsymbol{R_l}+\boldsymbol{r}_j)} e^{i\boldsymbol{Q}\cdot\boldsymbol{A}(\sin(\boldsymbol{q}\cdot\boldsymbol{R_l}+\phi_j)}$$

Using the Auger – Jacobi formula $\mathrm{e}^{\mathrm{ixsin}(\varphi)} = \sum_{\mathrm{n}=-\infty}^{+\infty} \mathrm{J_n(x)e^{in\varphi}}$, where $\mathrm{J_n(x)}$ is a Bessel function of the first kind :

$$F(\boldsymbol{Q}) = \sum_{m=-\infty}^{+\infty}\left(\sum_{j=1}^{N} f_j J_m(\boldsymbol{Q}\cdot\boldsymbol{A}) e^{i\boldsymbol{Q}\cdot r_j} e^{im\phi_j} \sum_{G} \delta(\boldsymbol{Q} + m\boldsymbol{q} - \boldsymbol{G})\right)$$

the satellites intensities are :

$$I(\boldsymbol{G} \pm m\boldsymbol{q}) = \left|\sum_{j} f_j J_m[(\boldsymbol{G} \pm m\boldsymbol{q})\cdot\boldsymbol{A}] e^{i(\boldsymbol{G}\pm m\boldsymbol{q})\cdot\boldsymbol{r}_j} e^{im\phi_j}\right|^2$$

If we consider, just for simplicity a unit cell with one atom modulated with an amplitude of modulation **A**, intensity for satellite reflections of order m is proportional to $J_m[(\boldsymbol{G} \pm m\boldsymbol{q}) \cdot \boldsymbol{A}]^2$.

We can conclude that a displacive modulation with a single harmonic yields non-zero intensities for, theoretically, all orders of satellite reflections. For small modulation amplitudes, $[(\boldsymbol{G} \pm m\boldsymbol{q}). \boldsymbol{A}]$ is small (less than 1) and the intensities decrease quickly as the satellite order increases, as illustrated by the values of Jn(x) in Figure 2-4.

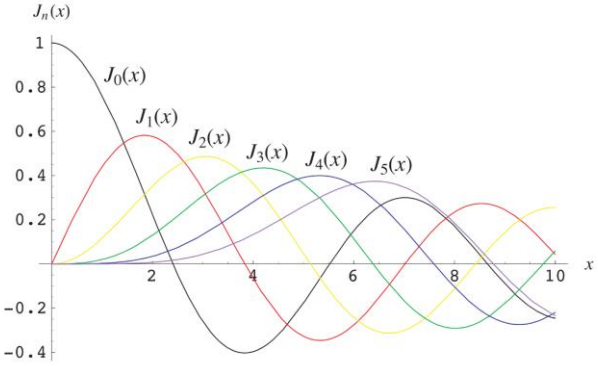

Figure 2-4 : Bessel function of the first kind. The amplitude for small value of x decrease rapidly with the order n of the Bessel function. (From Wolfram Mathworld website)

In theory, there is an infinite number of Bragg peaks evenly distributed in reciprocal space. However, as the intensity of the satellite peaks decreases rapidly with their order m, only satellites of small orders are generally observable. This criterion is even more stringent in the case of occupancy modulation, where it can be easily demonstrated that the intensity is non-zero only for satellite orders +/-1 [16]. In the general case, however, the modulation is not purely sinusoidal but, being periodic, can always be decomposed into a Fourier series. There is then no strict rule regarding the relative intensity of different satellite peaks. The following Figure 2-5 presents an hypothetical modulated crystal showing order -2, -1, 1and 2 satellites.

2.1.3 Superspace group

The set of symmetry operations forms a space group of dimension n, referred to as a superspace group. Superspace groups have been introduced to characterize the symmetry of n-dimensional incommensurate crystal phases. Superspace groups are not merely (3 + d)-dimensional space groups but possess additional structure. Generalizing what we did for 3d periodic crystals, this superspace group is determined by observing reflection conditions that apply not to 3 indices but to n indices. Thus, a centering operation in a superspace of dimension 4 translates into the reflection condition of h+k+l+m being even ([21–23]). To precisely define the symmetry of an aperiodic crystal, it is crucial to identify the basic vectors of a system of dimension d, which will define the nomenclature of the superspace group. These vectors consist of the three basic vectors **a***, **b***, **c*** characterizing the physical reciprocal space and d **q**vectors (with d being the dimension of the internal space) expressed in terms of these three basic vectors.

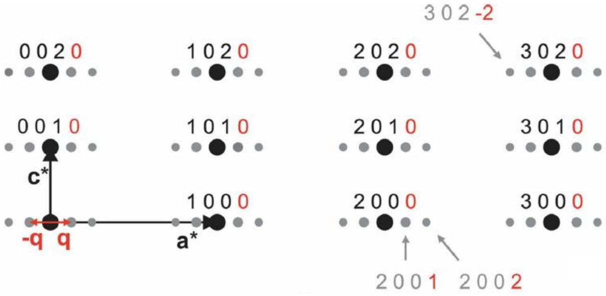

Figure 2-5 : Four-dimensionally indexed diffraction pattern of a hypothetical modulated structure (a). The vectors a* and c* which define the basic cell are derived from the positions of the main reflections. The additional vector q, reaching from the main reflection to the satellite, can be expressed in fractions of those basic vectors: in the present example **q** =0.125 **a*** + 0 **b*** + 0 **c***. Note that by introducing only one additional vector it is possible to uniquely index all reflections with four integer numbers. The fourth index also reveals the satellite order.

The notation of superspace groups is derived from that of rank-3 space groups, with the addition, in parentheses, of the three components of the n modulation vectors. For a compound with an average structure of high-symmetry monoclinic type C2/c and an incommensurate modulation vector along **b**, the superspace group would be C2/c (0β0). Superspace groups of one, two, and three dimensions have been tabulated, and a complete list is available [17,24,25]. There are 756 superspace groups for one-dimensional modulated structures (rank 3+1), 3355 for two-dimensional modulation (rank 3+2), and 11764 for three-dimensional modulation (rank 3+3).

2.1.4 Structure determination and analysis

The structure factor is expressed as a sum over all the atoms of the periodic supercell of the integrated atomic function over one period along the supplementary dimension of the crystallographic superspace [26]. In the case of a four dimensional superspace group, solving the structure means determining the **atomic modulation**

function of all the atoms of the mean three dimensional unit cell as function of the period along the fourth dimension, which is called conventionally the variable **t**. Dual-space methods like charge flipping algorithm do not impose restrictions on the form of the reconstructed scattering density, allowing for a direct generalization to superspace. This generalization is straightforward, with no changes required in the iteration scheme or the form of magnitude and positivity constraints. The only difference is that the density is sampled on a (3+d)-dimensional grid, where d depends on the rank of the modulation. The potential application of the CFA to incommensurately modulated structures was demonstrated soon after its publication [2]. This showed that the algorithm could directly solve many modulated structures in superspace without the need to determine the average structure first. The implementation of the CFA in the Superflip program available in JANA software, allowing the direct solution of structures in superspace, has elevated charge flipping to a preferred method for the ab initio solution of complex incommensurately modulated structures and quasicrystals.

One way to analyze the structure in the superspace is to look at t-plots. A t-plot is constructed by looking at structural parameters like distances between two atoms as a function of **t**. A curious feature of the t-plot is that the order in the t-plot doesn't reflect the order in the physical space. In Figure 2-3, the position of the atom in the real space is obtained by the intersection of a line called the physical space and the atomic modulation function in the superspace or by the projection of the atomic modulation onto the physical space, as shown by the dashed lines. The three modulated positions of the atoms denoted by pink circles in three adjacent unit cell, projected back along the **t** direction, does not correspond to adjacent point of the atomic modulation function. Nevertheless, structural information concerning intramolecular or intermolecular distances between atoms or intramolecular angles can be obtained by the t-plot representation.

2.1.5 An incommensurate modulated phase in $Et_2Me_2Sb[Pd(dmit)_2]_2$ molecular conductors

In order to illustrate the concept of superspace crystallography for incommensurate modulated structure, as a first example, I will present the study on the molecular conductor $Et_2Me_2Sb[Pd(dmit)_2]_2$. This work was done in collaboration with

Reizo Kato of the RIKEN institute in Wako, Japan and was published in 2023 in Physical Review B [27] .

Crystallographic studies of the periodic phases

$Et_2Me_2Sb[Pd(dmit)_2]_2$ crystal structure is composed of alternately stacked anion layers consisting of $Pd(dmit)_2$ and insulating cation layers (Figure 2-6). Basic crystallography studies showed that its room temperature space group is monoclinic C2/c (a=14.62 Å, b=6.40 Å, c=37.51 Å, β=97.72° at 250K). The unit cell contains two conduction layers related by the c-glide symmetry to each other. Each layer is parallel to the (**a**,**b**) plane and is composed of crystallographic equivalent $Pd(dmit)_2$ molecules stacking along the **a**+**b** or **a**-**b** direction. At room temperature, $Et_2Me_2Sb[Pd(dmit)_2]_2$ is a dimer Mott insulator, the charge on each $[Pd(dmit)_2]_2$ dimers being uniformly −1 (monovalent).

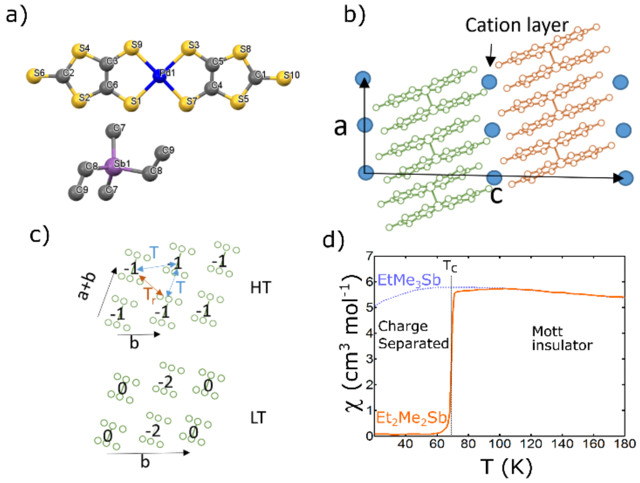

Figure 2-6 : (a) The complex molecule $Pd(dmit)_2$ and the Et_2Me_2Sb cation. (b) Schematic representation of *ac* plane. (c) End-on projection of the anion layer in the high temperature (HT) and low temperature (LT) phases. The anion layer in the HT phase forms a triangular lattice of monovalent dimers. Neutral and divalent dimers are formed in the LT phase. (d) Temperature dependence of the magnetic susceptibility (red solid line) in $Et_2Me_2Sb[Pd(dmit)_2]_2$ and a candidate of quantum spin liquids $EtMe_3Sb[Pd(dmit)_2]_2$ as a reference compound (blue dotted line).

At low temperatures, $Et_2Me_2Sb[Pd(dmit)_2]_2$ undergoes a phase transition around 70K, as illustrated through the dependence of the magnetic susceptibility in Figure 2-6(d). Space group is monoclinic $P2_1/c$ (a'=14.50 Å, b'=12.65 Å, c'=37.18 Å, β'=98.09° at 25K). The low temperature structure is formed of dimers with different valence states arranged alternatively along the **b** direction. This indicates that the phase transition is associated with charge separation, loose divalent and tight neutral dimer being ordered (Figure 2-6(c)).

Sequence of phases of Et$_2$Me$_2$Sb[Pd(dmit)$_2$]$_2$

Figure 2-7(a) presents, between 110K and 15K, several Mo-K$_\alpha$ diffraction images along the direction **b***. Three differently assigned Bragg peaks are observed. Above 105K, only Bragg peaks signing the C2/c space group are observed. Between 70K and 100K, supplementary satellites Bragg peaks are present at a position $\mathbf{q_s}$= β **b***, with β of the order of 0.45 in **b*** units. In the low temperature phase, these satellites Bragg peaks become commensurate and additional superstructure Bragg peaks appears. The superspace group is determined by the observation of the conditions for main and satellites reflections. In the present case, the mean structure is monoclinic C2/c and the critical wave vector is **q**= β $\mathbf{b}^*$, so the superspace group is C2/c (0β0). For the satellite reflections, an additional extinction rule for reflections 0k0m with m ≠ 2n is observed suggesting the superspace symmetry element s. The only (3+1)-dimensional superspace group in compliance with this condition is C2/c (0 β 0) s0 [17,24,25,28].

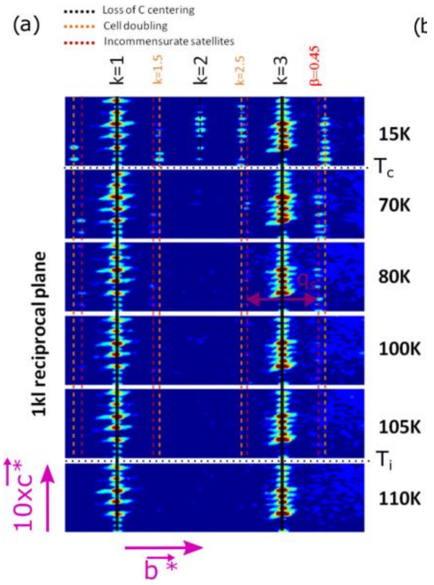

Figure 2-7 : (a) Diffraction imaging of Et2Me2Sb[Pd(dmit)2]2. The diffraction plane (1, k, l) is shown at several temperatures. The frames at 110 and 105 K reflect theC2/c symmetry of the high symmetry phase. The images at 100, 80, and 70 K show a supplementary set of satellite Bragg peaks at incommensurate positions q = β b∗ . The lowest temperature image, at 15 K, shows a cell doubling along b∗ and the appearance of Bragg peaks indicating the loss of the C centering, in agreement with the three-dimensional space group P21/c.

The actual sequence of three phases of $Et_2Me_2Sb[Pd(dmit)_2]_2$ is shown in Figure 2-8. The phase transition from the monoclinic high symmetry phase C2/c to the incommensurate one denoted as phase II is marked by a continuous increase of the intensity of the satellite Bragg peaks. The diffraction signature presents two characteristic features. First, a jump from incommensurate satellite $\mathbf{q}_s= \beta\, \mathbf{b}^*$ having an irrational β to commensurate satellite $\mathbf{q} = 1/2\, \mathbf{b}^*$. Second, at this temperature, the mean structure lowers the symmetry from C2/c to $P2_1/c$ yielding the appearance of Bragg peaks at h+k odd (Figure 2-8). The observed sequence of phases corresponds to the usual sequence of phases in incommensurate modulated crystals with a jump of the incommensurate vector **q** to a commensurate one [29,30].

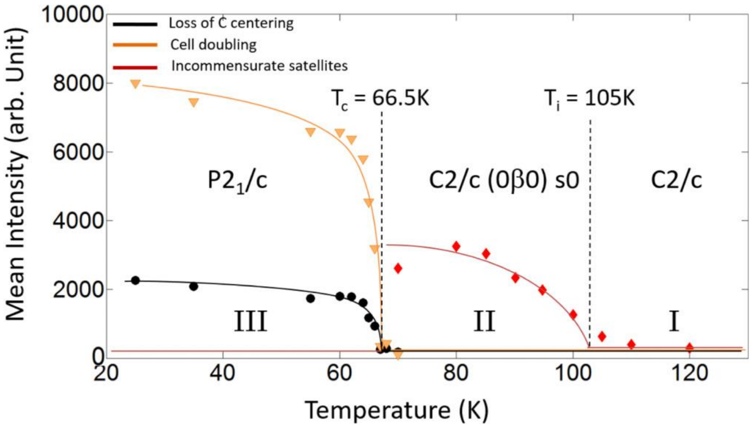

Figure 2-8 : Phase diagram of Et2Me2Sb[Pd(dmit)2]2 defined by temperature evolution of the intensities of satellite Bragg peaks. Diamonds: intensity of the satellites in the incommensurate phase C2/c (0 β 0) s0 defining Ti = 105 K. Triangle and circle: Bragg peak intensities indicating respectively the cell doubling and the loss of the centering due to the commensurate lock-in phase transition at Tc = 66.5 K towards the space group P21/c.

Structure determination

The structure of $Et_2Me_2Sb[Pd(dmit)_2]_2$ within its incommensurate phase was refined in such a (3+1)-dimensional superspace using JANA and SUPERFLIP Programs. [26]. As only satellites of order 1 were observed, only one harmonic modulation wave was refined for each atom. A typical result obtained by such a study is the electronic density associated to the atoms along one period **t**, as shown along the **c** direction (ΔSb is defined as the displacement along c) in the Figure 2-9 for the antimony atom Sb.

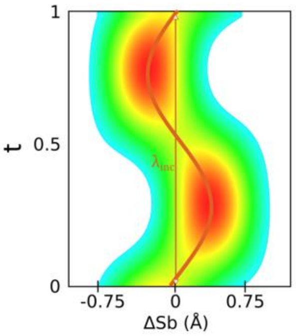

Figure 2-9 : the electronic density in the **c** direction of the antimony atom Sb extracted from the analysis of the X-ray measured in the incommensurate phase of $Et_2Me_2Sb[Pd(dmit)_2]_2$ along one period **t** of the internal space of the superspace.

Knowing these different electronic density functions for the different atoms, it is possible to get direct information on the anisotropic modulations of the different atoms from the molecule of $Et_2Me_2Sb[Pd(dmit)_2]$. The different parameters $d_{Pd\text{-}Pd}$, α, Ψ, and ΔSb are defined in Figure 2-10: $d_{Pd\text{-}Pd}$ is the distance between the two palladium atoms within a dimer, α is an intramolecular angle of the molecule $Pd(dmit)_2$, Ψ is the intramolecular torsion angle between the two ethyl groups in the Et_2Me_2Sb cation and ΔSb is the displacement in the low symmetry phase of the Sb atom along the **c** direction. In phase III, the two different values correspond to the values measured in two non-crystallographic equivalent dimers or cations.

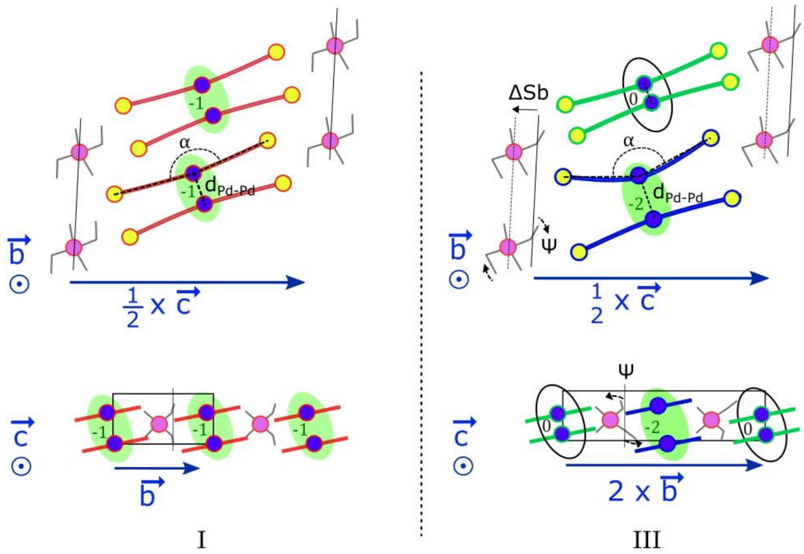

Figure 2-10 : Schematic representation of the structural ordering and in the high symmetry phase *C2/c* and in the low symmetry phase *P2₁/c*. The symbols *α, Ψ,* $d_{Pd\text{-}Pd}$, and Δ_{Sb} correspond to molecular and dimer structural parameters which are significantly different in the high and in the low temperature phases.

As shown in Figure 2-11, strong modulation of the structure of the dimer as well as the cation can be observed. The position of the Sb atom ΔSb is strongly modulated in the incommensurate phase with a displacement from one-unit cell to another that could be as large as 0.35Å. The torsion angle Ψ between the two ethyl groups in the Et$_2$Me$_2$Sb cation shows also a wide range of modulation This is surprisingly not observed for the intermolecular distance d$_{\text{Pd-Pd}}$ between the two Pd(dmit)$_2$ units forming the dimer (Figure 2-11(d)). A strong structural signature of the charge separation state is the distance d$_{\text{Pd-Pd}}$. It emerges from this structural analysis that the amplitude of the modulation of the palladium atom in the incommensurate phase is negligible compared to the effective jump at the lock-in transition. We can conclude that no charge separation is observed in the incommensurate phase and the average charge of the dimer is -1 similar to the high temperature phase.

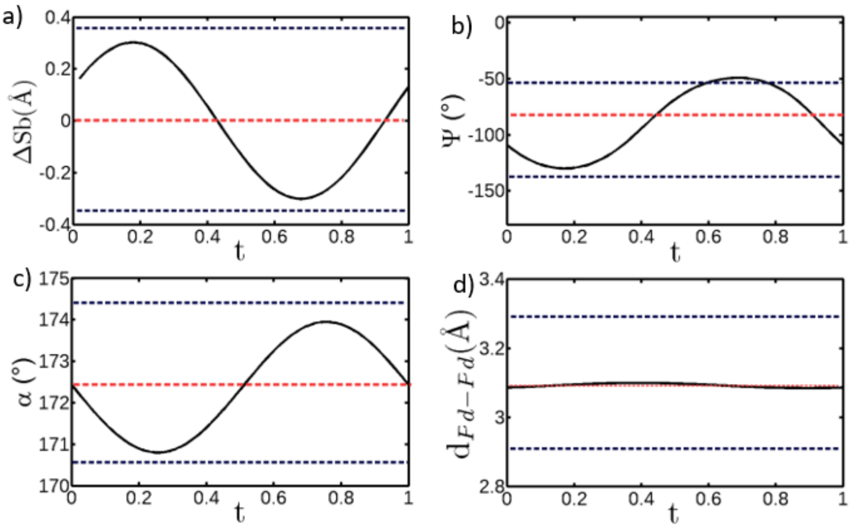

Figure 2-11: t-plot of different structural parameters obtained at 80 K in phase II. (a) Positional modulated displacement along the c direction of antinomy atom Sb in the Et2Me2Sb cation; (b) Modulation of the intramolecular torsion angle Ψ between the two ethyl groups in the Et2Me2Sb cation; (c) Rotational modulation of the internal angle in the molecule Pd(dmit)2; (d) t-plot of the distance dPd-Pd between two adjacent Pd(dmit)2 molecules in the dimer. The dense dotted lines in red and blue indicate the corresponding values in the high and low symmetric periodic phases, respectively.

Why is it interesting ?

As for periodic structure, to be able to know the structure of the incommensurate phase is a very valuable assets to discuss the property of the modulated phase and how this phase is related to the commensurate ones. I will not go too much in the details of the interpretation of the origin of the incommensurate phase and I highly encourage the reader to read our Physical review B article [27]. But in a general way, an incommensurate phase arises from a frustration between competitive forces. The main characteristic of this system (that I didn't not mention) is that he high temperature phase I is characterized by a geometric frustration due to its 2D equilateral triangular lattice. We saw also that the low temperature phase III presents two different dimers with two distinct charges in the charge separation state. Within this phase II, the strong steric interaction as well as the degree of spin frustration are incommensurately modulated but there is no modulation of the charge of the dimers as the distance Pd-Pd remains constant. The competition among the steric effect, the magnetic frustration, and the CS state leads to the emergence of the incommensurate modulation in phase II.

2.1.6 The second plateau γHS ≈ 0.34 in $\{Fe[(Hg(SCN)_3)_2](4,4'\text{-bipy})_2\}_n$

For the second example, let's return to the second plateau observed in the magnetic susceptibility measurement in the compound $\{Fe[(Hg(SCN)_3)_2](4,4'\text{-bipy})_2\}_n$ [14]. As shown in Figure 2-12 and discussed in the chapter 1.5.2, additional Bragg peaks appears with their position defines by a fourth vector $\mathbf{q_i}$:

$$\boldsymbol{Q} = \mathrm{h}\boldsymbol{a}^* + \mathrm{k}\boldsymbol{b}^* + \mathrm{l}\boldsymbol{c}^* + \mathrm{m}\boldsymbol{q_i}$$

and $\boldsymbol{q}_i = \alpha\boldsymbol{a}^* + \beta\boldsymbol{b}^* + \gamma\boldsymbol{c}^*$.

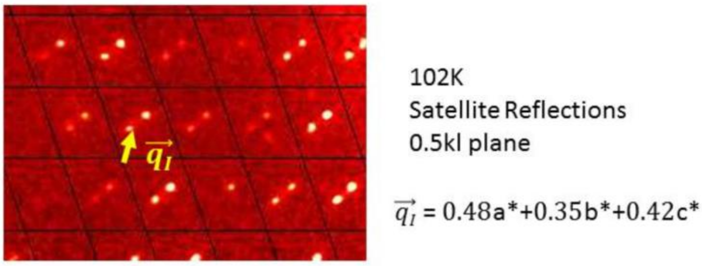

Figure 2-12 : Reconstructed diffracted intensity of the reciprocal-space in the 0kl and 0.5kl planes in the second plateau.

At 102 K, α=0.48 Å, β=0.35 Å, and γ=0.42 Å cannot be expressed as simple fractions, indicating that the structure is no longer 3D periodic. Instead, it exhibits incommensurate modulation with respect to the initial (a, b, c) lattice. The structure belongs to the 4D superspace group $P\bar{1}(\alpha,\beta,\gamma)0$. Discontinuous changes in satellite intensities around 96 and 108 K underscore the first-order nature of the transitions defining the stability region of the incommensurate phase.

The incommensurate structure was refined in a (3+1)-dimensional superspace, where atomic coordinates are defined by their positions in the average 3D unit cell, along with the modulation functions of these coordinates along the fourth dimension coordinate x_4 (corresponding to the **t** parameter).

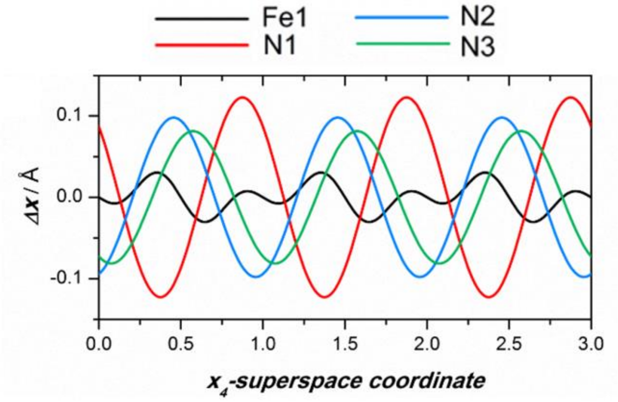

Figure 2-13 : Modulation of the x of the Fe1, N1, N2 and N3 atoms along the x4-superspace coordinate, obtained from the structural refinement at 102 K for data at 102K.

This modulation influences the Fe-N bond distances (Figure 2-13). The in-phase modulation of these bonds along x_4 serves as direct evidence of the formation of a SSCW along **qi**, incommensurate with the average 3D periodic crystal lattice. The average modulation of the six Fe-N bonds suggests an almost sinusoidal modulation function of γHS: $\gamma_{\mathrm{HS}}{}^{i}(\boldsymbol{r}) = \gamma_{\mathrm{HS}}{}^{i} + (\eta^{i}/2)\cos(\boldsymbol{q_i}\boldsymbol{r})$, where $\gamma_{\mathrm{HS}}{}^{i} = 0.34$ and ηi = 0.85.

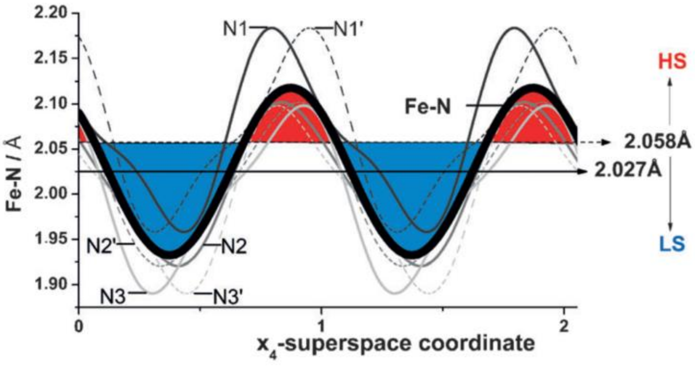

Figure 2-14 : Modulation of the Fe-N bonds along the superspace coordinate x_4 with an almost sinusoidal modulation of Fe-N (thick line) around ca. 2.027 Å corresponding to $\gamma_{\mathrm{HS}}{}^{i} = 0.34$. The fraction of the Fe-N modulation larger than ca. 2.058 Å corresponding primarily to the HS state is also close to $\gamma_{\mathrm{HS}}{}^{i} = 0.34$.

The modulation vector $\mathbf{q_i}$ of $\gamma_{HS}{}^{i}(r)$ forming HS and LS stripes, is incommensurate with the (a, b, c) lattice. This 4D structure can then be projected into physical 3D space to reveal the aperiodic spatial distribution of LS and HS states (Figure 2-15). Note that this representation is false and does not represent the real structure as closed points in the x4 direction are not necessarily adjacent in the real space.

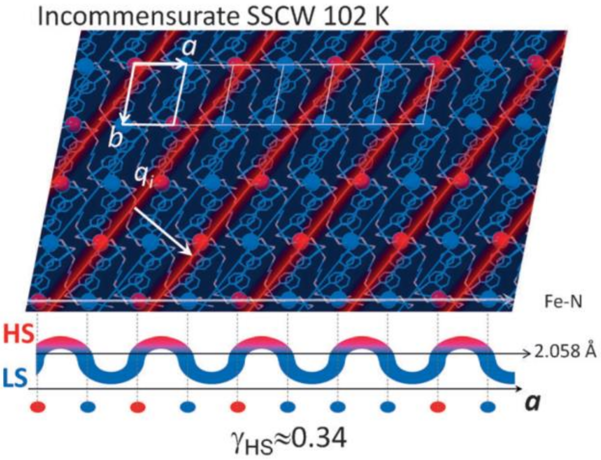

Figure 2-15 : Slice in the (a,b) plane of the aperiodic projected structure, forming an incommensurate SSCW with HS and LS stripes along qi (projected).

2.1.7 Incommensurate charge density wave state of $P_4W_{12}O_{44}$

In the two previous examples, the incommensurate modulated structure are described with one wave vector $\mathbf{q}$ but it is not necessarely everytime the case. Phosphate tungsten Bronzes with pentagonal tunnels are conductors of low dimensionality characterized by several phase transitions through unusual charge density waves states [31]. These transitions are coupled with the appearance of incommensurate modulation phenomena occuring at different temperature. In the tungsten bronze $P_4W_{11}O_{44}$, we evidenced, using synchrotron radiation at SOLEIL synchrotron, an incommensurate charge density wave state that requires two wave vectors $\mathbf{q}$ (Figure 2-16). The full diffraction pattern at T = 45 K is compatible with a two-dimensional incommensurate modulated structure where all the satellite reflections can be indexed using $\mathbf{q_1}$, $\mathbf{q_2}$, and $\mathbf{q_1} \pm \mathbf{q_2}$. This CDW induces the partial destruction of the Fermi surface, and the reduction of the carrier concentration. By analysing the CDW and doing additional transport properties measurements, we could demonstrate that both condensation of the electronic carriers in the charge density wave state and the existence of high-mobility electrons and holes originating from the small pockets remaining in the incompletely nested Fermi surface give rise to a giant Nernst effect.

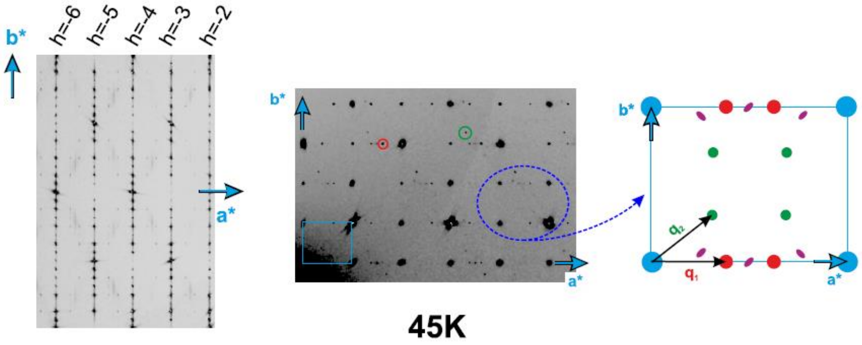

Figure 2-16 : . Region of the (h0l) (left part) and (hk0) (middle part) planes assembled from frames collected at T = 45 K. The red and green circles show, respectively, satellite reflections associated with q_1 and q_2; the light blue rectangle correspond to the average unit cell. The right part is a schematic representation of the area blue-dashed circled in the (hk0) plane. Burgundy ellipsoids and red and green circles summarized all the diffraction features visible on the (hk0) plane.

With this three examples, we illustrate the capacity of the superspace formalism to determine and describe the structure of incommensurate modulated structure. Let’s apply this formalism to another class of aperiodic material : the composite aperiodic materials.

2.2 SUPERSPACE APPROACH TO APERIODIC COMPOSITE

Incommensurate composite crystals are based on two, interpenetrating lattice periodic structures that are mutually incommensurate. Because of the incommensurability, each subsystem attains an incommensurately modulated structure, where the other subsystems act as incommensurate external potentials for the subsystem under consideration. Therefore, aperiodic composites can be viewed as the nesting of two subsystems modulated in an incommensurate manner [32]. Well-known examples include inorganic misfit layers [33–37], two-dimensional compounds whose various "layers" exhibit periodicities in an irrational ratio. The crucial distinction from modulated incommensurable compounds is that aperiodic composites are typically aperiodic by construction: there is no high-symmetry periodic phase, no periodic average structure, and consequently, no average Brillouin zone.

2.2.1 Superspace description of 1D composite crystal

In Figure 2-17, we examine a 1D system comprising two distinct types of atoms, depicted in red and blue. Initially, both red and blue atoms occupy individual positions within 1D unit cells, each containing only one atom. The complexity arises from the fundamental difference in the unit-cell lengths of the red and blue atoms: the former has a length of c_1, and the latter has a length of c_2, where the ratio c_1/c_2 equals γ, with γ being an irrational number.

Now, let's consider the interaction between the red and blue atoms. For instance, we suppose that red and blue atoms exert a gentle repulsion on each other. As each atom type repels the other, it feels a potential determined by the positions of atoms of the opposing type. The resulting displacements are depicted in Figure 2-17. Positive values of the displacement curves signify atomic shifts to the left, while negative values represent shifts to the right.

The foundational assumption is that the displacement curves arise from the original positions of atoms in the other chain. Consequently, the displacement curves possess the wavelength of the original unit cell of the other atom type. Thus, the displacement curve for the red atoms (red curve) has a wavelength of $\lambda_1=c_2$. In contrast, the displacement curves for the blue atoms (blue curve) have a wavelength of $\lambda_2=c_1$.

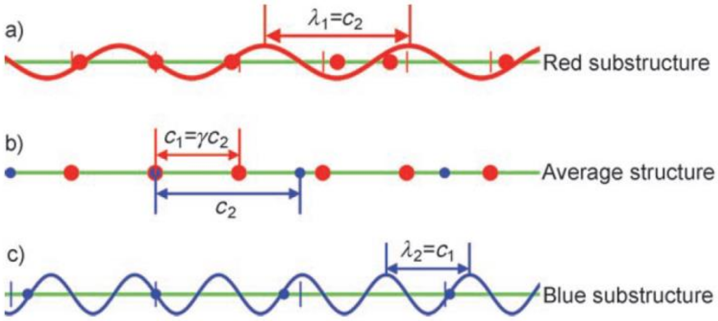

Figure 2-17 : The 1D incommensurate composite system (b) made up of two separate incommensurate components (see Figure 2) superimposed on to each other. The two separate systems are shown in red and blue . The two component incommensurate systems are shown separately in a) and c). The periodic distortion of each component has a wavelength equal to the unit-cell length of the other component. (From Sun et al, Chemistry, an Asian journal 2007 [38])

We can see that the description of an intermodulated aperiodic composite is not very different than an incommensurate modulated crystal. We can applied what we learned and describe the composite using the superspace formalism by describing the supercell (Figure 2-18). We have to combine the two displacement curves in order to form a 2D superspace periodic lattice. The crossing of the red and blue curved lines of this 2D lattice (or more properly, (1+1)D crystal) with the horizontal axis gives the exact location of the red and blue atoms, respectively. The average structure is one in which both red and blue atoms lie unchanged from the potentials caused by the other atom type. It is the simple structure for which the displacement curves can be represented as flat lines (all displacements are equal to zero). The average structure represented as a (1+1)D crystal is shown in Figure.

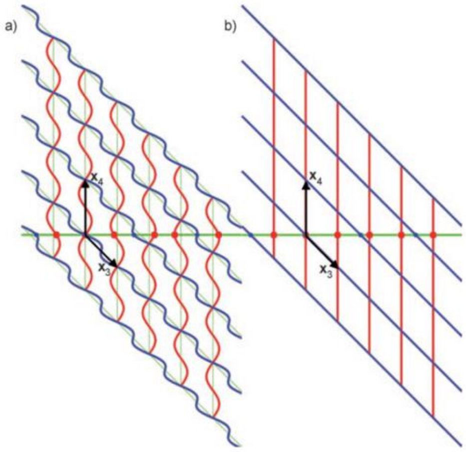

Figure 2-18 : 1D incommensurate composite structure viewed as a 2D crystal. The atoms (red and blue filled circles) lie at the intersection of the horizontal axis (the physical space) with a series of vertical (red) and diagonal periodic curves (blue). b) 1D composite structure with no periodic distortion to the atomic positions. In b), the periodic curves of part a) are simplified to straight lines. Both a) and b) have the same 2D unit-cell parameters. (From Sun et al, Chemistry, an Asian journal 2007 [38])

The reciprocal superspace can be computed using $\boldsymbol{a_{si}}.\,\boldsymbol{a_{sj}^*} = 2\pi\delta_{ij}$, with i, j = 1, *2* for 1D composite crystal. The projection of the nodes of the reciprocal supercell onto the physical reciprocal space determine the position of the Bragg peaks and are given by (Figure 2-19):

$\mathbf{Q} = l\,\mathbf{c_1^*} + m\,\mathbf{c_2^*}$ **,** where $\mathbf{c_1^*}$ and $\mathbf{c_2^*}$ are reciprocal vector associated to the two sub-lattice. (similar to the **q** vector for incommensurate modulated structure)

There are thus four different types of Bragg peaks:

(0 0): Common Bragg peaks

(l 0): Bragg peaks associated with the periodicity of sub-network 1

(0 m): Bragg peaks associated with the periodicity of sub-network 2

(l m): satellite of intermodulation where l and m ≠ 0

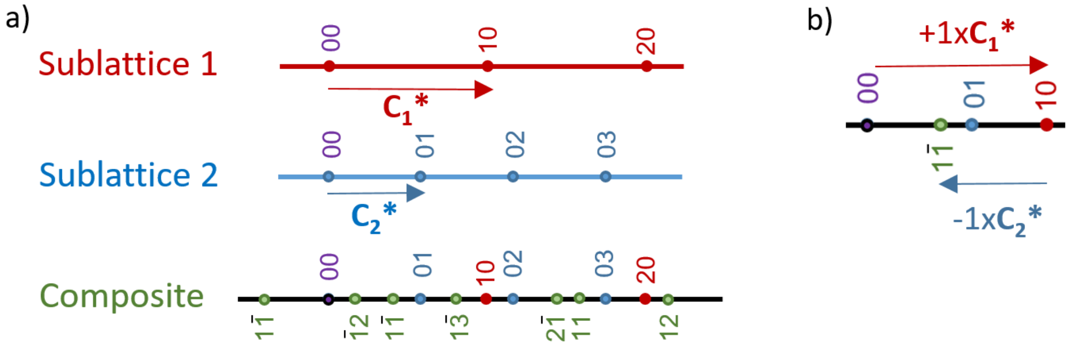

Figure 2-19 : a) diffraction pattern of 1D composite crystals showing common, sublattice1, sublattice2 and intermodulation satellite in purple, blue, red and green respectively. b) position of intermodulation satellites are obtained by linear combination of the two reciprocal vectors $\mathbf{C_1^*}$ and $\mathbf{C_2^*}$.

Contrary to modulated structure, computation of the intensity of satellites Bragg peaks are not very straightforward because in reality, both sub-networks contribute to the intensity of all Bragg peaks. This makes structure resolution much more complicated than for modulated incommensurate structures, and to date, there are only few completely solved structures of aperiodic composites.

2.2.2 Superspace group of composite crystals

For the determination of the superspace group of an aperiodic composite, the first step is to establish subspace and superspace groups associated with the various subsystems considered separately [37]. The superspace group associated with the composite as a whole will be the largest common subgroup among the superspace groups of the different subsystems. As we will see later in this chapter, for the compounds of interest *n*-alkane-urea, a host-guest composite with a host periodicity c_h and guest periodicity c_g along the **c** direction, the average structure of the high-symmetry phase is generally hexagonal of type $P6_122$. The intermodulation vector will be unique, associated with a 3+1-dimensional phase. It is typically oriented along the c* direction and thus of the type (00γ), i.e., in $\gamma\ c_h^*$ where γ characterizes the aperiodicity ($\gamma=c_h/c_g$). The superspace group will be $P6_122(00\gamma)$. The complete list of superspace groups concerning uniaxial 3+1-dimensional aperiodic composites has been provided by van Smaalen and Harris [37].

2.3 THE CASE STUDY OF *n*-ALKANE – UREA APERIODIC COMPOSITES

Alkane-urea composites, formed by the intergrowth of urea ($CO(NH_2)_2$) and alkane (C_nH_{2n+2}) molecules, represent supramolecular compounds with intricate crystal structures. When isolated, urea crystallizes in a quadratic structure, and alkane molecules exhibit rotator phases with various orientational disorders. In the context of composite aperiodic crystals, these materials are designed through supramolecular chemistry and crystal engineering, resulting in attractive aperiodic host-guest architectures where guest molecules are confined in nanochannels. In urea inclusion compounds, urea molecules, connected by hydrogen bonds, form two rigid helices that arrange themselves into hexagonal channels. The crystallographic directions of the two subsystems perpendicular to the channels are commensurable. The composite's structure results from strong interactions between urea and alkane; it is stable only for sufficiently long guest molecules, with heptane (n=7) being the shortest alkane molecule to crystallize with urea to date.

Urea molecules strictly confine alkane molecules, forming a composite crystal consisting of two subsystems with parameters along the channel direction generally in irrational ratios (Figure 2-20). Conventionally, the c-axis of the lattice is taken along this incommensurability direction, denoting c_h as the host urea lattice parameter, c_g as the guest alkane lattice parameter, and $\gamma = c_h/c_g$ as the ratio of the two lengths. The urea parameter is independent of the guest molecule (11.02Å at room temperature). An empirical formula, given by Lenne (Lenne 1970), predicts a linear variation of c_g with the number n of carbon atoms in the alkane chain: $c_g = [1.270\ (n - 1) + 3.658]$Å, in excellent agreement with observed experimental values. In the plane perpendicular to the channel direction, the structure is hexagonal with lattice parameters a=b=8.2Å at room temperature. By changing the alkane guest, one can modify the periodicity of the guest sublattice C_g and therefore change the incommensurability ratio $\gamma = c_h/c_g$. Most of these materials exhibit incommensurate composite features since periodicity along the channel of the guest alkane does not fit rationally with the helical parameter of the host urea matrix (Figure 2-20).

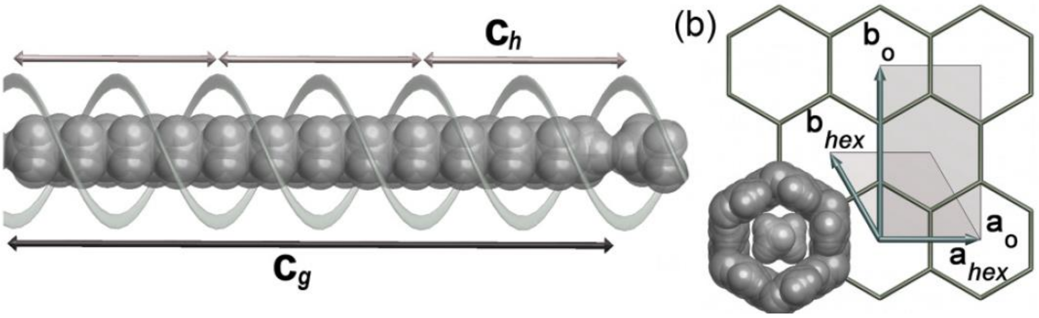

Figure 2-20 : a) n-Tetracosane/urea viewed perpendicular to the channel axis with the host shown schematically. (b) Projection of the n-tetracosane/urea structure onto the ab plane (with arbitrary guest orientation) showing the hexagonal and orthorhombic definitions of the basis vectors. (From L.Guérin et al, PRB 2015 [39])

The crystallographic superspace that describes such materials decomposes into two orthogonal subspaces, the usual physical space and an internal one. For intergrowth nanotubular structures that have a single incommensurate direction ***c***, a four-dimensional (4D) superspace description gives the positions of all of the Bragg peaks :

$$\boldsymbol{Q}_{hklm} = h\boldsymbol{a}^* + \boldsymbol{kb}^* + l\boldsymbol{c_h}^* + m\boldsymbol{c}_g{}^*,$$

where $\boldsymbol{a}*$, $\boldsymbol{b}*$, $\boldsymbol{c_h*}$, and $\boldsymbol{c_g*}$ are the conventional reciprocal unit cell vectors. Four indices (*h*, *k*, *l*, and *m*) are needed to describe the four different types of structure Bragg peaks: (hk 00) , (hk l 0), (hk 0m), and (hk lm), with l and m different from zero, correspond to the common, host, guest, and satellite Bragg peaks, respectively.

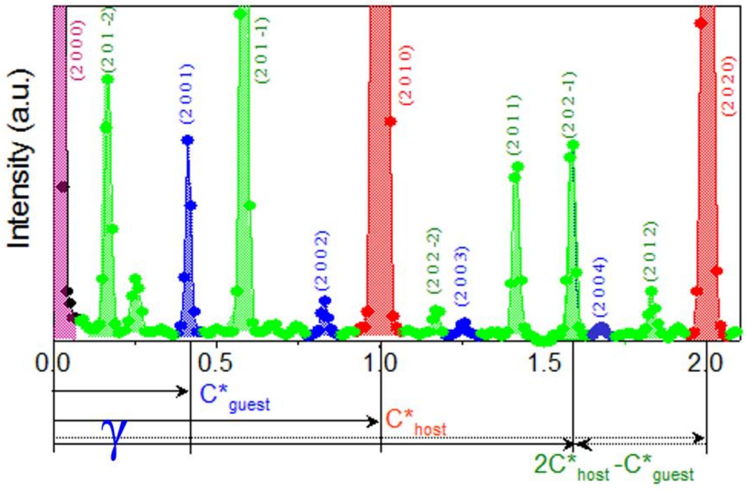

Figure 2-21 : Bragg peaks along c* direction showing the indexation of common (purple), host (red), guest (blue) Bragg peaks and intermodulation satellites (green). (From R. Lefort et al, PRL 1996 [40])

In all the family of n-alkane/urea, the average structure of the high-symmetry phase is hexagonal of type $P6_122$. The intermodulation vector is unique, associated with superspace of dimension 3+1. It is generally along the c* direction and therefore of type (00γ), where γ characterizes the aperiodicity $\gamma=c_h/c_g$. The space group is therefore the hexagonal group of dimension 4, $P6_122$ (00γ).

Direct evidence of the mutual intermodulation of the two substructures was demonstrated by the existence of satellite Bragg peaks in this family of inclusion compounds [40]. Such organic materials, with internal and/or external degrees of freedom, often present phase transitions well below room temperature. The family of *n*-alkane/urea inclusion presents a unique opportunity to explore sequences of phases within crystallographic superspace. During 10 years, I and my colleagues explore the landscape of possibilities playing with alkane length, incommensurate ratio, temperature, pression while using X-ray lab source, synchrotron all over the world, neutron, NRM, DSC… There is too much to present here so I've decided to focus on three results. The first is the investigation of the phase transition in n-tetracosane/urea with the apparition of long range modulation along the channel that requires an additional modulation vector and a description in a 5D superspace. The second is the investigation of the phase transition in n-dodecane/urea. it belongs to the class of alkane/urea crystal with quasi-liquid state for the confined guest molecules at room temperature and shows a phase transition with the creation of a modulated monoclinic lattice for the guest molecule at low temperature. The last is the general study of phase transitions in alkane/urea, a nice summary of our works.

2.3.1 Long-range modulation of a composite crystal in a five-dimensional superspace

The *n*-tetracosane⁄urea [*n*-$C_{24}H_{50}$⁄urea] is an aperiodic composite characterized by a misfit parameter very close to a rational number at ambient conditions: $\gamma=c_h/c_g = 0.3335$. The superspace group of the high-symmetry phase has been determined to be hexagonal of rank 4, P6122(00γ). The n-tetracosane/urea composite exhibits two phase transitions from 90K to 300K. From the high temperature phase I to phase II at Tc_1 = 179K to phase III at Tc_2 =163K

The first is the ferroelastic transition from hexagonal to orthorhombic (unit cell is presented in Figure 2-21) characterized by two distinct features. The first crystallographic signature concerns the existence of six symmetry-related orthorhombic domains. This is manifested in the low-temperature diffraction image shown in Figure 2-22 through the vertical splitting of the structure Bragg peaks. The temperature evolution of this splitting leads to a transition temperature, called Tc_1, of 179 K. The second crystallographic signature is marked by the appearance of “superstructure” Bragg peaks in the orthorhombic phase. This is clearly evidenced by comparing the diffraction images of the high symmetry phase (left) and low symmetry phase (right). At 100 K the superstructure Bragg peaks obey the condition h+k = odd, using the orthorhombic notation.

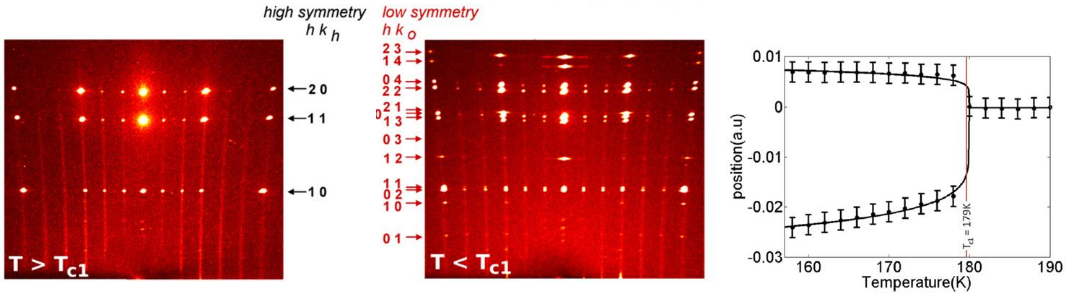

Figure 2-22 : 60° Rotating crystal x-ray diffraction images measured in the high-symmetry phase (phase I) at room temperature (left) and in the lowest symmetry phase (phase III) at 100 K (right). The guest diffraction appears as diffuse layers perpendicular to $c*$ (which is horizontal) with superimposed Bragg peaks. Miller indices (hk) along the reciprocal directions $a*$ and $b*$ correspond to the hexagonal cell for the HS phase and the orthorhombic cell for phase III. Evidence for the ferroelastic phase transition from hexagonal to orthorhombic symmetry at Tc1 = 179K in n-tetracosane/urea, through the domain-induced splitting of a structure Bragg peak. Here the (20l)h structure line splits into the (22l)o and (04l)o structure lines

Because of the complexities of the phase II, I will only discuss here the characteristics of the lowest temperature phase (phase III), I invite the interested reader to read the article “Long-range modulation of a composite crystal in a five-dimensional superspace” by L. Guérin et al published in Physical Review B in 2015 [39] for more complex superspace phase and more fun.

In the diffraction pattern measured at 90 K using the CRISTAL beamline at synchrotron SOLEIL, each of the superstructure lines exhibits a set of closely spaced Bragg peaks with maxima around 0, γ , 2γ , and 1 in urea reciprocal units along $\boldsymbol{c}^*$ (Figure 2-23). Essentially perfect agreement with the experimental data was obtained by fitting the superstructure Bragg peaks to multiple positions of a modulation vector $\boldsymbol{c_m}^* = (0.025 \pm 0.001)\boldsymbol{c_h}^*$. In order to describe the new superstructure Bragg peaks, a fifth, independent reciprocal vector must be introduced. This yields the following expression for the set of vectors $\mathbf{Q}_{hklmn}$, which give the positions of the whole set of Bragg peaks in this phase:

$$\boldsymbol{Q}_{hklmn} = h\boldsymbol{a}^* + \boldsymbol{k}\boldsymbol{b}^* + l\boldsymbol{c}_{\boldsymbol{h}}{}^* + m\boldsymbol{c}_g{}^* + n\,\boldsymbol{c}_{\boldsymbol{m}}{}^*$$

Full characterization of the diffraction pattern of this lowest temperature phase therefore requires five independent parameters (h, k, l, m, and n). The fifth index is associated with the fifth independent parameter $\boldsymbol{c_m}^*$, which appears in this orthorhombic phase and characterizes the supplementary modulation in this phase.

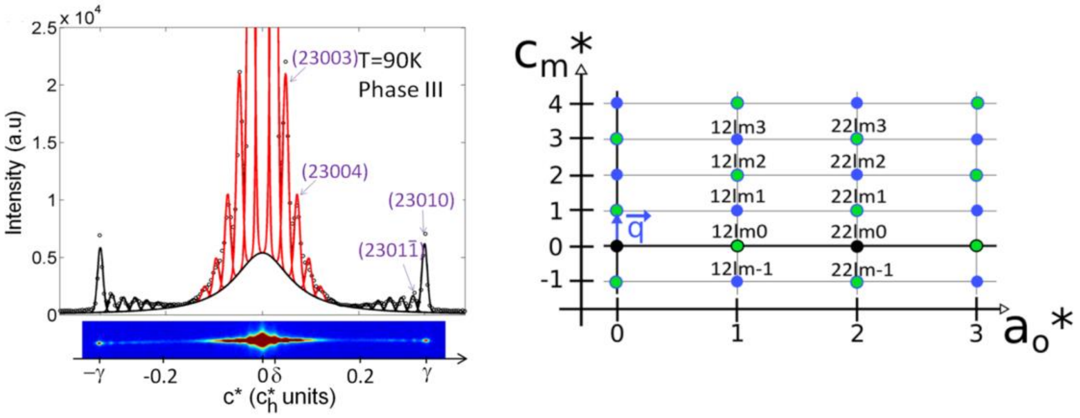

Figure 2-23 : (left) Diffraction image and extracted profile of the $(2\ 3\ 0\ m\ n)_o$ superstructure line between $-0.4\boldsymbol{c_h}^*$ and $+0.4\boldsymbol{c_h}^*$. Superstructure satellite Bragg peaks are associated with a modulation vector $\boldsymbol{c_m}^* = \pm 0.025\boldsymbol{c_h}^*$. Satellite peaks were fit using Gaussians and are indexed as $(2\ 3\ 0\ 0\ m)_o$ in red and $(2\ 3\ 0\ 1\ m)_o$ in black. (right) Schematic representation of the $(\boldsymbol{a_o}^*, \boldsymbol{c}^*)$ diffraction plane for $k = 2$ in phase III : The black points denote the structure Bragg peaks of the high symmetry phase, whereas the blue and green points indicate the positions of Bragg peaks representing the supplementary modulation.

Superspace groups must be discussed in terms of the presence conditions for the $(h\ k\ l\ m\ n)$ Bragg peaks. The modulation vector $\boldsymbol{q}$ characterizing phase III is $\boldsymbol{c_m}^* = (0,0,\delta)$, and the reflection conditions for this superspace group are $00lmn : l =$ even; $h0000 : h =$ even; $0k000 : k =$ even, with no condition on the sum $(h + k + n)$, as illustrated in Figure 2-23. The superspace group describing phase III is: $P\ 2_12_12_1(00\gamma)(00\delta)$. The change from $P6_122$ to $P2_12_121$ correspond to the transition from the hexagonal to the orthogonal lattice, (00γ) to the composite structure along c with a misfit parameter γ and (00δ) to the new modulation along c with a misfit parameter δ.

The phase transition correspond to a transition within the superspace with an increase of the dimensionality of the superspace from a rank 3+1 to a rank 3+2.

The conclusion regarding n-tetracosane/urea is that the wavelength of the modulation along the channel axis, deduced from the parameter δ, is on the order of 425 Å in real space. This corresponds to an exceptionally large period, approximately 40 times the pitch of the urea helix. This study demonstrates that, instead of seeking a commensurate lock-in solution, which it evidently never approaches, this inclusion compound choses to create an additional modulation with a very long period to satisfy the interaction between the two sub-networks following the orthogonal shearing. This structural solution is found in several compounds within this family, exhibiting the phase sequence.

2.3.2 The creation of modulated monoclinic aperiodic composite in n-dodecane/urea

At room temperature, n-dodecane/urea exhibits a "liquid" phase confined within the solid urea matrix (Figure 2-24). This phase, of rank 3 and characterized by the space group $P6_122$ for the host sub-network, persists until approximately 250K. This liquid phase is evidenced in the diffracted pattern by diffuse planes perpendicular to **c***. This diffuse scattering will be analyzed in chapter 3 where we will deal with disorder. Our focus here is solely on the phase transition leading from this hexagonal structure to a monoclinic structure of rank 4 below.

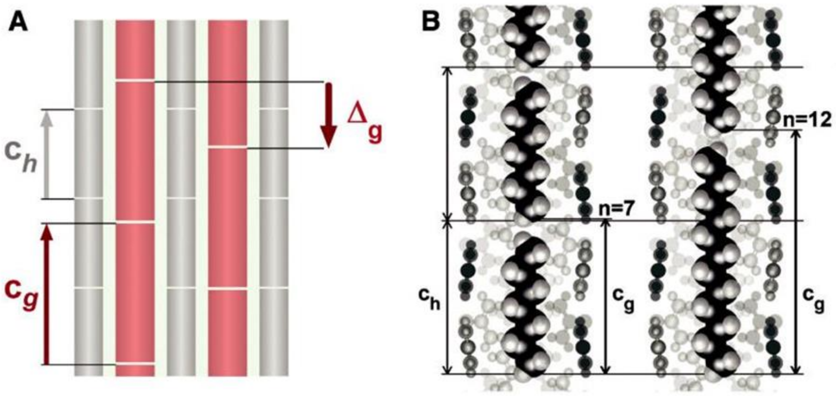

Figure 2-24 : : (A) Definitions of the different parameters along the channel direction for a uniaxial composite made of ultimately confined guest molecules within a host subsystem (c_h (c_{host}), c_g (c_{guest}), and Δ_g, the relative shift of the guest chains from channel to channel); (B) the *n*-alkane/urea prototype family with n=7 (*n*-heptane/urea) and n=12 (*n*-dodecane/urea).

Below 248 K, a phase (Phase I) emerges with a set of Bragg peaks corresponding to the periodicity of the guest along the incommensurate direction, indicating 3-D ordering of the guest subsystem (Figure 2-25). It corresponds to a crystallization of the guest molecules inside the urea channel and it is the standard phase observed in n-alkane/urea inclusion compounds, namely the hexagonal phase $P6_122(00\gamma)$, of rank 4. The incommensurability parameter for this transition is $\gamma=0.632$.

In the low-symmetry phase II below 124 K, the Bragg peaks associated with the alkane sub-network are indexed using a reciprocal base vector $\mathbf{c_g*}$ having a non-zero component along the $\mathbf{a*}$ axis: $\mathbf{c_g*}=\alpha\mathbf{a*}+\gamma\mathbf{c_h*}=\alpha\mathbf{a*}+\gamma\mathbf{c_h*}$. The parameter α is irrational and equals 0.160. In this phase, all reciprocal lattice vectors are indexed using four base vectors:

$$\boldsymbol{Q}_{hklmn} = h\boldsymbol{a}^* + \boldsymbol{kb}^* + l\boldsymbol{c_h}^* + m\boldsymbol{c_g}^* + n\,\boldsymbol{c_m}^*$$

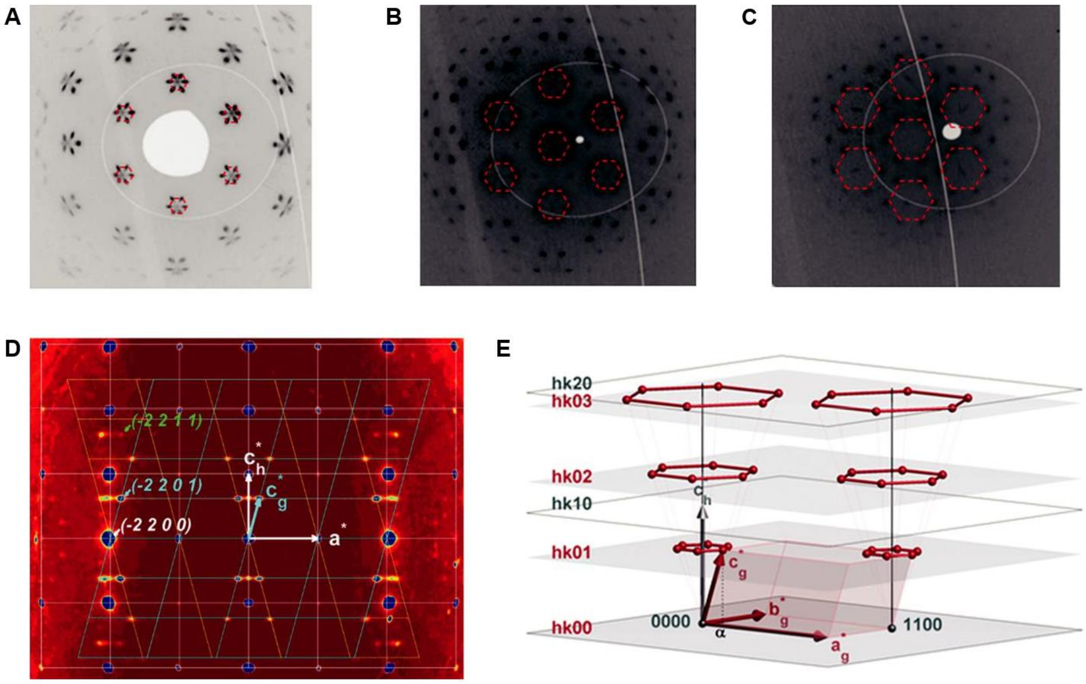

Figure 2-25 : (A), (B) and (c) Reciprocal planes ($h\ k\ 0\ m$) with $m=1$ (A), 2 (B) and 3 (C) reconstructed from measurements in the low symmetry phase of *n*-dodecane/urea (T=100 K, 14-BM-C, APS). Red hexagons are guides for the eyes. (D) reconstructed ($h\ 2\ l\ m$) plane of *n*-dodecane/ urea in the same phase. The red lines represent the monoclinic cell, and the green arrow points to an intermodulation satellite. (E) 3-D schematic representation of the reciprocal space of *n*-dodecane/urea in the low symmetry phase.

The key feature of phase II is that the reciprocal vectors $\mathbf{c_h^*}$ and $\mathbf{c_g^*}$ are no longer parallel. This indicates that the two sublattices do not have the same mean crystal system. The host subsystem remains orthorhombic whereas the guest subsystem is monoclinic. Symmetry reduction gives rise to twinning. The six c_g^* vectors are independent, and a single domain is associated with each one. The highest superspace group compatible with the extinction conditions related to the composite, having a dimension of 4, is $P12_11(\alpha 0\gamma)$.

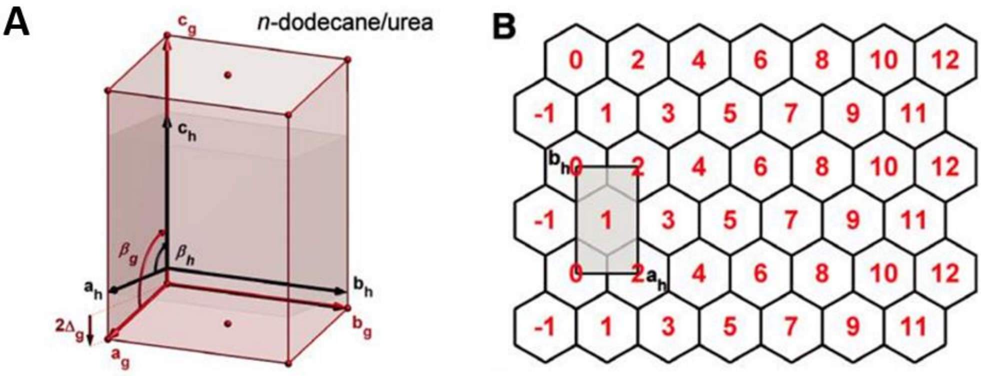

Figure 2-26 : Schematic real space representations of *n*-dodecane/urea in real space. (A) Schematic representation of the real unit cell associated with the host substructure in gray and the guest substructure in red, with an arbitrary shift of the two unit cells along ***c***. (B) projections in real space along the *c* direction. The black hexagons represent the urea subsystem. The red numbers indicate the relative displacements of the guest molecules along ***c*** in Δ_g units. The black arrows indicate the basic vectors associated with the urea subsystem.

The symmetries observed in the reciprocal lattice imply a monoclinic unit cell in real space for the composite. For the alkane sub-network, the unit cell is centrally positioned, and the angle βg corresponds to a translational shift in the channel of 2Δg =2.8 Å between two adjacent channels along the *a* direction. This means that alkane chains from one channel to another in the a_h direction shifts of 2.8 Å along the channel direction forming a monoclinic ordering of the guests (Figure 2-26).

In conclusion, short guest composites appear quite rich because they possess much larger mean square amplitudes of translation along the channels than longer guests. At room temperature, they show a liquid-like state for the guest sub-system confined within the rigid, hexagonal host matrix. At lower temperature, the quasi liquid solidifies and because of the strong intermodulation between the urea and the guest, they can form monoclinic order corresponding to a constant shift of the alkane chains from channel to channel.

2.3.3 Phase transitions within crystals that are aperiodic by construction

As I already said, we spent many years to study the phase diagrams of n-alkane/urea composite systems, from short guest like heptane (n=7) to very long guests like tetracosane (n=24). The idea was to find some universal properties and characteristics of the different phase transitions within crystals that are aperiodic by construction.

Diffraction measurements permit to measure very precisely the position of the host and guest Bragg peaks along c* and thus determine with a very good accuracy the misfit parameter $\gamma = c_h/c_g$. In Figure 2-27, the continuous line corresponds to the function $\gamma = c_h/c_g$, where $c_h = 11.02$ Å and $c_g = [1.270\,(n-1) + 3.658]$Å. It is consistent with the one derived previously by Lenné et al. for a different range hydrocarbon chain lengths. With the exception of n = 8 and 11, which become commensurate on cooling, these misfit parameters remain constant across the range of temperatures measured between 260 K and 80 K. Several other members of this series are very close to commensurate at 260 K (n = 7, 16, 24), but remain incommensurate on cooling. For *n* = 16, the crystal becomes commensurate under hydrostatic pressure. For *n* = 20, the crystal is periodic by construction.

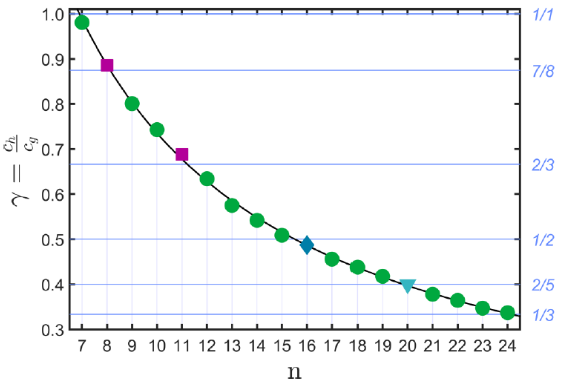

Figure 2-27 : Evolution of the misfit parameter γ in *n*-alkane/urea inclusion compounds as a function of the number of carbon atoms (*n*) in the *n*-alkane guest molecule. Apart from *n* = 8 and 11, the misfit parameter remains constant across the range of temperatures measured

The diversity of phase transition pathways observed in inclusion compounds of n-alkane/urea is presented in the Figure 2-28. The numbers 7–24 correspond to the carbon count, n, in the linear alkane guest with the formula $n - C_nH_{2n+2}$. For each n and each phase depicted in the phase diagram, the maximal superspace group was determined by analysing the systematic absences of Bragg peaks. n-alkane/urea crystals manifest two distinct high-symmetry hexagonal phases. For the shortest guests (n = 7–12), no Bragg peaks are associated with the guest periodicity, and the diffraction pattern of the guest substructure appears solely as diffuse planes perpendicular to the channel axis. In this context, the guests exhibit a one-dimensional quasi-liquid phase along the channel, with no long-range order between guests in adjacent channels. The space group assignment is then exclusively attributed to the host subsystem, identified as hexagonal $P6_122$. A different structural solution is found for longer guests ($n > 13$). These materials are 3 + 1 incommensurate composites at 260 K, exhibiting Bragg peaks at host, guest, and satellite positions. Such incommensurate composites are described by the following rank-4 and with the superspace group $P6_122(00\gamma)$.

When cooling from room temperature, the phase transitions in these composite crystals reveal three main characteristics :

Solidification with lock-in or monoclinic ordering : The first corresponds to a transition towards monoclinic symmetry, particularly observed in compounds featuring short-chain guests (n = 7, 8, 11, 12), which exhibit a greater translational degree of freedom along the channels. Notably, one of them (n = 11) undergoes a transition to a commensurate structure, described by a monoclinic three-dimensional space group, leading to a reduction in the dimension of the crystallographic space. Others undergo transitions to monoclinic intermodulated composites described by four-dimensional monoclinic superspace groups.

Ferroelastic transition : The second group of compounds undergoes phase transitions that maintain the four dimensions of crystallographic superspace, corresponding to shifts from the hexagonal superspace group $P6_122(00\gamma)$ to the orthorhombic $P2_12_12_1(00\gamma)$.

Transition within the superspace : Particularly intriguing is the third group, which experiences an increase in the dimension of the crystallographic superspace from 4 to 5 (n = 15, 16, 18, 19, 21, 24), as presented earlier for tetracosane/urea. For n= 15 , 18, 19 and 24, an even more intriguing phase appears with the space group $C2221(00\gamma)(10\delta)$ which corresponds to a centering within the superspace. In the low symmetry phase $P2_12_12_1(00\gamma)(00\delta)$, all channels are equivalently modulated, whereas in this C centered phase, there is a shift of one-half the period of the long-range modulation function in adjacent channels. Why the system choose this solution ? It is a complete mystery.

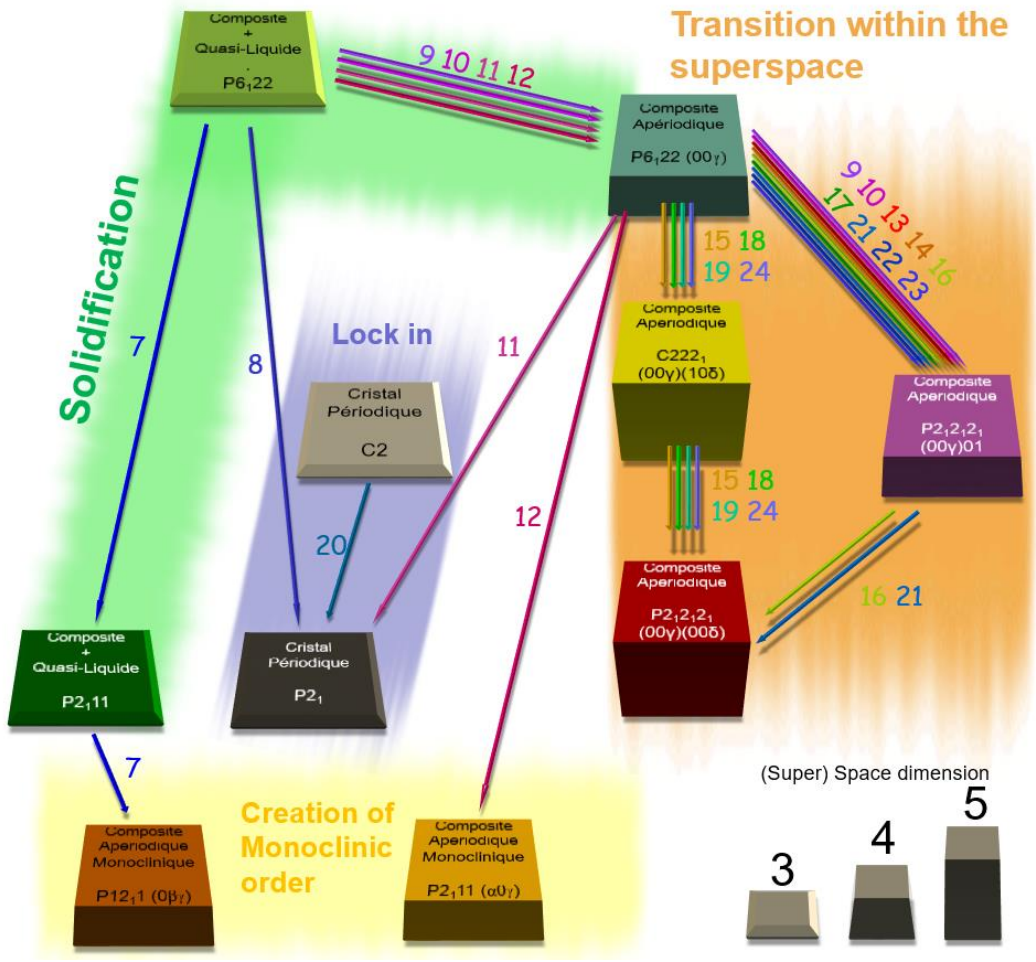

Figure 2-28 : The n-alkane/urea superspace sequence of phase. Numbers corresponds to the number of carbon in the alkane chain. For each phase in the superspace (square with different height), the characteristic feature of the phase and the superspace group is noted. Direction of arrows corresponds to cooling, height of square to dimension of superspace.

Describing the phase transitions in aperiodic composites like n-alkane/urea is a highly complicated task. As mentioned earlier, the incommensurability arises from the irrational ratio of lattice parameters between the host and guest subsystems. Our study of alkane ranging from n = 7 to 24 reveals the existence of multiple phases characterized by many types of phase transitions. Notably, there is a observed variability in the space group dimensionality, transitioning between ranks 3, 4, and 5.

Group/subgroup relationships

We saw in the chapter 1 that we could use the group/subgroup relationship in order to analyze phase transition. We can ask the question of the validity of this relation in the case of aperiodic materials. To understand why a group/subgroup phase transition may lead to an increase in the dimensionality of crystallographic space, it is essential to consider that a periodic 3 dimensional crystal can be described in a 3+d dimensional space where there are no additional modulations along the d internal dimensions of the superspace. Therefore periodic 3+0 crystals can be considered a specific case within crystallographic superspace namely, 3+d crystals where the amplitudes of supplementary modulations along the d dimensions are zero. The high temperature phase being embedded in a superspace of the same dimension as the incommensurate phase, it exits a group/subgroup phase transition between a D+0 dimensional space group (the high-symmetry periodic crystal) and the corresponding D+d superspace group of lower symmetry.

We can extend this concept to crystals inherently aperiodic by construction (here of 3+1 dimension). In the case of the transition in the superspace like $P6_122(00\gamma)$ to $C2221(00\gamma)(10\delta)$ for example, we can treat the 3+1 dimensional superspace as a 3+2 dimensional superspace, with the amplitude of the modulation in the fifth dimension becoming nonzero at the phase transition. If we look at each phase transition in the n-alkane/urea superspace sequence of phase tree (Figure 2-28), we can see that the group-subgroup relationship remains intact during a phase transition, irrespective of the change in rank. We could conclude the group/subgroup relationship is valid for any class of materials from the periodic one to incommensurate or aperiodic composite crystals.

2.4 PHASE TRANISTION IN QUASICRYSTALS

The last category of aperiodic materials is the quasicrystal. Quasicrystals are long range ordered materials that lack translational symmetry. While periodic crystals, can possess only two-, three-, four-, and six-fold rotational symmetries, the Bragg diffraction pattern of quasicrystals shows sharp peaks with other symmetry orders for instance, five-fold. The discovery of the CdYb icosahedral quasicrystal [41] has been a breakthrough in the field allowing a detailed understanding of its atomic structure [42]. In the same system there are also, for small chemical changes, periodic approximant, having the same local order as the quasicrystal. It has been shown that the $YbCd_{5.7}$ quasicrystal and its periodic approximant $YbCd_6$ are built up with the same atomic cluster shown on the Figure 2-29, packed on a quasiperiodic lattice or a body centered cubic lattice. These so-called Tsai-type QCs feature aperiodic ordering of large atomic clusters composed of 5 layers, with a tetrahedron at their center (Figure 2-29).

The comparison of the quasicrystal and their approximant allows thus to get insight in stabilizing mechanisms, here believed to be a combination of geometrical frustration (atomic clusters) and electronic effect. Their structures are now well understood using the superspace formalism by treating the aperiodicity as a 3+3 periodic structure and a detailed understanding has been achieved for the icosahedral $YbCd_{5.7}$ phase [41,42]

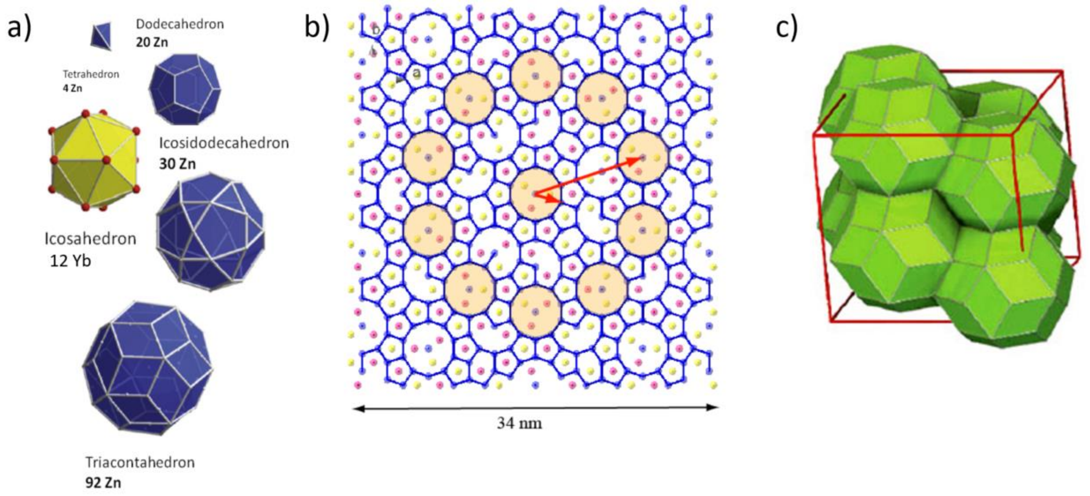

Figure 2-29 : Illustration of the structure of the CdYb icosahedral quasicrystal. a) Tsai-type cluster : successive shells of the Tsai type cluster. The first shell is a tetrahedron. Grey and blue colours stand for Cd and Yb atoms respectively. b) 34 nm portion of a 5-fold plane of the Cd5.7Yb icosahedral quasicrystal. Only cluster centers are displayed c) This cluster can be packed periodically in the Cd6Yb approximant.

In the Cd_6Yb periodic approximant phase, a low temperature order-disorder type transition has been observed and attributed to the central tetrahedron ordering [43,44]. Neutron scattering measurements on an approximant have shown a dynamic response of these tetrahedra [45]. Their ordering is thought to be at the origin of a low-temperature phase transition accompanied by a Cp signature. Fundamental questions remain open, in particular as regards the dynamics of the tetrahedron in the case of quasicrystals and the coupling of this rotation mode with deformation modes of the different layers within the cluster. In collaboration with Professor An Pang Tsai and Doctor Tsunetomo Yamada from Tohoku University, we focused on the phase transition in the approximant and quasicrystal. The idea of this project was to gather experimental evidence of the phase transition using diffraction and NMR spectroscopy.

High resolution X-ray diffraction at IPR

We carried out experiments using the high resolution X-ray diffractometer at the Institut de Physique de Rennes on the $Cd_{5.7}Yb$. We observed sharp Bragg peaks suggesting that the quasicrystal crystals have good crystallinity. While cooling the sample using He flow cryojet at 40 K, the phase transition was visible on selected area of the X-ray diffraction patterns, where distortions of the high temperature icosahedral phase are observed. Some weak reflections are displaced from their ideal position when compared with the diffraction pattern at 300 K (Figure 2-30). Using superspace formalism, we could show that the peak displacement can be understood as a consequence of the uniform phason strain, a collective excitation found in aperiodic material, that is related to the orientational ordering of the central tetrahedron in the low temperature phase coupled to the deformation of the different shells of the cluster.

^{67}Zn NMR investigation of 1/1 Zn_6Sc approximant and quasicrystal

The tetrahedron is composed exclusively of zinc atoms. As NMR is a probe sensitive to local dynamics, high-field NMR of zinc ^{67}Zn could answer our questions. We performed ^{67}Zn NMR measurement at the Pole RMN- Institut Chevreul – Université de Lille equipped by high field 18.8 T – 800MHz NMR spectrometer. We acquired the ^{67}Zn NMR in CPMG mode at the magic angle, in order to highlight an NMR signal associated with the central tetrahedron of the structure (Figure 2-30). We could observe a peak in the NMR spectrum of the approximant that was absent in the quasicrystal. This peak was interpreted as the signature of the dynamic rotational nature of the central tetrahedron. Additional measurements were performed by my colleagues at IPR on the approximant at low temperature and showed that the peak disappeared at the phase transition. (unpublished data)

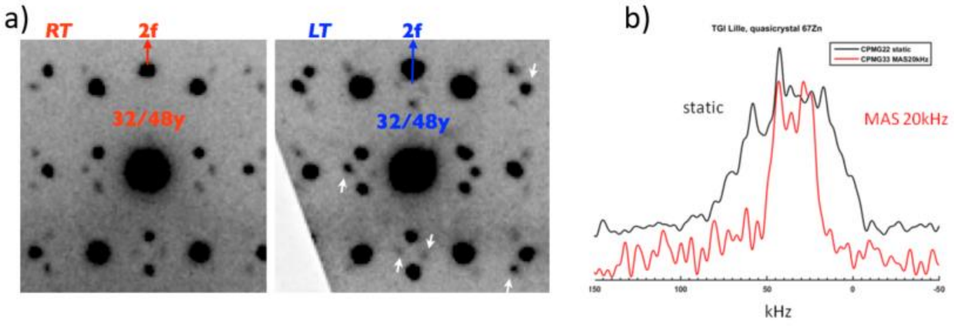

Figure 2-30 : a) diffraction taken at RT (left) and 40 K (right) Bragg peak displacements are indicated by white arrows. b) ^{67}Zn NMR spectrum of the Zn_6Sc approximant

In the case of the approximant, which are periodic crystal, the transition from a cubic cell to a monoclinic cell is very simple to spot as splitting of Bragg peaks due to formation of monoclinic domains are clear signals in the diffraction pattern. This symmetry breaking is due to the ordering of the central tetrahedron of the Tsai type clusters that deforms the different shells in one direction forming domains with different orientation. In the case of quasicrystal, there is no, a priori, a direction of high symmetry in our 3d space as clusters are arrange in an aperiodic fashion. At low temperature, the tetrahedron freezes its orientation but this not couple to other cluster in a periodic and coherent way. In the superspace, this deformation can be related to a phason mode (collective excitation found in aperiodic crystal) that is signed by a peak shift in the diffraction pattern. For NMR, which is a local probe, we could observe the dynamics of tetrahedron but only in the case of the approximant. The Zn tetrahedron represents only 2.3% of the Zn atoms presents in the Tsai-type cluster and if in addition we consider that in the quasicrystal, those tetrahedron are not coupled, it may be not surprising that the NMR signal, if it exits, must be very weak.

In any case, due to the aperiodic nature of quasicrystals, those signals are very weak and subtle, analysis using 3+3 dimension superspace are also very complicated. The investigation of the phase transition in quasicrystal was a very difficult project and after a couple of years working in the subject, I moved on leaving this problem to the next generation of crystallographers.

2.5 CONCLUSION

Aperiodic orders are ubiquitous in nature. The use of superspace crystallography allows to recover the lost periodicity by embedding the 3d aperiodic crystal into 3+d superspace periodic space. Because of the recovered periodicity, diffraction patterns are comprised of sharp Bragg peaks allowing the crystallographer to apply the usual tools to the case of superspace. We saw that we can solve an determine structure of aperiodic crystals and study group-subgroup relations in order to understand the different phase transitions that occurs in the 3d space or even more intriguing inside the superspace.

The question one can asked is, after looking at those aperiodic crystal, is the nature of a crystal. Aperiodic crystal are not that different that a 3d periodic crystals. It is not that they are disordered, it is just that they are ordered in a different way and they are even periodic in the superspace. They behave the same, they show phase transition that can be described using Landau theory for instance. In 1991, the International Union of Crystallography reported :

> “In the following by 'crystal' we mean any solid having an essentially discrete diffraction diagram, and by 'aperiodic crystal' we mean any crystal in which three- dimensional lattice periodicity can be considered to be absent. As an extension, the latter term will also include those crystals in which three-dimensional periodicity is too weak to describe significant correlations in the atomic configuration, but which can be properly described by crystallographic methods developed for actual aperiodic crystals.”

I think it is quite interesting that we define the nature of something not by it is inner structure but by the result of the interaction with its structure. It is like defining a carrot by “a carrot is a substance when ingested by a human body increases the level of vitamin A in the organism through the absorption of β-carotene”. Imagine that we would need a blood test to determine that a carrot is a carrot. Maybe that’s why some of my colleague crystallographers dislike the “new” definition of the crystal.

In the diffraction pattern, we observed very sharp Bragg peaks (it is a crystal) but we also, in some case, observed very weak and diffuse signals out of the Bragg peaks which are called diffuse scattering. For instance, n-alkane urea with short guest shows a liquid phase of the guest at room temperature that is evidenced in the diffracted pattern by diffuse planes perpendicular to the channel. We also know that near the critical point, fluctuations of the order parameter correspond to the apparition of a local order defined by correlation length and in the reciprocal space, this local order gives rise to diffuse scattering. Therefore, order (even aperiodic one) equal Bragg peaks and disorder equal diffuse scattering. The next chapter will deal with the analysis of diffuse scattering where we will try to tidy a little bit at least our knowledge of the subject.

Essentials of correlated disorder and diffuse scattering

The deviation from perfect translational symmetry manifests as "diffuse scattering," where a notable fraction of diffracted intensity, distributed in reciprocal space beyond Bragg peaks, becomes a key indicator of **correlated disorder**: a situation where disorder within a crystal lattice exhibits some form of correlation.

As presented in chapter 1, advances in experimental techniques, including brighter X-ray sources and noiseless detectors, as well as developments in crystallographic methods provides insight into correlated disorder. In this chapter 3, we present the theory and analysis method such as 3D-ΔPDF of the diffuse scattering in order to characterize disorder in crystal.

SCATTERING FROM DISORDERED CRYSTALS

Dimensionality and correlation length

The correlation length refers to a characteristic distance over which disorder or variations in the crystal lattice persist and exhibit statistical correlation. Dynamic disorder, with long correlation lengths, appear highly localized in reciprocal space, causing diffuse intensity around the Bragg nodes. In contrast, static disorder is characterized by short correlation lengths, such as precipitates or clusters of vacancies, involving only a few atoms. The diffuse intensity resulting from static disorder is more spread out in reciprocal space.

Using the equations from chapter 1, we show that in case of 1D correlated disorder along the a direction, diffuse planes are formed perpendicular to a. The width of the planes $1/\xi$ are inverse of the size ξ of the correlation in the real space. For 2D correlated disorder forming correlated domains of size ξ_a along a and ξ_b along b, diffuse scattering appears as diffuse rods along c* with a width $1/\xi_a$ along a* and $1/\xi_b$ along b*. (figure 0-1)

Thermal diffuse scattering (TDS)

In a crystal, the vibrations of the atoms are not independent but are collective motions that are referred as normal modes or phonons. Consequently, the diffuse scattering associated to this long range collective motions emerges from the Bragg peak. The TDS decreases as one moves away from the Bragg peak and is weak when the speed of sound of the acoustic mode is high.

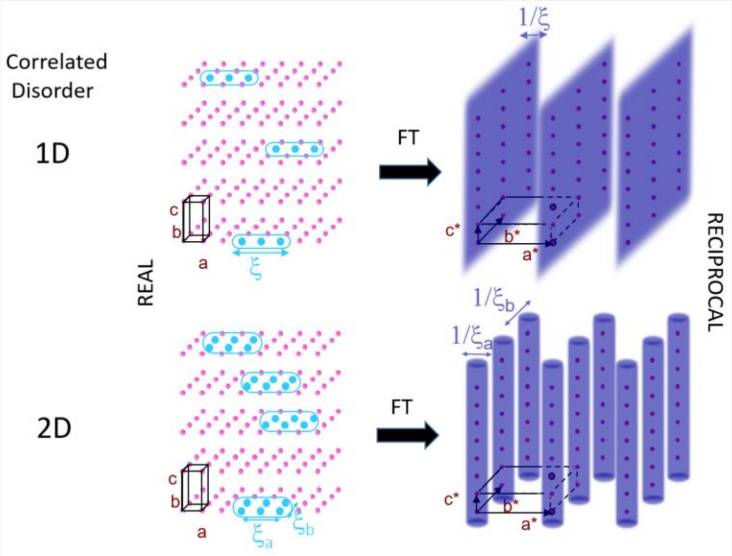

Figure 0-1 : Correlated disorder and its associated diffuse scattering

Diffuse scattering from correlated disorder

In the case of static correlated disorder, calculation of the diffuse scattering lead to two different signal depending on the type of correlation in the disorder. In the case of positive correlation, diffuse scattering condenses at the Bragg peak position. Figure 0-2 shows the condensation of diffuse scattering at the edge of BZ in the case of negative correlation (anti-ferro) for disorder that are correlated and expand to several unit cells. For infinite correlation, meaning a completer ordering, the diffuse scattering condenses as Bragg peak and lead to cell doubling characteristic of an anti-ferro ordering.

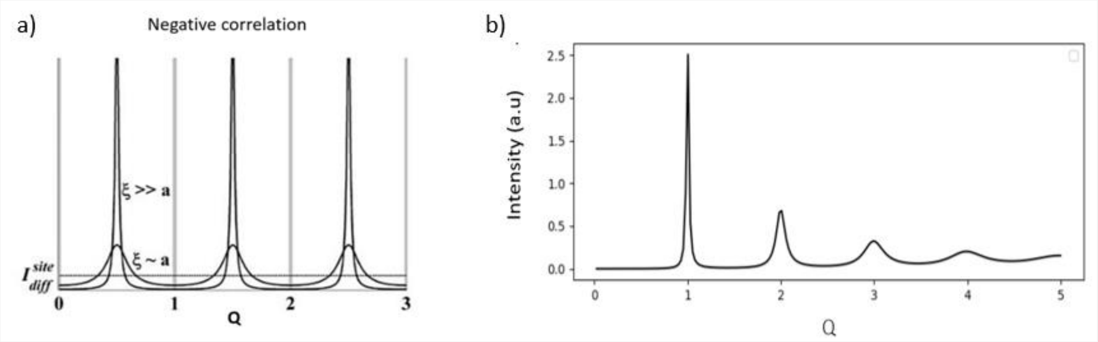

Figure 0-2 : (a) effect of negative pair correlation on the diffuse scattering (b) Diffuse scattering of disorder of 2nd kind that disrupts translation symmetry.

Diffuse scattering from disorder that disrupted the translational symmetry.

Disorder of 2nd kind is a type of disorder that disrupts the translation symmetry. This disorder arises when interactions between lattice sites are limited to immediate neighbors. We can calculate the diffuse scattering for such disorder in the case of 1D crystal : the diffuse scattering shows maximum at the nodes of the reciprocal lattice. The width of the peak increase with the index of the node m following a quadratic law. (Figure 0-2)

Diffuse scattering from critical phenomena

Critical phenomena occur near the phase transition. In a very naïve way, we can describe the apparition of the low symmetry phase as the formation of local domains with a finite size that fluctuate within the high symmetry phase. Near the critical point, fluctuations of the order parameter correspond to the apparition of a local order defined by correlation length.

THE CASE STUDY OF ALKANE-UREA

Pretransitionnal diffuse scattering

Nonadecane-urea shows a phase transition from a superspace of rank 4 to a rank 5.

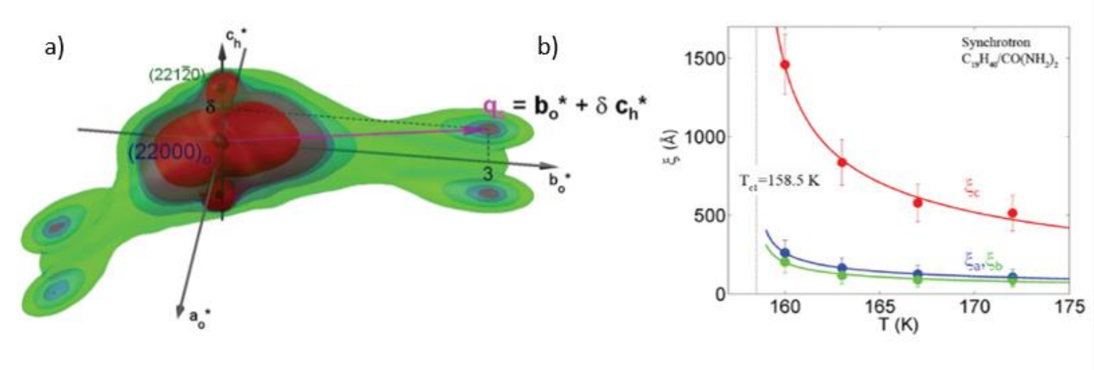

Figure 0-3 : (a) pretransitional diffuse scattering. (b) Temperature evolution of correlation length

Figure 0-3 shows that the pretransitionnal diffuse scattering (i.e., that not associated with a Bragg peak from the high-symmetry phase) is most intense at the location of critical wave vector $\mathbf{q}_s$ associated to the transition from rank 4 to 5. The analysis of this disc-shaped pretransitionnal x-ray diffuse scattering around the critical wave vector allows the determination of the correlation lengths (ξ_a, ξ_b, ξ_c). These correlation lengths appear isotropic in the (a, b) plane. Along the aperiodic direction c, the extracted length is much larger and is associated with quasi one-dimensional fluctuations along the aperiodic direction c. The noteworthy aspect of almost infinite correlation lengths along the aperiodic direction suggests the possibility of phase fluctuation leading to antiferro-ordering along the supplementary internal space of the superspace. This experimental work extends the treatment of pretransitionnal phenomena to higher-dimensional space.

Quasi liquid and 2nd kind disorder

The fluctuations of short-chain guest molecules inside the urea disrupt the guest ordering leading to a disorder of 2nd kind. The guest subsystem primarily manifests as sharp, parallel diffuse planes, referred to as s-planes located at multiple value of $2\pi/C_g$. This disorder has been characterized as the "paracrystalline state". Figure 0-4 shows the evolution of the experimental width of s planes as a function of the order m of the plane. The value of Δ, characterizing the liquid-like feature, can be determined from this analysis.

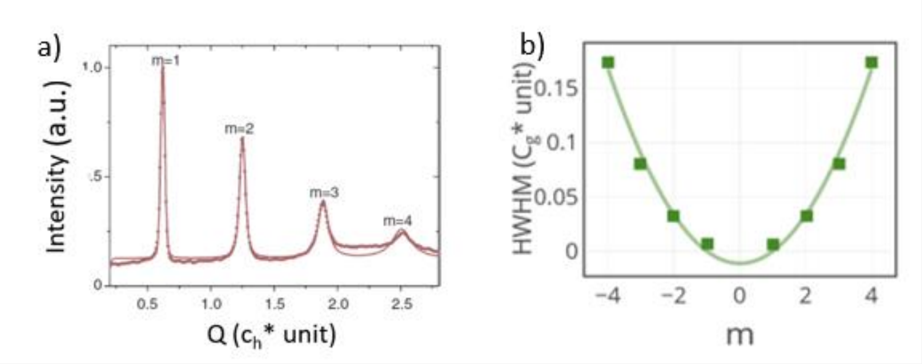

Figure 0-4 : Profile along the *c* direction showing the broadening of the planes with their order *m*. b) Half-width at half-maximum of the diffuse planes of order m=1,2,3, and 4.

THE 3D-ΔPDF METHOD

The 3D-ΔPDF involves calculating the Fourier transform of the diffuse scattering alone in order to draw a 3D map of the correlations of the disorder. It provides a way to analyze correlated disorder in the real space.

Diffuse scattering and the 3D- ΔPair Distribution Function

One can show that the 3D-ΔPDF, noted $[P_\Delta(\mathbf{r})]$ is expressed as :

$$\langle I_{diffuse}(\mathbf{q})\rangle = \mathfrak{F}[P_\Delta(\mathbf{r})]$$

Experimentally, $P_\Delta(\mathbf{r})$ can be obtained by calculating the (inverse) Fourier transform of the diffuse scattering only. The 3D-ΔPDF captures the correlated disorder in the crystal that is not reflected in the average structure. Peaks in the map corresponds to the probability of a specific interatomic vector being found in the real structure rather than in the average one. Positive values indicate that corresponding interatomic vectors appear more frequently in the real structure than in the average structure, and negative values indicate the opposite. (figure 0-5)

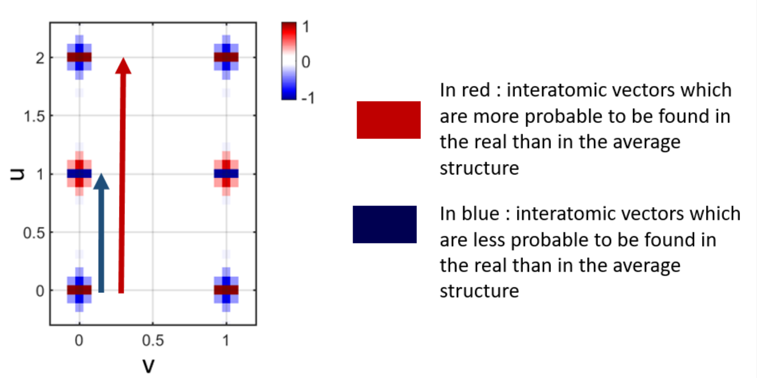

Figure 0-5 : example of a 3D-ΔPDF map

To illustrate this method, we introduce a 1D - model of dimerization. We consider a real crystal composed of two different structures A and B generated by anti-phase displacement (δ) of nearest atoms, each structure related to the other by a one-half translation along a. Model diffraction patterns can be obtained from the calculation of the autocorrelation function of the electron density known as the PDF and the Patterson calculated from the real structure and the average structure, respectively. The ΔPDF is the difference between the PDF and the Patterson function. In the specific case of dimerization, we observe a distinct repetition of negative-positive-negative peaks (positive Mexican hat) and positive-negative-positive (negative Mexican hat).

2D CHARGE-DENSITY-WAVE ATOMIC STRUCTURE IN AN MX–CHAIN BY THE 3D-ΔPDF METHOD

Quasi-one-dimensional halogen-bridged metal complex so called MX-Chains have an isolated one-dimensional (1D) electronic system. The very large majority of M=Pd compound which have a $–X\cdots M^{II}\cdots X–M^{IV}–X\cdots$ Peierls distorted 1D structure, are in a mixed-valence charge-density-wave (MV-CDW) state. This mixed-valence state is accompanied by a strong dimerization along the chain, with two competing CDW ground states. However, some Pd complexes shows a Mott-Hubbard (MH) sate. In such a case, at variance with CDW, the X-M-X bonds are completely symmetric.

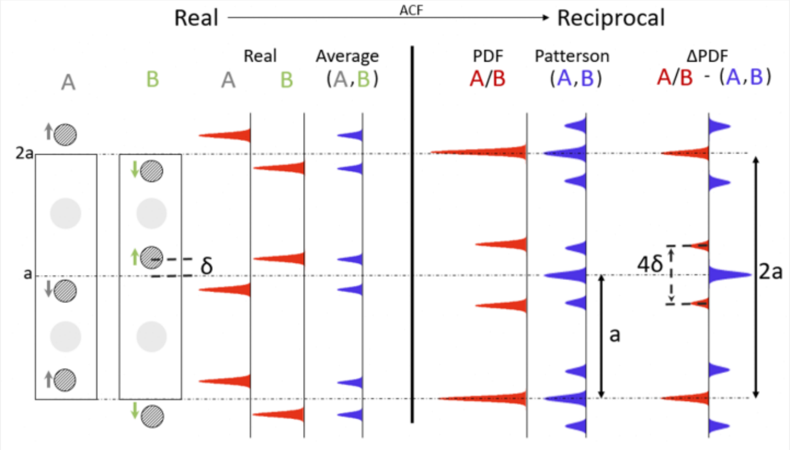

Figure 0-6 : ΔPDF of 1D-Chains. a) (left) simple model of a + δ dimerization along a with equal probability of A and B atomic configurations. Electron density of the individual A, B atomic positions (real structure) and the average structure. (right) Associated autocorrelated function (ACF) of the A/B structure (PDF), of the average (Patterson) and their difference (ΔPDF = PDF-Patterson).

Determination of the average structure

X-ray experiment leads to the structure determination of $[Pd(cptn)_2Br]Br_2$ that consists of a body-centered arrangement of MX chains. The important observation is that the Pd-Br-Pd distance is symmetric, and no sign of dimerization is observed in the average structure. There is no evidence of a CDW organization regarding the average structure from this single crystal structural analysis.

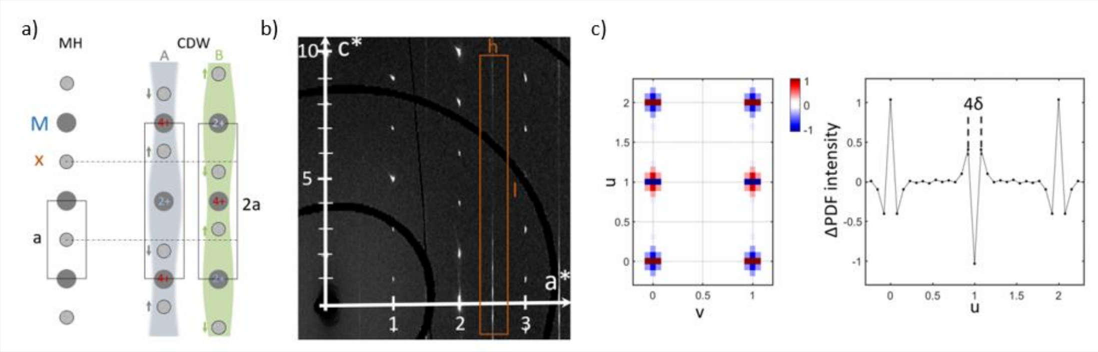

Figure 0-7 : (a) Schematic representation in halogen-bridged metal compounds (MX chains) of the Mott Hubbard (left) and the Charge Density Wave states (right) showing the two competitive ground states (A and B). (b) reconstructed (h 0 l) reciprocal plane shows c* diffuse streaks at half integer values of a*. (c) experimental normalized ΔPDF of the (a,b) plane (left) and its profile along a (right). The displacement is $\delta = 0.038a = 0.2$ Å.

Analysis of the diffuse scattering

A set of diffuse streaks parallel to the c* axis and perpendicular to the (a*, b*) plane are observed, suggesting the existence of a two-dimensional (a, b) ordering in real space with disorder along the c direction. (figure 0-7)

Application of the 3D –ΔPDF method

The inverse Fourier transform of the normalized diffuse scattering function yields the 3D-ΔPDF. Figure 0-7 shows a section of the ΔPDF corresponding to the (*u*, *v*, 0) plane. The analysis of the ΔPDF indicates that the (*a*, *b*) plane consists of long-range ordered dimerized chains in the CDW state contradicting the result of the analysis of the average structure.

The present study demonstrates the great power of the 3D-ΔPDF method in analyzing diffuse scattering data and provide insights into the disorder present inside a material. The absence of superstructure Bragg peaks and the wrong assumption that the crystal structure lies in the MH state is due to the fact that the information lies within the diffuse scattering.

Due to remarkable advances in experimental capabilities at synchrotron facilities, particularly in beam flux and detector technologies, 3D-ΔPDF approaches are expected to become standard methods for addressing the investigation of correlated disorder in more complex systems. One can define strategies with the ultimate objective to master and harness correlated disorder intentionally. This signifies a shift from merely understanding disorder's role in producing interesting physical properties to using it as a deliberate design element for engineering materials with innovative functionalities.

The chapter 3 is based on the following papers :

A. Simonov, P. Rabiller, C. Mariette, **L. Guérin**, A. Bosak, A. Popov, and B. Toudic, Short-Range Order in the Quasiliquid Phases of Alkane Substructures within Aperiodic Urea Inclusion Crystals, **Physical Review B** 106, 054206 (2022).

L. Guérin*, T. Yoshida*, E. Zatterin, A. Simonov, D. Chernyshov, H. Iguchi, B. Toudic, S. Takaishi, and M. Yamashita, Elucidating 2D Charge-Density-Wave Atomic Structure in an MX–Chain by the 3D-ΔPair Distribution Function Method, ***ChemPhysChem*** 23 (2022).

VIP + COVER

Céline Mariette, **Laurent Guérin**, Philippe Rabiller, Yu-Sheng Chen, Alexei Bosak, et al.. The creation of modulated monoclinic aperiodic composites in n-alkane/urea compounds. ***Zeitschrift für Kristallographie***, 2015, 230 (1), pp.5--11.

Céline Mariette, **Laurent Guérin**, Philippe Rabiller, Claude Ecolivet, P. Garcia-Orduna, et al.. Critical phenomena in higher dimensional spaces : The hexagonal-to-orthorhombic phase transition in aperiodic n-nonadecane/urea.. ***Physical Review B*****,** 2013, 87 (10), pp.104101.

Concepts presented in the chapter 3 were used in the following works :

T. Yoshida, S. Takaishi, **L. Guérin**, T. Kojima, H. Ohtsu, M. Kawano, T. Miyamoto, H. Okamoto, K. Kato, M. Takata, Y. Hosomi, S. Yoshida, H. Shigekawa, H. Tanaka, S. Kuroda, H. Iguchi, B. K. Breedlove, Z.-Y. Li, and M. Yamashita, Hydrogen Bonding Propagated Phase Separation in Quasi-Epitaxial Single Crystals: A Pd–Br Molecular Insulator, **Inorganic Chemistry**,61,35,14067 (2022)

C. Mariette, Ilya Frantsuzov, Bo Wang, **Laurent Guérin**, P. Rabiller, et al.. Frustrated pretransitional phenomena in aperiodic composites. ***Physical Review B***, 2016, 94 (18).

T. Yoshida, S. Takaishi, H. Iguchi, H. Okamoto, H. Tanaka, S. Kuroda, Y. Hosomi, S. Yoshida, H. Shigekawa, T. Kojima, H. Ohtsu, M. Kawano, B. K. Breedlove, **L. Guérin**, and M. Yamashita, Optically Visible Phase Separation between Mott-Hubbard and Charge-Density-Wave Domains in a Pd-Br Chain Complex, ***ChemistrySelect*** 1, 259 (2016).

Laurent Guérin, Johan Hébert, Marylise Buron-Le Cointe, Shin-Ichi Adachi, Shin-Ya Koshihara, et al.. Capturing One-Dimensional Precursors of a Photoinduced Transformation in a Material. ***Physical Review Letters***, 2010, 105, pp.246101.

Chapter 3: Correlated disorder and diffuse scattering

The exploration of crystal structures, with the use of X-ray diffraction, is based on the inherent long range ordering in crystals. As we saw in the previous chapter, this property facilitated the determination of average atomic positions within the crystal lattice through the measurement of diffracted intensity at discrete Bragg peaks. However, the pursuit of understanding crystalline order encountered a significant limit as real crystals, laden with static or dynamic defects, deviate from perfect translational symmetry. This deviation manifests as "diffuse scattering," where a notable fraction of diffracted intensity, distributed in reciprocal space beyond Bragg peaks, becomes a key indicator of **correlated disorder** [46,47] : a situation where disorder or variability in the arrangement of atoms within a crystal lattice is not entirely random but exhibits some form of correlation or interdependence. In that case, the disorder in the arrangement of atoms at one position within the crystal lattice is related to or influenced by the disorder at another position.

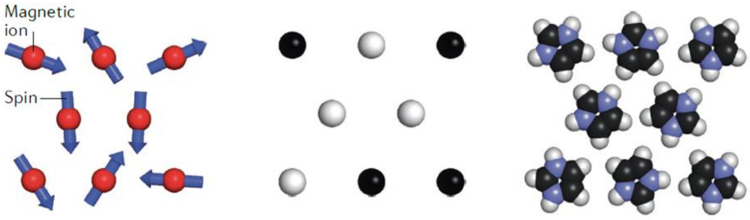

Figure 3-1 : canonical disorder. from left to right, up to down : disorder in paramagnet, compositional disorder, orientational disorder. (Figure from [48])

Crystals may exhibit disorder through various mechanisms, especially when certain elements of their structure possess internal degrees of freedom (Figure 3-1). For example, the crystal structure of paramagnetic MnO is order but not the magnetic moments of Mn^{2+} ions. Alloys present positional order while maintaining compositional disorder. Plastic crystals, as observed in substances like ices, shows long-range order for the center of mass of the molecule, but lack ordered molecular orientations. We can see from this three examples of canonical disorder in crystals that the correlated disorder is described on top of an average periodic ordered structure. It is another layer of description of what is the real structure of a material. This way of describing the correlated disorder is coming also from the way we analyze it. The average structure analysis come from the analysis of the Bragg peaks intensity and the correlated disorder from the diffuse scattering as we will see below.

Figure 3-2 illustrates an example of correlated disorder using the simple model of square ice, a simplified two-dimensional representation where water molecules are arranged periodically on a node of a square lattice. The structure b shows the case of correlated disorder : There is a correlation where all O-H bonds align in the same direction within each row and column. However, the structure is considered disordered because these directional alignments are not consistent across rows or columns. The typical crystallographic unit cell of square ice involves two hydrogen sites that are 50% occupied between each pair of oxygen sites. This correlated disorder gives rise to diffuse scattering.

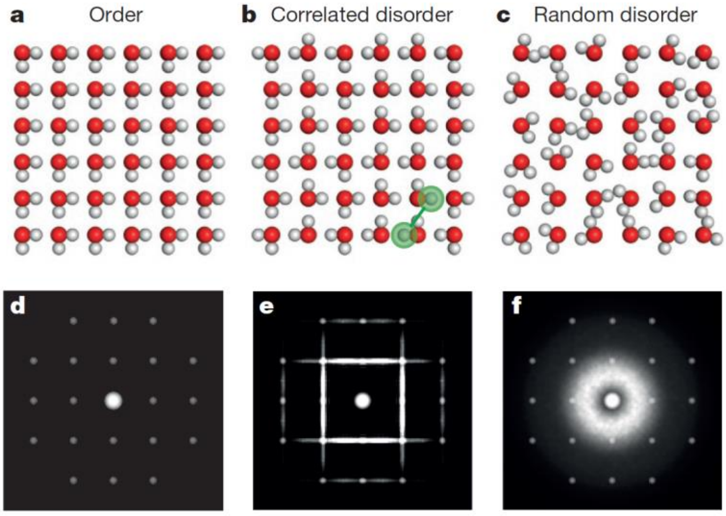

Figure 3-2 : illustration of different structures of square ice, a simplified model of water ice: completely ordered (a, d, g), randomly disordered (c, f, i), and those with correlated disorder (b, e, h). Despite a simple rule governing oxygen and hydrogen atom positions, the short-range nature of the rule leads to correlated disorder in structure b. This disorder involves aligned O-H bonds within rows or columns but no correlation across rows or columns, resulting in a disordered structure. The diffraction patterns (d-f) highlight the differences between these structures. Structure b shows diffuse scattering due to locally correlated hydrogen positions, unlike the ordered structure a or randomly arranged structure c. (From D. Keen and A. Goodwin, Nature 2015 [49])

Diffuse scattering, which is often hard to measure because it's generally a very weak signal, is crucial for the analysis of material properties. Despite the formalization of the effects of such fluctuations in the late 1930s, the exploration of diffuse scattering lagged behind due to experimental limitations associated with its low intensity.

As presented in chapter 1, advances in experimental techniques, including brighter X-ray sources, rotating anode generators, synchrotron sources, and sophisticated detectors, such as flat panel detectors and CCD cameras, coupled with efficient data processing capabilities, have renewed the study of correlated disorder through diffuse scattering. Canonical examples can be found in molecular conductor [50–54], in metal organic material [55–57], in fullerene or nanotubes [58–60], in biological system [61,62]. Recent examples shows the possibility to harness disorder and analyze it using diffuse scattering [63,64].

The convergence of modern developments in crystallographic methods, experimental, computational, and algorithmic, provides insight into correlated disorder, allowing us to address long-standing problems in the field. In this chapter 3, I will present the simple theory to describe the disorder and how we can analyze the diffuse scattering to understand the origin of the disorder. I will introduce the analysis technique called 3D-ΔPDF that I used in collaboration with Dr. Arkadiy Simonov which allows the analysis in 3D of local correlations. And finally, to illustrate those concepts, I will use scientific cases that I and my colleagues of the group worked on the last ten years.

3.1 SCATTERING FROM DISORDERED CRYSTALS

The scattering from a periodic crystal or aperiodic crystals is set of discrete sharp peaks in the diffraction pattern. It comes from the property than we saw in chapter 1 that the Fourier transform of a periodic lattice (in any dimension) is a periodic lattice i.e the reciprocal lattice. In complete disordered systems like in liquids or gas, the scattering consists of broad and large rings with no Bragg peaks.

The case of correlated disordered crystals is something in the middle. Because the average structure is periodic, the diffraction pattern consists of Bragg peaks but due to local ordering or correlation in the disorder, diffuse scattering appears in top of that. In the reciprocal space, the diffuse scattering is structured depending of the kind of correlation and their spatial extension and dimensionality on the real space [46,48,49]. For the case of the simple substitution model with two species arranged randomly on a lattice, the diffuse scattering shows no structuration like in liquid or gaz (see figure 1 in [65]). Whereas, for antiferro type correlation between two species, diffuse scattering is more condensed in between Bragg peaks as we will calculate later.

Disorder of the first kind and disorder of the second kind refer to different types of structural irregularities or deviations in a crystal :

- Disorder of the First Kind involves fluctuations or variations in the positions of atoms within a crystal lattice. These fluctuations can result from thermal agitation, dynamic modes of vibrations (phonons), or imperfections such as stacking defects, vacancies, or interstitials. Despite these fluctuations, the long-range order and translation symmetry of the crystal lattice are preserved.
- Disorder of the Second Kind refers to disruptions in long-range order and translation symmetry in a crystal lattice. This disorder arises when interactions between lattice sites are limited to immediate neighbors, and local fluctuations cannot be propagated over long distances. As a result, materials exhibiting disorder of the second kind lack the translation symmetry observed in more ordered crystals.

I will not go in all the details of the calculation and will present and comment only the main results. Readers can consult the article of T.R Welberry and B.D Butler 1994 [65] or the chapter 1 by R. Rabiller, C. Mariette, L. Guérin and B. Toudic of the book Rayons X et Matière 5 [66] or S. Ravy, P. Launois, R. Moret and J.P. Pouget [52] for a complete and lengthy computation.

3.1.1 Dimensionality and correlation length

The correlation length refers to a characteristic distance over which disorder or variations in the crystal lattice persist and exhibit statistical correlation. It provides a measure of the extent to which deviations from the idealized crystal structure are correlated as for example, dynamic disorder due to temperature effects or static disorder associated with defects in the crystal. In cases of dynamic disorder, it may represent the characteristic distance over which collective atomic motions are coordinated. For static disorder, the correlation length could indicate the size of clusters or domains with similar deviations from the ordered structure.

Collective phenomena (phonons) characterizing one of the dynamic disorder, have long correlation lengths and therefore appear highly localized in reciprocal space, causing diffuse intensity around the Bragg nodes. In contrast, static disorder is often characterized by short correlation lengths, such as precipitates or clusters of vacancies, involving only a few atoms. Therefore, in general, the diffuse intensity resulting from static disorder is more spread out in reciprocal space. It is a very simple classification and should not be used as a way to distinguish between static and dynamic. In the following section on alkane-urea system or in fullerene, dynamical disorder is spread out in the reciprocal space. (see figure 1 in [58])

It's important to note that correlation lengths can exist in three dimensions. For instance, dislocations where additional atomic planes disturb the lattice periodicity in one dimension while remaining perfectly ordered in the other two may have an infinite correlation length in two dimension (complete order) and a finite one in the other. In such case, we say that the dimensionality of the correlated disorder is two.

Scattered intensity of a 2D infinite periodic crystal :

Depending on the dimensionality, the scattered intensity shows very characteristic structures in the reciprocal space (Figure 3-3). Let’s consider a 2D infinite periodic crystal formed by a periodic (**a**,**b**) lattice.

Recall that :

$$\rho_{crystal}(\boldsymbol{r}) = L(\boldsymbol{r}) \otimes \rho\,(\boldsymbol{r})$$

With $\rho(r)$ the electron density of the unit cell and $L(\boldsymbol{r})$ the lattice distribution of the 2D infinite periodic lattice :

$$L(\boldsymbol{r}) = \sum_{u} \delta(x - ua) \times \sum_{v} \delta(y - vb) \times \delta(z)$$

The scattered amplitude is the Fourier transform of $\rho_{crystal}(\boldsymbol{r})$:

$$A(\boldsymbol{q}) = \mathfrak{F}\{\rho_{crystal}(\boldsymbol{r})\}$$

$$A(\boldsymbol{q}) = \mathfrak{F}\{L(r) \otimes \rho(r)\} = \mathfrak{F}\{L(r)\} \times \mathfrak{F}\{\rho(r)\} = S(\boldsymbol{q}) \times F(\boldsymbol{q})$$

and

$$S(\boldsymbol{q}) = \mathfrak{F}\{L(r)\} = \int L(\boldsymbol{r}) e^{iq\cdot r} dr$$

$$= \int \sum_{u} \delta(x - ua) \times \sum_{v} \delta(y - vb) \times \delta(z) e^{-i\boldsymbol{q}\cdot\boldsymbol{r}} d^3\boldsymbol{r}$$

$$with\ \boldsymbol{q} = q_x\boldsymbol{a}^* + q_y\boldsymbol{b}^* + q_z\boldsymbol{c}^*\ and\ \boldsymbol{r} = x\boldsymbol{a} + y\boldsymbol{b} + z\boldsymbol{c}$$

$$= \sum_u e^{-i\mathrm{q}_x u} \sum_v e^{-i\mathrm{q}_y v}$$

$$= \sum_h \delta(q_x - h) \sum_k \delta(q_y - k)$$

And therefore :

$$A(\boldsymbol{q}) = \mathfrak{F}\{\rho(\boldsymbol{r})\} \times \sum_h \delta(q_x - h) \sum_k \delta(q_y - k)$$

The scattered amplitude is non zero only at the node of the 2D reciprocal lattice (**a***,**b***) with no localization along **c*** giving rise to periodically arranged diffuse rods perpendicular to the plane. In this simple model, the intensity of the rods along **c*** are modulated by the structure factor $\mathfrak{F}\{\rho(\boldsymbol{r})\}$. They are infinitely long along **c*** and infinitely thin along **a*** and **b*** illustrating the inverse relation between the reciprocal and the real space where correlations along c are infinitely small and infinitely long in the (**a**,**b**) plane.

Note that similar computation with 1D infinite crystal gives rise to infinitely thin planes perpendicular to the 1D lattice.

Correlation lengths :

In reality, the disorder is characterized by finite correlation lengths resulting in diffuse intensity spread out in reciprocal space. The Lorentzian function is often employed in the reciprocal space to model the spatial correlations or disorder-related effects within the crystal lattice. Its shape allows for the representation of phenomena with long-range correlations.

Disorder-related effects may extend over considerable distance, known as correlation length ξ. One of the most common statistical model to describe the correlation is the Ornstein-Zernike model [67]. It treats the correlation with a pair correlation function that decay exponentially similarly to the 2D Ising model.

The mathematical expression for the correlation between two correlated species i and j can be written as:

$$\Gamma_{ij} = \gamma e^{-\frac{|i-j|}{\xi}}$$

with ξ representing the characteristic length of the correlation in the real space.

The Fourier transform of the correlation is a Lorentzian function and the diffuse scattering signal can be expressed as:

$$\mathrm{I(q)} = A\frac{1}{\pi}\frac{{}^{1}/_{\xi}}{q^2 + {}^{1}/_{\xi^2}}$$

With $1/\xi$ the full width at half maximum (FWHM), representing the characteristic width of the diffuse scattering and A a scaling factor.

It exists therefore an inverse relation between the width of the diffuse signal and the correlation length.

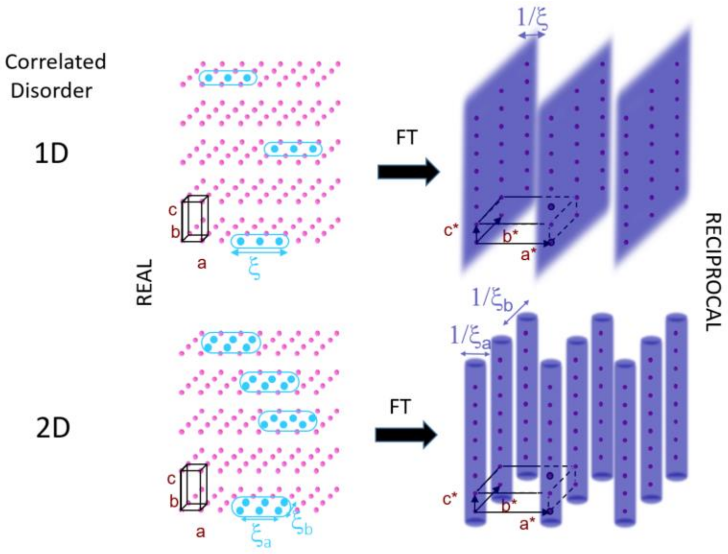

Figure 3-3 : Correlated disorder and its associated diffuse scattering

It's important to note that while the Lorentzian function has its advantages, its selection is not universal. The choice of a particular function depends on the specific characteristics of the disorder being studied and the goals of the analysis. In many cases, one might explore different functions or combinations of functions to better capture the complexities of disorder. [68]

Figure 3-3 summarize the idea presented in this section. In case of 1D correlated disorder along the a direction, diffuse planes are formed perpendicular to a. The width of the planes $1/\xi$ are inverse of the size ξ of the correlation in the real space. For 2D correlated disorder forming correlated domains of size ξ_a along a and ξ_b along b, diffuse scattering appears as diffuse rods along c* with a width $1/\xi_a$ along a* and $1/\xi_b$ along b*.

3.1.2 Diffuse scattering intensity from disorder of 1st kind

The scattering intensity for disorder that keeps the translational symmetry can be expressed as follow :

$$I(\vec{Q}) \propto I_{\text{Bragg}}(\vec{Q}) + I_{\text{diffuse}}(\vec{Q})$$
$$I_{\text{Bragg}}(\vec{Q}) = \left|\langle F_m(\vec{Q})\rangle\right|^2 \sum_m e^{i\vec{Q}\cdot\vec{T}_m}$$
$$I_{\text{diffuse}}(\vec{Q}) = \sum_m \left(\langle F_o(\vec{Q})F_m^*(\vec{Q})\rangle - \left|\langle F_m(\vec{Q})\rangle\right|^2\right) e^{i\vec{Q}\cdot\vec{T}_m}$$

The first contribution corresponds to the Bragg diffraction as presented in chapter 1. The second contribution is the diffuse scattering. F_m is the structure factor of the unit cell m.

We can decompose the diffuse scattering in two contributions. The first corresponds to the subscript m = 0 and is associated to the local disorder or on-site disorder :

$$I_{\text{diffuse}}^{\text{site}}(\vec{Q}) = \left\langle \left|F_o(\vec{Q})\right|^2 \right\rangle - \left|\langle F_o(\vec{Q})\rangle\right|^2$$

The second contribution corresponds to the subscript m ≠ 0 and is associated to pair correlation : (Notice that for any m it exits m' so that $\vec{T}_{m'} = -\vec{T}_m$)

$$I_{\text{diffuse}}^{\text{pairs}}(\vec{Q}) = 2\sum_{m>0} \left(\langle F_o(\vec{Q})F_m^*(\vec{Q})\rangle - \left|\langle F_m(\vec{Q})\rangle\right|^2\right) \cos(\vec{Q}\cdot\vec{T}_m)$$

Thermal diffuse scattering (TDS)

In a crystal, the vibrations of the atoms are not independent but are collective motions that are referred as normal modes or phonons in the second quantification. If we note u, the displacement of the atom from its equilibrium position, the classical treatment of the 1d chain gives the following quadratic thermal fluctuation :

$$\sigma_T^2 = \langle u^2 \rangle = \frac{k_B T}{m\omega^2}$$

The fluctuations are proportional to the inverse square of frequency ω of the phonon and therefore low frequency modes gives the most contribution. In all basic introduction to solid physics, it can be demonstrated that the frequency of acoustic modes varies linearly with the wave vector q at low frequency. The slope of the dispersion curve is the speed of sound. Optical modes typically have a higher frequency that varies little in the Brillouin zone. Therefore the acoustic phonons in the case of small wave vector q are the ones that contribute to the diffuse scattering.

As the crystal is periodic, this is valid in the vicinity of each Bragg peak, and one should interpret the vector $\vec{\mathrm{Q}} = \vec{\mathrm{Q}}_{\mathrm{Bragg}} + \vec{q}$.

Using a force-constant formalism of the lattice dynamics, also known as the Born–von Karman model and taking into account the following factor :

- the density of modes $n(\omega) \approx \frac{k_B T}{\hbar\omega}$
- the polarization factor $\left(\vec{\mathrm{Q}} \cdot \vec{\boldsymbol{\varepsilon}}_s\right)^2$
- the dependencies of the frequency of acoustic modes with q : $\omega = v$ q, v is the speed of sound.
- the dependencies of the damping of acoustic modes with q : $\Gamma = Dq^2$, D the diffusion factor.

It can be shown that the diffuse intensity associated with a mode is given by:

$$I_{\mathrm{diffuse}}^{\mathrm{phonon}}(\vec{\mathrm{Q}}) \propto \left(\vec{\mathrm{Q}} \cdot \vec{\boldsymbol{\varepsilon}}_s\right)^2 n(\omega) \frac{1}{\gamma^2 + q^2}$$

Where $\gamma = \frac{v}{D}$

The TDS is located around the Bragg peak. It decreases as one moves away from the Bragg peak in $\frac{1}{q^2}$ and is weak when the speed of sound of the acoustic mode is high. The term $\left(\vec{\mathrm{Q}} \cdot \vec{\boldsymbol{\varepsilon}}_s\right)^2$ representing the projection of the vector **Q** onto the direction of the polarization **ε** of the mode leads, for diffuse scattering, to a characteristic "peanut" (or "butterfly") shape, as schematically depicted in Figure 3-4. This shape is very recognizable when the longitudinal speed of sound is much greater than the transverse speed.

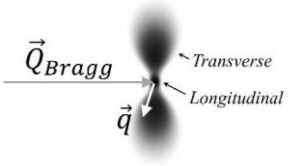

Figure 3-4 : Contributions of longitudinal and transverse modes to diffuse scattering by acoustic phonons (TDS) when the speed of the longitudinal mode is much greater than that of the transverse mode.

It should be noted that it is possible from the accurate measurement of diffuse scattering, i.e reciprocal space reconstruction with very high accuracy, to determine the phonon dispersion from the measurement of TDS. Holt et al [69] showed such possibility by determining the phonon dispersion of silicon (Figure 3-5). Wehinger et al made a step further by determining the full elastic tensor from thermal diffuse scattering [70].

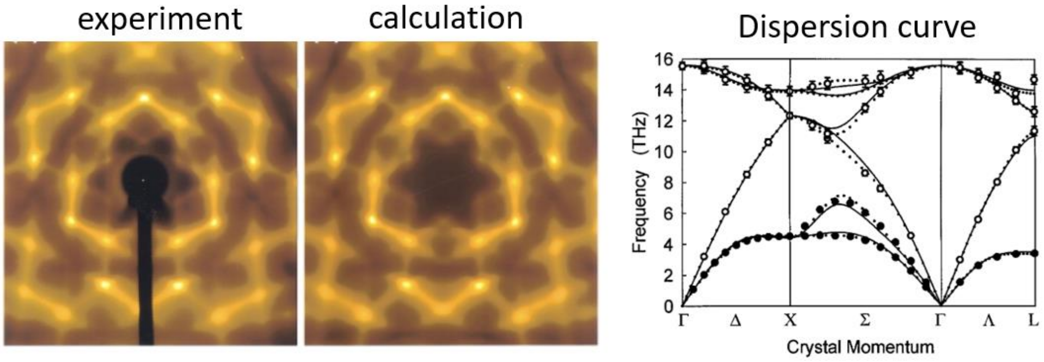

Figure 3-5 : X-ray diffraction pattern of silicon crystal showing the experimental TDS (left) and the calculated (middle) thermal diffuse scattering. Right : dispersion curve obtained from the refinement of the calculated TDS to the experimental one. (From [53])

Diffuse scattering from correlated disorder

The second contribution corresponds to disorder that are correlated and expand to several unit cells. In simple case of simple disorder due to ferro or anti-ferro correlation, we can introduce the parameter ξ that express the spatial extension of the correlation and treat the pair correlation as a power law :

$$\left|\langle F_o(\vec{Q})F_m^*(\vec{Q})\rangle - \left|\langle F_m(\vec{Q})\rangle\right|^2\right| \approx |I^{\text{site}}_{\text{diffuse}}(\vec{Q})|\, e^{-|\vec{T}_m|/\xi}$$

And therefore for an infinite 1D crystal with a periodicity a :

$$I_{\text{diffuse}}(\vec{Q}) = I^{\text{site}}_{\text{diffuse}}(\vec{Q})\frac{1-e^{-2a/\xi}}{1\pm 2e^{-a/\xi}\cos(Qa)+e^{-2a/\xi}}$$

The ± corresponds to positive correlation (ferro type ordering) or negative correlation (anti-ferro type ordering).

Figure 3-6 shows that the diffuse scattering condenses at the Bragg position in the case of positive correlation (ferro) or at the edge of BZ for negative correlation (anti-ferro). When ξ increase, diffuse signal becomes sharper (recall the inverse relation). If ξ is infinite, diffuse signal is infinitely sharp and become a Bragg peak. For negative total correlation, it will give rise to superstructure Bragg peaks located at one half in the reciprocal cell that corresponds to a cell doubling along a, a common signature of the anti-ferro ordering.

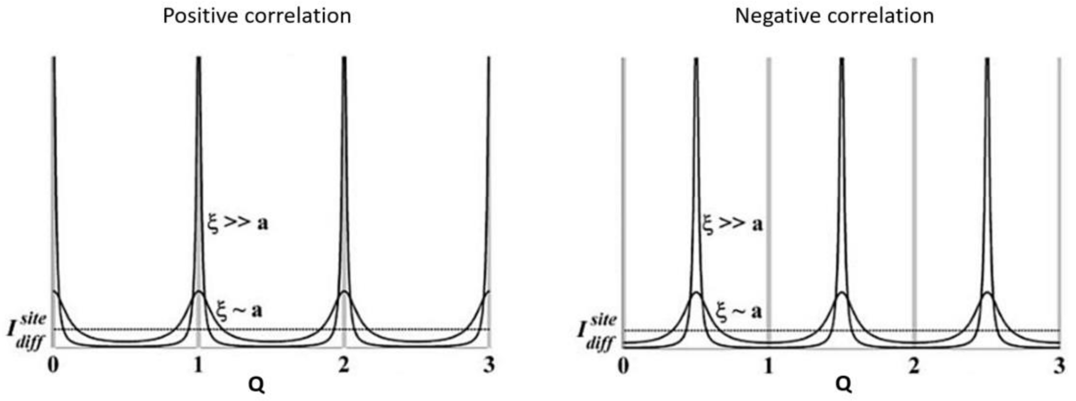

Figure 3-6 : effect of pair correlation on the diffuse scattering function of the sign of the correlation and the correlation length (From R. Rabiller, C. Mariette, L. Guérin et B. Toudic of the book Rayons X et Matière 5)

In the case of disorder of the 2nd kind, the long-range order that preserves translation symmetry is disrupted. Correlations only exist among immediate neighbors. To illustrate the behavior of diffuse scattering induced by this type of short-range order, it is sufficient to consider a one-dimensional system where a first motif is located at a fixed origin position. A second motif is replicated in the vicinity, at an average distance of a=1 distance unit, with bounded fluctuations around this average unitary distance. A third motif is replicated with the same average distance and fluctuations around the position of the second motif, and so on. The probability of having a motif at position x=0 is 1. The probability of having a first neighbor around the position x=1 follows a probability distribution function g(x) characterized by a finite standard deviation σ. (Figure 3-7)

The corresponding electron density distribution is in this case :

$$\rho(x) = \delta(x) + \sum_{n>0} \left(g \otimes^{(n)} g(x-n) + g \otimes^{(n)} g(-x+n)\right)$$

Where $\otimes^{(n)}$ is the operator $\otimes$ applied n times.

Figure 3-7 shows the distribution of the electron density in the case of disorder of 2nd kind. The properties of this distribution are such that the mean value of the position of the nth neighbor is precisely n times the average distance between the first neighbors, and the mean quadratic fluctuations around this position vary linearly with n. The mean positions of the motifs are distributed on a periodic lattice, but the fluctuations are such that long-range order does not exist, and translation symmetry is lost.

For a Gaussian probability distribution, the Fourier transform of the above density distribution gives the following scattering intensity :

$$I_{\text{diff}}\,(Q) = \frac{1 - e^{-2Q^2\sigma^2}}{1 - 2e^{-Q^2\sigma^2}\cos(Qa) + e^{-2Q^2\sigma^2}}$$

The diffuse scattering shows maximum at the nodes of the reciprocal lattice. The width of the peak increases with the index of the node m following a quadratic law.

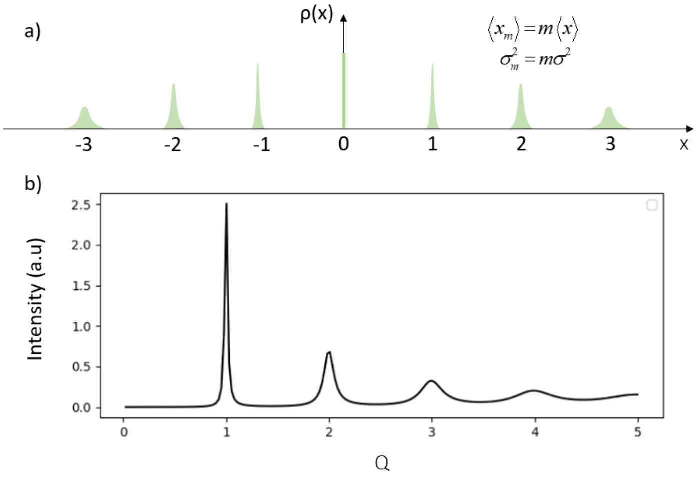

Figure 3-7 : a) Distribution density in real space for a 1D system exhibiting disorder of 2nd kind that disrupts translation symmetry. b) Associated structure factor for this distribution.

3.2 THE CASE STUDY OF ALKANE-UREA

Now that we know how to characterize the diffuse scattering in the reciprocal space and relate it to the disorder in the real space, I will show some examples based on the alkane-urea systems. Figure 3-8 shows the diffraction pattern and the diffuse scattering of a nonadecane-urea crystal obtained on the beamline ID29 at the ESRF with a PILATUS 6M. On the top of the rich diffraction patterns due to the aperiodic nature of this crystal (see chapter 2), different diffuse scattering signals can be clearly observed :

- **Thermal diffuse scattering (TDS)** : In a crystal at finite temperature, atoms experience thermal vibrations around their equilibrium positions. These vibrations induce fluctuations in the electron density, leading to variations in the scattered intensity, which can be observed in diffraction patterns at the base of the Bragg peaks.
- **Pretransitionnal diffuse scattering** : this type of diffuse scattering appears as a precursor or an early indication of structural changes in a material as it approaches a phase transition temperature or other critical conditions. The diffuse scattering results from fluctuations or disorder that precede the establishment of a new ordered phase. It can often be spotted close to the phase transition temperature at the position of the critical wave vector.
- **Local disorder** : the presence of diffuse planes, referred to as "d" planes. These planes result from the internal periodicity of the alkane molecules in the CH_2 groups.
- **Quasi liquid state** : The diffraction pattern of the guest lattice is manifested by fine diffuse planes with the reciprocal period of the alkane lattice. This is characteristic of periodic chains with a random disorder in position along the c-axis from channel to channel. The diffraction pattern of this sub lattice then results in Bragg peaks in the (a*, b*) plane and periodic planes referred to as "s" planes.

The quality of the measurement is astonishing with a very high signal over the noise ratio that allowed us to make quantitative analysis. We performed full data collection at different temperature and reciprocal planes were reconstructed using XCAVATE software [71]. Data were averaged over Laue symmetry to improve the signal-to-noise ratio and to remove the artifacts related to the gaps in the detector. Data analysis, 3D reconstruction, profiles and fits were performed using Matlab programs that I wrote at that time.

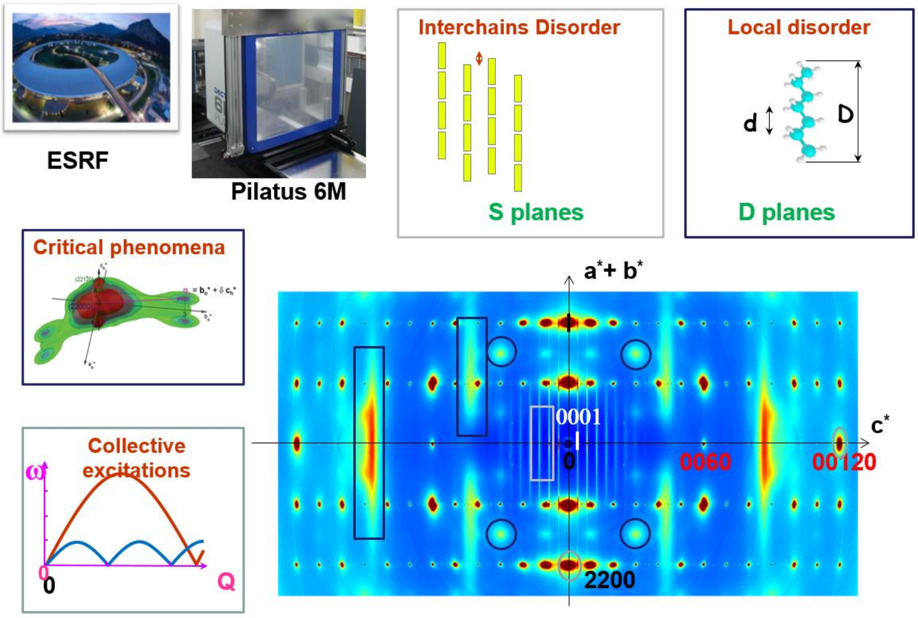

Figure 3-8 : diffraction pattern of the nonadodecane-urea crystal (ID29-ESRF). Diffuse scattering is associated to different phenomena, collective excitations (TDS), critical phenome (pretransitionnal diffuse scattering), local disorder (d-plane) and interchains disorder (s-plans)

3.2.1 Thermal diffuse scattering (TDS)

Figure 3-9 shows the planes (hk000) and (hk001) reconstructed from these measurements at ESRF. For now, we will concentrate on the thermal diffuse scattering centered on the intense Bragg peak (22000) which has its maximum in the plane (hk000).

We performed calculations of the contribution of longitudinal and transverse acoustic phonons to X-ray diffraction using the sound velocities measured by Brillouin scattering by J. Olliver (PhD thesis Ollivier 1997) in nonadecane/urea at room temperature. In this system, the longitudinal sound velocity is more than three times higher than the transverse one. In the figure, it is clear that the TDS is highly anisotropic : the vast majority of the diffuse contribution is at the base of the Bragg peaks and perpendicular to the wave vector Q_{Bragg} thus comes from transverse acoustic phonons. That makes sense as the transverse acoustic phonons have a much shallower slope than longitudinal phonons.

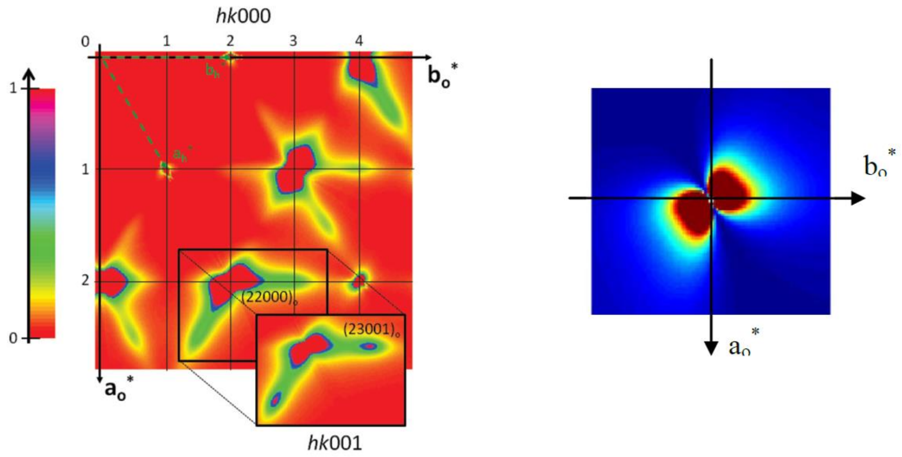

Figure 3-9 : : left : (*h k* 0 0 0) and (*h k* 0 0 1) diffraction planes using the 5D low-symmetry notation. Right : calculated TDS pattern using sound velocities from Brillouin scattering.

In order to measure the dispersion curve in nonadecane-urea, we combined different techniques like Raman, Brillouin, inelastic neutron scattering and inelastic X-ray scattering. The inelastic X-ray scattering project was a very interesting one, I had the responsibility of the master thesis of Mariana Verezhak, wrote the proposal to the ESRF and conduct the experiment. Nevertheless, I have decided that this is beyond the scope of this manuscript as it involves inelastic scattering resolved in energy which is the opposite of diffuse scattering that integrates in energy all the inelastic scattering. You can refer to C. Ecolivet and al., PRB 2018 [72] for a complete analysis of the dispersion curves in alkane-urea and some special features of the aperiodic order.

3.2.2 Pretransitionnal diffuse scattering

Nonadecane-urea shows a phase transition from $P6_122(00\gamma)$ to $C2221(00\gamma)(10\delta)$ at 158.5K. This corresponds to a transition in the superspace from a rank 4 to a rank 5 [73]. This phase is interpreted by the appearance of a modulation with a period of approximately 120 Å along the direction of the channels, and this modulation is in antiphase from one channel to another as already discussed in the chapter 2. Five indices (*h k l m n*) defined in the orthorhombic basis of the low temperature phase ($\mathbf{a}*$, $\mathbf{b}*$, $\mathbf{c_h}*$, $\mathbf{c_g}*$, and $\delta\mathbf{c_h}*$) are necessary to index each Bragg peak. The critical wave vector associated to this transition is $\mathbf{q_s} = \mathbf{b}* + \delta\mathbf{c_h}*$, which is along (0 1 0 0 1) [74].

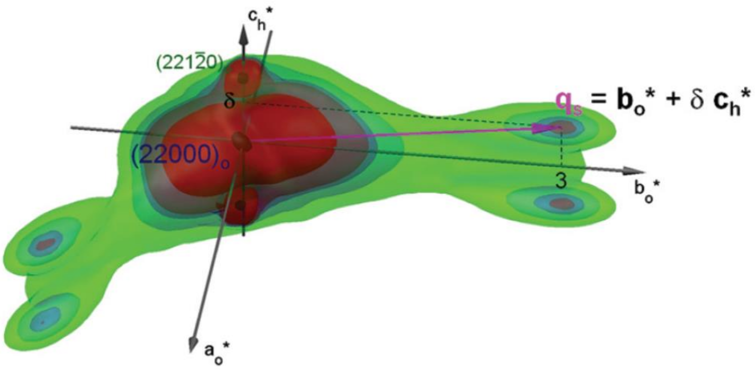

Figure 3-10 : False color reconstructed three-dimensional image of this pretransitional diffuse scattering, as seen from a general direction; the color palette goes from green to brown as intensities increase [74].

Figure 3-10 shows that the pretransitionnal diffuse scattering is most intense in the (*hk*001) plane with a maximum at the location of $\mathbf{q_s}$. The analysis of this disc-shaped pretransitionnal x-ray diffuse scattering around the critical wave vector (0 1 0 0 1) allows the determination of the ellipsoid associated with the correlation lengths (ξ_a, ξ_b, ξ_c), the principal axes of this ellipsoid being found along the directions **a∗** , **b∗** , and **c∗** of the orthorhombic reciprocal cell:

$$S(q,T) \propto \frac{k_B T}{1 + \xi_a^2 q_a^2 + \xi_b^2 q_b^2 + \xi_c^2 q_c^2}$$

Slices along these directions give the profiles shown in Figure 3-11. In each case, the correlation lengths were extracted by fitting the data with a Lorentzian function. The extracted correlation lengths are shown in Figure 3-11. These correlation lengths appear isotropic in the (a, b) plane. Along the aperiodic direction c, the extracted lengths are much larger. On approaching Tc, they are very close to the experimental resolution limit even with this very high-resolution synchrotron diffractometer. The pretransitionnal effects appear to be associated with quasi one-dimensional fluctuations along the aperiodic direction c accompanied by a lateral ordering in the (a, b) plane upon approaching Tc.

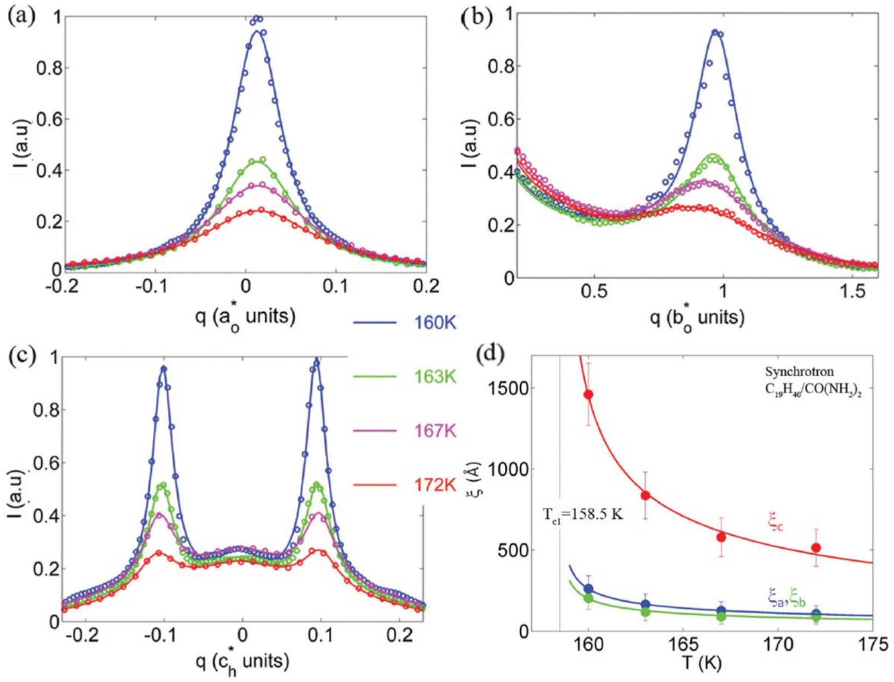

Figure 3-11 : Temperature dependence of the diffuse scattering associated with the critical wave vector (0 1 0 0 1) along the directions (a) $\mathbf{a}^*$, (b) $\mathbf{b}^*$, and (c) $\mathbf{c}^*$, as measured in fully hydrogenated *n*-nonadecane/urea at 160 K (blue), 163 K (green), 167 K (pink), and 172 K (red). Temperature dependence of the correlation lengths ξ_a, ξ_b, and ξ_c, respectively, along the directions **a** (blue), **b** (green), and **c** (red).

The critical phenomena can be attributed to low-frequency excitations in the high-symmetry phase, which undergo softening at Tc. This interpretation is supported by the observed increase in diffuse scattering intensity around $\mathbf{q}_s$ (Figure 3-11). The low temperature phase seems to result from the condensation of a collective mode, analogous to what is reported in three-dimensional crystals approaching incommensurately modulated phases. In the latter case, the softening is associated to phonons, the sole excitations present in the periodic high-symmetry phase. In a four-dimensional aperiodic composite, an additional phason branch is present in the high-symmetry phase. The noteworthy aspect of almost infinite correlation lengths along the aperiodic direction suggests the possibility of phase fluctuation leading to antiferro-ordering along the supplementary internal space of the superspace [74].

This experimental work extends the treatment of pretransitionnal phenomena to higher-dimensional space, a concept previously developed for phase transitions transforming periodic structures into either commensurate or incommensurate ones.

3.2.3 Local disorder

The alkane molecule that possesses an internal symmetry (repetition of the C_2H_4 unit, as shown in Figure 3-12), has the characteristic of concentrating its molecular diffuse scattering in very specific regions of reciprocal space called d planes. As all molecules are inherently parallel along the channel direction, the diffuse planes are periodic with a period of $2\pi/\mathrm{d}_{\mathrm{C_2H_4}}$, equivalent to 2.47 $Å^{-1}$. Considering that the diffracting object has a finite length L_g, the width of this diffuse scattering along the c* direction is on the order of $2\pi/L_g$. The presence of a symmetry axis 2_1 in the construction of this molecule implies extinction along the axis for diffuse planes of odd order. This extinction is observed in a diffraction measurement conducted on n-nonadecane/urea at the ID29 beamline diffractometer (see Figure 3-12). The diffuse plane of order 2 has maximum intensity along the c* axis.

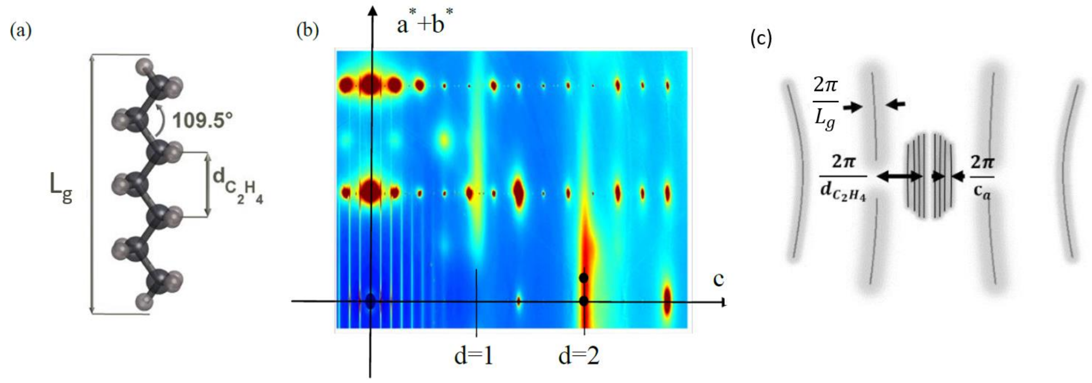

Figure 3-12 : a) alkane molecule of length Lg showing internal periodicity $\mathrm{d}_{\mathrm{C_2H_4}}$. b) reconstructed scattering pattern of nonadecane/urea, strong diffuse planes appears with a periodicity $2\pi/\mathrm{d}_{\mathrm{C_2H_4}}$. c) schematic drawing of the diffuse scattering of alkane molecules confined in channel.

Analysis with X-ray inelastic scattering showed that the diffuse d planes are entirely inelastic at room temperature [72]. The second "d" plane, with maximum intensity along the axis, reflects translational molecular disorder along the channel direction. The analysis of the first "d" plane, which is extinguished along the axis, is more complex as it simultaneously reflects rotational and translational disorder of molecules within the channels. It is important to note that this diffuse scattering is of molecular origin but coherent. In this sense, its intensity is primarily defined by the molecular form factor.

3.2.4 Quasi liquid and 2^{nd} kind disorder

In the case of short-chain guest molecules, the mean squared amplitude of the vibration along the channels is large due to the low mass and weak interaction with the urea host. These substantial fluctuations may potentially disrupt the interchannel guest ordering and disrupt the translational symmetry of the alkane sub lattice leading to a disorder of 2^{nd} kind. From a diffraction standpoint, the guest subsystem primarily manifests as sharp, parallel diffuse planes, referred to as s-planes located at multiple value of $2\pi/C_g$ (Figure 3-13). This disorder has been characterized as the "paracrystalline state".

The Fourier transform of a static, one-dimensional (1-D) system with long-range order yields a set of diffuse sheets perpendicular to the 1-D axis. However, in real 1-D systems, no long-range order can exist, as fluctuations broaden the diffuse ("s") planes along c*.

Assuming a Gaussian pair correlation function, of the form:

$$G(z) = \frac{1}{\Delta\sqrt{2\pi}} e^{-(z-c_g)/2\Delta^2}$$

Δ quantifies the 2^{nd} kind disorder inside the 1D infinite chain.

Similar calculation as in 3.1.3 gives for small values of Δ, repeated Gaussian function located at $q = m \times c_g^*$ with a half-width at half-maximum equal to :

$$HWHM(m) = \frac{\pi^2 m^2}{C_g^3} \Delta^2$$

Here, the mean squared displacement Δ^2 of the guest molecule is related to the width HWHM along c* of the s-plane of order m by the above relation, which is a function of the mean guest repeat distance.

Applying Gaussian lineshapes, the data from four reconstructed diffuse planes were fit at mean positions representing multiple values of the misfit parameter $\gamma = 0.63$, defining a mean guest repeat distance of $C_g = 17.5$ Å. Figure 3-13(d) shows the evolution of the experimental width as a function of the order m of the plane. These data are described in the Gaussian approximation by a quadratic function $\Delta^2 m^2$. [75] The value of Δ, characterizing the liquid-like feature, is determined to be 0.61 Å in n-dodecane/urea, consistent with those reported previously by Weber et al. in other n-alkane/urea compounds (n = 14, 17) [76].

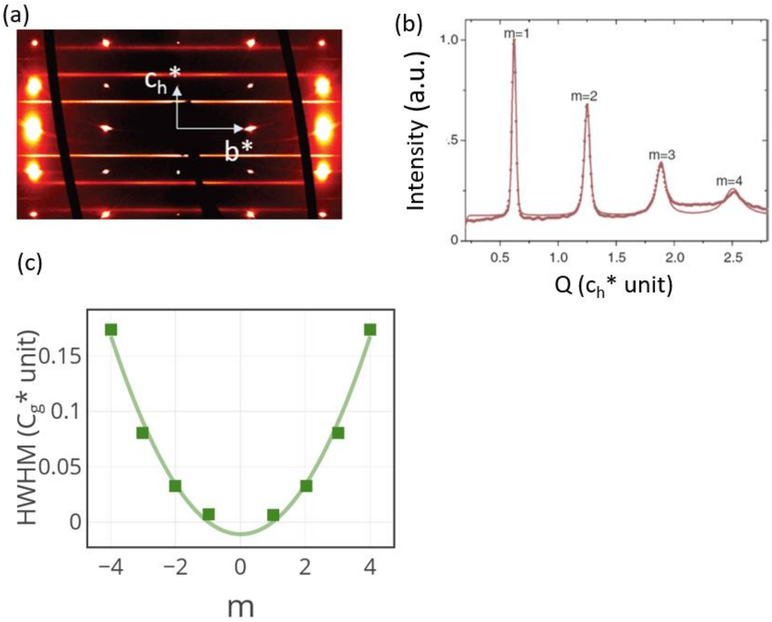

Figure 3-13 : a) The reconstructed *b*c* plane in dodecane-urea. b) Profile along the *c* direction showing the broadening of the planes with their order *m*. c) Half-width at half-maximum of the diffuse planes of order m=1,2,3, and 4. The fitting curve is a quadratic function with Δ = 0.61 Å (From [75])

In practice, the method described here is too simple to describe the case of alkane-urea since the assumption of a 1D liquid does not allow the existence of lateral order. We will demonstrate that the introduction of lateral order on adjacent hexagonal sites has the potential to induce a remarkably intricate modulation of intensity within the diffuse planes. To unravel this complexity in the diffuse scattering, we employed a relatively novel analytical method known as the 3D – ΔPDF method, which is the topic of the next section.

3.3 THE 3D-ΔPDF METHOD

In this section, I will introduce the theory and principles of the three-dimensional Δ Pair Distribution Function (3D-ΔPDF) analysis for disordered single crystals [77]. In contrast to the total 3D-PDF (Three-Dimensional Pair Distribution Function), which considers the entire single crystal diffraction pattern, the 3D-ΔPDF specifically focuses on the diffuse scattering component. This method involves calculating the Fourier transform of the diffuse scattering alone in order to draw a 3D map of the correlations of the disorder. The 3D-ΔPDF method is advantageous because as we will see it provides a way to analyze correlated disorder in the real space.

3.3.1 Autocorrelation function – interatomic vector and Patterson map

Before going into the details of the mathematical framework of the 3D-ΔPDF, let's remind the basics idea and vocabulary of the Patterson method that will be useful to understand the 3D-ΔPDF method.

As we saw in the chapter 1, the inability to directly measure relative phases among diffracted beams posed a challenge in calculating the electron density function. Arthur Lindo Patterson addressed this issue in 1934 with his ground-breaking idea, leading to the first solution to the phase problem.

The Patterson function is defined as the Fourier transform of the Bragg peak intensities :

$$\begin{aligned} Pat(\boldsymbol{r}) &= \mathfrak{F}[I_{hkl}] = \mathfrak{F}[\langle F_{hkl} \rangle \langle F^*_{hkl} \rangle] \\ &= \mathfrak{F}[\langle F_{hkl} \rangle] \otimes \mathfrak{F}[\langle F^*_{hkl} \rangle] \\ &= \langle \rho(\boldsymbol{r}) \rangle \otimes \langle \rho(-\boldsymbol{r}) \rangle \\ &= ACF(\langle \rho(\boldsymbol{r}) \rangle) \end{aligned}$$

here the brackets $\langle\rangle$ denote averaging over exposure time and scattering volume.

Note that in principle, $\rho(\boldsymbol{r})$ is defined as the inverse Fourier Transform of the structure factor but in order to simplify the mathematical expression, I will use the Fourier Transform $\mathfrak{F}$. From a mathematical point of view, it doesn't change anything.

We can see that the Patterson function is the autocorrelation function $ACF(\langle \rho(\boldsymbol{r}) \rangle)$ of the average structure.

The autocorrelation function is defined as :

$$\mathrm{ACF}(\rho(\boldsymbol{r})) = \int_V \rho(\boldsymbol{r})\rho(\boldsymbol{r}+\boldsymbol{r}')d^3\boldsymbol{r}'$$

The computation of the auto correlation function involves shifting the entire $\rho(\boldsymbol{r})$ function by a translation vector $\boldsymbol{r}'$, multiplying the values of the two datasets, and then averaging this product over the entire volume to obtain a single number. As we will see, it produces large value for specific interatomic vectors.

Using a similar approach than in the chapter 1, if the unit cell is composed of N atoms, we can define the motif as follow :

$$\langle\rho(\boldsymbol{r})\rangle = \sum_{i}^{N}\langle\rho_i(\boldsymbol{r})\rangle \otimes \delta(\boldsymbol{r}-\boldsymbol{r_i})$$

And calculate the Patterson function :

$$Pat(\boldsymbol{r}) = ACF(\langle\rho(\boldsymbol{r})\rangle) = \langle\rho(\boldsymbol{r})\rangle \otimes \langle\rho(-\boldsymbol{r})\rangle$$

$$= \sum_{i}\langle\rho_i(\boldsymbol{r})\rangle \otimes \delta(\boldsymbol{r}-\boldsymbol{r_i}) \otimes \sum_{j}\langle\rho_j(-\boldsymbol{r})\rangle \otimes \delta(-\boldsymbol{r}+\boldsymbol{r_j})$$

$$= \sum_{i}\sum_{j}\langle\rho_i(\boldsymbol{r})\rangle \otimes \langle\rho_j(-\boldsymbol{r})\rangle \otimes \delta(\boldsymbol{r}-\boldsymbol{r_i}) \otimes \delta(-\boldsymbol{r}+\boldsymbol{r_j})$$

$$\delta(\boldsymbol{r}-\boldsymbol{r_i}) \otimes \delta\left(-\boldsymbol{r}+\boldsymbol{r_j}\right) = \int \delta(\boldsymbol{r}-\boldsymbol{y}-\boldsymbol{r_i}) \times \delta\left(-\boldsymbol{y}+\boldsymbol{r_j}\right)\boldsymbol{dy}$$

$$= \delta\left(\boldsymbol{r}+\boldsymbol{r_j}-\boldsymbol{r_i}\right) = \delta\left(\boldsymbol{r}-\boldsymbol{r_{ij}}\right)$$

Which gives :

$$Pat(\boldsymbol{r}) = \sum_{i}\sum_{j}\langle\rho_i(\boldsymbol{r})\rangle \otimes \langle\rho_j(-\boldsymbol{r})\rangle \otimes \delta(\boldsymbol{r}-\boldsymbol{r_{ij}})$$

The computation of the Patterson function for any vector **r** gives the **Patterson map**. To illustrate some properties, let's calculate the Patterson map in the case of a simple 1D crystal composed of a red atom (ρ_1) at position x_1 and a blue atom (ρ_2) at position x_2 (Figure 3-14). There are no fluctuations whatsoever and the atoms are considered to be infinitely small (Dirac distribution)

$$Pat(\boldsymbol{r}) = \sum_{i=1}^{2}\sum_{j=1}^{2}\rho_i(\boldsymbol{r}) \otimes \rho_j(-\boldsymbol{r}) \otimes \delta\left(\boldsymbol{r}-\boldsymbol{r_{ij}}\right)$$

$$= \rho_1(\boldsymbol{r}) \otimes \rho_1(-\boldsymbol{r}) \otimes \delta(\boldsymbol{r}-\boldsymbol{r_{11}})$$

$$+ \rho_2(\boldsymbol{r}) \otimes \rho_2(-\boldsymbol{r}) \otimes \delta(\boldsymbol{r}-\boldsymbol{r_{22}})$$

$$+ \rho_1(\boldsymbol{r}) \otimes \rho_2(-\boldsymbol{r}) \otimes \delta(\boldsymbol{r}-\boldsymbol{r_{12}})$$

$$+ \rho_2(\boldsymbol{r}) \otimes \rho_1(-\boldsymbol{r}) \otimes \delta(\boldsymbol{r}-\boldsymbol{r_{21}})$$

Because of the convolution with a Dirac distribution, Pat($\mathbf{r}$) is non null only for specific vectors $\mathbf{r}$:

For $\boldsymbol{r} = \boldsymbol{r}_{11} = \boldsymbol{r}_{22} = \mathbf{0}$, $\mathrm{Pat}(\mathbf{0}) = {\rho_1}^2 + {\rho_2}^2$

For $\boldsymbol{r} = \boldsymbol{r}_{12}$, $\mathrm{Pat}(\boldsymbol{r}_{12}) = \rho_1\rho_2$

For $\boldsymbol{r} = \boldsymbol{r}_{21}$, $\mathrm{Pat}(\boldsymbol{r}_{21}) = \rho_1\rho_2$

The Figure 3-14 shows the Patterson map of this crystal. The Patterson map displays the following features :

- The map is periodic whose unit cell is identical to the crystal unit cell.
- The Patterson function contains the information about **interatomic vectors** of the average structure. For each pair of atoms i and j, the Patterson map contains a peak at the interatomic vector $\mathbf{r}_{ij} = \mathbf{r}_j - \mathbf{r}_i$.
- The Patterson map of a crystal formed by N atoms in the unit cell, will show $N^2 - N$ maxima.
- The height of the peaks is proportional to the product of atomic numbers of the atoms involved. Therefore, the highest maxima in the Patterson function correspond to vectors between atoms with highest atomic numbers.
- The height at the origin is the sum of the square of the atomic numbers of all the atoms in the unit cell.
- The map is centro-symmetric.

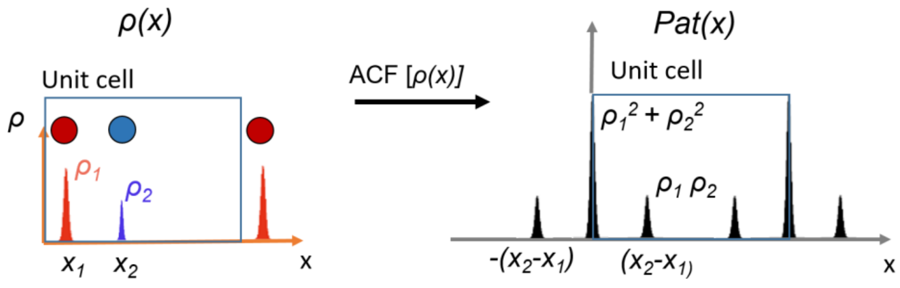

Figure 3-14 : schematic representation of the electron density of 1D crystal composed of 2 atoms and the associated Patterson map.

These properties come from the computation of the ACF. Therefore every time we calculate the ACF, the resulting map will have similar properties than the Patterson map.

3.3.2 The Three-Dimensional Pair Distribution Function

Up to this point, the discussion has assumed an ideal crystal with a diffraction pattern consists of Bragg peaks. In reality, it is never the case and the diffraction pattern is constituted of Braggs and diffuse scattering so that the total scattering can be expressed as :

$$\langle \mathrm{I}_{total}\,(\mathbf{q})\rangle \;=\; \langle \mathrm{I}_{hkl}\,(\mathbf{q})\rangle \;+\; \langle \mathrm{I}_{diffuse}(\mathbf{q})\rangle$$

Where ⟨ ⟩ denotes intensity averaging in time and over the whole scattered volume.

The 3D-Pair distribution function (3D-PDF) is the defined as the (inverse) Fourier Transform of the total scattering from a single crystal :

$$P\mathrm{DF}(\boldsymbol{r}) = \mathfrak{F}[\langle I_{total}\rangle] = \langle \rho(\mathbf{r})\otimes\rho(-\mathbf{r})\rangle$$

And correspond to the autocorrelation function of the real electron density, real meaning here that disorder is present and the real structure deviates from the average structure.

Similar calculation to the Patterson function gives for the whole crystal :

$$P\mathrm{DF}(\boldsymbol{r}) = \sum_{ij}^{crystal} \rho_i(\boldsymbol{r})\otimes\rho_j(-\boldsymbol{r})\otimes\langle\delta(\boldsymbol{r}-\boldsymbol{r_{ij}})\rangle$$

The above equation can be further expanded considering that 1) one is dealing with a crystal, so that the density $\rho(\mathbf{r})$ is invariant under translation of a lattice vector $\boldsymbol{R}_{\mathrm{uvw}}$ and 2), that the position of whatever composes the crystal is in fact the sum of its average position $\langle\boldsymbol{r}_{ij}\rangle$ along with a deviation $\boldsymbol{u}_{ij}$ from it :

$$\boldsymbol{r}_{ij} = \langle\boldsymbol{r}_{ij}\rangle + \boldsymbol{u}_{ij} = \bar{\mathbf{r}}_{\boldsymbol{ij}} + \boldsymbol{R}_{\mathrm{uvw}} + \boldsymbol{u}_{ij} \text{ with } \langle\boldsymbol{r}_{ij}\rangle = \bar{\mathbf{r}}_{\boldsymbol{ij}} + \boldsymbol{R}_{\mathrm{uvw}}$$

and

$$P\mathrm{DF}(\boldsymbol{r}) = \sum_{uvw}^{cryst}\sum_{ij}^{cell} \rho_i(\boldsymbol{r})\otimes\rho_j(-\boldsymbol{r})\otimes\delta(\boldsymbol{r}-\boldsymbol{R}_{\mathrm{uvw}}-\bar{\mathbf{r}}_{\boldsymbol{ij}})\otimes\langle\delta(\boldsymbol{r}-\boldsymbol{u}_{ij})\rangle$$

where $\boldsymbol{R}_{\mathrm{uvw}}$ is the lattice vector between the unit cells occupied by the atoms i and j, and $\boldsymbol{u}_{ij}$ is the difference between the real vector $\boldsymbol{r}_{ij}$ and the average structure related vector $\langle\boldsymbol{r}_{ij}\rangle = \bar{\mathbf{r}}_{\boldsymbol{ij}} + \boldsymbol{R}_{\mathrm{uvw}}$.

The PDF provides information about the deviation from the average structure in a real crystal. However, this deviation is not explicitly defined in the above equation. To address this, the PDF needs to be expressed not in terms of the atomic species i and j, but in terms of the atomic sites m and n that can be occupied by atomic species in the unit cell.

Atomic sites are necessary for describing real structures because more than one atom can occupy a given crystallographic position. Each atom found at that position corresponds to a site with a certain probability of occupation. In the average structure, this implies that each crystallographic position is occupied by a "fraction" of different atoms, and this fraction corresponds to the respective occupational probabilities. This behavior is known as Occupational or Substitutional disorder, falling under the category of static disorder of first kind.

The PDF is now expressed in terms of the sites m and n in the unit cell, and the summation is carried out over all pairs contained within one cell. Additionally, consideration is given to all pairs m and n that are located in different unit cells. This is expressed through a sum over all lattice vectors $\boldsymbol{R}_{\mathrm{uvw}}$ in the crystal:

$$PDF(\boldsymbol{r}) = \sum_{uvw}^{cryst}\sum_{mn}^{cell} P_{uvw}^{mn}\rho_m(\boldsymbol{r})\otimes\rho_n(-\boldsymbol{r})\otimes\delta(\boldsymbol{r}-\boldsymbol{R}_{\mathrm{uvw}}-\bar{\mathbf{r}}_{\boldsymbol{mn}})\otimes\langle\delta(\boldsymbol{r}-\mathbf{u}_{uvw}^{mn})\rangle$$

The term P_{uvw}^{mn} represents the joint probability of finding an atom at site m and another at site n in two distinct unit cells separated by a lattice vector $\boldsymbol{R}_{\mathrm{uvw}}$. Likewise, The term $\langle\delta(\boldsymbol{r}-\mathbf{u}_{uvw}^{mn})\rangle$ represents the probability density distribution of the variable $\mathbf{u}_{uvw}^{mn}$, which denotes the difference between the real and average distances of atoms occupying sites m and n that are $\boldsymbol{R}_{\mathrm{uvw}}$ unit cells apart.

The joint probabilities of the pairs P_{uvw}^{mn} can be more conveniently expressed in terms of their conditional probabilities and an occupation factor :

$$\mathrm{Pr}(m,n) = \mathrm{Pr}(n)\mathrm{Pr}(m \mid n) = \mathrm{Pr}(m)\mathrm{Pr}(n \mid m)$$

i.e.,

$$p_{\mathrm{uvw}}^{mn} = c_m p_{\mathrm{uvw}}(n \mid m) = c_n p_{\overline{\mathrm{u}}\overline{\mathrm{v}}\overline{\mathrm{w}}}(m \mid n)$$

Where c_m and c_n are the average site occupation factors of atomic sites m and n, respectively. The term $p_{uvw}(n \mid m)$ denotes the conditional probability that a site n is occupied, provided that the $\boldsymbol{R}_{\mathrm{uvw}}$ unit cells separated site m is also occupied.

3.3.3 Diffuse scattering and the 3D- ΔPair Distribution Function

Recall that the total scattering is :

$$\langle \mathrm{I}_{total}\,(\mathbf{q})\rangle \;=\; \langle \mathrm{I}_{hkl}\,(\mathbf{q})\rangle \;+\; \langle \mathrm{I}_{diffuse}(\mathbf{q})\rangle$$

We can calculate

$$\langle \mathrm{I}_{diffuse}(\mathbf{q})\rangle = \langle \mathrm{I}_{total}\,(\mathbf{q})\rangle - \langle \mathrm{I}_{hkl}\,(\mathbf{q})\rangle = \mathrm{I}_{total}\,(\mathbf{q}) - \langle \mathrm{F}_{\mathrm{hkl}}\,(\mathbf{q})\rangle\langle \mathrm{F}^{*}_{\mathrm{hkl}}\,(\mathbf{q})\rangle$$

$$= \mathfrak{F}[\langle \rho(\mathbf{r})\otimes\rho(-\mathbf{r})\rangle] - \mathfrak{F}[\langle \rho(\mathbf{r})\rangle\otimes\langle \rho(-\mathbf{r})\rangle] =$$

$$\mathfrak{F}[\mathrm{PDF}(\mathbf{r}) - \mathrm{Pat}(\mathbf{r})] =$$

$$= \mathfrak{F}[\mathrm{P}_{\Delta}(\mathbf{r})]$$

The average autocorrelation of the real structure $P\mathrm{DF}(\boldsymbol{r}) = \langle \rho(\mathbf{r})\otimes\rho(-\mathbf{r})\rangle$ is the 3D-PDF.

The autocorrelation of the average structure $P\mathrm{at}(\boldsymbol{r}) = \langle \rho(\boldsymbol{r})\rangle\otimes\langle \rho(-\boldsymbol{r})\rangle$ is the Patterson function.

The difference between the two noted $\mathrm{P}_{\Delta}(\mathbf{r})$ is the 3D-ΔPDF :

$$\mathrm{P}_{\Delta}(\mathbf{r}) = \;[\mathrm{PDF}(\mathbf{r}) - \mathrm{Pat}(\mathbf{r})]$$

Experimentally, it can be obtained by calculating the (inverse) Fourier transform of the diffuse scattering only (Figure 3-15).

$$\mathrm{P}_{\Delta}(\mathbf{r}) = \mathfrak{F}\left[\langle \mathrm{I}_{diffuse}(\mathbf{q})\rangle\right]$$

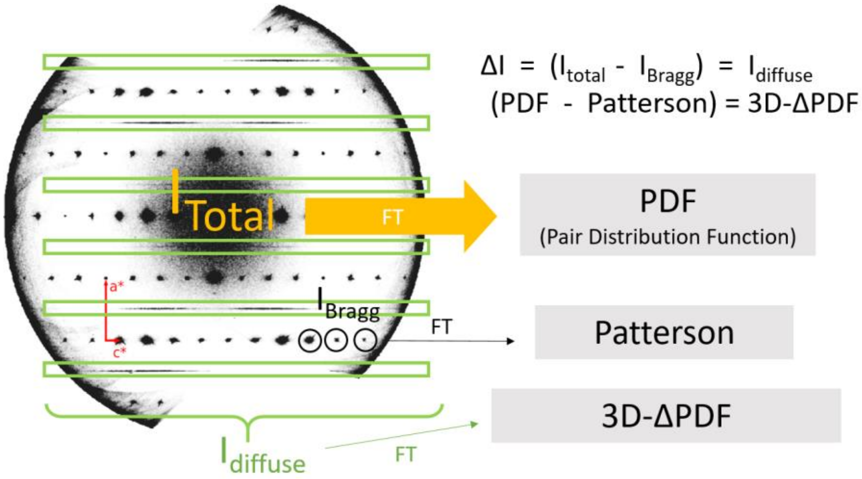

Figure 3-15 : illustration of the relation between the reciprocal space intensities and mapping of the real space. The Fourier Transform of the total scattering , the Bragg peaks and the diffuse scattering gives respectively the PDF. Patterson and 3D-ΔPDF maps.

The 3D-ΔPDF is the difference between the ACF of the real structure and the ACF of the average structure and represents the ACF of the disorder. If the Patterson function contains information about interatomic vectors in the average structure and the PDF describes interatomic vectors in the real structure, the 3D-ΔPDF captures the correlated disorder in the crystal that is not reflected in the average structure.

Because it is an ACF, peaks appear in the 3D-ΔPDF map but contrary to the Patterson map, peaks can take both positive and negative values (Figure 3-16). The amplitudes of 3D-ΔPDF peaks primarily rely on the intensity of pair correlations (positive or negative), the product of the scattering power of the relevant atomic pairs, the distinction between the average and real structures, and the multiplicity of interatomic vectors. They correspond to the probability of a specific interatomic vector being found in the real structure rather than in the average one. Positive values indicate that corresponding interatomic vectors appear more frequently in the real structure than in the average structure, and negative values indicate the opposite. Note that the contrast of the map depends on the strength of the correlation but also the scattering power of atoms involved in the pair so that heavy atoms participating in the disorder will contribute vastly to the ΔPDF signal.

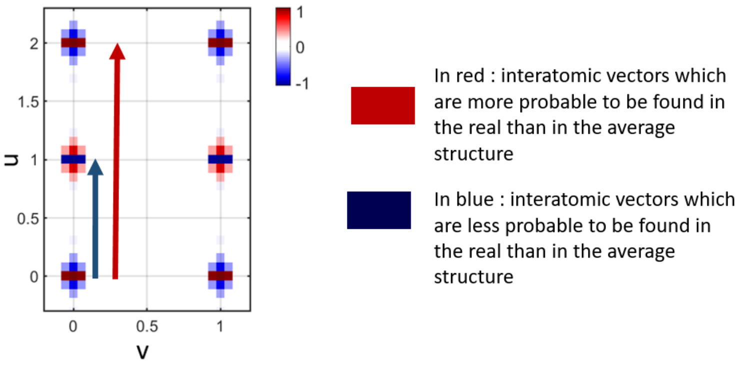

Figure 3-16 : example of a 3D-ΔPDF map. The position of each voxel with respect to the center of the ΔPDF represents an interatomic vector. The normalized intensity of a voxel corresponds to the probability of that specific interatomic vector being found in the real structure rather than the average one.

Opting for the analysis of disorder using the 3D-ΔPDF instead of the total 3D-PDF offers several advantages [77]:

Firstly, the reduction in the number of peaks in PDF space is notable, as only interatomic vectors having different real and average structure properties contribute to the 3D-ΔPDF. This excludes atoms that are fully ordered and atomic pairs that exhibit complete lack of correlation due to substantial separation for example.

Secondly, statistical errors on Bragg intensities are comparable to or even exceed those of diffuse scattering intensities. In many cases, by eliminating Bragg intensities, it leads to a substantial improvement in the quality of local structure information as it only relies on the diffuse scattering intensity.

Lastly, the enhanced contrast in 3D-ΔPDF maps facilitates qualitative and semi-quantitative assessments of the underlying disorder issue through visual inspection of the patterns.

3.3.4 Computation of the 3D-ΔPDF function and the associated diffuse scattering

The 3D-ΔPDF function $\mathrm{P}_{\Delta}(\mathbf{r})$ can be compute starting from the following relation :

$$\mathrm{P}_{\Delta}(\mathbf{r}) = [\mathrm{PDF}(\mathbf{r}) - \mathrm{Pat}(\mathbf{r})]$$

and

$$PDF(\boldsymbol{r}) = \sum_{uvw}^{cryst}\sum_{mn}^{cell} P_{uvw}^{mn}\rho_m(\boldsymbol{r})\otimes\rho_n(-\boldsymbol{r})\otimes\delta(\boldsymbol{r}-\boldsymbol{R}_{\mathrm{uvw}}-\bar{\mathbf{r}}_{\boldsymbol{mn}})\otimes\langle\delta(\boldsymbol{r}-\mathbf{u}_{uvw}^{mn})\rangle$$

The Patterson function $\mathrm{Pat}(\mathbf{r})$ is the ACF of the average structure and can be obtained by averaging $P\mathrm{DF}(\boldsymbol{r})$ over all lattice vectors.

The joint occupational probability for each pair of average atoms is the product of the individual atom occupancies : $p_{\mathrm{uvw}}^{mn} = c_m c_n$. The distributions $\boldsymbol{u}_{\mathrm{uvw}}^{mn}$ will separate into two independent distributions, $\boldsymbol{u}_m$ and $\boldsymbol{u}_n$.

$$P\mathrm{at}(\boldsymbol{r}) = \sum_{uvw}^{cryst}\sum_{mn}^{cell} c_m c_n \rho_m(\boldsymbol{r})\otimes\rho_n(-\boldsymbol{r})\otimes\delta(\boldsymbol{r}-\boldsymbol{R}_{\mathrm{uvw}}-\bar{\mathbf{r}}_{\boldsymbol{mn}})\otimes\langle\delta(\boldsymbol{r}-\boldsymbol{u}_m)\rangle\otimes\langle\delta(\boldsymbol{r}-\boldsymbol{u}_n)\rangle$$

Before the investigation of the disorder, the average structure is usually well known and therefore it is very useful to analyze the deviations from the average structure to understand the correlated disorder by computing $\mathrm{P}_{\Delta}(\mathbf{r})$. $\mathrm{P}_{\Delta}(\mathbf{r})$ is obtained by subtracting $P\mathrm{at}(\boldsymbol{r})$ from $P\mathrm{DF}(\boldsymbol{r})$:

$$\mathrm{P}_{\Delta}(\mathbf{r}) = \sum_{uvw}^{cryst}\sum_{mn}^{cell}[P_{uvw}^{mn}\langle\delta(\boldsymbol{r}-\mathbf{u}_{uvw}^{mn})\rangle \\ - c_m c_n\langle\delta(\boldsymbol{r}-\boldsymbol{u}_m)\rangle\otimes\langle\delta(\boldsymbol{r}-\boldsymbol{u}_n)\rangle]\otimes\rho_m(\boldsymbol{r})\otimes\rho_n(-\boldsymbol{r})\otimes\delta(\boldsymbol{r}-\boldsymbol{R}_{\mathrm{uvw}}-\bar{\mathbf{r}}_{\boldsymbol{mn}})$$

The corresponding diffuse scattering is very straightforward to calculate :

$$I_{\mathrm{diffuse}}(\mathbf{q}) = \sum_{uvw}^{cryst}\sum_{mn}^{cell}[P_{uvw}^{mn}\langle\exp(2\pi i\mathbf{q}\cdot\mathbf{u}_{uvw}^{mn})\rangle - c_m c_n\langle\exp(2\pi i\mathbf{q}\cdot\mathbf{u}_m)\rangle\langle\exp(2\pi i\mathbf{q}\cdot\mathbf{u}_n)\rangle] \\ f_m(\mathbf{q})f_n^*(\mathbf{q})\exp[2\pi i\mathbf{q}\cdot(\mathbf{R}_{uvw}+\bar{\mathbf{r}}_{\boldsymbol{mn}})]$$

We can simplify this expression by approximating the expressions in angle brackets (average) by Gaussians such as $\langle\exp(2\pi i\mathbf{q}\mathbf{u}_m)\rangle = \exp[-2\pi^2\langle(\mathbf{q}\mathbf{u}_m)^2\rangle] = \exp(-\mathbf{q}^T\beta_m^{aver}\mathbf{q})$ where β_m^{aver} is a space and time average matrix representing the frequently used (dimensionless) atomic displacement parameters (ADP) of atom m. The expression $\langle\exp(2\pi i\mathbf{q}\cdot\mathbf{u}_{uvw}^{mn})\rangle$ can be approximate by $\exp(-\mathbf{q}^T\beta_{uvw}^{mn}\mathbf{q})\exp(2\pi i\mathbf{q}\cdot(\mathbf{R}_{uvw}+\bar{\mathbf{r}}_{\boldsymbol{mn}}+\bar{\boldsymbol{u}}_{uvw}^{mn}))$ where β_{uvw}^{mn} and $\bar{u}_{uvw}^{mn}$ indicate displacement correlation and size effect correlation. Taking the real part of the above expression, the complete expression for the diffuse intensity is :

$$I_{\mathrm{diffuse}}(\mathbf{q}) = \sum_{\mathbf{R}_{uvw}}^{\mathrm{cryst}}\sum_{mn}^{\mathrm{cell}}\{p_{uvw}^{mn}\exp(-\mathbf{q}^T\beta_{uvw}^{mn}\mathbf{q})\cos[2\pi\mathbf{q}\cdot(\mathbf{R}_{uvw}+\bar{\mathbf{r}}_{\boldsymbol{mn}}+\bar{\boldsymbol{u}}_{uvw}^{mn})] \\ -c_m c_n\exp[-\mathbf{q}^T(\beta_m^{\mathrm{aver}}+\beta_n^{\mathrm{aver}})\mathbf{q}]\cos[2\pi\mathbf{q}(\mathbf{R}_{uvw}+\bar{\mathbf{r}}_{\boldsymbol{mn}})]\}f_m(\mathbf{q})f_n(\mathbf{q})$$

The variables with sub- and super-script notation [$^{mn}_{uvw}$] represent the parameters which quantify the correlations related to the disorder that gives rise to diffuse scattering:

- **Occupational correlation** P^{mn}_{uvw}: Joint probability of finding atoms m and n separated by a vector $\mathbf{R}_{uvw} + \bar{\mathbf{r}}_{mn}$, representing This parameter addresses occupancy disorder.
- **Displacive correlation** β^{mn}_{uvw} : joint probability atomic displacement parameter of atom n as seen from atom m separated by a vector $\mathbf{R}_{uvw} + \bar{\mathbf{r}}_{mn}$. This parameter addresses the displacive disorder.
- **Size effect parameter** $\bar{\boldsymbol{u}}^{mn}_{uvw}$: quantifies the difference between the real and average interatomic vector between atoms m and n. This parameter corresponds to size-effect disorder induced by occupational disorder.

This expression can be a little bit overwhelming so in order to decipher it, let's take a simple example of a 1D displacive disorder.

3.4 1D DISPLACIVE DISORDER, DIFFUSE SCATTERING AND ΔPDF

I consider here a 2D crystal composed of atom A on square lattice, u (h) and v (k) are the dimensionless fractional real (reciprocal) lattice units along **a(*)** an **b(*)** respectively (Figure 3-17).

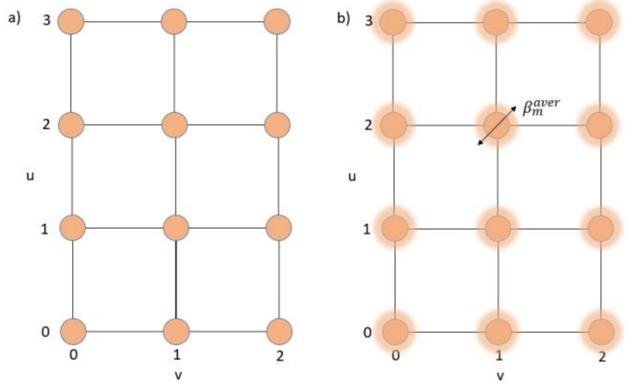

Figure 3-17 : a) Average structure compose of atom at the node of a square lattice. b) real structure with uncorrelated displacive disorder.

For the calculation, we use the atomic form factor of Al on a square lattice of a length of 5Å. In the displacive model, we consider the absence of occupancy disorder and size effect : $P_{uvw}^{mn} = 1$ and $\bar{\boldsymbol{u}}_{uvw}^{mn} = 0$. The displacements are considered isotropic and harmonic : $\beta_{Al}^{aver} = 0.04$ corresponding to $U_{\text{iso}} = 0.05$ Å^2.

The general expression for the diffuse scattering in case of this 2D structure with only displacive disorder becomes :

$$I_{\text{diffuse}}(\mathbf{q}) = \sum_{\mathbf{R}_{uv}}^{\text{cryst}} \sum_{mn}^{\text{cell}} \{\exp(-\mathbf{q}^T \beta_{uv}^{mn} \mathbf{q}) - \exp(-\mathbf{q}^T (2\beta_m^{\text{aver}}) \mathbf{q})\}$$

$$f_m^2(\mathbf{q}) \cos[2\pi \mathbf{q}(\mathbf{R}_{uv} + \bar{\mathbf{r}}_{\boldsymbol{mn}})]$$

3.4.1 No correlation

In the first example of displacive disorder, we consider no correlation between the displacement of the atoms, i.e displacement are independent to each other.

The joint probability displacement $\beta_{uv}^{mn}$is defined as follow :

$$\beta_{00}^{mm} = 0$$

$$\beta_{uv}^{mn} = 2\beta_m^{\text{aver}} \text{, for any other case}$$

The joint probability $\beta_{uv}^{mn} = 2\beta_m^{\text{aver}}$ except for $\beta_{00}^{mm} = 0$ because a real atom is never displaced with respect to itself and correlation between neighboring atoms (u or v $\neq 0$) correspond to the average correlations in this case. The diffuse scattering can be calculated and its associated ΔPDF map by applying the Fourier Transform :

$$I_{\text{diffuse}}(\mathbf{q}) = [1 - \exp(-2\beta^{aver} \text{q}^2)]\, f_m^2(\mathbf{q})$$

and $$\text{P}_\Delta(\text{u}, \text{v}) = \mathfrak{F}[I_{\text{diffuse}}(\text{h}, \text{k})]$$

Figure 3-18 displays both the diffuse scattering and the corresponding ΔPDF maps obtained using a homemade Python program. Intensities start at zero in reciprocal space and steadily increase with distance. The reduction in intensities at large q vectors is due to the decrease of the atomic form factor. The 2D-ΔPDF results from the Fourier transform of the diffuse scattering, revealing a distinct signal at the origin with a Mexican hat shape—high densities at the center surrounded by a ring of negative densities. No signals appear at larger distances due to uncorrelated displacements undistinguishable from average correlations. The Mexican hat profile stems from the likelihood of an atom being at a distance of zero from itself, more probable in the real structure than the average structure. Conversely, any distance larger than zero between an atom and itself is never present in a real structure, resulting in negative ΔPDF intensities around the positive peak at the origin.

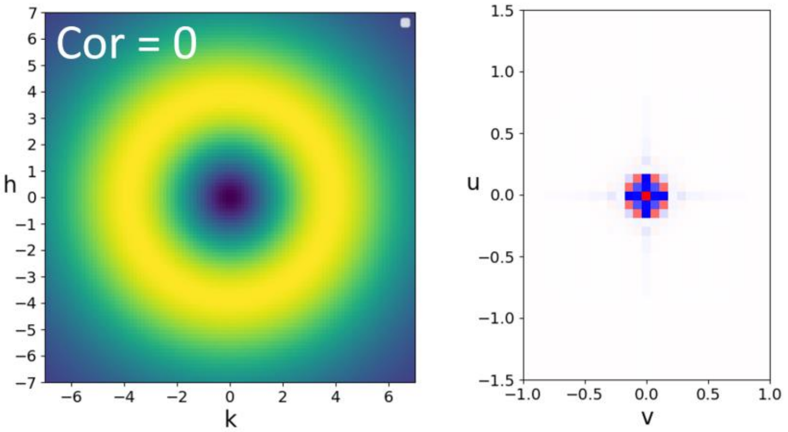

Figure 3-18 : (left) diffuse scattering signal in the reciprocal space for the case of uncorrelated displace disorder. Yellow signifies high value of the intensity. (right) ΔPDF map in the real space. Positive values are in red and negative values in blue.

3.4.2 Negative correlation

In the second example, we consider a correlation in the displacement along the **a** direction and no correlation along **b** (Figure 3-19). We allow negative correlations between the displacements, i.e next neighboring atoms tend to move along anti-parallel directions. The real structure is composed of two kinds of chains along **a** depending on the direction of the correlated displacement. The real structure periodicity is twice the periodicity of the average structure. If we were solving the structure of the average structure using Bragg peaks intensity, we would measure large ADPs along the **a** direction and the dimerization mechanism due to the correlated displacement would be completely unrevealed. All the information are in the diffuse scattering.

The calculation of the diffuse scattering is similar to the first example except that we consider that the site m in the unit cell : m [0,0] is correlated to the atom separated to the lattice vector $\mathbf{R}_{uv} = [1{,}0]$ so the negative correlation extends only to the first neighbour atom. Self-correlation is zero and other correlations with other atoms are equal to the average correlation as in the previous example.

The joint probability displacement $\beta_{uv}^{mn}$is then defined as follow :

$$\beta_{00}^{mm} = 0$$

$$\beta_{10}^{mm} = 2\beta_m^{\text{aver}}\,(1 + cor)$$

$$\beta_{uv}^{mn} = 2\beta_m^{\text{aver}}\text{, for any other case}$$

We introduce the parameter cor that represent the negative correlation between two neighbouring atom along the **a** direction.

And, the diffuse scattering can be calculated with the following formula :

$$\begin{aligned} I_{\text{diffuse}}(\mathbf{q}) = \{1 - \exp(-2\beta^{aver}\mathrm{q}^2) &\\ &+ [\exp(-2\beta^{aver}(1 + cor)\mathrm{q}^2) \\ &- \exp(-2\beta^{aver}\mathrm{q}^2)]\, cos(2\pi h)\}\, f_m^2(\mathbf{q}) \end{aligned}$$

with $\mathbf{q} = [\mathrm{h}, \mathrm{k}]$

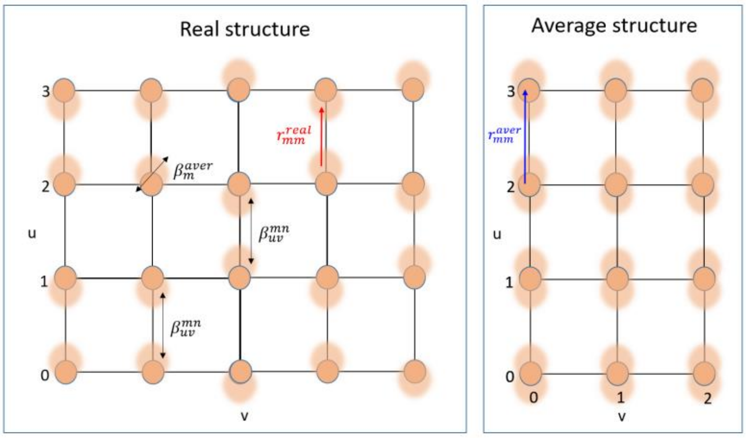

Figure 3-19 : the real structure composed of types of correlated chains of periodicity 2a. The average structure of periodicity a shows large ADP along the **a** direction.

The diffuse scattering pattern and their associated 2D-ΔPDF maps are presented in Figure 3-20 for the case of no correlation ($cor = 0$), small negative correlation ($cor = 0.2$) and high correlation ($cor = 0.6$). It shows very characteristic pattern of 1D correlated disorder : as already discussed in 3.1.1, the diffuse scattering of 1D correlated chains are diffuse streaks (planes for a 3D crystal) perpendicular to the chains and the intensity of the streaks is correlated by the atomic form factor. The diffuse scattering condense at half integer position (h =0.5, 1.5, 2.5…) meaning that the real structure shows a correlated disorder of twice periodicity of the average structure. The fact that it condenses only at half integer is the signature of the anti-ferro ordering, i.e negative displacement correlation. We already see this feature in 3.1.1.

In the 2D-ΔPDF map, the central peak remains identical to that observed in uncorrelated displacements, primarily determined by the average structure : a positive Mexican hat shape. Due to the negative correlations between neighboring atoms along the **a** direction, two neighbouring atoms along **a** exhibit opposing displacement. Consequently, the interatomic vector between those two atoms have a low probability to be as long as the average interatomic distances r_{mm}^{aver}. Therefore, the ΔPDF is negative at such average positions. Conversely, the interatomic distance corresponding to the displacement r_{mm}^{real} is more probable in the real structure than in the average leading to two positive peaks surrounding the negative peak resembling a negative Mexican hat.

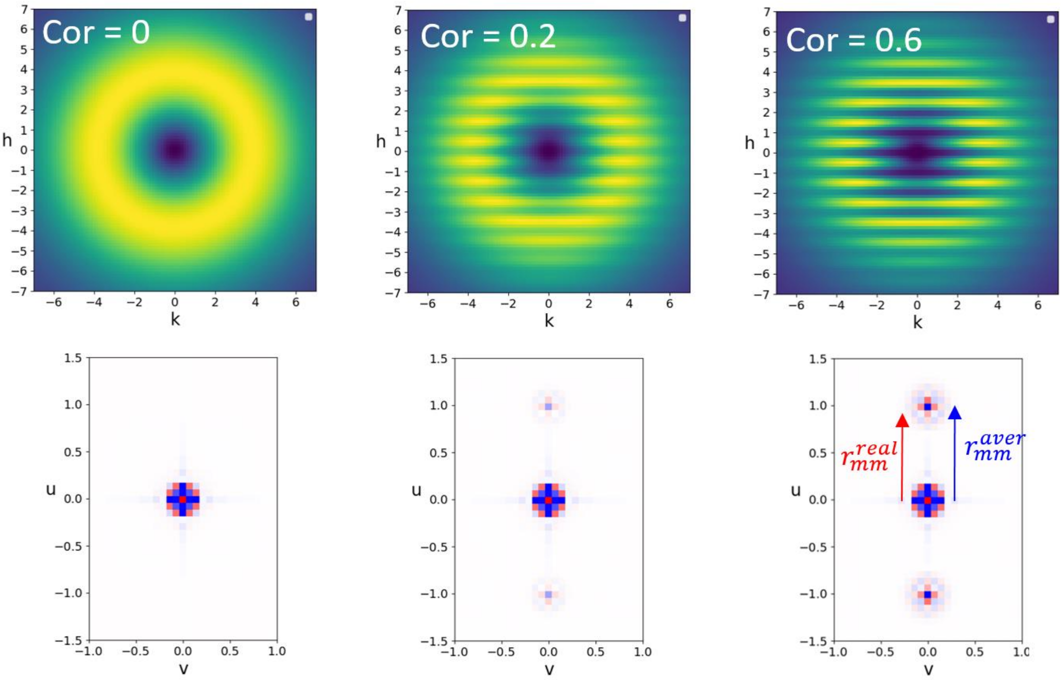

Figure 3-20 : (up panel from left to right) diffuse scattering pattern for the case of uncorrelated displacement disorder, small and large negative correlation along a. Yellow signifies high value of the intensity. (low panel) Corresponding ΔPDF maps in the real space. Positive values are in red and negative values in blue. Negative Mexican hat appears at u = 1, signing the anti-ferro ordering along a.

The 3D-ΔPDF is the difference between the ACF of the real structure and the ACF of the average structure and represents the ACF of the disorder. It is possible knowing the real structure and the average structure to calculate the corresponding ΔPDF. To illustrate this method, we introduce a 1D - model of dimerization (Figure 3-21). We consider a real crystal composed of two different structures A and B generated by anti-phase displacement (δ) of nearest atoms, each structure related to the other by a one-half translation along a. Each structure has an equal probability, and no correlation is assumed, so the "real" crystal is highly disordered. Electron density peaks of the average structure are located at the position of the electron density peaks of the two real structures giving rise to a periodicity of half the real periodicity.

Model diffraction patterns can be obtained from the autocorrelation function of the electron density known as the PDF and the Patterson calculated from the real structure and the average structure, respectively. The ΔPDF is the difference between the PDF and the Patterson function. In the specific case of dimerization, we observe a distinct repetition of negative-positive-negative peaks (positive Mexican hat) and positive-negative-positive (negative Mexican hat). The distance 4δ within these profiles is directly related to the displacement of the dimerization. Its periodicity, the same as the real structure, is twice the periodicity of the average structure.

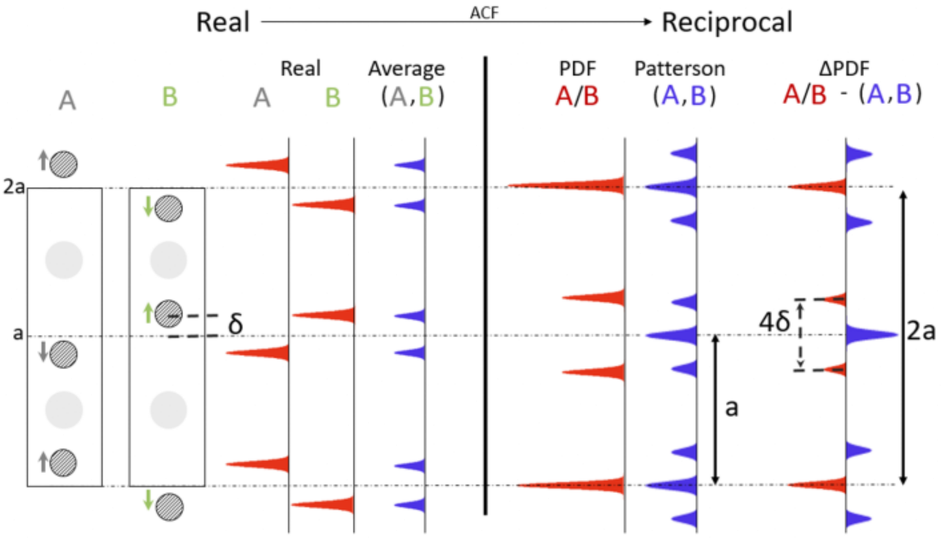

Figure 3-21 : ΔPDF of 1D-Chains. a) (left) simple model of a + δ dimerization along a with equal probability of A and B atomic configurations. Electron density of the individual A, B atomic positions (real structure) and the average structure. (right) Associated autocorrelated function (ACF) of the A/B structure (PDF), of the average (Patterson) and their difference (ΔPDF = PDF-Patterson). Note the cell doubling in the ΔPDF. The distance of two characteristic positive peaks in the ΔPDF corresponds to 4δ. (From L.Guérin et al, ChemPhysChem, 2022 [78])

We can see that we get the same results than in the previous section where we start from the real structure (correlation) and calculate the diffuse scattering and the ΔPDF map. In reality, we don't know the real structure so it can be used a posteriori after determination of the ΔPDF from the integration of the diffuse scattering. This technique of calculation of ACF to determine the ΔPDF is therefore more a pedagogical approach and can be used to present the ΔPDF to a larger audience.

The last part of this chapter dealing with correlated disorder are two applications of the 3D-ΔPDF method that I and my colleague worked on the last few years.

3.5 2D CHARGE-DENSITY-WAVE ATOMIC STRUCTURE IN AN MX–CHAIN BY THE 3D-ΔPDF METHOD

The first case is good illustration of what we've just calculated. Quasi-one-dimensional halogen-bridged metal complex so called MX-Chains have an isolated one-dimensional (1D) electronic system composed of d_{z2} orbital of metal ions (M) and p_z orbital of bridging halide ions (X). [57] The very large majority of M=Pd compound which have a $–X\cdots M^{II}\cdots X–M^{IV}–X\cdots$ Peierls distorted 1D structure, are in a mixed-valence charge-density-wave (MV-CDW) state. This mixed-valence state is accompanied by a strong dimerization along the chain, with two competing CDW ground states (Figure 3-22). However, some Pd complexes which show a CDW-to-Mott-Hubbard (MH) phase transition have been reported [79]. In such a case, at variance with CDW, the X-M-X bonds are completely symmetric.

The question is : what is the electronic state of $[Pd(cptn)_2Br]Br_2$ crystal ? It should be very simple to answer with diffraction. The chains are periodic of period a in case of MH because X-M-X is completely symmetric. The Peierls distorsion associated to the CDW induce a cell doubling $X\cdots M^{II}\cdots X–M^{IV}–X$. Therefore in case of the CDW state, we should observe Bragg peaks at half integer value along **a*** corresponding to the 2a periodicity.

3.5.1 Determination of the average structure.

A set of single crystals of $[Pd(cptn)_2Br]Br_2$ were studied by X-Ray diffraction at 260 K. X-ray measurements were carried out at the Swiss Norwegian Beamline BM01 at the European Synchrotron Research Facility using monochromatized X-rays. Structure solution and refinement using the software Jana yielded an orthorhombic structure of space group I222 with the lattice parameters a = 5.249 Å, b = 6.972 Å, c

= 22.711 Å. As illustrated in Figure 3-23 the structure consists of a body-centered arrangement of [Pd(cptn)$_2$Br]Br$_2$ chains. A single chain is composed of an alternation of Pd(cptn)$_2$ units bridged by Br ions along the a axis; the amine (NH$_2$) groups of the cptn ligand provide cohesion between chains in the b direction through hydrogen bonds formed with the Br−. The cptn ligands extend from each chain in the c direction. The important observation is that the Pd-Br-Pd distance is symmetric, and no sign of dimerization is observed in the average structure. There is no evidence of a CDW organization regarding the average structure from this single crystal structural analysis.

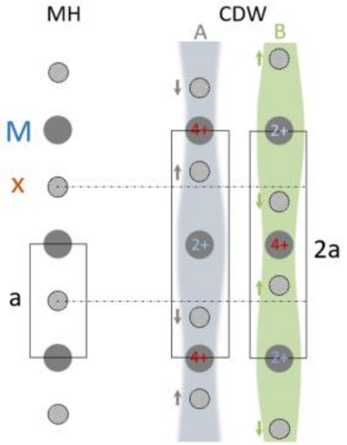

Figure 3-22 : Schematic representation in halogen-bridged metal compounds (MX chains) of the Mott Hubbard (left) and the Charge Density Wave states (right) showing the two competitive ground states (A and B). Note the cell doubling along *a* associated to the dimerization of the halogen ion X in the CDW state.

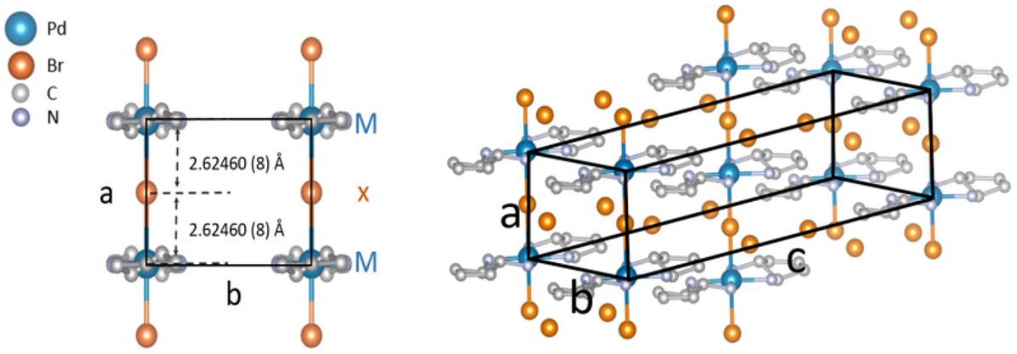

Figure 3-23 : the orthorhombic structure of the MX-Chain compound Pd(cptn)2Br]Br2. The Br atom is found exactly in the middle of the Pd atoms.

3.5.2 Analysis of the diffuse scattering

A representative (h 0 l) section of the three-dimensional scattering pattern is shown in Figure 3-24. It contains weak but highly structured diffuse scattering, which is the signature of the strongly correlated disorder. A set of streaks parallel to the c* axis and perpendicular to the (a*, b*) plane are observed, suggesting the existence of a two-dimensional (a, b) ordering in real space with disorder along the c direction. Correlation lengths of 2100 Å (400 unit cells) and 480 Å (70 unit cells) in the a and b crystallographic directions, respectively, were extracted from a Lorentzian fit of the profile of the diffuse streaks along the a* and b* directions. The streaks intersect the H direction at half-integer values, while along the K direction only integer values are met. This means that the ordering phenomenon results in a double periodicity in terms of structural displacements along a with respect to the average structure defined by the Bragg peaks position. On the other hand, the same periodicity between average and real structure occurs in the b direction. Individual (a, b) planes in the crystal are composed of chains with a double periodicity compared to the average structure, with each neighboring chain in the b direction being ordered in phase. Thus, one can say that a long-range order occurs in individual planes.

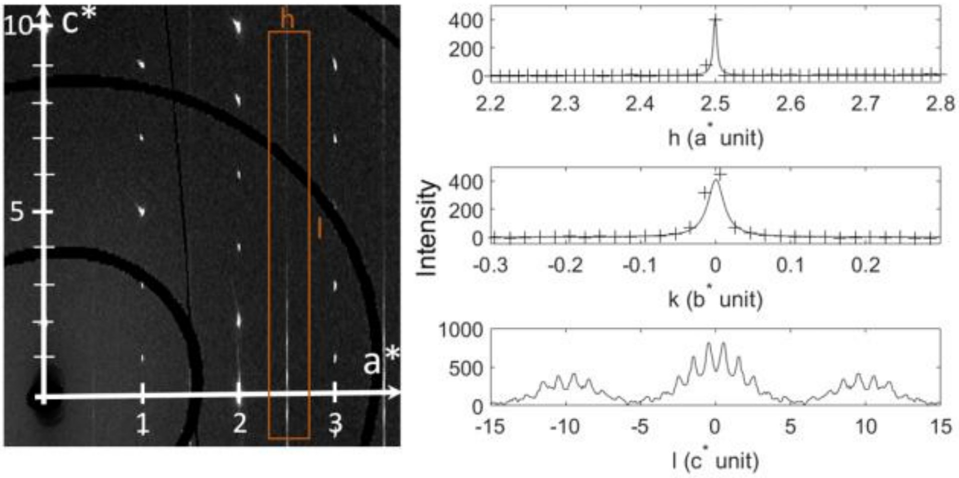

Figure 3-24 : (left) reconstructed (h 0 l) reciprocal plane shows c* diffuse streaks at half integer values of a*. (right) (h = 2.5) streak profiles and their lorentzian fit.

3.5.3 Application of the 3D –ΔPDF method

The inverse Fourier transform of the normalized diffuse scattering function yields the 3D-ΔPDF, [77] a three-dimensional real space reconstruction consisting of voxels. The quality and the resolution of the ΔPDF are defined by the number of streaks collected and their intensities compared to the background. [80] The size of the present ΔPDF (26 x 18 x 800 voxels) and the corresponding voxel size (0.40 x 0.58 x 0.03 Å) stems from the data acquisition strategy and the integration procedure. The reciprocal volume of diffuse streaks was merged into 1D pixel arrays to increase the data statistics (Figure 3-24), thus implicitly assuming perfect (infinite) correlation in the *a** and *b** directions. Figure 3-25 shows a section of the ΔPDF corresponding to the (*u*, *v*, 0) plane. As already discussed in the previous section, cell doubling along the chain (*a* direction) is observed in the ΔPDF while the periodicity perpendicular to the chain along the *b* direction remains unvaried. The typical pattern of dimerization with the negative Mexican hat is clearly revealed in the profile along the *a* direction corresponding to an overall displacement of $\delta = 0.038\,a = 0.2$ Å.

The analysis of the ΔPDF and width of the diffuse streaks indicate that the (*a*, *b*) plane consists of long-range ordered dimerized chains in the CDW state.

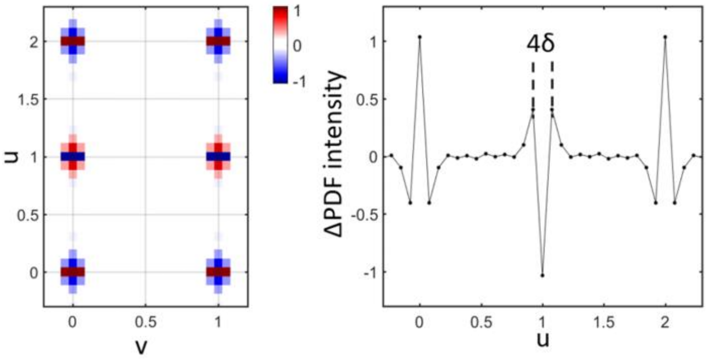

Figure 3-25 : experimental normalized ΔPDF of the (*a*,*b*) plane (left) and its profile along a (right). The displacement is $\delta = 0.038a = 0.2$ Å

3.5.4 Yell model and determination of the electronic state

The software Yell [81] allows for the specification of a disorder model, starting from the average structure of the crystal that we determined previously. A displacive model using 3 parameters corresponding to a displacement along a direction of the Br^- bridging anion (Br1), the Br^- counteranion (Br2) and the terminal carbon atom of cptn ligand (so-called C atom) is used to generate a ΔPDF. The Figure 3-26 shows the results of the Yell model. We can see that the generated maps by Yell are in good agreement with the experimental ones.

A displacement of $\Delta = 0.136$ Å of the Br bridging atom (Br1) along the chain is obtained. It has been established that the distortion parameter defined as $d = 2\Delta/a$, bears a linear relationship to a : $d = 0.165\,a - 0.81$. The obtained value of $d = 2\Delta/a = 0.052$ for $a = 5.25$ Å is in perfect agreement with other Pd-based MX chains found in a CDW state, confirming the CDW nature of the electronic state (Figure 3-27). [82,83]

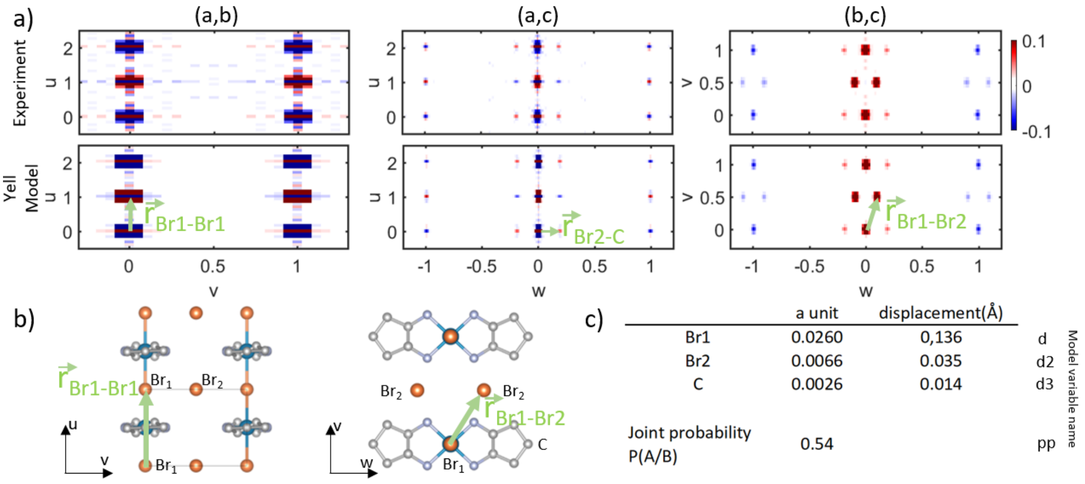

Figure 3-26 : (a) experimental ΔPDF and Yell generated ΔPDF for three section of the real space Interatomic vectors corresponding to intense peaks in the ΔPDF are shown. . The negative correlation corresponding to Br1-Br1 is a signature of the dimerization along the chain (b) structure with relevant interatomic vectors. (c) result of the Yell model.

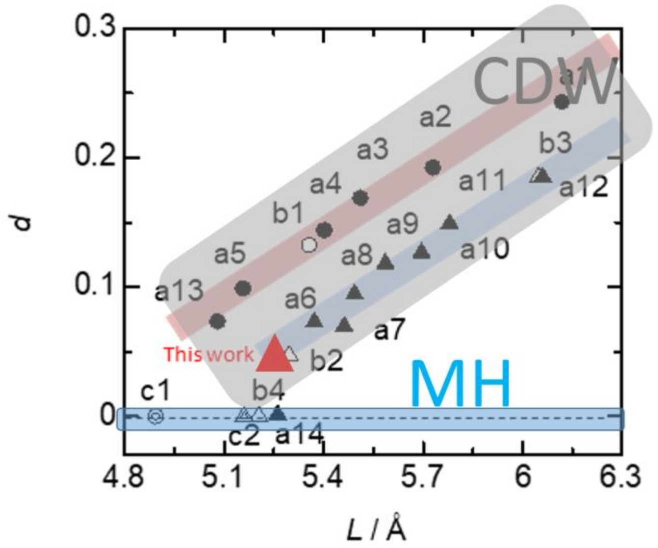

Figure 3-27 : Correlation between d (= $(l_2 - l_1)$/L, where $l_2 = d(\mathrm{M}^{\mathrm{II}}\cdots\mathrm{X})$ and $l_1 = d(\mathrm{M}^{\mathrm{IV}}-\mathrm{X})$) and L (M−X−M distance). Circles and triangles represent Cl- and Br-bridged MX chains, respectively. Filled, hollow, and double markers show Pt-, Pd-, and Ni-based MX chains, respectively. Red color represents the this work. Data are shown for $[\mathrm{Pt(en)_2Cl}](\mathrm{ReO_4})_2$ (a1), $[\mathrm{Pt(chxn)_2Cl}](\mathrm{ClO_4})_2$ (a2), $[\mathrm{Pt\text{-}(pn)_2Cl}](\mathrm{ClO_4})_2$ (a3), $[\mathrm{Pt(en)_2Cl}](\mathrm{ClO_4})_2$ (a4), $[\mathrm{Pt\text{-}(chxn)_2Cl}]\mathrm{Cl_2}$ (a5), $[\mathrm{Pt(chxn)_2Br}]\mathrm{Br_2}$ (a6), $[\mathrm{Pt(tn)_2Br}](\mathrm{BF_4})_2$ (a7), $[\mathrm{Pt(en)_2Br}](\mathrm{ClO_4})_2$-1 (a8), $[\mathrm{Pt(etn)_4Br}]\mathrm{Br_2}$ (a9), $[\mathrm{Pt\text{-}(en)_2Br}](\mathrm{ClO_4})_2$-2 (a10), $[\mathrm{Pt(chxn)_2Br}](\mathrm{ClO_4})_2$ (a11), $[\mathrm{Pt\text{-}(en)_2Br}](\mathrm{ReO_4})_2$ (a12), $[\mathrm{Pd(en)_2Cl}](\mathrm{ClO_4})_2$ (b1), $[\mathrm{Pd\text{-}(chxn)_2Br}]\mathrm{Br_2}$ (b2), $[\mathrm{Pd(en)_2Br}](\mathrm{ReO_4})_2$ (b3), $[\mathrm{Ni(chxn)_2Cl}]\text{-}\mathrm{Cl_2}$ (c1), $[\mathrm{Ni(chxn)_2Br}]\mathrm{Br_2}$ (c2), $[\mathrm{Pt(dabdOH)_2Cl}]\mathrm{Cl_2}$, $[\mathrm{Pt(dabdOH)_2Br}]\mathrm{Br_2}$, and $[\mathrm{Pd(dabdOH)_2Br}]\mathrm{Br_2}$. Pink and blue highlight lines are guides for the eyes for each X− ion. (chxn = cyclohexanediamine; en = ethylenediamine; etn = ethylamine; tn = 1,3-diaminopropane, pn = 1,2-diaminopropane). references in sup. mat [78]

3.5.5 Structure of the 2D-CDW

In Figure 3-26, the (0, v, w) plane shows strong positive peaks corresponding to the interatomic vector between Br1 and Br2 (Figure 3-28). It indicates that the Br1 and Br2 atoms are displaced in phase in the a direction. The counteranion Br2 displaces in phase with Br1. Looking at the average structure, one can notice that the Br bridging and counteranions are connected by a hydrogen-bonding network (Figure 3-28). Once a dimerization starts occurring locally in the *a* direction (either A or B type) along the chain axis, it is easily propagated in the *b* direction due to the presence of the H-bonds (which provides interchain cohesion in the *b* direction) and mediated by the Br2 counteranions. All the chains contained in the same (*a*, *b*) plane dimerize in the same way, and a 2D-CDW state is stabilized.

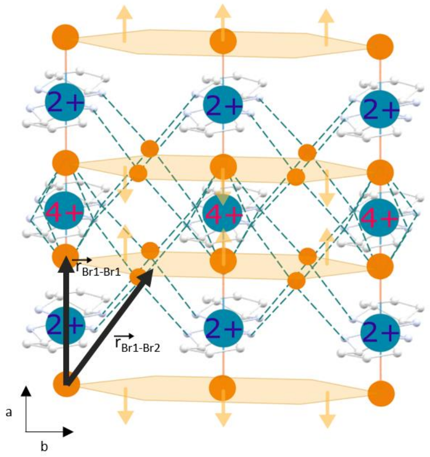

Figure 3-28 : : a schematic diagram of the two types of 2D CDW arrangements (A and B) c) The mixed-valence 2D CDW schematic structure in the (*a*, *b*) plane. The hydrogen-bonding network (green dashed lines) is shown. Yellow arrows represent the dimerization of the Br1-Br2 molecules along the chain direction.

The (*u*, 0, *w*) and (0, *v*, *w*) sections shown in Figure 3-26 further allow the interpretation of the correlated disorder between the two-dimensional CDW (*a*, *b*) planes stacked and shuffled along the orthogonal direction. Because of the degenerate ground state of the CDW state (A/B in Figure 3-22) and weak plane-to-plane interaction, disorder appears along the **c** direction. Both the (*a*, *c*) and (*b*, *c*) section of the ΔPDF show opposite signs of features for adjacent unit cells along *c* direction, indicating negative correlation between adjacent (*a*, *b*) plane. Experimentally, this negative correlation originating from the one-half *c** periodicity manifests itself as sharper peaks in the intensity profile of the streaks (Figure 3-24). One can then assume a small displacement of the Br1 and Br2 atoms as derived from the first model, apply it to entire (*a*, *b*) planes, and derive a substitutional model in order to investigate the correlations along the **c** direction. The obtained joint probability P(A/B) that planes separated by a given vector in **c** are ordered in a different way is found to be equal to 0.54. This indicates that there is not a complete disorder along **c** (which would be characterized by a probability 0.5) (Figure 3-29). The 2D-CDW of a given (*a***,** *b*) plane tends to slightly order in an anti-phase manner, with the CDW being shifted by a/2 between two adjacent planes with a very short correlation length. The value of this length was estimated from the fit of the sharper peaks along **c** and was found to be equal to 52 Å (2.3 unit cells). This anti-phase process is known as the Coulomb coupling and is illustrated schematically in Figure 3-29. This mechanism is usually invoked to account for the CDW transverse ordering in TTF-TCNQ and related compounds where these interactions make the diffuse scattering condensed in commensurate positions at the phase transition [50,84].

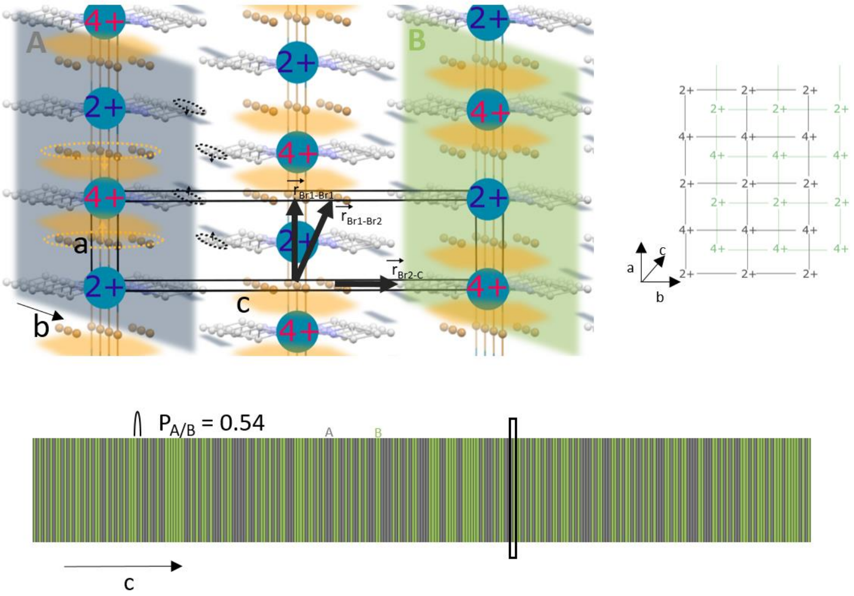

Figure 3-29 : (up left) The mixed-valence 2D CDW schematic structure along the c direction. The interatomic vector between bromide counteranion and terminal carbon atom (black arrow) and the displacement of bromine atoms (yellow glooms) and of terminal carbon atom of cptn ligand (yellow glooms and arrows) are represented. Note the a/2 phase shift of the CDW from plane to plane. (up right) Schematic structure of stacking of two 2D CDW planes. (down) Schematic representation of A/B ordering along the c direction. The joint probability PA/B is found to be 0.54, complete disorder corresponding to 0.5. Alternation of A/B planes is more probable. (PA/B=0.60 was chosen in this schematic representation to enhance the anti-phase ordering)

The present study demonstrates the great power of the 3D-ΔPDF method in analyzing diffuse scattering data and provide insights into the disorder present inside a material. The absence of superstructure Bragg peaks and the wrong assumption that the crystal structure lies in the MH state is due to the fact that the information lies within the diffuse scattering. Here the MX-Chain compound $[Pd(cptn)_2Br]Br_2$ was studied by analyzing qualitatively and quantitatively the 3D-ΔPDF maps that unambiguously show that 2D sheets in CDW states are formed. It also reveals that the ordering of one given sheet is only slightly correlated with the ordering of the adjacent ones [78].

3.6 3D- ΔPDF METHOD APPLIED TO SHORT-RANGE ORDER OF ALKANE IN THE QUASI-LIQUID PHASES WITHIN APERIODIC UREA INCLUSION CRYSTALS

For the second example, we will look at how can we use the 3D- ΔPDF method to understand the local ordering of the alkane in the quasiliquid phase when they are confined aperiodically within the urea channels. Full disclosure, this works is more the work of my colleagues as I only personally participate to the data collection and in some discussions on the interpretation of the diffuse scattering. The 3D-ΔPDF method with the modelling with Yell was the work of Arkadiy Simonov, Post-doc at that time in our group. As a consequence, I will discuss the main results and I encourage the reader to look at the article Simonov et al., PRB,2022 for a complete explanation [85].

We recall from 3.1.3 that at high temperature, alkane molecules confined in the host urea channel are, especially for short alkanes, in a quasi-liquid state that disrupts the translational symmetry of the alkane sub lattice leading to a disorder of 2nd kind. This is evidenced in the diffraction pattern by sharp parallel diffuse planes, referred to as s-planes located at multiple value of $2\pi/C_g$. In chapter 3.2.4, we used a simple model to relate the evolution of the experimental width of s-planes as a function of the order m of the plane and we extracted the value of Δ, the relative shift between two alkanes in adjacent channel, to characterize the liquid-like feature. But this 1D liquid model does not allow the existence of lateral order and this is a too much simplification of the problem as the remarkably intricate modulation of intensity within the diffuse planes can be only explained by the introduction of lateral order on adjacent hexagonal sites.

3.6.1 s-planes intensity modulation

The experiments were performed on the *n*-alkane⁄urea inclusions compounds at room temperature. The diffraction measurements were performed on beamline ID-23 at the ESRF synchrotron, which is equipped with a Pilatus 6M detector. The crystal orientations were determined with the program XDS, and the total scattering was reconstructed in reciprocal coordinates using the program MEERKAT.

The s layers of diffuse scattering were extracted and integrated along c^* . Layers until m = ±3 were extracted for n-octane and n-decane, while for n-nonane and n dodecane, layers were extracted until m = ±4. The background for each layer was estimated as the average of intensities slightly above and below the layer and was then subtracted. The adjusted layer intensities were averaged over 6/mmm Laue symmetry. Of the five crystals, n-undecane/urea was not pursued any further because the proximity of Bragg peaks to the third s-layer line at (3γ - l = 2) seriously complicated the extraction of reliable diffuse scattering data. Refinement of the diffuse scattering was performed with the program YELL [81]. Diffuse scattering extracted in (hk01) and (hk02) layers are reported on Figure 3-30.

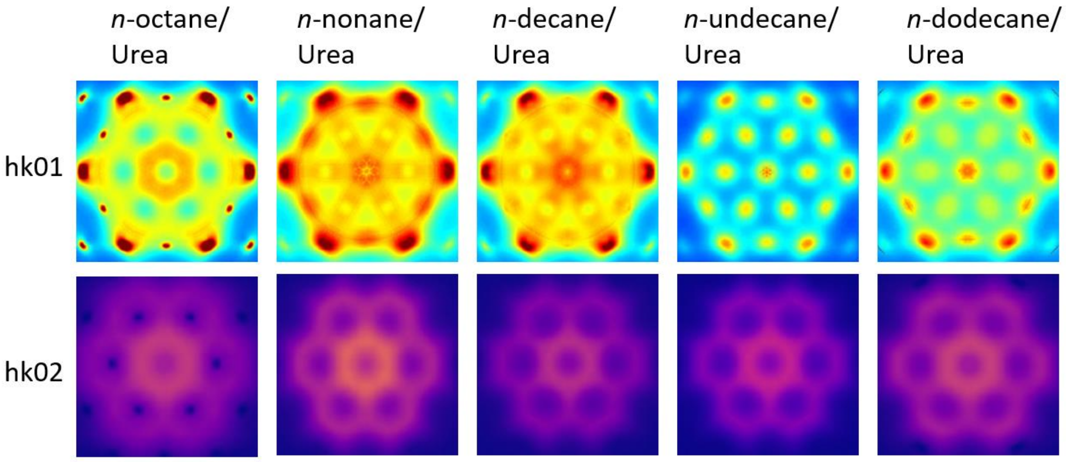

Figure 3-30 : diffuse scattering from the (*hk*01) and (*hk*02) *s* layers. The diffuse scattering is presented in a shape of hexagons or clouds centered at the position of Bragg peaks.

In the reconstructed "s" planes, the intensity in the "s" planes is not uniformly distributed; instead, these planes exhibit strong structuring. However, the absence of any discrete signature (Bragg peak) on these "s" planes is notable. Therefore, it can be concluded that there is no long-range correlation between the alkane chains of different channels (planes a, b). On the other hand, the structure of these planes indicates a strong correlation between the states of neighboring channel chains (pair correlations).

From the qualitative analysis of the diffuse scattering, we can say that fluctuations in the relative shift Δ between two alkanes in adjacent channel give rise to this hexagon-shaped diffraction patterns, with intensity being zero at positions corresponding to the nodes of the urea sub-lattice in the plane perpendicular to c*. Furthermore, the observed alternation of "holes/fills" between the first and second "s" planes can be explained by the introduction of negative correlation between nearest neighbors in the adjacent channels.

3.6.2 The 3D- ΔPDF analysis

The 3D-PDF maps were calculated with the Fourier transform of the intensities extracted from the diffuse scattering layers. The 3D-PDF map for n-dodecane/urea is illustrated in Figure 3-31, featuring signals categorized into three regions (refer to the insert). The first region (labeled 1) corresponds to the channel center, displaying periodic positive and negative signals along the channel axis. This suggests a nearly periodic arrangement of alkane molecules within a channel, in agreement with the quasi-liquid model [75,76]. Near the lattice points marked 3, correlations exhibit a similar positive-negative alternation along c, albeit with lower intensities, indicating correlations in positions between alkanes in neighboring channels. In the uv0 section, the flowerlike shape surrounding the central feature (marked 2) corresponds to interatomic vectors between alkanes and urea. This characteristic shape results from the relaxation of urea walls around alkane molecules, known as the size effect [77].

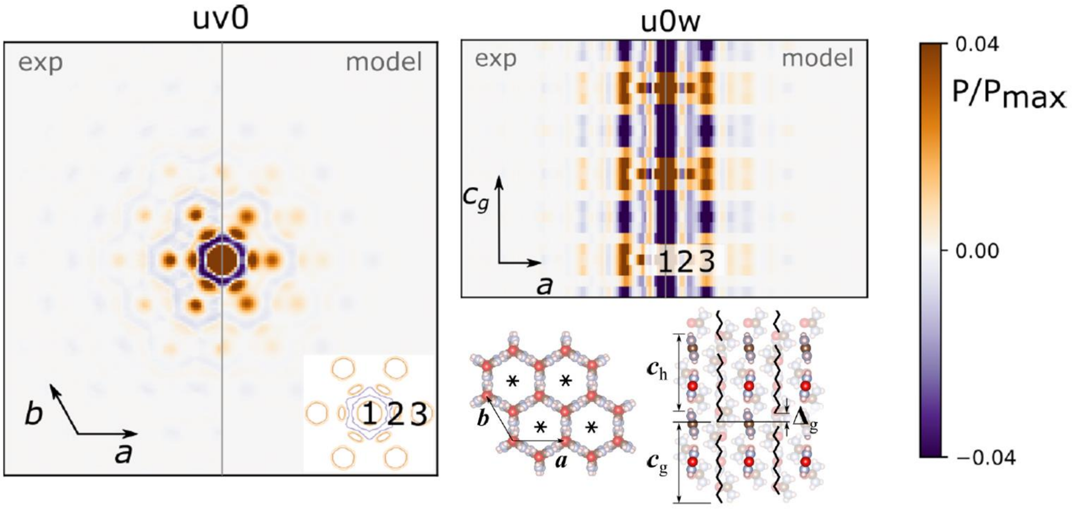

Figure 3-31 : Comparison between experiment and model 3D-ΔPDF map for *n*-dodecane⁄urea inclusion compound. The strongest contrast represents the correlation between alkane molecules within the same channel (1), relaxation of urea walls around the alkanes (2), and correlation between alkane molecules in the neighboring channels (3). The average crystal structure of urea inclusion compound is shown as reference.

The 3D-ΔPDF maps were utilized in the YELL program for fitting, employing least-squares minimization against experimental data. YELL currently operates in 3D space, and while it doesn't support higher-dimensional crystallographic formalism, it proved adequate for modelling sharp diffuse planes related to the guest substructure. The 3D-ΔPDF model, governed by the $P6_122$ symmetry of the host, consists of three parts:

Alkane Molecules within the Channels

The model assumes an all-anti conformation, represented by a zigzag chain, and incorporates rotational disorder with equal probabilities for six orientations. It lacks correlations between molecular orientations and focuses on s-diffuse scattering in (hk0m) layers. Experimental observations reveal the vanishing long-range order along channel directions, characterized by broadened s layers as already analyzed in chapter 3.2.4. The 3D-ΔPDF quasi-liquid model considers N intermolecular pairs, with joint displacement parameters determined by the distance between molecules along the channel axis. Three neighbors are sufficient to describe the experimental 3D-ΔPDF.

Urea wall relaxation

The 3D-ΔPDF maps reveal the relaxation of urea walls around alkane molecules. Modelling urea in this scenario is intricate due to the incommensurability of urea periodicity with that of alkane molecules. From the alkane substructure's perspective, urea walls exhibit continuous electron density in the c direction. The interaction between alkane and urea molecules is evident through the modulation of urea in the (a, b) plane, depending on the relative position of urea with respect to alkane molecules. The alkane-alkane interactions are likely mediated by the relaxation of urea molecules, exhibiting similarity across all investigated crystals. For instance, in the n-dodecane/urea crystal, oxygen atoms exhibit minimal displacement, while carbon and nitrogen atoms move away from alkane and toward the van der Waals gap between guest molecules within a channel, with an amplitude of ~0.3Å. A schematic representation of the relaxation of the Urea wall is presented in Figure 3-32 .

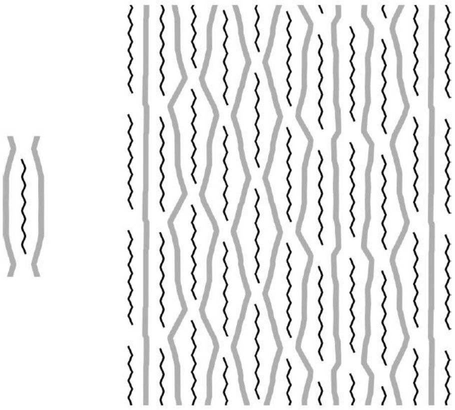

Figure 3-32 : The relaxation of urea walls (gray) in an *n*-dodecane⁄urea structure

Nearest neighbor interactions

In neighboring channels, alkane molecules exhibit a range of relative positions along the channel axis (Δ). The model utilizes discrete positions, determined by the limited resolution of diffuse scattering data along c∗. The refinement in 3D-ΔPDF enables the determination of the probability distribution p(Δ) for relative displacements of alkane molecules in neighboring channels (Figure 3-33). The analysis reveales only significant correlations for the first nearest neighbors.

The first region (I) is centered on zero shift, representing the minimum probability, except for n-dodecane, where it is a local minimum above the equipartition value. Two side regions are observed: the first one (II) corresponds to the maximum probability, and the other one (III) corresponds to a local minimum of probability as the molecule shift approaches 1/2. Despite being associated with the average value, the zero shift is not favored. A minimum shift is identified and associated with the observed relaxation of urea molecules previously described. Urea tends to relax in the gap formed by alkane molecules inside the channel. This relaxation correlates to the shift of the alkane molecules and is the mediator of the correlation between alkane in neighboring channels.

The challenge of understanding short-range order in quasiliquid phases is complex. The aperiodicity of the system allows for an infinite number of equivalent relative positions of the guest within the host, leading to a near-zero energy sliding mode along this aperiodic direction. The 3D-ΔPDF method was employed and we constructed a model where alkane molecules within channels form a quasi-liquid, positions of alkanes in neighboring channels are correlated with decreasing correlation over distance and urea walls relaxes by pushing away from alkane and into the gap between alkane molecules.

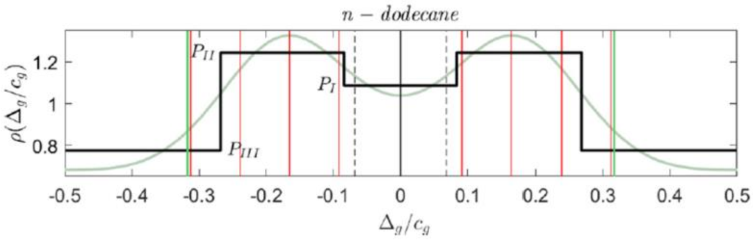

Figure 3-33 : density probabilities normalized to equipartition for *n*octane, *n*-nonane, *n*-dodecane, and *n* decane, as a function of the relative shift $\Delta \,/ c_g$ between alkane molecules from channel to channel.

3.7 CONCLUSION

Due to remarkable advancements in experimental capabilities at synchrotron facilities, particularly in beam flux and detector technologies, 3D-ΔPDF approaches are expected to become standard methods for addressing the investigation of correlated disorder in more complex systems [63,77,78,85–88].

In the case of MX chains, our study provides a method to identify and measure the key interaction responsible for the dimensionality and stability of the CDW that can help further progress of rational design [55,89,90]. We showed that the formation of large CDW domains is influenced by a strong 2D hydrogen-bonding network within ligand chains and counter anions. The choice of ingredients in chemical synthesis can modulate these interactions, impacting material properties like conductivity. Recent research has utilized multiple hydrogen bonds to enhance conductivity and form conductive chains [83,91,92]. The CDW dimensionality can be tailored by adjusting these interactions through quantitative disorder model refinement. As examples of sophisticated chemical synthesis, the incorporation of aromatic in-plane ligands leads to the stabilization of the 1D chain structure in Pt-based MX-Chains [92], the 2D hydrogen-bonding network gives the 2D-CDW in the study presented in this chapter [78,93,94], and the fastener effect acting between alkyl chains leads to a phase transition between 3D CDW and MH state [57,79].

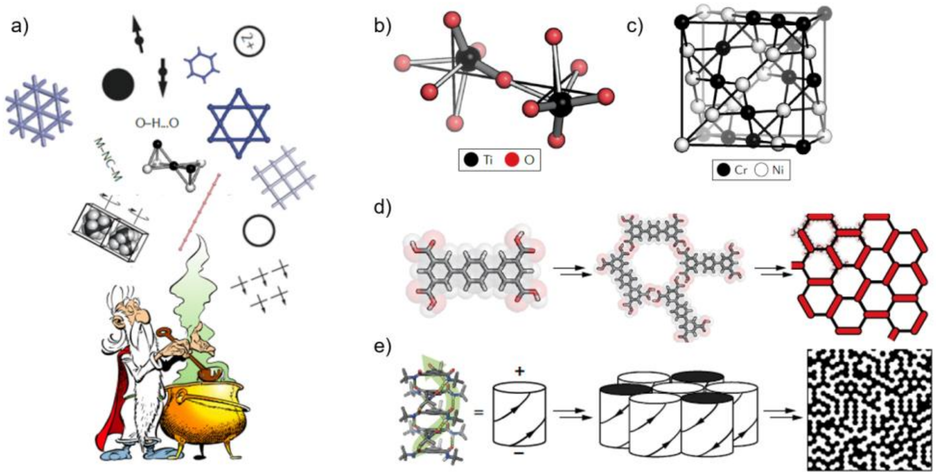

Figure 3-34 : (a) ingredients for preparing a good correlated disorder, correlated disorder from (b) electronic instabilities, (c) compositional complexity, (d-e) by self-assembly. (adapted from [48])

The fundamental ingredients of correlated disorder are based on three different aspects (Figure 3-34) : the relevant degrees of freedom (spin, charge, composition…), the interaction between those degrees of freedoms (ferro, antiferro, external field like pressure or light…) and the lattice where the interactions occur (triangle, hexagonal, Kagome…) [48]. One can take those ingredients and define strategies to design correlated disorder in order to tune the properties of the material. Such design can be based on electronic instabilities like in $LaMnO_3$ manganite perovskite, compositional complexity like in alloys or perovskites or through self-assembly using directional hydrogen bond network for example. Ultimately, the objective and challenge is to master and harness correlated disorder intentionally. This signifies a shift from merely understanding disorder's role in producing interesting physical properties to using it as a deliberate design element for engineering materials with innovative functionalities.

Essentials of Crystallography of Photoinduced Phases

Strong light causes materials to absorb energy, which in turn excites electrons and creates extremely non-equilibrium states. A series of processes, such as modifications to the electrical configurations, crystal structure, or even the formation of novel collective behaviors, can be driven by these excited states: this is the photoinduced phase transition (PIPT). Because light can alter the crystal structure with subsequent changes in the crystal lattice, time resolved X-ray diffraction allows us to probe these changes in real-time, offering a glimpse into the dynamic processes unfolding at the atomic scale.

BASIC CRYSTALLOGRAPHY OF PHOTOINDUCED PHASE TRANSITION

The LIESST effect, or Light-Induced Excited Spin State Trapping, is a phenomenon observed in certain spin transition compounds, particularly transition metal complexes or coordination compounds. These materials undergo a reversible change in their electronic spin state when exposed to light, leading to significant alterations of the structure. At low temperature, in most spin crossover compounds, the photoinduced state is photosteady. It is therefore possible to make a full data collection under light irradiation in order to solve the structure of the photoinduced phase. This technique is referred as **photocrystallography.** It can be implemented on laboratory diffractometer or at synchrotron and necessitate diode lasers at different wavelength and nitrogen or helium jet cryostat. At the Institut de Physique de Rennes, our PhD students are working on a new setup with a helium cryostat in order to perform photocrystallography at low(er) cost.

At 10 K, a single crystal of $[Fe(pic)_3]Cl_2EtOH$ was continuously irradiated in order to convert the crystal, of about 150 mm thick, from the LS state to the photoinduced HS state and a full data collection was performed. Fast and partial data collections were performed during the irradiation of the sample, allowing one to measure the intensity of some Bragg reflections but also to extract the value of the lattice parameters, with a time resolution of about 5 min. (figure 0-1)

Structure determination of the PIP:

An important signature characteristic of the spin phase transition is the change in the average (Fe-N) iron-nitrogen bond length from 2.190 Å in the HS state to 2.015 Å in the LS state. In the photoinduced state, an increase of the bond length (Fe-N) = 2.197 Å similar to the HS state is observed in relation to the switching to the HS state, in addition to the increase of the volume of the unit cell.

Shape of the peaks: A splitting of the Bragg reflections occurs during the excitation and the relaxation, indicating the coexistence of macroscopically excited HS domains and relaxed LS ones. This is a direct signature of the nucleation mechanism and the coexistence of the two phases at mesoscopic scale.

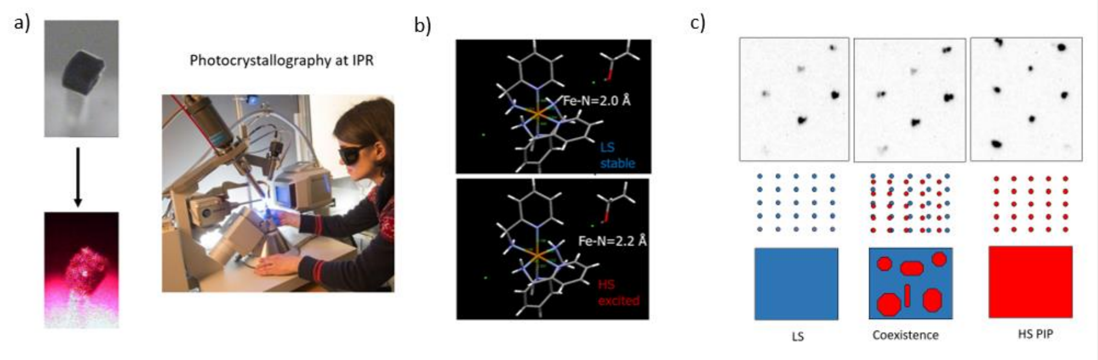

Figure 0-1: (a) photocrystallography Institut de Physique de Rennes (b) structure of the LS and the photoinduced HS.(c) diffraction pattern before, during and after laser irradiation showing the coexistence of HS photoinduced and LS mesoscopic domains.

Basic crystallography concepts can be employed to study the structure and the dynamics of the PIPT. It turns out that using pulsed laser pulse, it is possible to induce very fast change of the spin state and by following the diffraction pattern with a 100ps resolution, it is possible to understand the dynamics of the transformation from transformation of individual molecules to complete and macroscopic change of the phase. For this, we need time resolved techniques.

TIME RESOLVED DIFFRACTION TECHNIQUES

Time-resolved diffraction at synchrotrons or X-ray Free Electrons (XFEL) is an advanced technique that reveals ultrafast structural changes in materials. Using a pump-probe setup, this technique uses X-rays pulse as probe to record the changing structure at different time delays, while a pulsed laser starts (pump) the dynamic process. At each delay between the pump laser pulse and the probe X-ray pulse, a full data collection is realized. The structure is then solved for each delay, meaning that one can observe in the real space how atoms are moving after a laser excitation function of time.

CURRENT AND FUTURE ADVANCES IN CRYSTALLOGRAPHY FOR INVESTIGATING PIPT

The main problem of pump-probe studies is to ensure that the pumped volume is being probed. For molecular crystals, the laser penetration depth is often only a few microns, and for more correlated materials, it can even be below 100 nm due to the absorption coefficient at the pump wavelengths. To circumvent this problem, people in this field work with tiny crystals, nanocrystals.

The grazing incidence technique

To address the limitation of penetration depth, we developed a small grazing incidence experiment. Utilizing X-rays in total reflection becomes feasible due to the fact that the index of refraction of X-rays in matter is smaller than 1, allowing for the X-ray wave to probe only the skin depth (a few nanometers). We employed this technique at the SwissXFEL on nanocrystals of Ti_3O_5 provided by collaborators Shin-Ichi Ohkoshi and Hiroko Tokoro from the University of Tokyo and the University of Tsukuba. The quality of the TR data was remarkable and we could show that a transition from a β stable semiconductor phase and to a λ metallic photoinduced phase was occurring at the picosecond time scale. (figure 0-2)

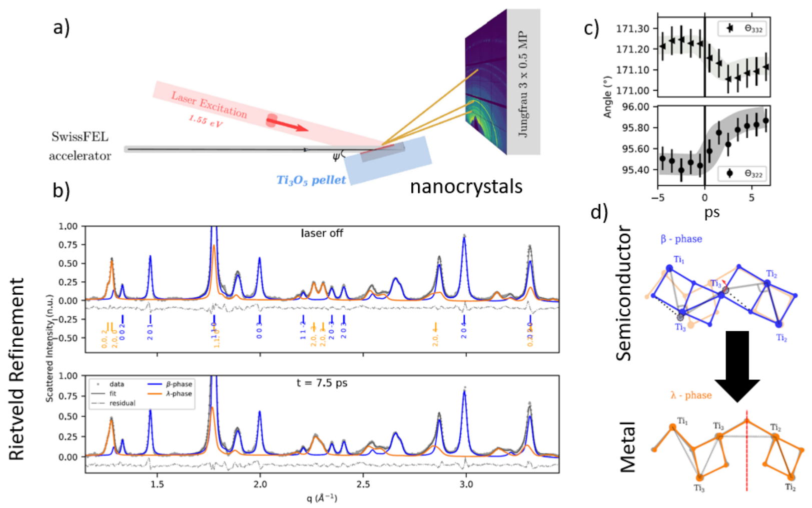

Figure 0-2 : (a) schematic drawing of the grazing incident technique at SwissFEL, (b) Rietveld refinement before and after laser excitation. (c) structural parameter function of the delay. (d) structure of the β stable phase and λ photoinduced phase.

The streaming crystallography and serial crystallography

A solution containing the crystallized samples is pressurized and forced through a fine nozzle to form a liquid jet. In streaming of serial crystallography experiments, a key component is the delivery system, often referred to as the "jet." This delivery system is responsible for transporting a stream of tiny crystals into the path of the X-ray beam for individual diffraction measurements.

In streaming crystallography, the continuous liquid jet is intersected by the X-ray beam of an hundred micron size. In this volume of interaction, hundreds of nanocrystal interact with the X-ray beam producing a powder pattern. My colleagues of Rennes developed this technique at ESRF and we recently employed it on Prussian blue analogues (PBA) nanocrystals. The transformation from a tetragonal low spin phase to a permanent high spin phase in the hysteresis were followed looking at the shift of powder rings in the Q direction allowing the analysis of the cell parameters and space group function of time at ESRF

In serial crystallography, the nozzle size is adjusted to produce a stream of tiny droplets, and within each droplet, there may be one or more crystals producing a diffraction pattern consisting of Bragg peaks from one or more crystals. E.A Schriber and al, developed a method of analysis called small-molecule serial femtosecond X-ray crystallography (smSFX) for the determination of material crystal structures from microcrystals. They indexed the sparse serial patterns by a graph theory approach and the resulting datasets was solved and refined using standard tools for single-crystal diffraction.

TR Electron diffraction

Time-resolved electron diffraction typically utilizes a pulsed electron source, such as a femtosecond laser-driven photocathode or a radiofrequency (RF) gun. The pulsed nature of the electron source allows for extremely short electron pulses, essential for capturing ultrafast processes typically on the order of femtoseconds to picoseconds.

DIFFRACTION PATTERN ANALYSIS TO STUDY THE PIPT

We can use the analysis of the diffraction pattern to characterize the structure of the photoinduced phase:

$[Fe^{II}H_2L^{2-Me}][SbF_6]_2$ spin crossover material shows a unique type of ordering phenomenon associated with the incommensurate occupational modulation of its bistable spin molecules. This occupational modulation is accompanied with a spatial modulation of the high-spin (HS) fraction γ_{HS}. Using the superspace crystallography and looking at the diffraction pattern, one can describe the concentration of high-spin (HS) molecules (γ_{HS}) and its incommensurate order.

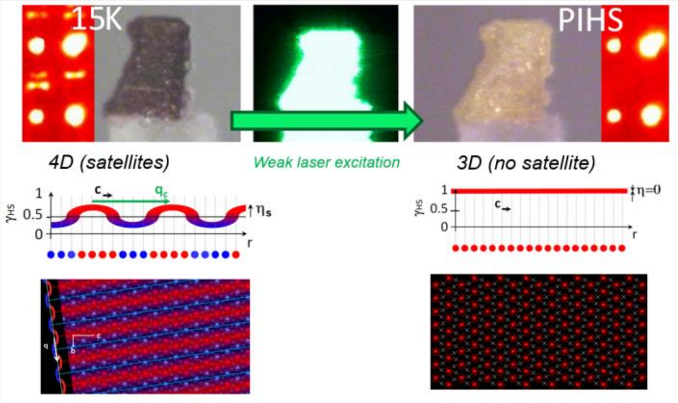

Figure 0-3 : (left) crystal at low temperature and its diffraction pattern showing satellite Bragg peaks. The incommensurate spin wave along the incommensurate **q** vector and a cut of the superspace. (right) crystal after laser irradiation and its diffraction pattern showing no satellites. HS for any position along the incommensurate **q** vector and the 3D HS photoinduced structure.

The crystal undergoes a transition from a four- to three-dimensional periodic structure when exposed to weak laser irradiation at 532 nm (Figure 4-17 0-3). This transition is associated with a change in the crystal color and the disappearance of satellite reflections and therefore the disappearance of the incommensurate modulation.

This type of analysis becomes standard to study PIPT and we employed this method on many different type of materials from organic crystal to inorganic semiconductors. (see list of references at the end of this chapter).

DIFFUSE SCATTERING ANALYSIS TO STUDY THE DYNAMICS OF PIPT

Precursor phenomena refer to phenomena that occur in a material before the photoinduced phase transition occurs after the absorption of light. The study of these precursor effects provide insights into the early stages of the dynamic process leading to the phase transition. Understanding precursor phenomena is crucial for unravelling the mechanisms and dynamics associated with photoinduced phase transitions.

We investigated the precursors of a photoinduced phase transition in the highly cooperative charge-transfer molecular crystal tetrathiafulvalene chloranil (TTF-CA). (figure 0-3) After laser irradiation, a diffuse plane perpendicular to the stacking axis a is revealed in the differential signal. This is the direct signature of the 1D nature of precursor phenomena of the photoinduced transition of TTF-CA. Laser irradiation generates at the first stage (500-fs–1-ps) I strings. It results in a quasi-instantaneous increase of the diffuse scattering (observation limited here by the 50-ps resolution). The 3D ordering of the (D+A-) dimers occurs only at the second stage (within 500 ps), and the establishment of the 3D long-range structural order is associated with the intensity change of the Bragg reflections.

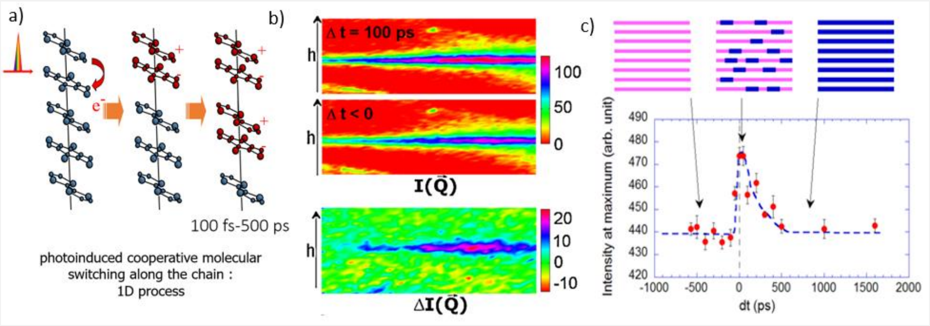

Figure 0-4 (a) photoinduced 1D ionic strings. (b) diffuse scattering before/after laser irradiation and their difference. (c) evolution of the diffuse scattering intensity function of time.

The analysis of diffuse scattering can be used to study the formation of charge density waves, the creation of defects or the generation of polarons induced by light.

TR SEGMENTED SCATTERING METHOD: A PROOF OF CONCEPT

What would be the ideal TR diffraction experiment?

It would be an experiment that allows us to follow the structure at any timescale and any length scale, a technique that could not only follow the movement of atoms in the photoinduced phase at any time but also follow the local correlations at the origin of the generation of the PIP with time. Because in single crystal, local and global structure have a different scattering signature, i.e diffuse scattering and Bragg, the technique could be separated into two techniques: the TR-segmented scattering method.

The experiment consists of calculating the total scattering pattern for the different steps of a transformation similar to Peierls mechanism induced by light using the theory developed in chapter 1 and 3. The total scattering is then segmented into two contributions: the diffuse scattering pattern and the Bragg peaks pattern. The two patterns are analyzed individually using the 2D-ΔPDF and diffraction analysis method.(figure 0-4)

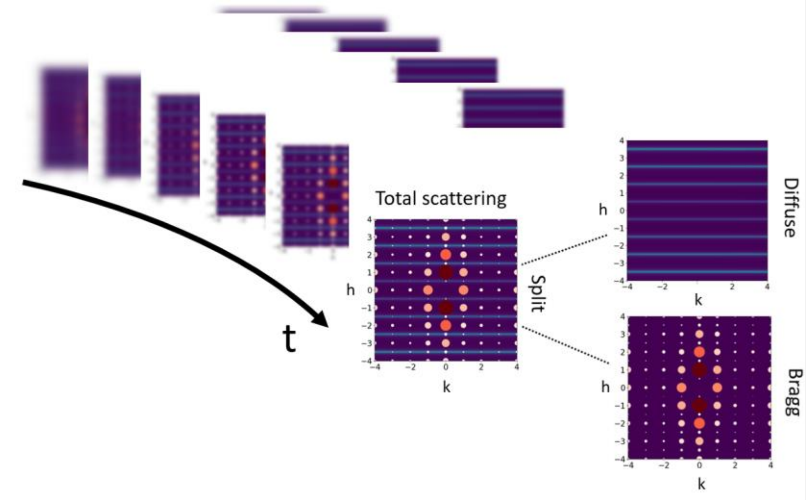

Figure 0-5 : The TR-segmented scattering method. For each time during the transformation, a total scattering pattern is collected and the 2d scattering pattern is split into two: a diffuse scattering pattern and Bragg peaks that are analyzed individually.

The 2D-ΔPDF method

The diffuse scattering shows the typical feature of a 1D correlated disorder along a axis with negative correlation: diffuse lines perpendicular to a* at half integer position indicating an anti-ferro type correlation.

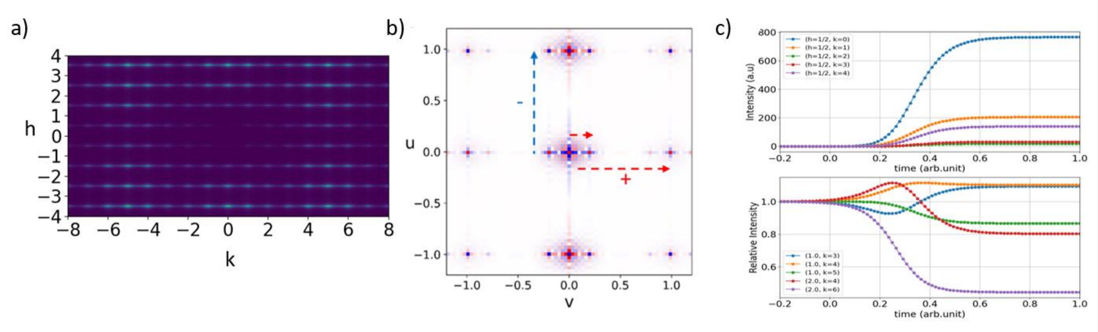

Figure 0-6 : (a) the diffuse scattering pattern and (b) the associated 2D-ΔPDF map (c) Evolution of the superstructure Bragg peaks intensity and structure Bragg peaks function of the time.

Fourier transform of the diffuse scattering gives the 2D-ΔPDF. A Negative correlation between atoms at (0,0) and (0,1) is clearly seen with the typical Mexican hat profile. It is associated to a local dimerization mechanism.

The diffraction method

One can follow with time the intensity of Bragg peaks in order to track some change of symetry (if any) and the structural reorganization. As already discussed in the chapter 1, the change of the intensity of the superstructure Bragg peaks measures the evolution of the order parameter during the transformation, which is in this case the displacement parameter corresponding to the dimerization. Before the transformation, the superstructure intensities are null and increase to reach a plateau when the transformation to the photoinduced phase is complete. The structure Bragg peaks shows a different evolution with time, some decreasing in intensity and some increasing in intensity. This is due to the change of the structure of the molecule during the transformation.

The use of diffraction and generally the analysis of the scattering pattern allows to get insight of the transformation of a material at the relevant time and length scale. The limitation due to the finite penetration depth of the laser requires the use of micro-crystal or nanocrystals. Scientists all over the world are now developing experimental techniques at synchrotron or XFEL to study a large collection of crystals with streaming crystallography or the analysis of shot to shot crystal structure with serial crystallography. In the future, one can dream of collecting the total scattering pattern and its evolution function of the time of the transformation.

The chapter 4 is based on the following papers :

Laurent Guérin*, Elzbieta Trzop, Tadahiko Ishikawa, Shinya Koshihara ,Takashi Yamamoto, Bertrand Toudic, Reizo Kato*, Frustrated competitive forces in the $Et_2Me_2Sb[Pd(dmit)_2]_2$ molecular conductor, **Physical Review B** 108, 134104 (2023).

Céline Mariette, Maciej Lorenc, Hervé Cailleau, Eric Collet, **Laurent Guérin**, et al.. Strain wave pathway to semiconductor-to-metal transition revealed by time-resolved X-ray powder diffraction. ***Nature Communications***, 12 (1), pp.1239. (2021)

Eric Collet, Maciej Lorenc, Marco Cammarata, **Laurent Guérin**, Marina Servol, et al.. 100 picosecond diffraction catches structural transients of laser-pulse triggered switching in a spin-crossover crystal.. ***Chemistry - A European Journal***, 2012, 18 (7), pp.2051-5.

Laurent Guérin, Qingyu Kong, Dmitry Khakhulin, Marco Cammarata, Hyotcherl Ihee, et al.. Tracking Atomic Positions in Molecular Reactions by Picosecond X-ray Scattering at the ESRF. ***Synchrotron Radiation News***, 2012, 25 (2), pp.25-31.

Laurent Guérin, Johan Hébert, Marylise Buron-Le Cointe, Shin-Ichi Adachi, Shin-Ya Koshihara, et al.. Capturing One-Dimensional Precursors of a Photoinduced Transformation in a Material. ***Physical Review Letters***, 2010, 105, pp.246101.

Shunsuke Nozawa, Shin-Ichi Adachi, Jun-Ichi Takahashi, Ryoko Tazaki, **Laurent Guérin**, et al.. Developing 100 ps-resolved X-ray structural analysis capabilities on beamline NW14A at the Photon Factory Advanced Ring. ***Journal of Synchrotron Radiation***, 2007, 14 (Pt 4), pp.313-9.

N. Huby, **L. Guérin**, E. Collet, L. Toupet, J.-C. Ameline, H. Cailleau, T. Roisnel, T. Tayagaki, and K. Tanaka, Photoinduced Spin Transition Probed by X-Ray Diffraction, ***Phys. Rev. B*** 69, (2004).

Concepts presented in the chapter 4 were used in the following works :

K. H. Kim, J. Kim, K. Y. Oang, J. H. Lee, D. Grolimund, C. J. Milne, T. J. Penfold, S. L. Johnson, A. Galler, T. W. Kim, J. G. Kim, D. Suh, J. Moon, J. Kim, K. Hong, **L. Guérin**, T. K. Kim, M. Wulff, C. Bressler, and H. Ihee, Identifying the Major Intermediate Species by Combining Time-Resolved X-Ray Solution Scattering and X-Ray Absorption Spectroscopy, **Phys. Chem. Chem. Phys**. 17, 23298 (2015).

J. H. Lee, M. Wulff, S. Bratos, J. Petersen, **L. Guerin**, J.-C. Leicknam, M. Cammarata, Q. Kong, J. Kim, K. B. Møller, and H. Ihee, Filming the Birth of Molecules and Accompanying Solvent Rearrangement, ***J. Am. Chem. Soc.*** 135, 3255 (2013)

H. Shimizu, M. Iwamoto, T. Konno, A. Royant, S. Von David, **L. Guérin**, M. Wulff, and S. Oiki, Laser-Triggered Single Molecular Gating Motions of the KcsA Potassium Channels Recorded in a Sub-Millisecond Time Resolution, ***Biophysical Journal*** 102, 37a (2012).

K. Haldrup, T. Harlang, M. Christensen, A. Dohn, T. B. van Driel, K. S. Kjær, N. Harrit, J. Vibenholt, **L. Guérin**, M. Wulff, and M. M. Nielsen, Bond Shortening (1.4 Å) in the Singlet and Triplet Excited States of [Ir2(Dimen)4]2+ in Solution Determined by Time-Resolved X-Ray Scattering, ***Inorg. Chem***. 50, 9329 (2011).

Nüske, A. Jurgilaitis, H. Enquist, S. D. Farahani, J. Gaudin, **L. Guérin**, M. Harb, C. v. K. Schmising, M. Störmer, M. Wulff, and J. Larsson, Picosecond Time-Resolved x-Ray Refectivity of a Laser-Heated Amorphous Carbon Film, ***Appl. Phys. Lett.*** 98, 101909 (2011).

J. Gaudin, B. Keitel, A. Jurgilaitis, R. Nüske, **L. Guérin**, J. Larsson, K. Mann, B. Schäfer, K. Tiedtke, A. Trapp, Th. Tschentscher, F. Yang, M. Wulff, H. Sinn, and B. Flöter, Time-Resolved Investigation of Nanometer Scale Deformations Induced by a High Flux x-Ray Beam*,* ***Opt. Express*** 19, 15516 (2011).

H. Ichikawa, S. Nozawa, T. Sato, A. Tomita, K. Ichiyanagi, M. Chollet, **L. Guérin**, N. Dean, A. Cavalleri, S. Adachi, T. Arima, H. Sawa, Y. Ogimoto, M. Nakamura, R. Tamaki, K. Miyano, and S. Koshihara, Transient Photoinduced ‘Hidden’ Phase in a Manganite, ***Nature Material*** 10, 101 (2011)

Hervé Cailleau, Maciej Lorenc, **Laurent Guérin**, Marina Servol, Eric Collet, et al.. Structural dynamics of photoinduced molecular switching in the solid state.. ***Acta Crystallographica Section A Foundations of Crystallography***, 2010, 66 (Pt 2), pp.189-97.

O. Mariager, D. Khakhulin, H. T. Lemke, K. S. Kjær, **L. Guérin**, L. Nuccio, C. B. Sørensen, M. M. Nielsen, and R. Feidenhans’l, Direct Observation of Acoustic Oscillations in InAs Nanowires, ***Nano Lett.*** 10, 2461 (2010)

M. Chollet, **L. Guérin**, N. Uchida, S. Fukaya, H. Shimoda, T. Ishikawa, K. Matsuda, T. Hasegawa, A. Ota, H. Yamochi, G. Saito, R. Tazaki, S. Adachi, and S. Koshihara, Gigantic Photoresponse in ¼-Filled-Band Organic Salt $(EDO\text{-}TTF)_2PF_6$, ***Science*** 307, 86 (2005).

Chapter 4: Crystallography of Photoinduced Phases

Photoinduced phase transition describes a fascinating phenomenon in which a material undergoes a phase transition caused by the irradiation of light, usually in the form of strong illumination or laser pulses. The complex interaction of a material's structural, electrical, and thermal dynamics is what drives photoinduced phase transition. Strong light causes materials to absorb energy, which in turn excites electrons and creates extremely non-equilibrium states. A series of processes, such as modifications to the electrical configurations, crystal structure, or even the formation of novel collective behaviors, can be driven by these excited states.

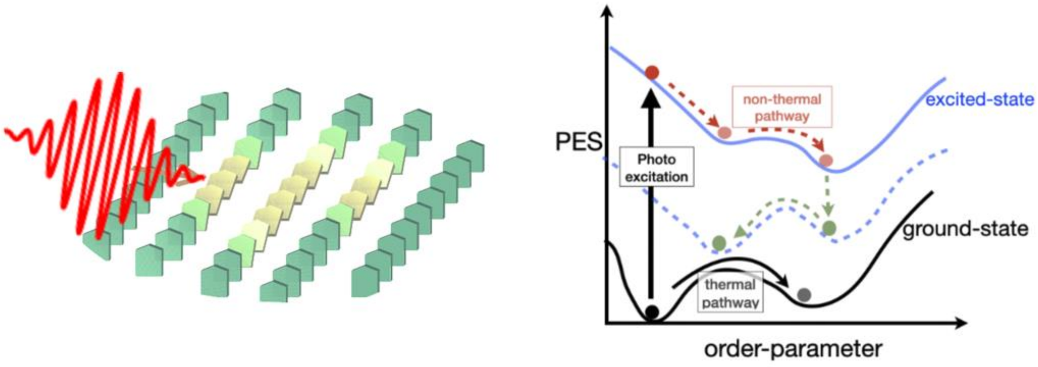

Figure 4-1 : (left) the domino effect, (right) simple schematic drawing of the photoinduced phase transition mechanism (from).

When a photon excites an insulating crystal, an electron induces a local distortion of the lattice around it. This well-known phenomenon is called lattice relaxation of an optical excitation, and the resulting state is often referred to as a photoinduced structural change. This relaxation phenomenon has been extensively studied in various types of insulators over the past 50 years. According to the original concepts of lattice relaxation, it is commonly accepted that this effect is microscopic and involves only a few electrons and atoms. Recently, several unconventional photoactive solids have been discovered. The relaxation of photo-excited states in these systems is strongly correlated with various collective movements involving a large number of atoms and electrons. Such process where one photon can convert multiple molecules and drives collective response of the material trough cooperative effects is named the domino effect by Pr. S. Koshihara. (Figure 4-1). [97] In some cases, it leads to a macroscopic-scale excited domain exhibiting a new electronic and structural order. This phenomenon is commonly referred to as a photoinduced phase transition (PIPT).

Professor K. Nasu was one of the first theoretician to come up with a simple model (Figure 4-1) [98]: in the case of cooperative molecular materials, the absorption of a photon can generate an excited electronic state (Franck-Condon) that is trapped at the molecular level by the structural relaxation of the molecule (conformational change, etc.) with dynamics specific to the molecular dynamics (100 fs- 1ps). In cooperative system, the system follows a non-thermal pathway where interactions between excited molecules induce a new phase (usually defined by an order parameter). The PIP characterized by its new macroscopic structure and electronic state can be the same as the one reached following the thermal pathway or can be different. In such case, the PIP is commonly referred as hidden phase. When collective effects predominate, delocalized electronic excitations due to an ultrashort laser pulse can destabilize the lattice and induce coherent atomic movements (aka coherent phonons) that can lead to a new phase on an ultra-fast time scale (a few hundred femtoseconds to a few picoseconds). Compared to coherent optical phonons observed in many conventional semiconductors, cooperative effects here lead to structural instability, with the control parameter being the photon density absorbed per pulse.

The PIPT involve different length scale and timescale (Figure 4-2). The initial excitation of the molecule or phonon at the femtosecond time scale, is followed by cooperative precursor phenomena associated with the formation of correlated objects at the nanoscopic scale. Photoinduced domains are formed typically on the scale of 100 picoseconds, corresponding to the propagation of acoustic phonons. PIPT can also occur between photo-stationary states, and the lifetime of the metastable state can range from minutes to hours; this is the case, for example, in photoinduced phase transitions in spin transition systems.

One famous example of PIPT occurs in strongly correlated electron materials, where electronic interactions are critical. Manganites have been well explored in this regard [99], they have interesting properties like charge ordering and massive magnetoresistance, and they can undergo reversible transitions between various electronic and magnetic states when exposed to light pulses.

Usually, it takes sophisticated experimental methods, such as pump-probe spectroscopy and femtosecond time-resolved measurements, to investigate the nature and the kinetics of photoinduced phase transitions. With the use of these techniques, one can monitor the material's properties on incredibly short durations, giving vital information about the underlying mechanisms driving the transformation.

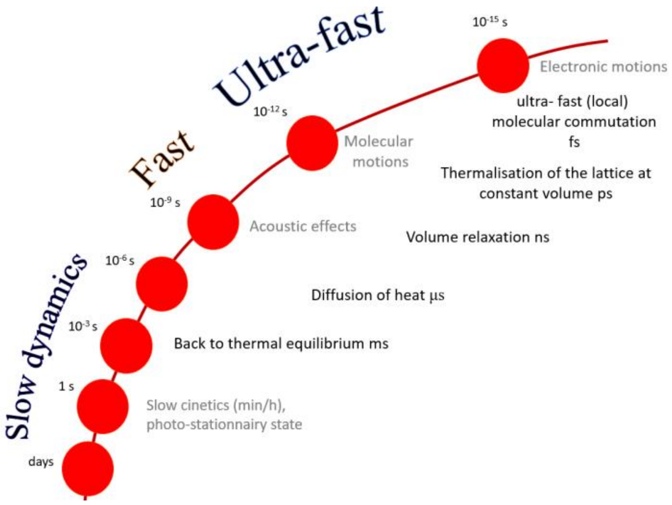

Figure 4-2 : timescales of photo induced processes (adapted from presentation of E.Collet)

Because light can alter the crystal structure with subsequent changes in the crystal lattice, time resolved X-ray diffraction allows us to probe these changes in real-time, offering a glimpse into the dynamic processes unfolding at the atomic scale. This capability is crucial for understanding how photoinduced phase transitions occur, including the generation, propagation, and relaxation of these transitions. The aim of this chapter is to present some application and some advances in crystallography to analyze PIPT. The idea is to use all the different crystallography concepts that we know from the first three chapters to the investigation of the structure of the photoinduced process : basic crystallography like space group analysis can be used to understand group/subgroup relationships, diffuse scattering analysis to understand the origin of the correlation of the nanoscopic photogenerated domains preceding the establishment of the macroscopic PI phase, superspace formalism because light can erase or even create aperiodic order. I will also present the technical part of the time resolved diffraction as I have dedicated 5 years of my scientific career as postdoc at the photon factory in Japan and ESRF in France to develop those extremely complicated experiments. In the meantime, I will present my previous, current and future works on the subject so that this final chapter can be seen as my research project for the next few years.

4.1 BASIC CRYSTALLOGRAPHY OF PHOTOINDUCED PHASE TRANSITION

Ideally, we would like to know what happens at the molecular level with an atomic resolution, what are the precursor phenomena, what is the relaxation process and what is the transformation pathway. Crystallography is suitable for this tasks. It is hard to refer the basic crystallography to the study of the modification of the structure under laser irradiation as the application of light on the material induces very intricate, in time and scale, phenomena. By basic, I mean here all the different concepts we studied in the first chapter. Remember that X-ray diffraction is a wonderful tool to study phase transition at thermal equilibrium, as it can probe symmetry change, structural reorganization, coexistence of phases or pretransitionnal phenomena. It shouldn’t be that different for the study of PIPT. To showcase this, let’s look at the spin transition. It is simple phenomenon, a prototype of bistability with a very large change of structure.

4.1.1 Photoinduced spin transition to a photosteady state

The LIESST effect, or Light-Induced Excited Spin State Trapping, is a phenomenon observed in certain spin transition compounds, particularly transition metal complexes or coordination compounds. [7] These materials undergo a reversible change in their electronic spin state when exposed to light, leading to significant alterations of the structure. Usually, the situation starts with a spin transition compound in the low-spin state. The material absorbs photons in response to a particular wavelength of light, usually in the visible or near-infrared range, which causes electronic excitations. The metal ions may be promoted by these excited electrons from a low-spin state to a higher energy state, usually the high-spin state. As we’ve seen in 1.5, this spin transition is associated to change at the molecular level of the metal-ligand distance.

At low temperature, in most spin crossover compounds, the photoinduced state is photosteady. It is therefore possible to make a full data collection under light irradiation in order to solve the structure of the photoinduced phase. This technique is referred as **photocrystallography** (Figure 4-3). [100] It can be implemented on laboratory diffractometer or at synchrotron and necessitate diode lasers at different wavelength and nitrogen or helium jet cryostat. At the Institut de Physique de Rennes, our PhD students are working on a new setup with a helium cryostat in order to perform photocrystallography at low(er) cost. Photocrystallography experiments on Ni-W cyano-bridged bimetallic crystals will be perform in the first semester of 2024 in the frame of the PhD of Maryam Alashoor.

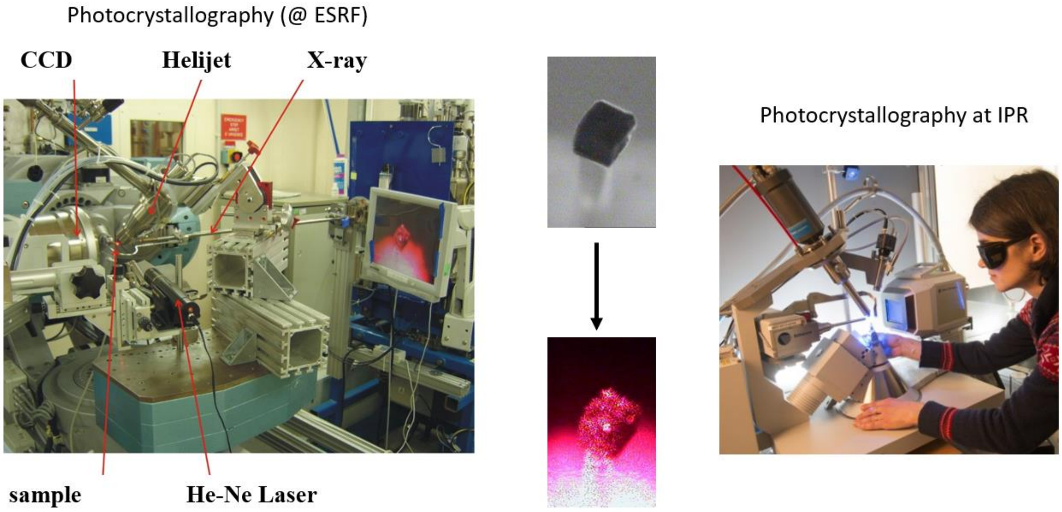

Figure 4-3 : photocrystallography setup at ESRF and Institut de Physique de Rennes (credit : CNRS image)

At 10 K, a single crystal of $[Fe(pic)_3]Cl_2EtOH$ was continuously irradiated in order to convert the crystal, of about 150 mm thick, from the LS state to the photoinduced HS state and a full data collection was performed [11]. Fast and partial data collections were performed during the irradiation of the sample, allowing one to measure the intensity of some Bragg reflections but also to extract the value of the lattice parameters, with a time resolution of about 5 min.

Structure determination of the PIP :

Because it is possible to make a full data collection under light irradiation, we could solve the structure of the PIP. An important signature characteristic of the spin phase transition is the change in the average (Fe-N) iron-nitrogen bond length from 2.190 Å in the HS state to 2.015 Å in the LS state. In the photoinduced state, an increase of the bond length (Fe-N) = 2.197 Å similar to the HS state is observed in relation to the switching to the HS state, in addition to the increase of the volume of the unit cell (Figure 4-4). The ligand structure of the photoinduced phase is similar to the one of the high temperature HS phase and, as the space group is conserved, no symmetry lowering is observed. Therefore the photoinduced HS phase is similar to the HS one at thermal equilibrium both for the volume and the molecular structure.

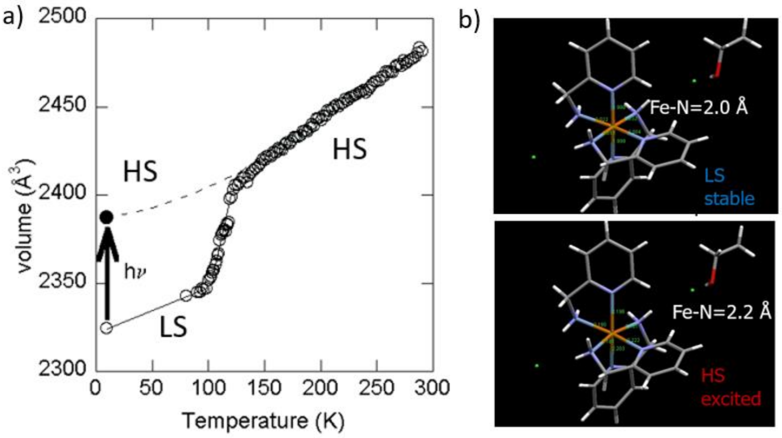

Figure 4-4 : (a) unit cell volume with temperature. The arrow indicates the transition to the photo-stationary state. (b) structure of the LS and the photoinduced HS.

Evolution of the diffraction pattern

In order to follow the dynamic of the phase transition, one can look directly at the evolution of the diffraction during the transformation or the relaxation.

Changes of the positions of the peaks : The average lattice expansion starts a few minutes after the beginning of the laser irradiation. The lattice parameters a, b, c, and β in the P21 /c space group shift respectively, in about 1 h, from 10.723 Å, 21.510 Å, 11.324 Å and 117.14 ° to 10.949 Å, 21.852 Å, 11.378 Å, and 118.71°. The volume of the unit cell therefore increases under light irradiation from 2324 to 2388 $Å^3$ that is of 2.8%.

Changes of the intensities : Important changes in the Bragg reflection intensities are observed some are decreasing but some are increasing, which is characteristic of a structural reorganization at the molecular level and not of light-induced disordering phenomena which only lower the intensities. All these changes occur on the same time scale, and after 1 h of irradiation the transformation is completed.

Shape of the peaks : As shown in Figure 4-5, there is an evolution of the diffraction pattern between the photostationary excited HS state and the LS one. A splitting of the Bragg reflections occurs during the excitation and the relaxation, indicating the coexistence of macroscopically excited HS domains and relaxed LS ones. Because of the significant difference in the lattice parameters, the position of the Bragg reflections are modified in the diffraction pattern between HS and LS states, and the coexistence of the two phases is associated with the coexistence of the peaks. This is a direct signature of the nucleation mechanism and the coexistence of the two phases at mesoscopic scale.

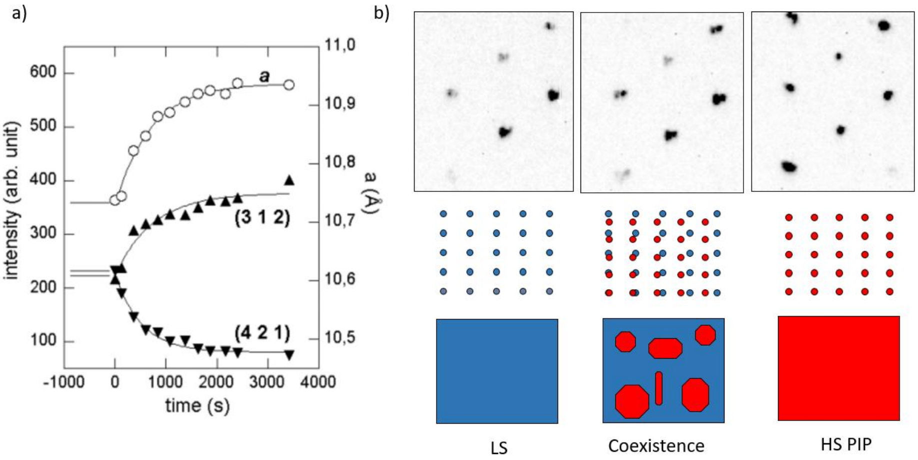

Figure 4-5 : : (a) evolution of the lattice parameter and intensities of two different Bragg peaks during laser irradiation. (b) diffraction pattern before, during and after laser irradiation showing the coexistence of HS photoinduced and LS mesoscopic domains.

These are interesting results because it shows one can get meaningful information on the nature and the dynamics of phase transition without having to solve the structure of the photoinduced phase. As we will see, this will be of very importance.

4.1.2 Things can go faster

The material is little bit different, it is a single crystal of (TPA)Fe (TCC)]PF$_6$ and the experiment quite a lot as we are now looking at the results of a time-resolved diffraction experiment at the beamline ID09B of ESRF. [101] I was postdoc at that time and I was collaborating with my old friends from Rennes. As we can see in the Figure 4-6, the results are sensibly the same as the photocrystallography presented before except that the time scale is no more the minutes or hour. We are looking at the evolution of structure and diffraction pattern at the time scale of the 100 picoseconds. For now, we are avoiding the question of how can we track this change at such fast time scale and just analyze the results.

(TPA)Fe (TCC)]PF_6 is spin crossover system showing a gradual transition from HS at high temperature to a LS state at low temperature centered at $T_{1/2}$=203 K. The experiment consists of exciting a single crystal with a 100 fs laser (λ=800 nm) and probing it with 100 ps X-ray pulses at different delays. The experiment was performed at 160 K where the majority of molecules are in LS state, and the crystal recovers equilibrium in the ms range.

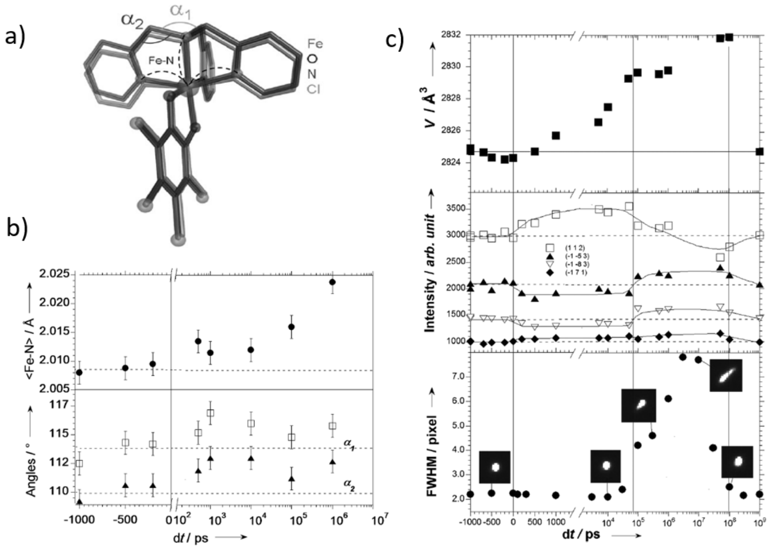

Figure 4-6 : (a) structure of the LS and HS state showing the change of Fe-N bond length and change of the angle in the ligand. (b) evolution of the angle and Fe-N bond length function of time after laser pulse excitation. (c) evolution of the volume of the unit cell, intensities and width of selected Bragg peaks function of time after laser pulse excitation.

Structure determination of the PIP :

The time-dependent structural analysis revealed different features, and in particular, the molecular reorganization observed after laser excitation. The most important transient structural changes observed in the time domain are presented in Figure 4-6 and correspond to the <Fe-N> elongation, as well as distortion of molecular angles. At dt=500 ps, <Fe-N> parameter increases of approximately 0.005 Å, and angles change of 2–38°. The <Fe-N> increases again around dt ≈ 100 ns, thus reaching a total elongation of about 0.016 Å observed at dt=1 μs. This elongation is a well-known fingerprint of molecular change from LS to HS state.

Dynamic of the PIPT :

We observed also volume expansion due to the transition to the HS state and change of Bragg peaks intensity due to a change of conformation of the molecule. The first stage of the transformation occurs at constant volume as it takes time for cell deformation to propagate. Volume expansion starts abruptly before 100 ns and smoothly continues up to 100 μs.

Important information on the transformation at the macroscopic scale is detected through the broadening of the Bragg reflections. Before laser excitation, sharp Bragg reflections are observed and remain sharp until dt ≈ 100 ns. After that, broadening is observed, reaching its maximum around 3 μs and narrow back to the initial width after 100 μs,. This behavior can be explained on the basis of a finite laser penetration depth. Even if it is of the order of the sample thickness, a gradient of deposited energy through the sample thickness still exists. The induced gradient of strain when the volume has relaxed, and before the temperature homogenization, results in a broadening of the Bragg peaks. The recovery to thermal equilibrium in the μs range is different in nature. It follows a single step reminiscent of a thermal stochastic process, the kinetics of which is governed by heat exchange with the sample environment. Consequently, the crystal remains homogeneous during this recovery step, with no Bragg peaks broadening.

As we saw, basic crystallography concepts can be employed to study the structure and the dynamics of the PIPT. It turns out that using pulsed laser pulse, it is possible to induce very fast change of the spin state and by following the diffraction pattern with a 100ps resolution, it is possible to understand the dynamics of the transformation from transformation of individual molecules to complete and macroscopic change of the phase. In the next section, we will see how we can reach such high resolution but before this, I would like to discuss the main limitations of crystallography to the study of PIPT.

4.1.3 Limitations of basic crystallography

While diffraction techniques have been essential in helping to understand the complex dynamics of photoinduced phase transitions, there are a number of limitations that need to be addressed.

1. **Penetration Depth:**

The low penetration depth of the exciting light is one of the main issues in photocrystallography or time-resolved diffraction. This restriction is particularly noticeable for thicker or highly absorbent materials, making it more difficult to conduct an extensive analysis of photoinduced phase transitions in these kinds of samples. There is often a mismatch in the penetration depth between the X-rays that probes the whole sample and the laser that excites usually just a part of the crystal.

2. **Excited and Unexcited Phases:**

Photoinduced phase are generated but not in the whole sample, meaning that the X-ray probes unexcited and excited domains at the same time. It could originate from the mismatch of the penetration depth or the time delay we look at the crystal that is shorter than the time the phase propagates in the sample. The interpretation of data might be complicated by the overlap of diffraction signals from both phases, which makes it challenging to discern the structural changes that are exclusively ascribed to the photoexcitation.

3. **Heat and Shock Wave Propagation:**

Further complexity is introduced by the shock waves or heat waves that propagate during photoexcitation. The excited and unexcited phases of the material may interact intricately as a result of heat or shock waves traveling through it. These waves can cause structural modification, making it difficult to distinguish between effects that are solely photoinduced and those that are the consequence of mechanical or thermal perturbations. It becomes more difficult to distinguish the contributions from various driving forces and to accurately interpret diffraction patterns.

4. **Sample Stability:**

Time-resolved diffraction investigations include usually high irradiation, which may cause sample damage or phase transitions that are not exclusively related to the photoexcitation. Keeping the sample steady during the experiment is essential to getting accurate results, and can be a difficulty when working with organic materials.

Although there are ways to analyze diffraction pattern and even solve the structure of a coexistence of two different phases, the fact that the crystal has to be rotated in different orientation lead to different proportion of photoinduced phase for different orientation. This makes the use of such techniques even more complicated. In the last ten years, researchers in the field have tended to work with nanocrystals in order to maximize the proportion of excited part of the crystal. This leads to other problems that the basic crystallography cannot fully solve. One has to develop new experimental techniques and advanced crystallography concepts to the study of the photoinduced phase transition. I will present those advances in a following section.

4.2 TIME RESOLVED DIFFRACTION TECHNIQUES

Time-resolved diffraction at synchrotrons or X-ray Free Electrons (XFEL) is an advanced technique that reveals ultrafast structural changes in materials. Using a pump-probe setup, this technique uses X-rays pulse as probes to record the changing structure at different time delays, while a pulsed laser starts (pump) the dynamic process.

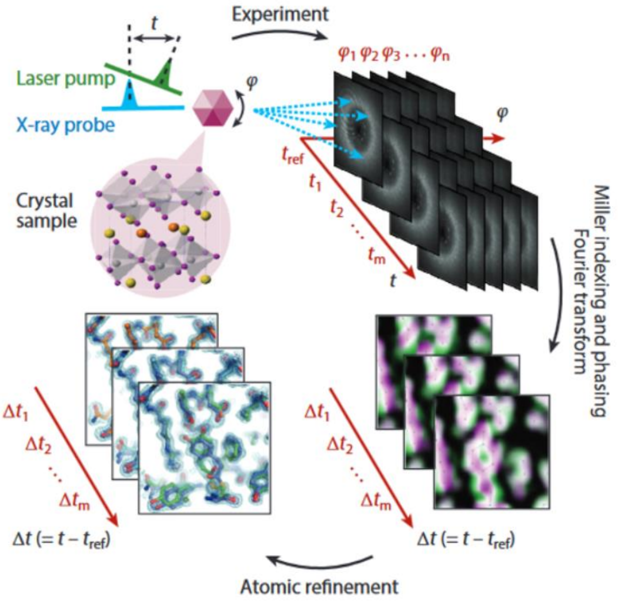

Figure 4-7 : a molecular movie (from Ki et al, Annu. Rev. Phys. Chem. 2017 [95,102])

4.2.1 How to shoot a molecular movie

Traditional imaging techniques often lack the temporal resolution required to observe rapid molecular transformations. Molecular movies excel at capturing ultrafast processes, where events unfold on timescales ranging from femtoseconds to milliseconds. The idea is quite simple (Figure 4-7). At each delay between the pump laser pulse and the probe X-ray pulse, one has to make a full data collection. [95] The structure is then solved for each delay, meaning that one can observe in the real space how atoms are moving after a laser excitation function of time. The number of frames of the movie is defined by the number of delays during the experiment with a minimum time resolution corresponding to the width of the X-ray pulse (10fs for XFEL and 100ps for synchrotron). The limitations are the one we’ve already discussed and in practical, shooting such movie is very complicated and it exists only few examples in the literature. Most of time resolved diffraction experiments are focusing on the analysis of the diffraction pattern.

4.2.2 Time-resolved pump-probe experiment at synchrotron

I have dedicated 5 years of my scientific career to the development of the time-resolved diffraction techniques at synchrotron : 3 years at the Photon factory synchrotron in Tsukuba, Japan and 2 years at the European synchrotron Research Facility, Grenoble, France. The two beamlines, NW14 and Id09B works basically on the same principle but because we built a beamline from scratch at Photon Factory, you can imagine how hard it was, I will present the work we did there (Figure 4-8). [103,104]

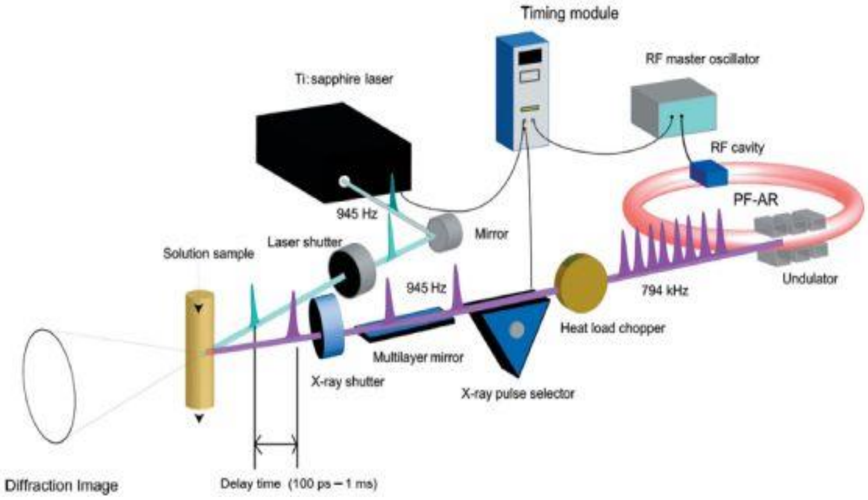

Figure 4-8 : schematic drawing of the pump and probe time resolved diffraction techniques at NW14 beamline (From)

The 6.5 GeV PF-AR is fully operated in single-bunch mode for about 5000 h per year. Electrons with a ring current of 60 mA (75.5 nC per bunch) are stored in a single bucket with a lifetime of ~20 h. The X-ray pulses are delivered at a frequency of 794 kHz with a pulse duration of about 100 ps. The beamline has two undulators with period lengths of 20 mm (U20) and 36 mm (U36). U20 gives the first harmonic in the energy range 13–18 keV. U36, which is used as a tunable and intense monochromatic X-ray source by use of a double-crystal monochromator and a focusing mirror. The Ti:sapphire laser system, which is operated at an 800 nm fundamental wavelength, is capable of reaching up to 1 mJ per pulse with a repetition rate of 945 Hz.

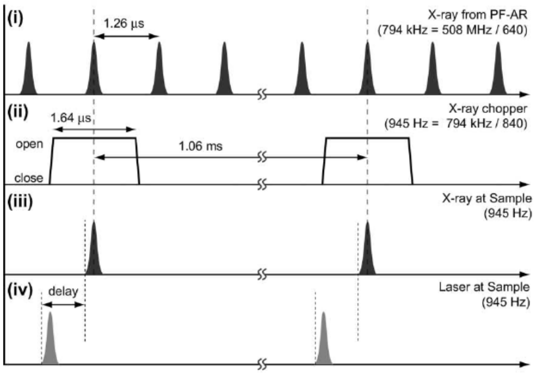

Figure 4-9 : Timing chart of the synchronization system when using the X-ray chopper to synchronize between 794 kHz X-rays and 945 Hz laser pulses in a 1:1 ratio.

The synchronization of X-ray and laser pulses is based on the RF master clock that drives the electron bunch in the storage ring (Figure 4-9). When the X-ray experiment is conducted with a 945 Hz Ti:sapphire laser and a detector with no gating such as a CCD or an imaging-plate detector, an X-ray chopper is required to synchronize the X-ray and the laser pulses at a 1:1 ratio. The X-ray chopper, made by Forschungszentrum Jülich (Lindenau et al., 2004), consists of a rotor constituted of a narrow channel for the beam passage permitting a continuous phase locking with a timing jitter of less than 2 ns. The timing electronic is controlling the opening phase of the chopper and the firing of the laser pulse so that any delays from 100fs to a ms can be achieved by computer control.

Different diffractometer, cameras and detector can be used in order to conduct different type of pump-probe time resolved experiments such as time resolved diffraction, SAXS,WAXS, XANES or EXAFS.

My main technical contribution to the field was the synchronization scheme and the commissioning of new multilayer system to increase the flux at Id09B that it still used today (Figure 4-10). [105]

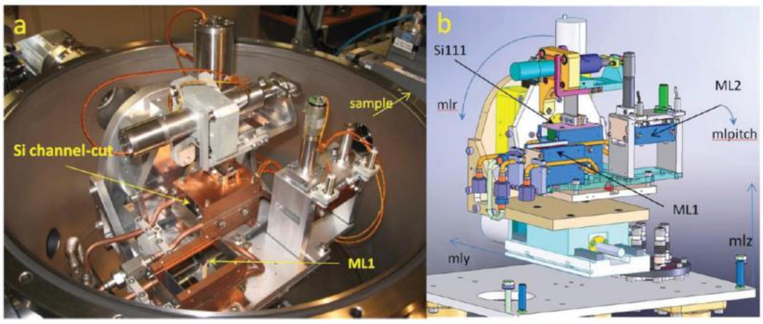

Figure 4-10 : “la casserole d’Id09B” composed of two multilayers [Ru/B$_4$C]$_{51}$ and [Ir/Al$_2$O$_3$]$_{100}$

4.2.3 Time resolved pump probe at XFEL

An acronym for X-ray free-electron laser is XFEL. [106] A specific kind of laser known as an XFEL generates X-ray pulses that are extremely powerful and coherent. XFELs, as opposed to traditional X-ray sources, produce X-rays by applying the following principle : Electrons are driven through a hundredths of meters long periodic magnetic arrangement called undulator at the speed of light. High-intensity radiation is produced through the interaction of the accelerated electrons with the periodic magnetic field. The light is coherent and therefore the produced X-ray is a laser. It has multiple advantages compare to synchrotron :

1. **Ultrafast Pulses**: XFELs generate extremely short and intense X-ray pulses on the order of femtoseconds (10-15 s). This ultrafast pulse duration enables the investigation of ultrafast processes, such as chemical reactions and structural changes, with unprecedented time resolution.

Synchrotron Comparison: Synchrotrons typically produce X-ray pulses with pulse durations in the range of picoseconds (10^{-12} s) to milliseconds (10^{-3} s), making it challenging to capture processes occurring on femtosecond timescales.

2. **High Peak Intensity:** XFELs provide exceptionally high peak intensities, significantly surpassing those attainable with synchrotron sources. This high intensity is particularly advantageous for studying weakly scattering samples and allows for the investigation of smaller sample volumes or less concentrated samples.

Synchrotron Comparison: Synchrotrons offer few order of magnitudes lower X-ray pulse making difficult the investigation of nanocrystals.

3. **Single-Shot Capability:** XFELs operate in a single-shot mode, meaning that each X-ray pulse captures a unique snapshot of the sample. This is crucial for studying dynamic processes or samples that may be destroyed or altered by the X-ray exposure.

Synchrotron Comparison: Synchrotron experiments typically involve accumulating data from multiple pulses to improve signal-to-noise ratios, which can limit their suitability for studying rapidly changing phenomena in a single shot.

The benchmark experiment for time-resolved fs diffraction is the photo induced A_{1g} coherent phonon of bismuth (Figure 4-11). The activation of the phonon induces a coherent displacement (x) of bismuth that can be probed looking at the intensity of the (111) Bragg reflection. Oscillation in the time resolved signal is related to the frequency of the A_{1g} activated coherent phonon. The period of the phonon is about 300fs, it is relatively easy to excite with a laser pulse and that's why this experiment is used to illustrate the capability of fs time resolved beamline line like in LCSL or SACLA XFEL. [107,108]

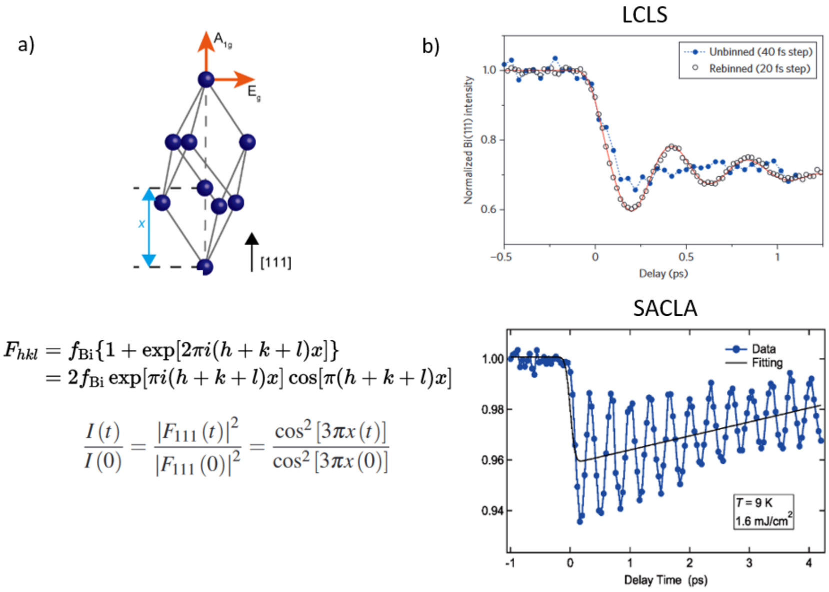

$$F_{hkl} = f_{\mathrm{Bi}}\{1+\exp[2\pi i(h+k+l)x]\} = 2f_{\mathrm{Bi}}\exp[\pi i(h+k+l)x]\cos[\pi(h+k+l)x]$$

$$\frac{I(t)}{I(0)} = \frac{|F_{111}(t)|^2}{|F_{111}(0)|^2} = \frac{\cos^2[3\pi x(t)]}{\cos^2[3\pi x(0)]}$$

Figure 4-11 : (a) structure of bismuth and calculation of the structure factor and intensity of the (111) Bragg reflection. (b) time resolved femtosecond diffraction of Bi at LCLS and SACLA.

XFEL and synchrotrons are wonderful machines that allow us to study photoinduced phase transition in a variety of materials. During my scientific career as beamline scientist, I worked on different scientific project ranging from plasma analysis, vibrations of nano-pillars, chemical reaction in solution, hidden phase in manganite to biological system. I had the opportunity to train many students from master to postdoc students. During the last ten years at the University de Rennes, I and my colleagues performed numerous experiment at large scale facility.

4.3 CURRENT AND FUTURE ADVANCES IN CRYSTALLOGRAPHY FOR INVESTIGATING PIPT

In this chapter, I will present the current advances in crystallography to study the physics of photoinduced phase transition. The first part is technical and present the latest development on measurements with nanocrystals. The second part deals with the physical mechanism of the PIPT and how we need to develop advanced analysis tools in crystallography and the last part is a proof of concept of an experiment I would like to perform.

4.3.1 The need of nanocrystals

The main problem of pump-probe studies is to ensure that the pumped volume is being probed. For molecular crystals, the laser penetration depth is often only a few microns, and for more correlated materials, it can even be below 100 nm due to the absorption coefficient at the pump wavelengths. To circumvent this problem, people in this field work with tiny crystals, nanocrystals. Because of the limited X-ray flux, we have to work with many nanocrystals (Figure 4-12). The two main forms are pellet of nanocrystals or nanocrystals in solution. Both solutions gives similar powder type diffraction pattern.

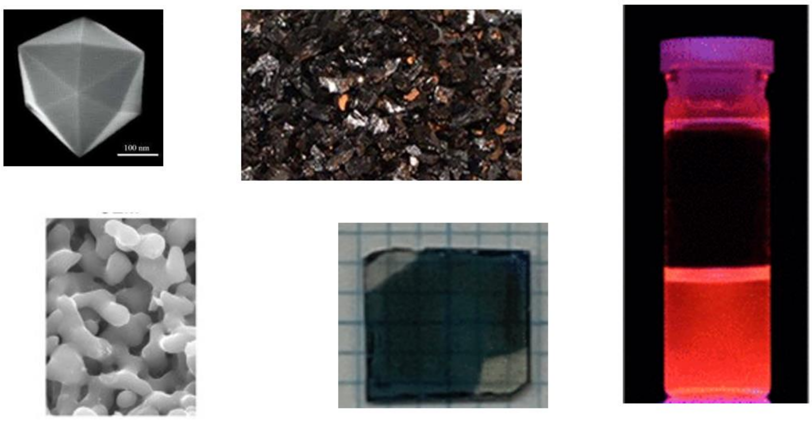

Figure 4-12 : different form of Titanium oxide nanocrystals. Single, pellet, grains, film and in solution.

The grazing incidence technique

To address the limitation of penetration depth, we developed a small grazing incidence experiment (Figure 4-13). Utilizing X-rays in total reflection becomes feasible due to the fact that the index of refraction of X-rays in matter is smaller than 1, allowing for the X-ray wave to probe only the skin depth (a few nanometers). However, the critical angle is extremely small, and working under such conditions can be challenging, especially with pellet with high rugosity. Typically, X-rays have an attenuation length of approximately 10 µm in the hard X-ray range (around 10 keV). At angles of 0.01 rad (equivalent to 0.57 degrees), the effective probed depth is on the order of 100 nm. Operating under such "extreme" conditions necessitates several corrections to the calculated powder pattern; for example, the peaks appear slightly shifted due to the angular dependence of absorption, with smaller angles experiencing stronger absorption as they travel inside the sample for longer distances. In our group, Celine Mariette (former PhD student that I “supervised” and now beamline scientist at Id09B) has developed different analysis program to achieve the determination of the unit cell with high time resolution and using Rietveld refinement the atomic positions as a function of time. [109]

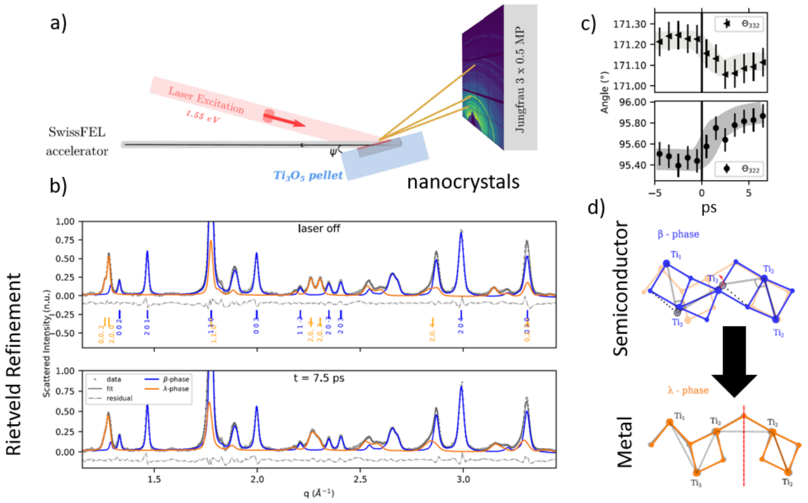

Figure 4-13 : (a) schematic drawing of the grazing incident technique at SwissFEL, (b) Rietveld refinement before and after laser excitation. (c) structural parameter function of the delay. (d) structure of the β stable phase and λ photoinduced phase.

We employed this technique on nanocrystals of Ti_3O_5 provided by collaborators Shin-Ichi Ohkoshi and Hiroko Tokoro from the University of Tokyo and the University of Tsukuba. Our team was selected to perform the first time resolved experiment at the SwissXFEL. The implementation of the technique was very successful. The quality of the TR data was remarkable and we could show that a transition from a β stable semiconductor phase and to a λ metallic photoinduced phase was occurring at the picosecond time scale and the generation of strain waves launched by electronic and structural precursor phenomena drive the coherent macroscopic transformation to the λ phase.

The streaming crystallography and serial crystallography

A solution containing the crystallized samples is pressurized and forced through a fine nozzle to form a liquid jet. In streaming or serial crystallography experiments, a key component is the delivery system, often referred to as the "jet". This delivery system is responsible for transporting a stream of tiny crystals into the path of the X-ray beam for individual diffraction measurements.

In streaming crystallography, the continuous liquid jet is intersected by the X-ray beam of an hundred micron size. In this volume of interaction, hundreds of nanocrystal interact with the X-ray beam producing a powder pattern (Figure 4-14).

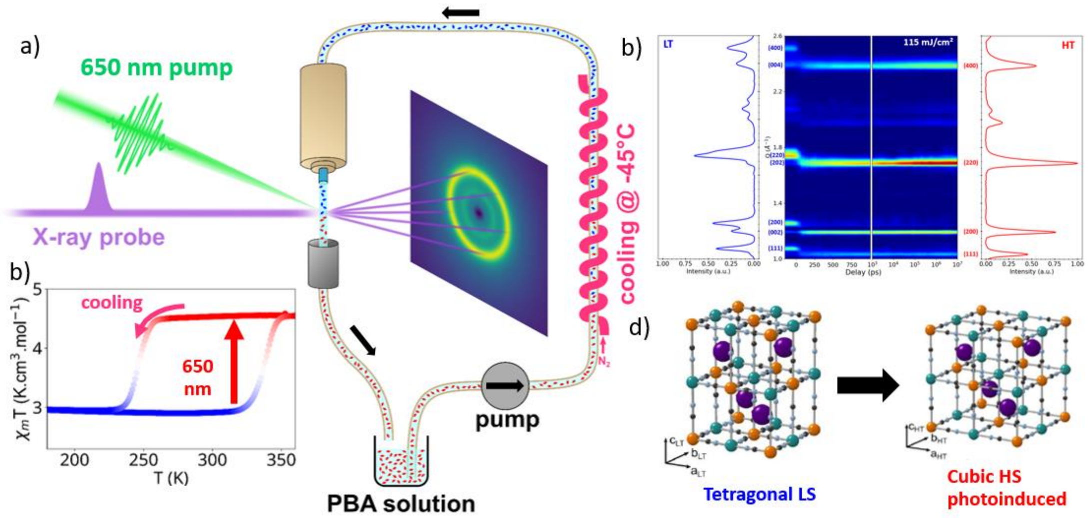

Figure 4-14 : (a) schematic drawing of the streaming crystallography setup. (b) hysteresis in the magnetic susceptibility showing a transition with light from a LS state to permanent high spin state. (c) powder pattern function of time. (d) photoinduced phase transition from a tetragonal LS to a cubic HS phase in a Prussian blue analog (From G. Privault PhD thesis and [110]).

My colleagues of Rennes developed this technique at ESRF and we recently employed it on Prussian blue analogues (PBA) nanocrystals. In addition to the limitation of the penetration depth that requires the use of nanocrystals, this compound shows a photoinduced spin transition from a tetragonal low spin phase to a permanent high spin phase in the hysteresis. Because pump-probe experiment are stroboscopic experiment, fresh samples are necessary for each X-ray pulse. Tetragonal LS nanocrystal were photoexcited to the permanent cubic high spin phase. The transformation were followed looking at the shift of powder rings in the Q direction allowing the analysis of the cell parameters and space group function of time. [110]

In serial crystallography, the nozzle size is adjusted to produce a stream of tiny droplets, and within each droplet, there may be one or more crystals producing a diffraction pattern consisting of Bragg peaks from one or more crystals. Multiple diffraction patterns are collected as the crystals flow continuously through the X-ray beam (Figure 4-15). The speed of the jet delivery system allows for the rapid collection of data from a large number of crystals. In principle, the diffraction pattern is recorded, and the position of each diffraction spot is used to reconstruct the electron density map of the crystal. The problem with small molecules is that the unit cell is usually small. The reciprocal space is consequently large and the amount of Bragg peaks for one nanocrystal in each frame is not enough to determine accurately the orientation of that given nanocrystal. E.A Schriber and al, developed a method of analysis called small-molecule serial femtosecond X-ray crystallography (smSFX) for the determination of material crystal structures from microcrystals. [96] After subjecting microcrystalline suspensions to XFEL radiation and obtaining thousands of randomly oriented diffraction patterns, they could determine the unit cells by aggregating spot-finding results into high-resolution powder diffraction image. They indexed the sparse serial patterns by a graph theory approach and the resulting datasets was solved and refined using standard tools for single-crystal diffraction.

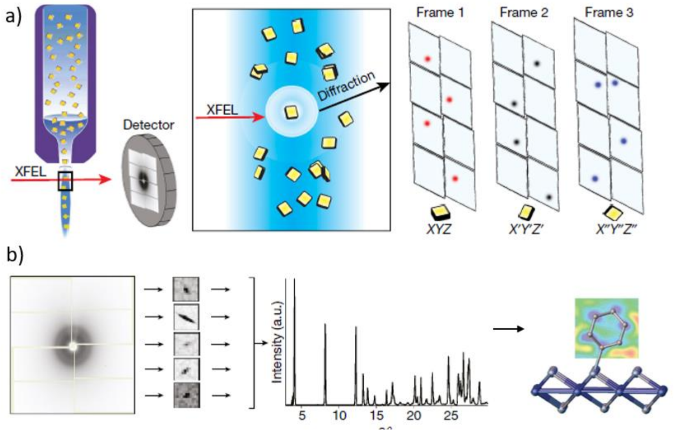

Figure 4-15 : (a) scheme of the small-molecule serial femtosecond X-ray crystallography technique. (b) analysis procedure for the structure determination

This amazing tour de force was obtained using advanced data analysis techniques, including computational algorithms and statistical methods, in order to handle large datasets from thousands of nanocrystals. This was done at thermal equilibrium without any laser but we can dream of doing similar experiments in a pump-probe scheme : no more problem of penetration depth or laser irradiation damage, determination of the structure at any time delay. This could be the ultimate time resolved diffraction experiment and it is certainly a path I would like to follow. Technically, we have all the skills, we need beam time at XFEL and a good PhD student. A PhD student that I could ideally supervise after getting my HDR.

TR Electron diffraction

Powder diffraction and electron micro-diffraction are established methods for determining structures of microcrystalline substances. Time-resolved electron diffraction typically utilizes a pulsed electron source, such as a femtosecond laser-driven photocathode or a radiofrequency (RF) gun. The pulsed nature of the electron source allows for extremely short electron pulses, essential for capturing ultrafast processes typically on the order of femtoseconds to picoseconds. Newly developed time-resolved electron diffraction setup, like in the Dr. M. Hada laboratory in University of Tsukuba has a pulse duration that is comparable to femtosecond laser pulse widths (35–100 fs) that fits perfectly with the timescale of photoinduced phenomena. [111] In 2015, T. Ishikawa et al, performed a time resolved electron diffraction on a system from a family that we already know from the chapter 2, the family of molecular conductor X(dmit)$_2$. [112] They studied the MeP$_4$[Pt(dmit)$_2$]$_2$ that shows a similar physics that the Et$_2$Me$_2$Sb[Pd(dmit)$_2$]$_2$ with the apparition at a low temperature phase a charge separated phase associated with a change of the dimerization in the [Pt(dmit)$_2$]$_2$. After laser irradiation, the intensity of Bragg peaks shows a large change in the 100fs time scale (Figure 4-16). Collecting sufficient Bragg peaks and using a structural model, they could relate this change to a change of the dimerization due to a charge transfer initiated by the laser pulse.

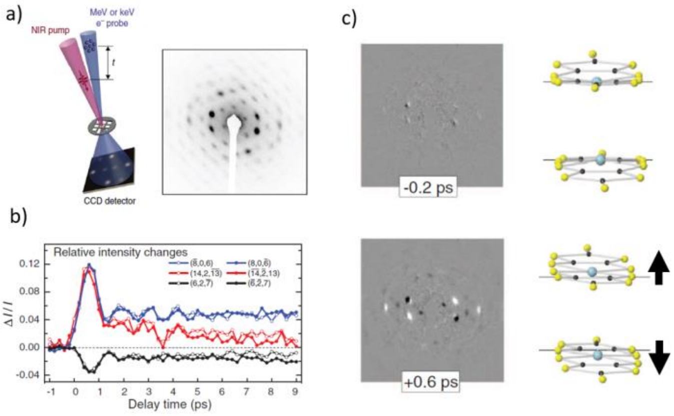

Figure 4-16 : (a) Pump probe electron diffraction scheme and an electron diffraction pattern. (b) relative intensity change function of delay. (c) difference electron diffraction pattern before and after laser irradiation and the structure modification. A change of the dimerization of [Pd(dmit)$_2$]$_2$ dimer is observed.

This example shows the capacity of the TR electron diffraction to provide structural information at the femtosecond time scale. The main advantage is its capacity to perform diffraction on very small crystal which is suitable for TR study. The main limitation is the challenge of obtaining high-quality diffraction patterns from extremely short electron pulses with sufficient Bragg peaks to solve a structure. My PhD student Maryam Alashoor is working on the indexation of Bragg peaks of electron diffraction and we plan to do some experiments at Hada laboratory in the year 2024.

The study of PIPT is grandly correlated to the technical advances. In the last twenty years, new detectors, powerful sources, sample preparation, new type of experiment like X-ray spectroscopy or HARPES emerged leading to new possibilities to explore materials under light irradiation and new physical questions. Can light induce order, what are the precursors of the phase transition, how correlation plays a role in the dynamics ?... Let me try to answer or at least let me propose some ways to answer.

4.3.2 Can light create aperiodic order ?

Can light create order or even aperiodic order ? It can certainly destroy it as we will see right now. But recent examples and ideas shows that light can also create it. If it is the case, then we need advanced crystallography concept to analyze the aperiodic photoinduced order and our knowledge of superspace could be an help.

Light and aperiodic spin waves

$[\mathrm{Fe^{II}H_2L^{2-Me}}][\mathrm{SbF_6}]_2$ spin crossover material shows a unique type of ordering phenomenon associated with the incommensurate occupational modulation of its bistable spin molecules. This occupational modulation is accompanied with a spatial modulation of the high-spin (HS) fraction γ_{HS}. Using the superspace crystallography and looking at the diffraction pattern, one can describe the concentration of high-spin (HS) molecules (γ_{HS}) and its incommensurate by following incommensurate function: $\gamma_{\mathrm{HS}}(\mathbf{r}) = \gamma_{\mathrm{HS}} + \eta \times \cos(\mathbf{q} \cdot \mathbf{r})$ with $\mathbf{q} = -\beta\mathbf{b}^* + \gamma\mathbf{c}^*$ and $\beta = 0.431$ and $\gamma = 0.131$. The structure is describe in the 4D superspace monoclinic group P211(0βγ). From the refined superspace structure model, the modulation of Fe-Ni along the internal direction of the superspace can be obtained from which the amplitude of the modulation was estimated to $\eta = 0.37$.

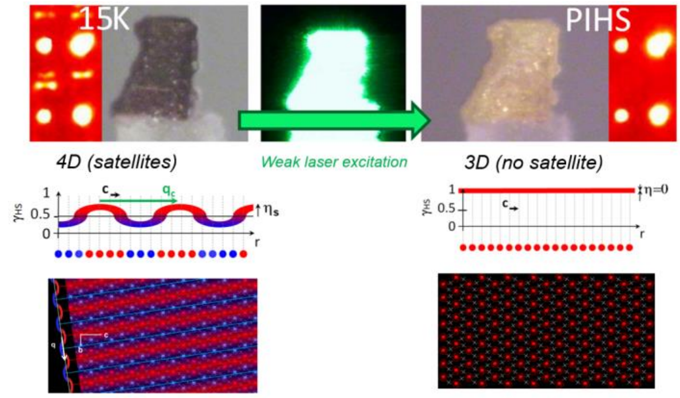

Figure 4-17 : (left) crystal at low temperature and its diffraction pattern showing satellite Bragg peaks. The incommensurate spin wave along the incommensurate **q** vector and a cut of the superspace. (right) crystal after laser irradiation and its diffraction pattern showing no satellites. HS for any position along the incommensurate **q** vector and the 3D HS photoinduced structure.

The crystal undergoes a transition from a four- to three-dimensional periodic structure when exposed to weak laser irradiation at 532 nm (Figure 4-17). This transition is associated with a change in the crystal color and the disappearance of satellite reflections and therefore the disappearance of the incommensurate modulation. [113] This demonstrates that light can erase the aperiodic order. The next question is : can it create it ?

Frustration and stability mechanism during PIPT

Lattice distortion plays a key role in stabilizing the photoinduced phase, as reported in $(TMTTF)_2X$, $(EDOTTF)_2X$ and X[Pd(dmit)$_2$] salts. [114–117] The lattice distortion is controlled by the interaction of the anion and cation, mostly from a steric nature and are governed by the shapes of the molecules, their relative positions and their compatibility (Figure 4-18). By compatibility, I mean the capacity of the anions or cations to modify its internal structural in a way that is compatible with the cation or counter anions, i.e avoid the frustration. The steric interaction can create a bottleneck in the photoinduced transformation with several effects like slowing down the dynamics, apparition of intermediate state and stabilization of the PIP. It has been shown for example that in the case of (EDO-TTF)$_2$PF$_6$ and SbF$_6$, the photoinduced transition towards the metallic phase is more difficult in SbF$_6$ because it costs more elastic energy for the SbF$_6$ than the PF$_6$ due to the larger size of SbF$_6$ anions.

In the Et$_2$Me$_2$Sb [Pd(dmit)$_2$] crystal, the crystal studied in chapter 2 showing a phase transition to an incommensurate modulated structure, the photoexcitation of the high-temperature phase from the low temperature phase emerges with a two-step sequence. [117] The slow emergence of the photoinduced state is considered to originate from lattice distortion induced by the cation. The lattice distortion is controlled by the cation's shape in [Pd(dmit)$_2$] salts. In the case of Cs[Pd(dmit)$_2$] salt, where the cation Cs is spherical without a hook, the emergence of the photoinduced high-temperature state is very fast and occurs in a single step. Conversely, the two-step photoinduced processes observed in the Et$_2$Me$_2$Sb salt are due to the steric effect between the hook-shaped Et$_2$Me$_2$Sb cations and Pd(dmit)$_2$ anions. To interpret the PIPT, I think that two highly symmetric phases should be taken into account: the incommensurate C2/c(0β0)s0 phase evidenced in the chapter 2.1.5 and the high temperature periodic C2/c phase. [27] There is a possibility that the short-time process corresponds to the formation of the intermediate incommensurate phase, and the long-time process corresponds to the erasing of the incommensurate modulation. As we've just seen, such suppression of the incommensurate modulation by light was reported previously by Collet et al. in a spin crossover system.

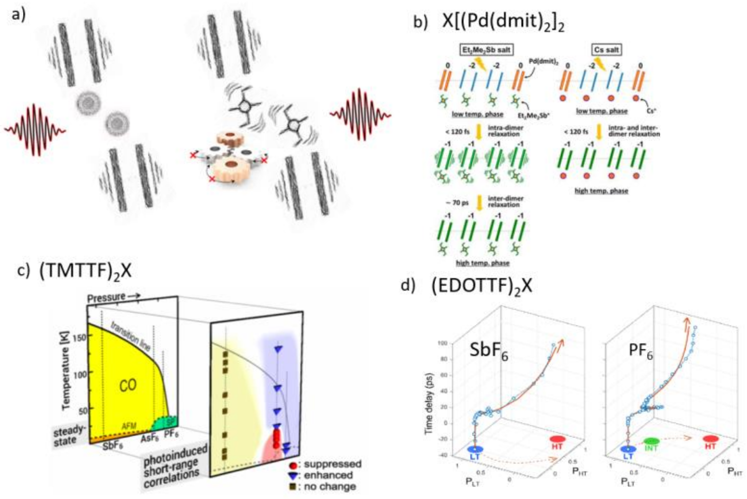

Figure 4-18 : (a) influence of the shape of anion and cations in the dynamic of the PIPT. Hooked shape anions leads to frustration. Different mechanisms or intermediate phase depending on the anion/cation are reported in several type of (b) X[Pd(dmit)$_2$], (c) (TMTTF)$_2$X and (d) (EDOTTF)$_2$X materials.

In order to answer the question about the nature of the intermediate state and its periodic or aperiodic nature, one has to perform a TR diffraction study. The idea is to do a similar experiment than in the spin crossover one but in a time-resolved fashion. If the first step of the transition involves the creation by light of an aperiodic order then the apparition of satellites Bragg peaks should be easy to spot. We plan to do this experiment using TR electron diffraction in collaboration with T. Ishikawa and M. Hada in a near future.

It is an hypothesis, a rather reasonable one but still, it doesn't answer the question. Can light induce aperiodic order ?

Photogeneration of incommensurate CDW

$LaTe_3$, a 2D layered compound with a small lattice anisotropy in the a–c plane material, exhibits a unidirectional charge density wave (CDW) along the c axis. TR fs-Ultrafast electron diffraction visualized two process simultaneously : the erase of the c axis CDW and the emergence of a competing CDW along the a axis (Figure 4-19). The intensity of the two types satellite Bragg peaks was used to track both order parameters ψc and ψa simultaneously and analyzed using the Ginzburg–Landau theory. The study reveals that the relaxation of the newly emerged a-axis CDW and the reestablishment of the original c-axis CDW occur on nearly identical timescales, indicating strong competition between the two CDW orders. [118] As always, aperiodicity originates from frustration.

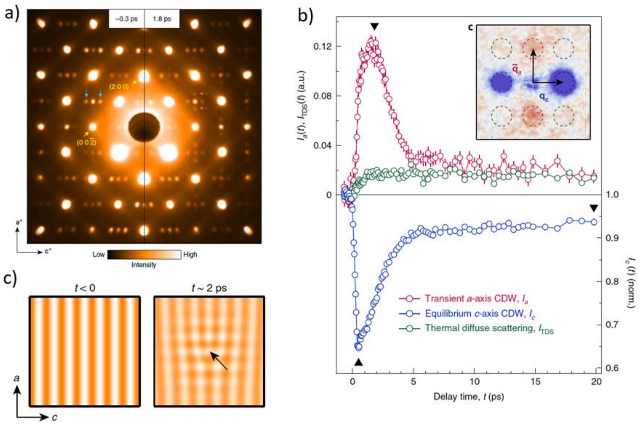

Figure 4-19 : (a) electron diffraction pattern before and after laser irradiation showing th apparition of additional satellites. (b) intensity time evolution of a-axis CDW satellites and c-axis CDW satellites. (c) illustration of the competition between the two CDW orders.

One last interesting point of this study is that the new a-axis CDW represents a transient non-equilibrium phase of matter with no equilibrium counterpart. It can be reached only using light : the famous hidden phase. It shows the unique and non-trivial nature of the induced structural and electronic changes in this material.

We have the answer of our question. Light can definitely create aperiodic order. The creation of aperiodic structures with light can lead to the emergence of novel phases or states of matter that may exhibit unique and useful properties. This opens up possibilities for discovering materials with unprecedented characteristics.

4.3.3 Diffuse scattering analysis to study the dynamics of PIPT

Precursor phenomena refer to phenomena that occur in a material before the photoinduced phase transition occurs after the absorption of light. The study of these precursor effects provide insights into the early stages of the dynamic process leading to the phase transition. Understanding precursor phenomena is crucial for unravelling the mechanisms and dynamics associated with photoinduced phase transitions.

From the crystallographic point of view, the technique allowing this study is the diffuse scattering as we already known from the chapter 3. The question is : can we used what we learned to the study of the PIPT. The answer is yes and no. In theory, it should be easy, one just need to collect diffuse scattering function of time to extract qualitative information of the type of local order of the precursor phenomena but also some quantitative information on the correlation length of photoexcited domains and their growth (Figure 4-20). In practice, it is very hard to do. Time resolved signals are usually very weak with relative changes with one or two order of magnitude lower that the equilibrium signal and if you add the fact that diffuse scattering are three or four order of magnitudes lower that a Bragg peak, it is easy understandable that there are not so much results from the analysis of TR diffuse scattering. Nevertheless, with the advance of X-ray source and the very good detectors allowing the measurements of very weak signals, this kind of study should be democratized in the future.

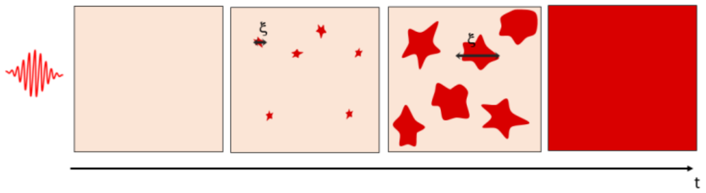

Figure 4-20 : schematic drawing of precursors phenomena of PIPT leading to a complete phase transformation.

1D-2D Correlated precursor of phase transition

We investigated the precursors of a photoinduced phase transition in the highly cooperative charge-transfer molecular crystal tetrathiafulvalene chloranil (TTF-CA). In this material, the neutral to ionic transition occurs after excitation by an ultrashort laser flash (100 fs) that can be tracked by a significant modification of the diffraction peak intensities after photo-irradiation. TR optical spectroscopy showed that the laser pulse generates a cooperative electron transfer between TTF donor (D) and CA acceptor (A) molecules, forming a train of pairs (D+A-):

$$h\nu \downarrow$$

$$\dots D^0\, A^0\, D^0\, A^0\, D^0\, A^0\, D^0\, A^0\, D^0\, A^0\, D^0\, A^0\, D^0\, A^0\, D^0\, A^0 \dots$$

$$\downarrow$$

$$\dots D^0\, A^0\, (D^+A^-)(D^+A^-)(D^+A^-)(D^+A^-)(D^+A^-)(D^+A^-)\, D^0\, A^0 \dots$$

To better understand the mechanism associated with the formation of 1D local excitations, I and Johan Hebert, PhD I supervised at that time, developed a time-resolved diffuse scattering experiment in Photon factory during my postdoc.

The 1D ionic strings (I strings) can be evidenced in the diffuse scattering signal as diffuse planes perpendicular to the strings with a width inversely proportional to the size of the exciton strings (Figure 4-21). A diffuse plane perpendicular to the stacking axis a is revealed in the differential signal. This is the direct signature of the 1D nature of precursor phenomena of the photoinduced transition of TTF-CA. Laser irradiation generates at the first stage (500-fs–1-ps) I strings. It results in a quasi-instantaneous increase of the diffuse scattering (observation limited here by the 50-ps resolution). The 3D ordering of the (D+A-) dimers occurs only at the second stage (within 500 ps), and the establishment of the 3D long-range structural order is associated with the intensity change of the Bragg reflections. [119]

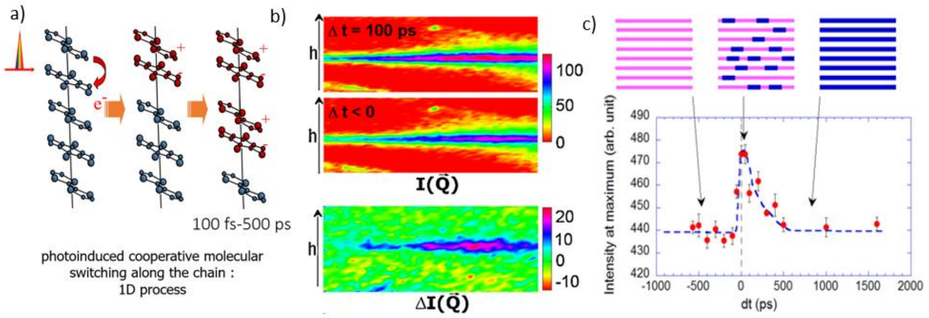

Figure 4-21 : (a) photoinduced 1D ionic strings. (b) diffuse scattering before/after laser irradiation and their difference. (c) evolution of the diffuse scattering intensity function of time.

Unfortunately, the accurate I-string length determination was not possible because of the limited spatial resolution in the setup used at that time. It would have been nice to follow the growth of the 1D strings and their correlation with adjacent chains until the establishment of the 3D ionic order.

Growths and coarsening

Some groups were more successful in the quantitative analysis of the diffuse scattering. C. Laulhé et al. have demonstrated that the lower-temperature, charge density wave (CDW) state of 1T-TaS$_2$ can be photoinduced to the high-temperature incommensurate (I) CDW phase. [120] At CRISTAL beamline of synchrotron SOLEIL, they followed the diffuse scattering signal and measuring the width as function of delay and observed a sharpening of the diffuse scattering indicating a growth of the photoinduced domains (Figure 4-22). They showed that light generates multidomain I-CDW phase, which experiences a progressive rise in the domain size or I-CDW correlation length, known as coarsening dynamics. They interpreted as a result from the photoinduced I-CDW self-doping, which is caused by trapped electrons near CDW dislocation sites.

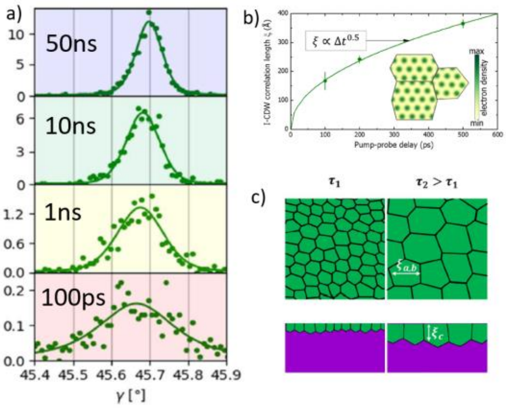

Figure 4-22 : (a) diffuse scattering profile at different time delays. (b) evolution of the correlation length with time and the associated coarsening models (c).

Defects

A similar study was reported by A. Zong et al. on LaTe$_3$ using this time TR electron diffraction. [121] After the light melts the CDW, they found that the fast recovery of the CDW amplitude (1ps) is followed by a slower re-establishment of phase coherence, which is influenced by the presence of defects. Not surprisingly, they did it by measuring the intensity and the width of diffuse scattering with time (Figure 4-23). Because the CDW as a 3D character in this system, the diffuse scattering emerges as diffuse peaks at the position of the CDW Bragg peaks. With time, they condense to a Bragg peak when the CDW recover from the excitation. The study highlights the generation of defects as a governing mechanism of the photoinduced CDW formation.

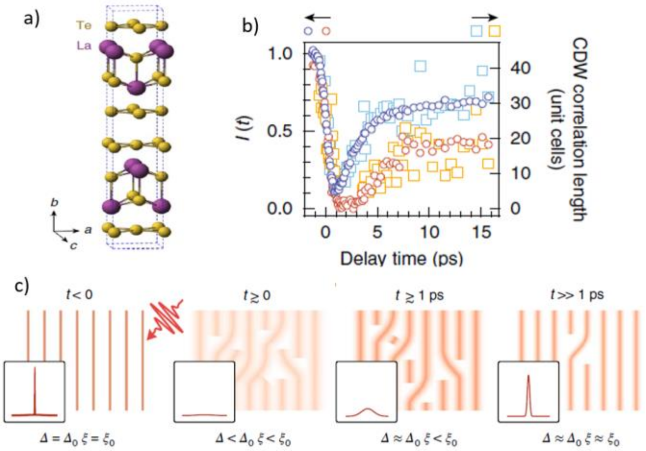

Figure 4-23 : (a) crystal structure of $LaTe_3$, (b) diffuse scattering intensity and CDW correlation length function of time. (c) mechanism of the defects generation by light and establishment of the CDW (from [121])

Polarons

In many photoinduced systems, the first process that occurs with light is the generation of polarons. Polarons are quasiparticules that consist of an electron or a hole dressed by a cloud of virtual phonons: an excess charge injected into a polarizable solid displaces the ions in its neighborhood and creates a polarization cloud that follows the charge carrier as it propagates through the crystal. [122] To experimentally characterize such distortions, it is crucial to employ techniques capable of detecting point-defect-like local structural rearrangements in real time. It was shown in the 90s by S. Shimomura et al. that this local distortion of the lattice can be evidenced by an increase of the diffuse scattering signal in the tail of the Bragg peaks similarly to the incoherent phonons in the thermal diffuse scattering. [123]

B. Guzelturk et al. employed femtosecond resolution diffuse X-ray scattering measurements to visualize excitation-induced strain fields in a lead halide perovskite (Figure 4-24). [124] Accurate quantitative assessments of the magnitude and shape of the polaronic distortion showed the expansion of nanometer-scale strain fields linked to the creation and relaxation of polarons in photoexcited perovskites.

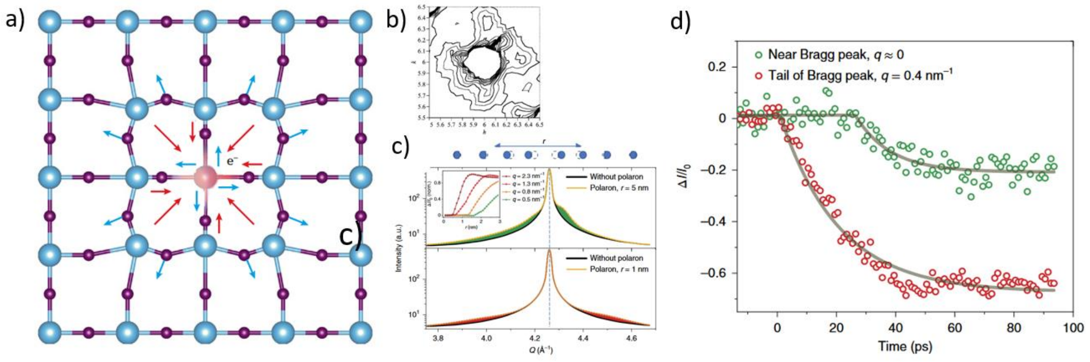

Figure 4-24 : (a) polaron induce local distortion of the lattice that is probed by (b) diffuse scattering. (c) TR diffuse scattering signal of the polaron (d) Intensity function of the delay. (From [124])

I believe that the exploration of excitation marked by dynamic nanoscale distortions, is a fundamental aspect in fields of PIPT. The generation of polaron modify the properties of the material such as the effective mass of electrons in perovskites or local pressure inducing spin state transition in spin crossover materials. The diffuse scattering analysis is therefore an important techniques for understanding the mechanism of generation and relaxation of PIP.

4.4 TR SEGMENTED SCATTERING METHOD : A PROOF OF CONCEPT

Twenty years ago, scientists were thinking about how to explore the transformation of materials with light but were very limited by the technology. Time resolution was poor, flux was low, detectors were slow with a low dynamics. I even did some experiments with point detectors with a 4 circle diffractometers, a true vintage diffraction experiment. Now, in 2024, thanks to the advances we saw before, scientists do almost routinely experiments that we never thought possible back then. Unfortunately there are still many limitations, an important one is the necessity to use nanocrystal or microcrystals and complicated techniques to solve the structure of the photoinduced phase. But let's imagine for this last part of this work that there was no limitation, what would be the ideal TR diffraction experiment ?

It would be an experiment that allows us to follow the structure at any timescale and any length scale, a technique that could not only follow the movement of atoms in the photoinduced phase at any time but also follow the local correlations at the origin of the generation of the PIP with time.

We know the technique, it is the total scattering because in the PDF, we have all the information about local and global structure. Because in single crystal, local and global structure have a different scattering signature, i.e diffuse scattering and Bragg, the technique could be separated into two techniques that we already know how to deal with : 3D-ΔPDF and diffraction. The diffraction provides insight into the average structure, the 3D-ΔPDF its deviation from the average. This would make sense because those two signals are not only different spatially but also in the time domain. Precursor phenomena and their diffuse scattering would rather appear earlier than the transformation at a larger scale signed by Bragg peaks. Obviously. Let me call this technique the TR-segmented scattering method (Figure 4-25).

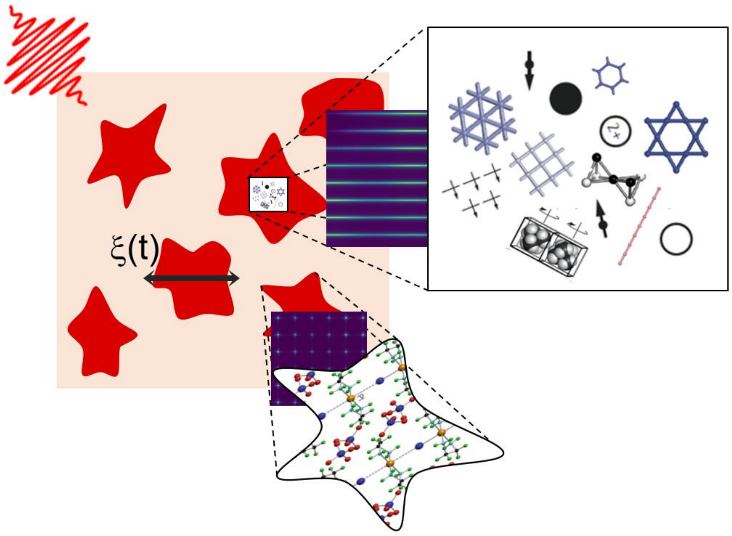

Figure 4-25 : the TR-segmented scattering method : after absorption of light, the type of correlations and their strength are determined by the 3D-ΔPDF method. This local precursor phenomena evolves to mesoscopic photoinduced domains whose the structure at the atomic scale is followed in time using TR-diffraction.

In chapter 1 and 3, we derived all the equations to compute the intensity of the Bragg peaks and the intensity of the diffuse scattering knowing the structure and the nature of the correlated disorder. I would like to propose a toy model of photoinduced phase transition and derived the diffraction pattern function of time in order to illustrate how the TR-segmented scattering method would work.

4.4.1 The model

This model is inspired by the MX crystal presented in the chapter 3.5. that was studied using the 3D-ΔPDF method. We consider two phases, the equilibrium and the photoinduced one. The crystal is cubic unit with a motif of three identical atoms at position (0,0), (0,0.2) and (0,-0.2), an atom (Matom) in the middle of two atoms on the side (Satom), so it is composed of chains of molecules of 3 atoms along the a axis. In the equilibrium phase, the unit cell is cubic of parameter a (Figure 4-26).

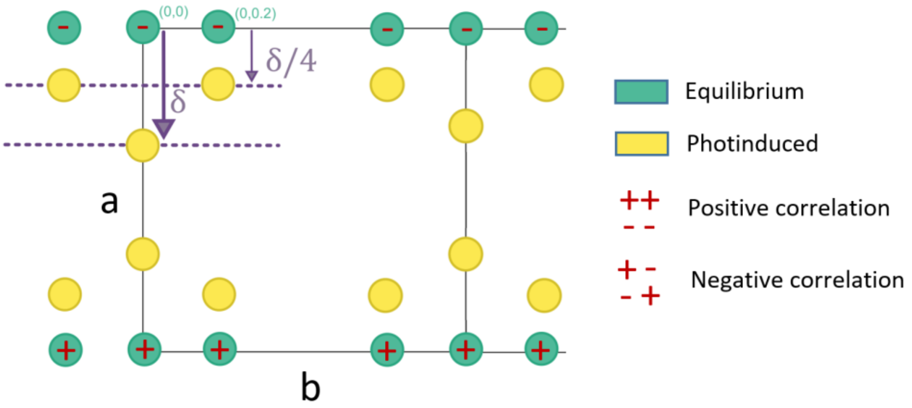

Figure 4-26 : structure of the equilibrium and photoinduced phase showing a dimerization along the chain associated to negative correlation in the a direction. Along b, dimerization is in phase due positive correlation in this direction.

After photoexcitation, the crystal undergoes a phase transition to the photoinduced phase. Along the a-axis, dimerization occurs along the chain associated to a Peierls mechanism. The displacement for Matom is noted δ and the displacement of the Satom atoms on the side are four times less important. This antiferro type arrangement is due to negative correlation between the atom at position 0 et 1 along the a-axis. Note that the unit cell is doubled along a. Along the b direction, dimerization are in phase between chains due to positive correlations present along the b direction.

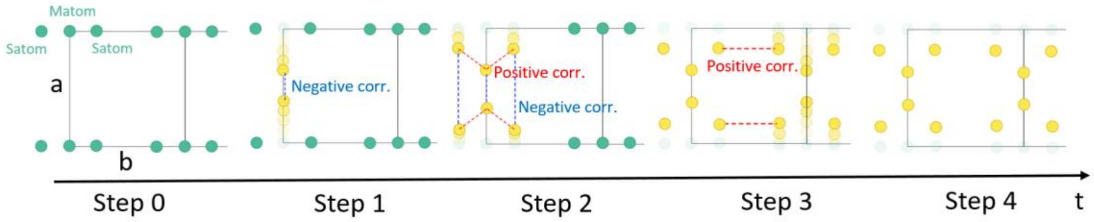

Figure 4-27 : Model of a photoinduced phase transition and its precursor correlated local order. Step 0: equilibrium. Step 1: dimerization of Matom. Step 2: dimerization of Satoms. Step 3 and 4: propagation to a macroscopic photoinduced phase.

We consider the following mechanism during the transformation (Figure 4-27). After laser irradiation from the equilibrium phase (step 0), due to negative correlation between the Matoms at (0,0) and (1,0), Matoms are displaced along the a direction (step 1). The displacement δ varies with time from 0 to 0.05 in a unit. We consider this displacement to be extremely fast due to its electronic origin. It is followed by a displacement of the Satoms in the same direction due to positive correlation (step 2). In the case of the MX system studied in chapter 3, those positive correlations originates from the hydrogen bond between the nitrogen in the ligand of M and the X atom. After this displacement kicks in along the chain, in phase displacement from chain to chain along the b axis occurs to finally reach a complete transformation (step 3 and 4). In the MX case, this positive correlation was carried out by the hydrogen bonding network.

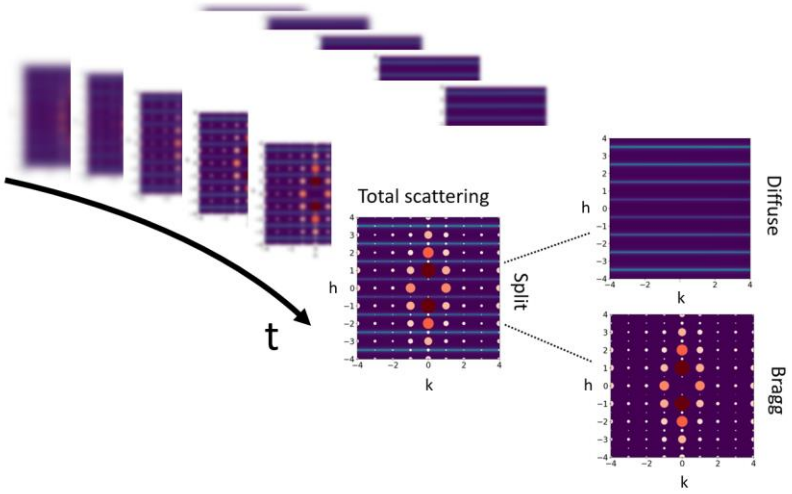

Figure 4-28 : The TR-segmented scattering method. For each time during the transformation, a total scattering pattern is collected and the 2d scattering pattern is split into two : a diffuse scattering pattern and Bragg peaks that are analyzed individually.

The experiment consists of calculating the total scattering pattern for the different steps of the transformation considering the correlations present in the model, the correlation length along a and b axis and the average position of the atoms during the transformation due to the displacement parameter δ.

The total scattering is then segmented into two contributions : the diffuse scattering pattern and the Bragg peaks pattern. The two patterns are analyzed individually using the 2D-ΔPDF and diffraction analysis method (Figure 4-28). Different techniques to remove Bragg peaks from a diffuse scattering pattern exit: "punch and fill" method, filtering in Fourier space, global background subtraction, windowing and filtering … [86]

4.4.2 The 2D-ΔPDF method

Before looking how evolve the average structure and the 2D-ΔPDF map with time, let’s look at the result of calculation during the propagation of the correlation along the b axis corresponding to the step 3 to 4 in the transformation (Figure 4-29).

The diffuse scattering shows the typical feature of a 1D correlated disorder along a axis with negative correlation : diffuse lines perpendicular to a* at half integer position indicating an anti-ferro type correlation. The correlation length are very long along a as the lines are quite sharp in the a*. Their width is inversely proportional to the correlation length along a and corresponds to correlation of 20 unit cell in the a direction.

We observe also modulation of the intensity of the lines along the b* direction. The intensity is modulated by two contributions :

- The first is the structure factor of the molecule. The molecule shows an internal periodicity of 0.2a, this corresponds in the reciprocal space to 5 times a*. Indeed the intensity of the diffuse scattering is stronger in the vicinity of k =5. Such expression of the structure factor in the scattering pattern will come up in the intensity of the Bragg peaks as we will see in the next section.
- The second contribution comes from the establishment of long range order along the b direction with positive correlation from chain to chain (ferro type) leading to stronger diffuse signal at integer k values.

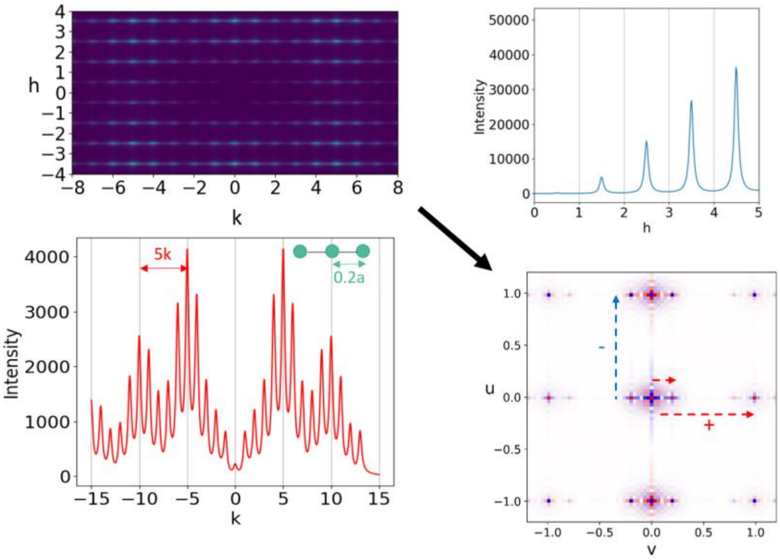

Figure 4-29 : the diffuse scattering pattern and its horizontal and vertical profile. (bottom right) the 2D-ΔPDF map : positive correlation and negative correlation interatomic vectors are represented by red and blue arrows.

Fourier transform of the diffuse scattering gives the 2D-ΔPDF. A negative correlation between atoms at (0,0) and (0,1) is clearly seen with the typical Mexican hat profile. It is associated to a local dimerization mechanism as already discussed in chapter 3. A positive peak is observed at (0,0.2) and (0,1) indicating positive correlation in the displacement of the atoms along a, meaning that when atoms are displaced positively in the a direction in one chain, the adjacent chains are displaced in the same way. Intensities of peak in the map are stronger in the chain direction than in the perpendicular direction indicating a difference of correlation length between the two directions.

Step 1 : displacement of Matoms and 1D propagation

We calculate, for a given correlation length along a, the diffuse scattering pattern for different values of the displacement parameter δ. The first observation is that the diffuse scattering intensity has a different dependence with h (Figure 4-30). In the case of small displacement, the modulation of the intensity with h follows the atomic form factors of the molecule, weak at low h, a maximum around 5h and decrease at low q. In the opposite, at large value of δ, the intensity continue to increase with h. We observed such dependence in the diffuse rods of the MX chains and the diffuse s planes of the alkane-urea crystal. This is characteristic of displacive correlated disorder.

The 2D-ΔPDF shows the typical Mexican hat profile along u at v=0 with no signals at u = +/- 0.2 and +/- 1 indicating correlation along the chain only. The width of central peaks at u = 0, +/- 1 increase with increasing the displacement parameter δ. The Yell program could be used extract the displacement parameter as it was done for the MX chain in chapter 3.

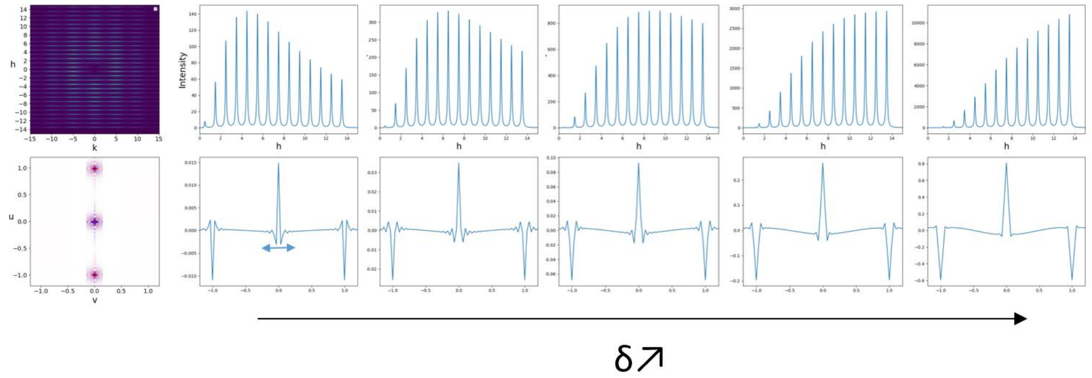

Figure 4-30 : Evolution of the diffuse scattering and ΔPDF profile along h and u respectively with increasing the displacement parameter δ.

Figure 4-31 shows the evolution of the diffuse scattering pattern and its 2D-ΔPDF function of the correlation parameter ξa along the chain. This corresponds in time to the evolution from step 1 to step 2 as we expect the correlated photoinduced domains to grow in size with time. As diffuse scattering condensed at the half h integer value, the signal increases and becomes sharper as t increases. The 2D-ΔPDF shows in the real space, the extension of the correlation to first, second and third unit cells. The intensity of the peaks in the maps are increasing with u indicating the first neighbor correlations are the strongest. The peaks intensity increases also with time because of the growing of the 1D correlated order along the chain.

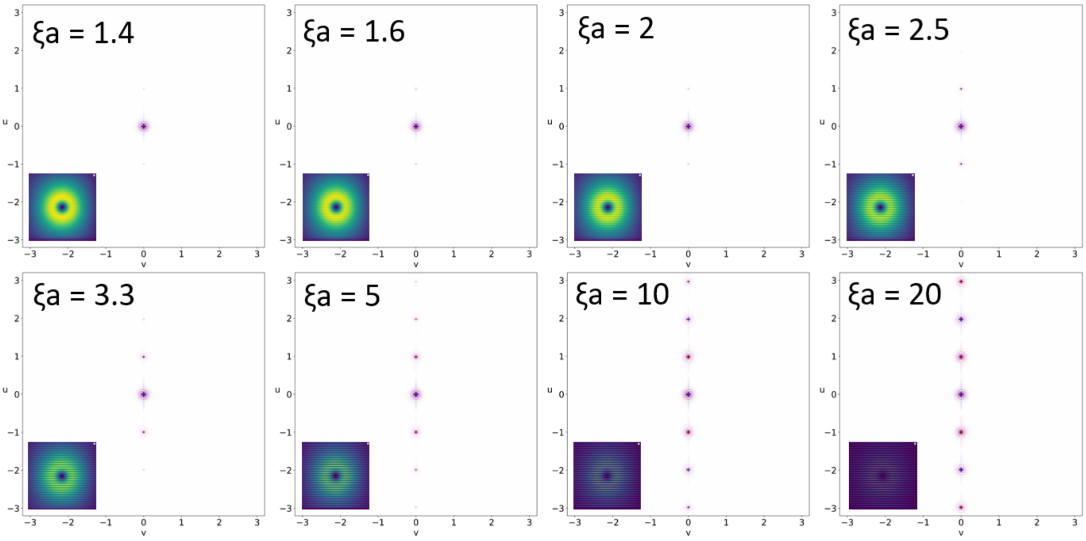

Figure 4-31: Evolution of the diffuse scattering and ΔPDF maps with increasing the correlation length ξa.

Step 2 : positive correlations induce displacement of Satoms.

During the step 2, positive correlations between the atoms inside the molecule increases with time inducing a displacement of side atoms Satoms in the same direction than the central atom Matom. Similar to the MX chain, we consider a displacement four times less important than the atom inside the chain. Increasing the correlation, the diffuse scattering along k is more and more modulated due to the change of the molecular structure factor during the transformation (Figure 4-32). The 2D-ΔPDF map shows two side positive peaks at the position 0.2a in the b direction corresponding to the interatomic vector linking the M and S atom. The positivity indicates the positivity of the correlation i.e the Satom is displaced in the same direction than the M atom. A rather surprisingly result, at least for me, is the sensitivity of the ΔPDF. In the case of very weak correlation (0.05 in arbitrary unit), the modulation of the diffuse scattering signal is barely noticeable whereas in the case of the ΔPDF map, positive peaks can be clearly observed at the interatomic vector M-S.

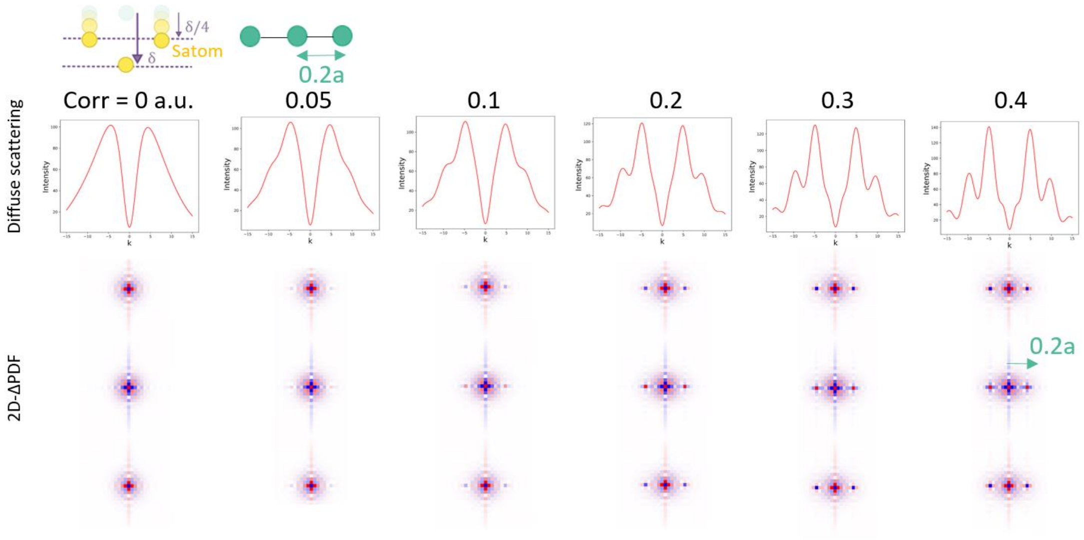

Figure 4-32 : The evolution of the diffuse scattering profile and the ΔPDF map along the b* direction function of the correlation between M and S atom.

Step 3 to 4 : propagation to adjacent chains

After long range order established along the chain and side atoms start to move, adjacent chains start to operate the same transformation. The positive correlation between the molecule in the chain A and the molecule in the adjacent chain B induces a correlated displacement of the whole molecule in B in the same manner as A. This new order propagates from to chain and forms correlated domains with correlation length ξb. Figure 4-33 shows the evolution of the diffuse scattering pattern and its 2D-ΔPDF function of the correlation parameter ξb. This corresponds in time to the evolution from step 3 to step 4 as correlated photoinduced domains grow in size with time. As expected for positive correlation along b, the diffuse scattering condensed at k integer value, the signal increases and becomes sharper as t increases. For ξb = 20 (and ξba = 20), the diffuse scattering condense to very intense sharp peaks : the Bragg peaks. They are positionned at half integer values along a* and integer value along b* corresponding to cell doubling along a for the average photoinduced structure.

The 2D-ΔPDF shows in the real space, the extension of the correlation to the adjacen unit cells. Positive peaks are observed at the interatomic vector Matom-Matom$_{\text{adjacent chain}}$. The peaks intensity increases with time because of the growth of the correlated phoinduced domains. For ξb = 1.3, we can do the same remark as for the side atom in the previous step. The modulation of the diffuse scattering is almost unnoticeable, however in the ΔPDF, a positive signal at v=1 can be cleary seen. Once again, the ΔPDF is very sensitive to small change in the structure. For ξb = 20 and ξa = 20, the ΔPDF extends to more than 3 unit cells in the a and b direction indicating the macroscopic ordering of the photoinduced phase of step 4.

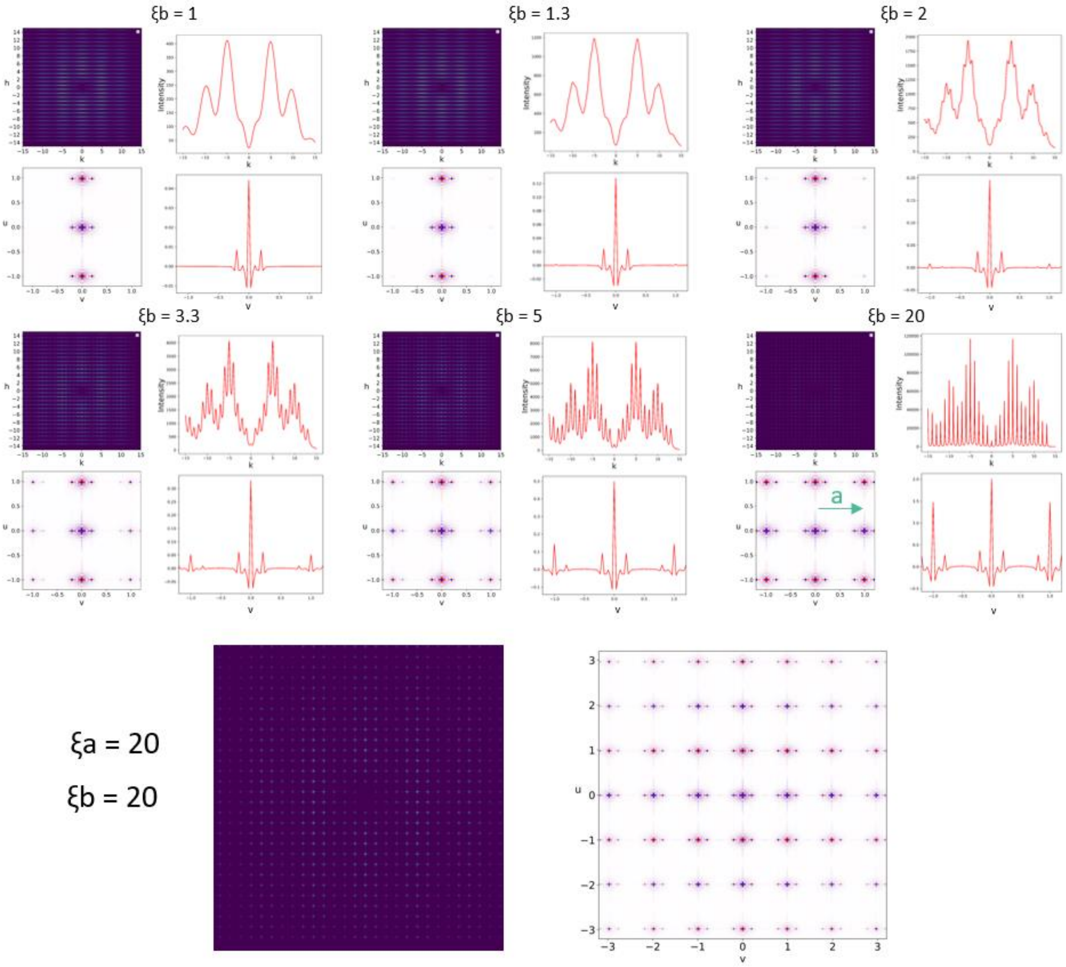

Figure 4-33 : evolution of the diffuse scattering pattern and ΔPDF with the correlation length ξb.

The determination of 2D-ΔPDF function of the time of transformation gives valuable insight of the photoinduced transformation : one can determine the origin and the type of correlations (positive and negative), how these correlations evolve in time and in space. In adition, It turns out from this simulation that the ΔPDF is very sensitive to a change of correlation. This work consists of calculating the scattering pattern by changing parameters of the model. In a real experiment, one have to do the opposite process : collect diffuse scattering and model the disorder in order to fit with the experimental data. This can be done using a program like Yell program as we did in the chapter 3.

4.4.3 The diffraction method

The other segmented part of the total scattering pattern is the Bragg peak pattern. The way to analyze it is similar to the TR-diffraction analysis. One can follow with time the intensity of Bragg peaks in order to track some change of symetry (if any) and the structural reorganization. The calculation of the diffraction pattern is obtained from the square of the structure factor :

$$F(\boldsymbol{G_{hkl}}) = F_{hkl} = \sum_j f_j(\boldsymbol{G_{hkl}})\, e^{i2\pi(hx_j+ky_j)}$$

With 3 identical atoms in unit cell : Matom at (δ(t),0) and Satom at (δ(t)/4,0.2) and (δ(t)/4,-0.2).

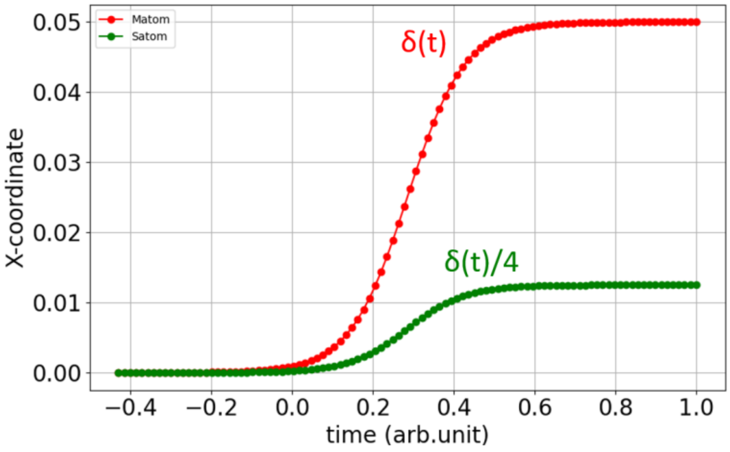

Figure 4-34: time evolution of the x coordinate of M and S atom. The x coordinate of M is the displacement parameter δ(t).

The evolution of the coodinate of the M and S atom along the chain with time is presented in Figure 4-34. A sigmoid function was used to represent the change of the average displacement δ function of the time t of the transformation. Remember that the obtained information concern the average structure so that the displacement parameter δ(t) for the calculation is in reality the average of the different displacements present in the photoinduced and equilibrium domains.

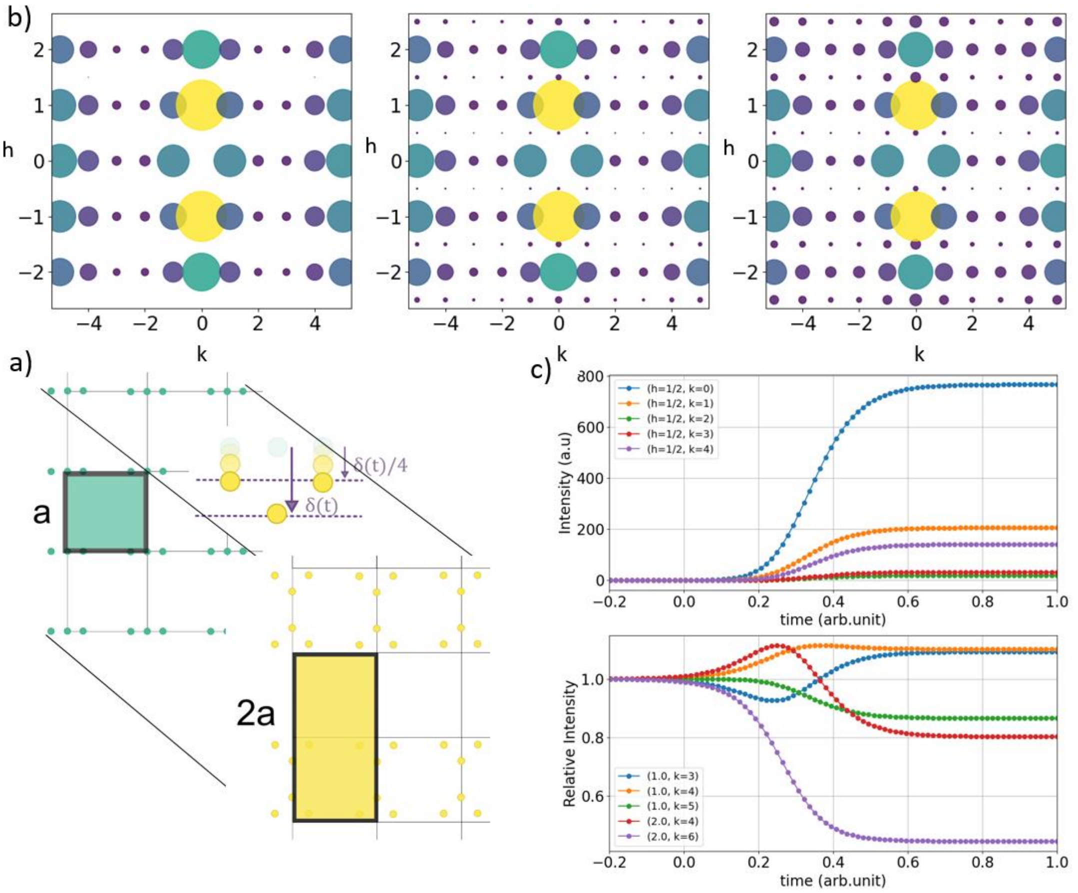

Figure 4-35 : (a) change of the structure with time after photoexcitation. The unit cell is doubled along a in the photoinduced phase. (b) calculated diffraction pattern for δ =0 , 0.025a and 0.05a. Apparition of superstructure Bragg peaks at half integer k values. (c) Evolution of the superstructure Bragg peaks intensity and structural Bragg peaks function of the time.

In the equilibrium phase, Bragg peaks are present at the node of the reciprocal lattice. Similarly to the diffuse scattering pattern, the Bragg peak intensity is modulated by the structure factor of the molecule (Figure 4-35). Larger intensity values appears in the vicinity of k=5 which corresponds to the internal periodicity of the molecule along b. After photoexcitation, superstructure Bragg peaks at half integer h value appears. This is the signature of a cell doubling along the a direction that corresponds to the dimerization process occurring along the chain.

As already discussed in the chapter 1, the change of the intensity of the superstructure Bragg peaks measures the evolution of the order parameter during the transformation, which is in this case the displacement parameter δ(t). Before the transformation, the superstructure intensity are null and increase following the same evolution as δ(t) to reach a plateau when the transformation to the photoinduced phase is complete.

The structure Bragg peaks shows a different evolution with time, some decreasing in intensity and some increasing in intensity (Figure 4-35). This is due to the change of the structure of the molecule during the transformation. By measuring the intensity of those Bragg peaks function, one could determine, using usual structure determination algorithm, the structure function of time. One interesting point that come up of this calculation is rather peculiar evolution of the several Bragg peaks. Some shows first a decrease of intensity and follow by an increase to reach the plateau when the transformation is over, some the opposite. This point should be investigated in more detail but my wife is telling me to stop writing my HDR for my sake and for the sake of my referees as it seems an endless work. 😉 This will be investigated in a later work.

The conclusion of the diffraction method are nothing new. By measuring the intensity of the superstructure Bragg peaks, one can have access to the order parameter function of the time of transformation and therefore the dynamic of the change of the average structure. The determination of the intensity of the Bragg peaks function of the time allows to determine the change of the average structure during the transformation and in fine to make the molecular movie that was discussed at the beginning of this chapter.

Using a simple toy model of a photoinduced phase transition, I could show that the TR-segmented method allows the determination of quantitative relevant parameters and their evolution during the transformation: the average structure, the correlation length and the origin of the correlation and their nature. The analysis is segmented, the result of one doesn’t not affect the result of the other. One could ask the question : can we make use of the information obtained from the analysis of the ΔPDF to the structure dtermination and vice versa ? I think the answer is yes. Actually the Yell program requires the knowledge of the average structure to determine the correlation. For the opposite, one could bounds positions and ADPs of atoms using the parameters of the ΔPDF during the structure refinement process. In my knowledge, nobody has ever tried to do this.

In the future, I will continue the investigation of TR-segmented method by changing the toy model. The first easy modification was to change the correlation along the chain from negative to positive. This gives a drastic change of the diffraction pattern with no cell doubling. I’m now considering other models.

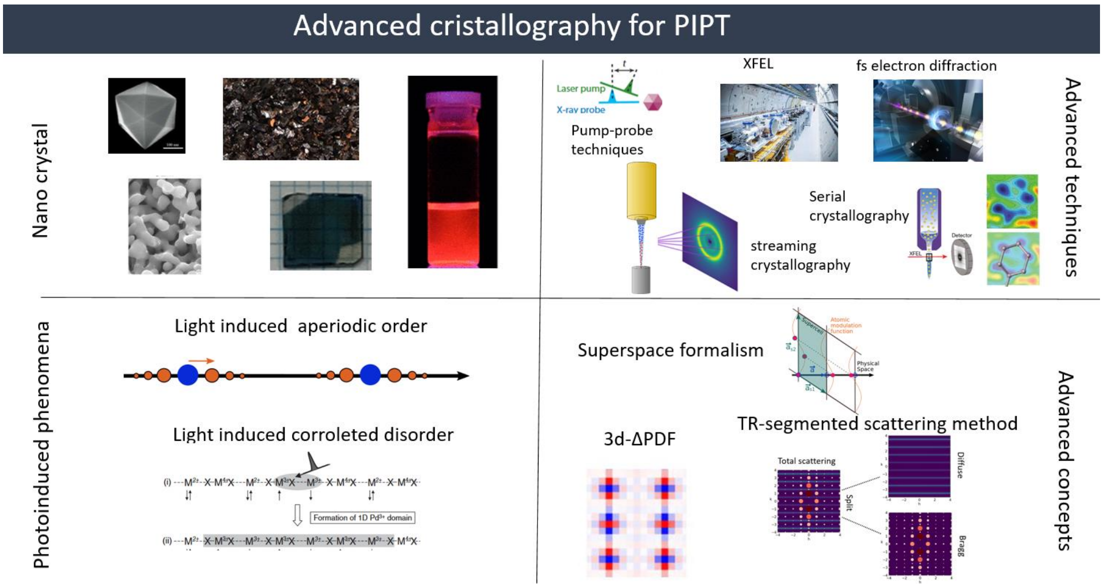

The use of diffraction and generally the analysis of the scattering pattern allows to get insight of the transformation of a material at the relevant time and length scale. The limitation due to the finite penetration depth of the laser requires the use of micro-crystal or nanocrystals. Scientists all over the world are now developing experimental techniques at synchrotron or XFEL to study a large collection of crystals with streaming crystallography or the analysis of shot to shot crystal structure with serial crystallography. Analysis techniques are also evaluating and more or more advanced concepts in crystallography, like aperiodic order or correlated disorder, are used in combination of the classical technique of analysis of diffraction.

In the future, one can dream of collecting the total scattering pattern and its evolution function of the time of the transformation. This time is going to come and the TR-segmented scattering method will be here to help.

Conclusion

In this manuscript that explores the topic of crystallography, we started with the foundation of crystallography looking at the fundamental principles and equations that define the discipline, with a focus on spin transition system compounds. Through X-ray diffraction, the chapter demonstrates the power of Bragg peaks in determining crystal structures, serving as invaluable probes for detecting phase transitions. Chapter 2 embarked on a journey into the world of aperiodic order. From incommensurate modulated structures to quasicrystals, crystallography is extended to the superspace to study materials exhibiting long-range order without translational symmetry. The chapter not only defines the categories of aperiodic materials but also shows how superspace crystallography serves as a bridge between 3D periodic lattice concepts and the intricate lattice of (3+d) dimensions in superspace. We then moved in Chapter 3 to correlated disorder which is characterized looking at the diffuse scattering. The chapter not only focus on the quantitative analysis of the diffuse scattering but also introduces the 3D-ΔPDF analysis. The final chapter explored the photoinduced phase transitions. From the relaxation of optical excitations to the formation of macroscopic excited domains, time resolved crystallography is a powerful technique to reveal the dynamic processes allowing the probing of atomic-scale changes in real-time.

The implications of the crystallographic advances will impact the design of future materials. From crafting materials with specific electronic properties to modifying structures for optimal functionality, crystallography is essential for material innovation. The study of aperiodic order and superspace crystallography pave the way for the design of materials with exotic properties. Future research could focus on understanding how these intricate structures respond to external stimuli and exploring the potential for tailoring their properties through controlled design. The insights collected from the analysis of correlated disorder and diffuse scattering could be used to design materials with specific properties.

The ability to induce phase transitions through light irradiation offers new possibilities for manipulating material properties. From triggering structural changes to electronic or magnetic states, the applications of photoinduced phase transitions extend to the development of optically controlled materials with applications in photonics or optoelectronics. The time-resolved techniques employed in studying photoinduced phase transitions give the opportunity to study ultrafast processes. Future research might focus on improving these methodologies to investigate more and more quicker process and more complex materials. In addition to expanding our knowledge of the dynamic behaviors of materials, this would open up new ways for the development of materials with extremely fast response times for a variety of applications.

In the conclusion, I proposed the TR-segmented total scattering method as an innovative approach to capture dynamic processes within materials with ultrafast resolution temporal resolution. This method combines time-resolved (TR) techniques with total scattering analysis, providing a comprehensive understanding of structural changes occurring on various timescales. By incorporating the analysis of the diffuse scattering, the method goes beyond traditional crystallography, offering a more complete understanding of materials.

As we moved through the manuscript, it became evident that crystallography serves as a versatile and indispensable tool and that this science is still advancing. New sources, new detectors, new analytical tools are developed every day and the science of crystallography in one hundred year from now will be certainly very different than the crystallography we are doing now.

Closing remarks and Project

This manuscript presents the scientific work I did in the last 20 years. In some of the works I was the principal investigator, some works the supervisor and other a simple collaborator. In an appendix of this manuscript, I'm listing my contribution to each research project I've worked on and the different projects and students I've supervised.

Due to multiple factors, I've already supervised a PhD thesis as a PhD director of the PhD thesis of Lucas Gournay at the University of Rennes 1 from 2018 to 2022 untitled : "Structural and electronic response of materials under intense THz radiation". Because the topic was out of the scope of the topic presented in my HDR, I've decided to include an appendix on the generation of intense terahertz pulse to control properties of materials.

Finally, readers may ask what I'm working on right now. Therefore in this closing remarks, I will present my research project I'm conducting at the department of Chemistry of the University of Tokyo as a CNRS researcher of the international research laboratory DYNACOM. During the writing of this HDR, I've developed some codes to calculate diffraction pattern and diffuse scattering. It was, at first, made for the educational purpose and illustration of the concepts that I presented in my HDR. However, I realized that it could give interesting insight on how one can observe the transformation of photoinduced materials. I analyzed a toy model of dimerization but I think I will continue this investigation on other kind of transformation like coherent phonon or polaron generation as a side project.

Project: Ultrafast Dynamics in Cobalt-Tungsten Cyanide Bridged Bimetallic Assemblies

There is notable progress in the field of ultrafast science in solids, employing laser pump pulses to prepare systems in highly excited states and subsequently tracking real-time induced electronic and/or structural dynamics with probe pulses. Modern laser sources can deliver ultra-short pulses, typically in the femtosecond range, shorter than the timescale of atomic movements. Additionally, these pulses can be intense, possessing a macroscopic number of photons and an extremely significant instantaneous electric field. The resulting out-of-equilibrium dynamics can lead to material transformations, inducing new phases with distinct physical properties. Utilizing light and electric fields for control allows us to strongly and rapidly influence atomic processes in a material. These photo-induced phenomena can trigger macroscopic state transformations, altering a material's functionality from insulating to metallic, non-magnetic to magnetic, referred to as photoinduced phase transitions. Time-resolved experiments, unraveling the complex electronic and structural processes, are crucial for studying these ultrafast phenomena.

Project Positioning: Our international research laboratory, Dynamical Control of Materials (IRL DYNACOM), a CNRS laboratory combining the Materials and Light Department of the Institute of Physics of Rennes and the laboratory of Shin-Ichi Ohkoshi at the University of Tokyo, aims to study multi-scale processes. Our collaborative approaches involve time-resolved exploration techniques using visible, infrared, and THz pulses or pulsed X sources (Synchrotron or XFEL) in Rennes and the development of new materials at the University of Tokyo. My project is part of DYNACOM, currently on CNRS delegation at the University of Tokyo from September 1, 2023, to August 31, 2024, seeking an extension for a full-time delegation for an additional year (September 2024 to August 2025) with a potential for an extra year based on project needs.

Scientific context: The objective of this project is to conduct a comprehensive study of phase transition mechanisms induced by light in bimetallic assemblies of Cobalt-Tungsten connected by a cyanide bridge (CN). This broad category includes analogs to Prussian blue, as illustrated in Figure 1.

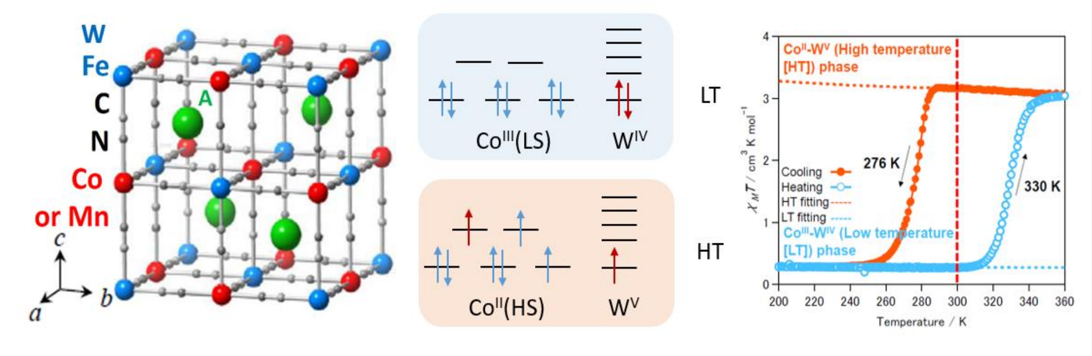

Figure 0-1 : left) Structure of Prussian blue analogs. They form a cubic structure where the basic building block is the bimetallic system Co/Mn – W/Fe connected by a cyanide bridge C-N. middle) The two electronic states of the low (low spin) and high-temperature (high spin) phases accompanied by charge transfer between tungsten and cobalt. right) Room temperature bistability showing a wide hysteresis.

One notable property of these compounds is the emergence of a wide magnetic hysteresis at room temperature. The spin transition in Cobalt is coupled with a charge transfer from tungsten to cobalt (Fig. 1). Professor Ohkoshi's laboratory focuses on developing new functionalities for applications such as humidity sensors, materials in lithium batteries, or biosensors. Consequently, a wide range of compounds based on these bimetallic assemblies is synthesized and characterized through various physico-chemical measurements (magnetism, structure, calorimetry, etc.). The response of such materials to light has been studied by various research groups, highlighting the crucial role of charge transfer in photomagnetism. In our department, the mechanisms at elementary time scales of the photoinduced transition in Co-Fe have been elucidated, distinguishing between a Spin Transition Induced Charge Transfer (STICT) mechanism and a Charge Transfer Induced Spin Transition (CTIST) mechanism. In other words, the spin transition induces charge transfer. The success of these studies relied on the experimental development of on-site pump-probe optics in Rennes or time-resolved X-ray absorption at XFEL.

Project Launch (Late 2022 - June 2023) : Our model compound Co-W exhibits strong photochromism depending on the temperature, characterized by the emergence of a charge transfer band $Co^{II}\rightarrow W^{IV}$ around 500nm at high temperature and $W^{IV}\rightarrow Co^{III}$ around 760nm at low temperature. The initial measurements, planned during my first delegation request, were carried out in the project's first year. The project implementation began with the arrival of Nakamura Kazuki, a doctoral student at the University of Tokyo, in October-December 2022 and May-June 2023. We conducted the first time-resolved pump-probe experiments on Co-W compounds starting from the low-temperature phase, probing the absorption bands and the isobestic point to access the intermediate state. The obtained results (Figure 2) are of very high quality. We were able to highlight the CTIST mechanism by activating a phonon and characterize the transformation pathway. The study of two Co-W compounds at different temperatures allowed us to understand the mechanism involved in the spin transition. I am currently in direct discussions on-site with Kazuki Nakamura regarding the writing of an article. The objective is to publish it in the middle of 2024.

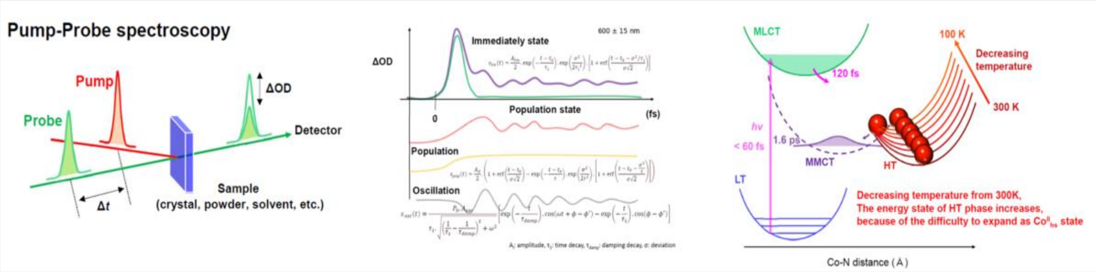

Figure 2: left) Principle of time-resolved optical absorption. middle) Variation of absorption over time and fitting considering the activation of phonons and the population factors of different states. right) Possible mechanism of the transition from low-spin phase to high-spin phase showing two intermediate states probed by time-resolved optical spectroscopy.

We are planning a campaign at the Institute of Physics in Rennes at the beginning of 2024 for these two compounds to conduct infrared spectroscopy measurements. The goal is to measure the infrared vibration modes of the CN bond (2100 cm-1) and their variation during the photoinduced phase transformation. We should be able to observe the generation of polarons through infrared spectroscopy, as demonstrated by our group in a similar compound [1], and understand the mechanisms of transformation from the local scale to the macroscopic scale.

In June 2023, we conducted a structural study using X-ray diffraction at the Institute of Physics in Rennes as a function of temperature on the Co-W-based PBA model material (Figure 3). We were able to highlight the spin transition through diffraction at different temperatures. From a crystallographic perspective, we characterized the two phases and solved the structure of the high-temperature phase (SHELXT). An important result is the identification of a two-dimensional structure. We believe that this 2D structure could give rise to confined charge transfer within a plane, inducing a two-dimensional local order. The next objective is to investigate this order through X-ray diffraction, highlighting the characteristic diffuse scattering of this local order.

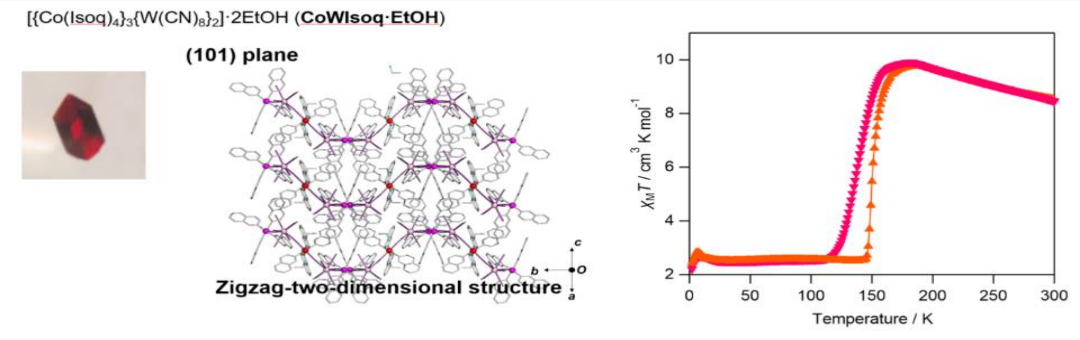

Figure 3: left) Single crystal of Co-W. middle) Structure of the high-temperature phase illustrating the 2D character of this compound. right) Magnetic susceptibility showing a spin transition at 150 K

I am beginning the second part of the project, which is conducted at the University of Tokyo in the international research laboratory DYNACOM located at the University of Tokyo. I arrived on August 1, 2023, and after a month of work to settle myself and my family, I started my duties on September 1.

The first aspect of my work involves coordinating the IRL on-site. Since my first delegation request in 2022, a significant part of my job has been managing and supervising projects and students. We responded to a joint CNRS/University of Tokyo program call for a doctoral thesis scholarship to strengthen my project locally and enhance the laboratory by integrating students. Maryam Alashoor was selected and joined our laboratory on October 1. She is currently in France at the Institute of Physics of Rennes. She will join me at the University of Tokyo in early November for a month and then for a minimum of six months starting in February 2024. She will work exclusively on the research project presented here. I also plan to intensify student exchanges in doctoral and master's programs. Professor Ohkoshi is in charge of the doctoral school at the University of Tokyo and supports this direction. I am in discussions to establish connections between our international ERASMUS master's program MAMASELF and the University of Tokyo. I will also respond to JSPS project calls, the Japanese equivalent of our ANR, to obtain a postdoctoral researcher and research credits for the DYNACOM laboratory, with the ultimate goal of setting up a first high-resolution diffraction experiment dedicated to photocrystallography studies and the development of a time-resolved optical absorption experiment using Ohkoshi's laboratory fs laser. A part of my project is to develop the DYNACOM laboratory on-site by strengthening it with human resources, funding, and experiments.

The second aspect concerns the research project itself. Now that we have understood the mechanisms of ultra-fast processes during the transition from the low to high spin phase investigated by ultra-fast optics, we will study in the same way the reverse transition, from the high spin high-temperature phase to the low spin low-temperature phase, to understand if the mechanisms involved are similar or if charge transfer occurs not from metal to metal but from metal to ligand and then by relaxation to metal. The answer to this question is completely unknown, but our initial pump-probe optical measurements should clarify the reverse mechanism. The next step will be to use other experimental techniques, especially time-resolved X-ray absorption at the Co and W absorption edge. This requires a time resolution in the range of tens of femtoseconds and therefore the use of XFEL sources [2,4]. Although there are different XFELs where we can conduct these experiments, access time is very limited. As part of my project, I propose to initiate collaborations with SACLA, the Japanese XFEL, during my stay in Japan to set up such experiments. In addition to these measurements at the XFEL, X-ray diffraction and static absorption experiments in both phases will be conducted at the Photon Factory and Spring8 synchrotron in collaboration with H. Tokoro, a member of our IRL and a professor at the University of Tsukuba.

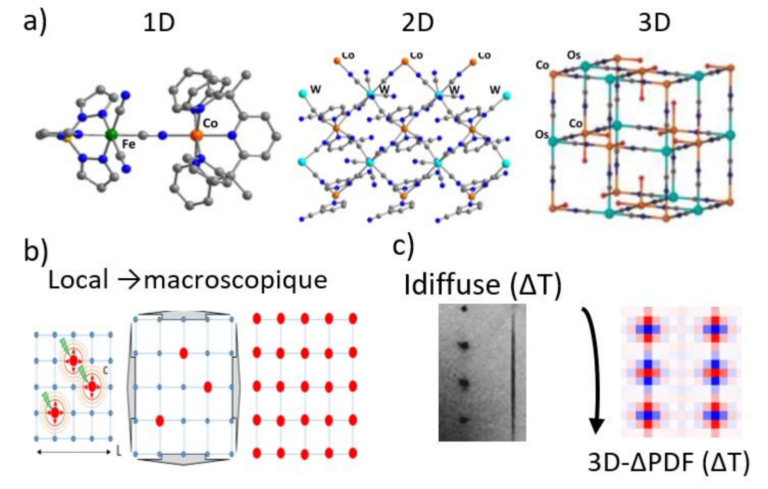

Figure 4: a) Bimetallic 1D/2D/3D assembly with cyanide bridge b) Mechanism of macroscopic domain stabilization through local-scale deformation and propagation of a pressure wave c) Time-resolved diffuse scattering and determination of the influence of local correlations on dynamics by 3D-ΔPDF resolved in time.

A plethora of compounds, molecules (0D), or 1D, 2D, 3D networks based on the elementary unit composed of a C-N group binding two metal atoms are currently synthesized and studied in Professor Ohkoshi's laboratory to understand the relationships between dimensionality and function (Fig. 4). Structurally, these compounds often exhibit local orders related to their dimensionality, which can be probed by analyzing diffuse scattering. We will perform high-resolution X-ray diffraction measurements at the synchrotron using zero-noise detectors to collect this diffuse scattering, and I plan to apply the 3D-ΔPDF analysis technique that I have been developing for several years in the laboratory [3] to these Co-W systems. The goal is to understand the correlations and local order in both phases. In the case of MX chain compounds, I have shown that the 2D charge density wave is stabilized by a network of hydrogen bonds existing between two chains. From a dynamic perspective, we expect that photoinduced processes will be strongly influenced by this dimensionality. It is not excluded that aperiodic orders may appear in the early stages of the transformation [5]. Pump-probe optical measurements will be carried out, and an analysis of the spectra of the intermediate phase will be conducted for each compound in the family.

The last issue concerns the mechanisms of the propagation of the local process, from photon absorption at the metal level to nucleation and macroscopic domain growth (Fig. 4). We now know that in spin transition compounds, where the spin change is associated with a significant volume variation, elastic coupling can lead to the propagation of a pressure wave when the material is excited by a light pulse. This pressure wave can induce cooperative phenomena and trigger a macroscopic transformation. To study these mechanisms, we will use two techniques: long-time pump-probe optics and time-resolved X-ray diffraction at the synchrotron. Structural characterization by X-ray diffraction in different phases and time-resolved pump-probe experiments will be conducted during my 2-year stay and should represent the work of half a thesis.

[1] G. Azzolina et al., Angewandte Chemie Int. Ed. 60, 232267-23273 (2021)
[2] M. Cammarata et al., Nature Chemistry 13, 10-14 (2021)
[3] Laurent Guérin et al., ChemPhysChem,23,6 (2022)
[4] C. Mariette et al., Nature Communication 12 1239 (2021)
[5] Laurent Guérin et al, Physical Review B 106,134104 (2023)

Bibliography

[1] G. Oszlányi and A. Sütő, *Ab Initio Structure Solution by Charge Flipping*, Acta Crystallogr. Sect. A **60**, 134 (2004).

[2] L. Palatinus, *The Charge-Flipping Algorithm in Crystallography*, Acta Crystallogr. Sect. B Struct. Sci. Cryst. Eng. Mater. **69**, 1 (2013).

[3] U. Muller, *Relating Crystal Structures by Group Subgroup Relations*, Urnisbn978-0-470-66079-0 **A1**, 44 (2011).

[4] P. Guionneau, *Crystallography and Spin-Crossover. A View of Breathing Materials*, Dalton Trans. **43**, 382 (2013).

[5] S. Pillet, *Spin-Crossover Materials: Getting the Most from x-Ray Crystallography*, J. Appl. Phys. **129**, 181101 (2021).

[6] *Front Matter*, in *Spin-Crossover Materials* (John Wiley & Sons, Ltd, 2013), pp. i–xviii.

[7] P. Gütlich, *Spin Crossover – Quo Vadis?*, Eur. J. Inorg. Chem. **2013**, 581 (2013).

[8] S. Decurtins, P. Gutlich, K. M. Hasselbach, A. Hauser, and H. Spiering, *Light-Induced Excited-Spin-State Trapping in Iron(II) Spin-Crossover Systems. Optical Spectroscopic and Magnetic Susceptibility Study*, Inorg. Chem. **24**, 2174 (1985).

[9] P. Gütlich, A. Hauser, and H. Spiering, *Thermal and Optical Switching of Iron(II) Complexes*, Angew. Chem. Int. Ed. Engl. **33**, 2024 (1994).

[10] E. Collet and G. Azzolina, *Coupling and Decoupling of Spin Crossover and Ferroelastic Distortion: Unsymmetric Hysteresis Loop, Phase Diagram, and Sequence of Phases*, Phys. Rev. Mater. **5**, 044401 (2021).

[11] N. Huby, L. Guerin, E. Collet, L. Toupet, J. Ameline, H. Cailleau, T. Roisnel, T. Tayagaki, and K. Tanaka, *Photoinduced Spin Transition Probed by X-Ray Diffraction*, Phys. Rev. B **69**, (2004).

[12] L. Guerin, N. Huby, E. Collet, L. Toupet, H. Cailleau, K. Tanaka, and M. Buron, *Structural Investigation of the Photoinduced Spin Transition in the Three States Molecular System [Fe(2-Pic)(3)]Cl-2 EtOH.*, in *Second International Conference on Photo-Induced Phase Transitions: Cooperative, Nonlinear and Functional Properties*, Vol. 21 (2005), pp. 136–141.

[13] D. Chernyshov, M. Hostettler, K. W. Törnroos, and H.-B. Bürgi, *Ordering Phenomena and Phase Transitions in a Spin-Crossover Compound—Uncovering the Nature of the Intermediate Phase of [Fe(2-Pic)3]Cl2·EtOH*, Angew. Chem. Int. Ed. **42**, 3825 (2003).

[14] E. Trzop, D. Zhang, L. Pineiro-Lopez, F. J. Valverde-Munoz, M. Carmen Munoz, L. Palatinus, L. Guerin, H. Cailleau, J. Antonio Real, and E. Collet, *First Step Towards a Devil's Staircase in Spin-Crossover Materials*, Angew. Chem.-Int. Ed. **55**, 8675 (2016).

[15] P. M. de Wolff, T. Janssen, and A. Janner, *The Superspace Groups for Incommensurate Crystal Structures with a One-Dimensional Modulation*, Acta Crystallogr. A **37**, 625 (1981).

[16] S. van Smaalen, *Incommensurate Crystallography* (Oxford University Press, 2007).

[17] S. van Smaalen, B. J. Campbell, and H. T. Stokes, Acta Crystallogr. A **69**, 75 (2012).

[18] T. Wagner and A. Schönleber, *A Non-Mathematical Introduction to the Superspace Description of Modulated Structures*, Acta Crystallogr. B **65**, 249 (2009).

[19] C. B. Pinheiro and A. M. Abakumov, *Superspace Crystallography: A Key to the Chemistry and Properties*, IUCrJ **2**, 137 (2015).

[20] L. Liang, Modulation of Incommensurately Modulated Structures Studied by the Maximum Entropy Method, Doctoral thesis, 2011.

[21] A. Janner and T. Janssen, *Symmetry of Periodically Distorted Crystals*, Phys. Rev. B **15**, 643 (1977).

[22] P. M. de Wolff, *The Pseudo-Symmetry of Modulated Crystal Structures*, Acta Crystallogr. A **30**, 777 (1974).

[23] P. M. de Wolff, *Symmetry Operations for Displacively Modulated Structures*, Acta Crystallogr. A **33**, 493 (1977).

[24] H. T. Stokes, D. M. Hatch, and B. J. Campbell, *ISO(3+d)D, ISOTROPY Software Suite, Iso.Byu.Edu.*, (2022).

[25] H. T. Stokes, B. J. Campbell, and S. van Smaalen, Acta Crystallogr. A **67**, 45 (2010).

[26] V. Petříček, M. Dušek, and L. Palatinus, Z. Für Krist. - Cryst. Mater. **229**, 345 (2014).

[27] L. Guérin, E. Trzop, T. Ishikawa, S. Koshihara, T. Yamamoto, B. Toudic, and R. Kato, *Frustrated Competitive Forces in the Et2Me2Sb[Pd(Dmit)2]2 Molecular Conductor*, Phys. Rev. B **108**, 134104 (2023).

[28] T. Janssen, A. Janner, A. Looijenga-Vos, and P. M. de Wolff, Int. Tables Crystallogr. 907 (2006).

[29] R. A. Cowley and A. D. Bruce, J. Phys. C Solid State Phys. **11**, 3577 (1978).

[30] R. Blinc and A. P. Levanyuk, *Incommensurate Phases in Dielectrics, Vols. 1 and 2* (R. Blinc,A. P. Levanyuk, Amsterdam, 1986).

[31] K. K. Kolincio, R. Daou, O. Perez, L. Guerin, P. Fertey, and A. Pautrat, *Giant Nernst Effect in the Incommensurate Charge Density Wave State of P4W12O44*, Phys. Rev. B **94**, (2016).

[32] T. Janssen, G. Chapuis, M. de Boissieu, T. Janssen, G. Chapuis, and M. de Boissieu, *Aperiodic Crystals: From Modulated Phases to Quasicrystals: Structure and Properties*, Second Edition, Second Edition (Oxford University Press, Oxford, New York, 2018).

[33] E. Castillo-Martínez, A. Schönleber, S. van Smaalen, A. M. Arévalo-López, and M. A. Alario-Franco, *Structure and Microstructure of the High Pressure Synthesised Misfit Layer Compound [Sr2O2][CrO2]1.85*, J. Solid State Chem. **181**, 1840 (2008).

[34] L. Cario, A. Meerschaut, B. Corraze, and O. Chauvet, *Determination of the Modulated Structure of the Misfit Layer Compound (LaS)1.196VS2*, Mater. Res. Bull. **40**, 125 (2005).

[35] H. Leligny, D. Grebille, O. Pérez, A. C. Masset, M. Hervieu, and B. Raveau, *A Five-Dimensional Structural Investigation of the Misfit Layer Compound [Bi0.87SrO2]2[CoO2]1.82*, Acta Crystallogr. B **56**, 173 (2000).

[36] O. Pérez, L. Adam, A. Guesdon, M. Daturi, and B. Raveau, *Complex Disorder in β-NH4Fe2(PO4)2: Deciphering from a Five-Dimensional Formalism*, Acta Crystallogr. B **63**, 521 (2007).

[37] S. van Smaalen, A. Meetsma, G. A. Wiegers, and J. L. de Boer, *Determination of the Modulated Structure of the Inorganic Misfit Layer Compound (PbS)1.18TiS2*, Acta Crystallogr. B **47**, 314 (1991).

[38] J. Sun, S. Lee, and J. Lin, *Four-Dimensional Space Groups for Pedestrians: Composite Structures*, Chem. – Asian J. **2**, 1204 (2007).

[39] L. Guerin et al., *Long-Range Modulation of a Composite Crystal in a Five-Dimensional Superspace*, Phys. Rev. B **91**, (2015).

[40] R. Lefort, J. Etrillard, B. Toudic, F. Guillaume, T. Breczewski, and P. Bourges, *Incommensurate Intermodulation of an Organic Intergrowth Compound Observed by Neutron Scattering*, Phys. Rev. Lett. **77**, 4027 (1996).

[41] A. P. Tsai, J. Q. Guo, E. Abe, H. Takakura, and T. J. Sato, *A Stable Binary Quasicrystal*, Nature **408**, 6812 (2000).

[42] H. Takakura, C. P. Gómez, A. Yamamoto, M. De Boissieu, and A. P. Tsai, *Atomic Structure of the Binary Icosahedral Yb–Cd Quasicrystal*, Nat. Mater. **6**, 1 (2007).

[43] R. Tamura, Y. Murao, S. Takeuchi, M. Ichihara, M. Isobe, and Y. Ueda, *A Low-Temperature Order-Disorder Transition in a Cubic Cd6Yb Crystalline Approximant*, Jpn. J. Appl. Phys. **41**, L524 (2002).

[44] R. Tamura, K. Edagawa, C. Aoki, S. Takeuchi, and K. Suzuki, *Low-Temperature Structural Phase Transition in a ${\mathrm{Cd}}_{6}\mathrm{Y}$ 1/1 Approximant*, Phys. Rev. B **68**, 174105 (2003).

[45] C. P. Gómez and S. Lidin, *Comparative Structural Study of the Disordered MCd6 Quasicrystal Approximants*, Phys. Rev. B **68**, 024203 (2003).

[46] T. R. Welberry, *Diffuse X-Ray Scattering and Models of Disorder*, Rep. Prog. Phys. **48**, 1543 (1985).

[47] T. R. Welberry and T. Weber, *One Hundred Years of Diffuse Scattering*, Crystallogr. Rev. **22**, 2 (2016).

[48] A. Simonov and A. L. Goodwin, *Designing Disorder into Crystalline Materials*, Nat. Rev. Chem. **4**, 12 (2020).

[49] D. A. Keen and A. L. Goodwin, *The Crystallography of Correlated Disorder*, Nature **521**, 7552 (2015).

[50] S. Ravy, *Diffuse X-Ray Scattering Studies of Molecular Conductors*, Annu. Rep. Sect. C Phys. Chem. **103**, 223 (2007).

[51] J.-P. Pouget, *X-Ray Diffuse Scattering as Precursor of Incommensurate Peierls Transitions in One-Dimensional Organic Charge Transfer Conductors*, Z. Für Krist. - Cryst. Mater. **219**, 711 (2004).

[52] S. Ravy, P. Launois, R. Moret, and J.-P. POUGET, *Case Studies of Molecular Disorder*, Z. Für Krist. **220**, 1059 (2005).

[53] E. Collet, M. H. Lemée-Cailleau, M. B.-L. Cointe, H. Cailleau, S. Ravy, T. Luty, J. F. Bérar, P. Czarnecki, and N. Karl, *Direct Evidence of Lattice-Relaxed Charge Transfer Exciton Strings*, Europhys. Lett. **57**, 67 (2002).

[54] M. Buron-Le Cointe, M. H. Lemée-Cailleau, H. Cailleau, S. Ravy, J. F. Bérar, S. Rouzière, E. Elkaïm, and E. Collet, *One-Dimensional Fluctuating Nanodomains in the Charge-Transfer Molecular System TTF-CA and Their First-Order Crystallization*, Phys. Rev. Lett. **96**, 205503 (2006).

[55] K. Otsubo, Y. Wakabayashi, J. Ohara, S. Yamamoto, H. Matsuzaki, H. Okamoto, K. Nitta, T. Uruga, and H. Kitagawa, *Bottom-up Realization of a Porous Metal–Organic Nanotubular Assembly*, Nat. Mater. **10**, 4 (2011).

[56] Y. Wakabayashi, N. Wakabayashi, M. Yamashita, T. Manabe, and N. Matsushita, *Spatial Correlations in the Valence of Metal Ions in Ni 1- xPd x(Chxn) 2Br 3*, J. Phys. Soc. Jpn. **68**, 3948 (1999).

[57] M. Yamashita, H. Okamoto, H. Iguchi, K. Iwano, H. Kishida, H. Matsuzaki, M. Mitsumi, A. Nakamura, S. Takaishi, and K. Yonemitsu, *Material Designs*

and New Physical Properties in MX-and MMX-Chain Compounds, in *Material Designs and New Physical Properties in MX- and MMX-Chain Compounds* (Springer-Verlag Wien, 2012), pp. 1–270.

[58] P. Launois, S. Ravy, and R. Moret, *Diffuse Scattering and Orientational Correlations in Solid ${\mathrm{C}}_{60}$*, Phys. Rev. B **52**, 5414 (1995).

[59] P. Launois, R. Moret, D. Le Bolloc'h, P. A. Albouy, Z. K. Tang, G. Li, and J. Chen, *Carbon Nanotubes Synthesised in Channels of AlPO4-5 Single Crystals: First X-Ray Scattering Investigations*, Solid State Commun. **116**, 99 (2000).

[60] R. Moret, P. Launois, T. Wågberg, B. Sundqvist, V. Agafonov, V. A. Davydov, and A. V. Rakhmanina, *Single-Crystal Structural Study of the Pressure-Temperature-Induced Dimerization of C60*, Eur. Phys. J. B - Condens. Matter Complex Syst. **37**, 25 (2004).

[61] S. P. Meisburger, D. A. Case, and N. Ando, *Diffuse X-Ray Scattering from Correlated Motions in a Protein Crystal*, Nat. Commun. **11**, 1 (2020).

[62] J.-P. Benoit and J. Doucet, *Diffuse Scattering in Protein Crystallography*, Q. Rev. Biophys. **28**, 131 (1995).

[63] A. Simonov, T. De Baerdemaeker, H. L. B. Boström, M. L. Ríos Gómez, H. J. Gray, D. Chernyshov, A. Bosak, H.-B. Bürgi, and A. L. Goodwin, *Hidden Diversity of Vacancy Networks in Prussian Blue Analogues*, Nature **578**, 7794 (2020).

[64] A. R. Overy, A. B. Cairns, M. J. Cliffe, A. Simonov, M. G. Tucker, and A. L. Goodwin, *Design of Crystal-like Aperiodic Solids with Selective Disorder–Phonon Coupling*, Nat. Commun. **7**, 1 (2016).

[65] T. R. Welberry and B. D. Butler, *Interpretation of Diffuse X-Ray Scattering via Models of Disorder*, J. Appl. Crystallogr. **27**, 205 (1994).

[66] P. Rabiller, C. Mariette, L. Guérin, and B. Toudic, *Rayons X et matière 5 : RX 2013* (ISTE editions, London, 2017).

[67] M. Greenholz and A. Kidron, *The Structure of Short-Range Ordered Alloys. I. Clustering of Ordered Cells*, Acta Crystallogr. A **26**, 306 (1970).

[68] A. Guinier, *X-Ray Diffraction in Crystals, Imperfect Crystals, and Amorphous Bodies*, No Title (n.d.).

[69] M. Holt, *Determination of Phonon Dispersions from X-Ray Transmission Scattering: The Example of Silicon*, Phys. Rev. Lett. **83**, 3317 (1999).

[70] B. Wehinger, A. Mirone, M. Krisch, and A. Bosak, *Full Elasticity Tensor from Thermal Diffuse Scattering*, Phys. Rev. Lett. **118**, 035502 (2017).

[71] M. A. Estermann and W. Steurer, *Diffuse Scattering Data Acquisition Techniques*, Phase Transit. **67**, 165 (1998).

[72] C. Ecolivet, M. Verezhak, C. Mariette, L. Guérin, P. Rabiller, J. Ollivier, A. Bosak, and B. Toudic, *Phonons in an Aperiodic Alkane/Urea Composite Crystal Studied by Inelastic x-Ray Scattering*, Phys. Rev. B **98**, 224308 (2018).

[73] B. Toudic, P. Garcia, C. Odin, P. Rabiller, C. Ecolivet, E. Collet, P. Bourges, G. J. McIntyre, M. D. Hollingsworth, and T. Breczewski, *Hidden Degrees of Freedom in Aperiodic Materials*, Science **319**, 69 (2008).

[74] C. Mariette et al., *Critical Phenomena in Higher Dimensional Spaces: The Hexagonal-to-Orthorhombic Phase Transition in Aperiodic n-Nonadecane/Urea*, Phys. Rev. B **87**, (2013).

[75] C. Mariette, L. Guerin, P. Rabiller, Y.-S. Chen, A. Bosak, A. Popov, M. D. Hollingsworth, and B. Toudic, *The Creation of Modulated Monoclinic Aperiodic Composites in N-Alkane/Urea Compounds*, Z. Krist. **230**, 5 (2015).

[76] T. Weber, H. Boysen, and F. Frey, *Longitudinal Positional Ordering of N-Alkane Molecules in Urea Inclusion Compounds*, Acta Crystallogr. B **56**, 132 (2000).

[77] T. Weber and A. Simonov, *The Three-Dimensional Pair Distribution Function Analysis of Disordered Single Crystals: Basic Concepts*, Z. Für Krist. **227**, 238 (2012).

[78] L. Guérin, T. Yoshida, E. Zatterin, A. Simonov, D. Chernyshov, H. Iguchi, B. Toudic, S. Takaishi, and M. Yamashita, *Elucidating 2D Charge-Density-Wave Atomic Structure in an MX–Chain by the 3D-${upDelta*, (2022).

[79] S. Takaishi et al., *Charge-Density-Wave to Mott−Hubbard Phase Transition in Quasi-One-Dimensional Bromo-Bridged Pd Compounds*, J. Am. Chem. Soc. **130**, 12080 (2008).

[80] V. Dyadkin, P. Pattison, V. Dmitriev, and D. Chernyshov, *A New Multipurpose Diffractometer PILATUS@SNBL*, J. Synchrotron Radiat. **23**, 825 (2016).

[81] A. Simonov, T. Weber, and W. Steurer, *Yell: A Computer Program for Diffuse Scattering Analysis via Three-Dimensional Delta Pair Distribution Function Refinement*, J. Appl. Crystallogr. **47**, 1146 (2014).

[82] K. Otake, K. Otsubo, and H. Kitagawa, *A Mixed-Valent Metal–Organic Ladder Linked by Pyrazine*, J. Phys. Condens. Matter **33**, 034002 (2020).

[83] M. R. Mian, H. Iguchi, S. Takaishi, U. Afrin, T. Miyamoto, H. Okamoto, and M. Yamashita, *Smallest Optical Gap for Pt(II)–Pt(IV) Mixed-Valence Pt–Cl and Pt–Br Chain Complexes Achieved by Using a Multiple-Hydrogen-Bond Approach*, Inorg. Chem. **58**, 114 (2019).

[84] S. Ravy, *Study of Molecular Conductors by X-Ray Diffuse Scattering*, Chem. Rev. **104**, 5609 (2004).

[85] A. Simonov, P. Rabiller, C. Mariette, L. Guérin, A. Bosak, A. Popov, and B. Toudic, *Short-Range Order in the Quasiliquid Phases of Alkane Substructures within Aperiodic Urea Inclusion Crystals*, Phys. Rev. B **106**, (2022).

[86] J. Weng, E. D. Dill, J. D. Martin, R. Whitfield, C. Hoffmann, and F. Ye, *K-Space Algorithmic Reconstruction (KAREN): A Robust Statistical Methodology to Separate Bragg and Diffuse Scattering*, J. Appl. Crystallogr. **53**, 159 (2020).

[87] E. M. Schmidt, P. B. Klar, Y. Krysiak, P. Svora, A. L. Goodwin, and L. Palatinus, *Quantitative Three-Dimensional Local Order Analysis of Nanomaterials through Electron Diffraction*, Nat. Commun. **14**, 1 (2023).

[88] *Truchet-Tile Structure of a Topologically Aperiodic Metal–Organic Framework | Science*, https://www.science.org/doi/full/10.1126/science.ade5239.

[89] M. Sadakiyo, T. Yamada, and H. Kitagawa, *Rational Designs for Highly Proton-Conductive Metal−Organic Frameworks*, J. Am. Chem. Soc. **131**, 9906 (2009).

[90] T. Yamada, K. Otsubo, R. Makiura, and H. Kitagawa, *Designer Coordination Polymers: Dimensional Crossover Architectures and Proton Conduction*, Chem. Soc. Rev. **42**, 6655 (2013).

[91] M. R. Mian, U. Afrin, H. Iguchi, S. Takaishi, T. Yoshida, T. Miyamoto, H. Okamoto, H. Tanaka, S. Kuroda, and M. Yamashita, *Conductive Zigzag Pd(III)–Br Chain Complex Realized by a Multiple-Hydrogen-Bond Approach*, CrystEngComm **22**, 3999 (2020).

[92] U. Afrin, H. Iguchi, M. R. Mian, S. Takaishi, H. Yamakawa, T. Terashige, T. Miyamoto, H. Okamoto, and M. Yamashita, *MX-Type Single Chain Complexes*

with an Aromatic in-Plane Ligand: Incorporation of Aromatic Interactions for Stabilizing the Chain Structure, Dalton Trans. **48**, 7828 (2019).

[93] T. Yoshida et al., *Hydrogen Bonding Propagated Phase Separation in Quasi-Epitaxial Single Crystals: A Pd-Br Molecular Insulator*, (2022).

[94] T. Yoshida et al., *Optically Visible Phase Separation between Mott-Hubbard and Charge-Density-Wave Domains in a Pd-Br Chain Complex*, Chemistryselect **1**, 259 (2016).

[95] H. Ki, K. Y. Oang, J. Kim, and H. Ihee, *Ultrafast X-Ray Crystallography and Liquidography*, Annu. Rev. Phys. Chem. **68**, 473 (2017).

[96] E. A. Schriber et al., *Chemical Crystallography by Serial Femtosecond X-Ray Diffraction*, Nature **601**, 7893 (2022).

[97] S. Koshihara, Y. Takahashi, H. Sakai, Y. Tokura, and T. Luty, *Photoinduced Cooperative Charge Transfer in Low-Dimensional Organic Crystals*, J. Phys. Chem. B **103**, 2592 (1999).

[98] K. Nasu, *Photoinduced Phase Transitions*, High Energy Accelerator Research Organization (KEK), Japan (2004).

[99] H. Ichikawa et al., *Transient Photoinduced "hidden" Phase in a Manganite*, Nat. Mater. **10**, 101 (2011).

[100] P. Coppens, D. V. Fomitchev, M. D. Carducci, and K. Culp, *Crystallography of Molecular Excited States. Transition-Metal Nitrosyl Complexes and the Study of Transient Species*, J. Chem. Soc. Dalton Trans. 865 (1998).

[101] E. Collet, M. Lorenc, M. Cammarata, L. Guerin, M. Servol, A. Tissot, M.-L. Boillot, H. Cailleau, and M. Buron-Le Cointe, *100 Picosecond Diffraction Catches Structural Transients of Laser-Pulse Triggered Switching in a Spin-Crossover Crystal*, Chem.- Eur. J. **18**, 2051 (2012).

[102] K. Nelson, *Watching Matter Rearrange | Science*, Science **286**, 1310 (1999).

[103] S. Nozawa et al., *Developing 100 Ps-Resolved X-Ray Structural Analysis Capabilities on Beamline NW14A at the Photon Factory Advanced Ring*, J. Synchrotron Radiat. **14**, 313 (2007).

[104] S. Adachi et al., *Pulsed Synchrotron X-Ray as a Tool for Providing Molecular Movies at 100-Picosecond Temporal and Sub-Nanometer Spatial Resolution*, Lxiii Yamada Conf. Photo-Induc. Phase Transit. Coop. Phenom. Pipt3 **148**, (2009).

[105] L. Guerin, Q. Kong, D. Khakhulin, M. Cammarata, H. Ihee, and M. Wulff, *Tracking Atomic Positions in Molecular Reactions by Picosecond X-Ray Scattering at the ESRF*, Synchrotron Radiat. News **25**, 25 (2012).

[106] C. Pellegrini, *The History of X-Ray Free-Electron Lasers*, Eur. Phys. J. H **37**, 659 (2012).

[107] Y. Kubota, Y. Tanaka, T. Togashi, T. Ebisu, K. Tamasaku, H. Osawa, T. Wada, O. Sugino, I. Matsuda, and M. Yabashi, *Suppression of Atomic Displacive Excitation in Photo-Induced A1g Phonon Mode of Bismuth Unveiled by Low-Temperature Time-Resolved x-Ray Diffraction*, Appl. Phys. Lett. **122**, 092201 (2023).

[108] M. Harmand et al., *Achieving Few-Femtosecond Time-Sorting at Hard X-Ray Free-Electron Lasers*, Nat. Photonics **7**, 3 (2013).

[109] C. Mariette et al., *Strain Wave Pathway to Semiconductor-to-Metal Transition Revealed by Time-Resolved X-Ray Powder Diffraction*, Nat. Commun. **12**, 1 (2021).

[110] M. Hervé et al., *Ultrafast and Persistent Photoinduced Phase Transition at Room Temperature Monitored by Streaming Powder Diffraction*, Nat. Commun. **15**, 267 (2024).

[111] K. Takubo et al., *Generation of Sub-100 Fs Electron Pulses for Time-Resolved Electron Diffraction Using a Direct Synchronization Method*, Rev. Sci. Instrum. **93**, 053005 (2022).

[112] T. Ishikawa, *Direct Observation of Collective Modes Coupled to Molecular Orbital–Driven Charge Transfer | Science*, Science **350**, 1501 (2015).

[113] E. Collet et al., *Aperiodic Spin State Ordering of Bistable Molecules and Its Photoinduced Erasing*, Phys. Rev. Lett. **109**, 257206 (2012).

[114] H. Itoh, H. Obatake, R. Fujiwara, Y. Kawakami, K. Yamamoto, M. Dressel, and S. Iwai, *Charge Correlations and Their Photoinduced Dynamics in Charge-Ordered Organic Ferroelectrics*, Phys. Rev. Res. **3**, L032043 (2021).

[115] M. Servol et al., Phys. Rev. B **92**, 024304 (2015).

[116] L. C. Liu, Y. Jiang, H. M. Mueller-Werkmeister, C. Lu, G. Moriena, M. Ishikawa, Y. Nakano, H. Yamochi, and R. J. D. Miller, *Ultrafast Electron Diffraction Study of Single-Crystal (EDO-TTF)2SbF6: Counterion Effect and Dimensionality Reduction*, Chem. Phys. Lett. **683**, 160 (2017).

[117] N. Fukazawa, T. Tanaka, T. Ishikawa, Y. Okimoto, S. Koshihara, T. Yamamoto, M. Tamura, R. Kato, and K. Onda, *Time-Resolved Infrared Vibrational Spectroscopy of the Photoinduced Phase Transition of Pd(Dmit)2 Salts Having Different Orders of Phase Transition*, J. Phys. Chem. C **117**, 13187 (2013).

[118] A. Kogar et al., *Light-Induced Charge Density Wave in LaTe3 | Nature Physics*, Nat. Phys. **16**, 159 (2020).

[119] L. Guerin, J. Hebert, M. B.-L. Cointe, S. Adachi, S. Koshihara, H. Cailleau, and E. Collet, *Capturing One-Dimensional Precursors of a Photoinduced Transformation in a Material*, Phys. Rev. Lett. **105**, (2010).

[120] C. Laulhé et al., *Ultrafast Formation of a Charge Density Wave State in 1T-TaS2: Observation at Nanometer Scales Using Time-Resolved X-Ray Diffraction*, Phys. Rev. Lett. **118**, 247401 (2017).

[121] A. Zong et al., *Evidence for Topological Defects in a Photoinduced Phase Transition*, Nat. Phys. **15**, 1 (2019).

[122] C. Franchini, M. Reticcioli, M. Setvin, and U. Diebold, *Polarons in Materials*, Nat. Rev. Mater. **6**, 7 (2021).

[123] S. Shimomura, *X-Ray Diffuse Scattering Due to Polarons in a Colossal Magnetoresistive Manganite*, Phys. Rev. Lett. **83**, 4389 (1999).

[124] B. Guzelturk et al., *Visualization of Dynamic Polaronic Strain Fields in Hybrid Lead Halide Perovskites | Nature Materials*, Nat. Mater. **20**, 618 (2021).

Appendices

Appendix A

Contributions

[1]Laurent Guérin*, Elzbieta Trzop, Tadahiko Ishikawa, Shinya Koshihara ,Takashi Yamamoto, Bertrand Toudic, Reizo Kato*, Frustrated competitive forces in the Et2Me2Sb[Pd(dmit)2]2 molecular conductor, Physical Review B 108, 134104 (2023).

> Principal investigator, coordination of the project, conduct the experiment, analyse of the data, Complete writing of the manuscript.

[2]Céline Mariette,Philippe Rabiller,Laurent Guérin, Claude Ecolivet ,Ilya Frantsuzov, Bo Wang, Shane M. Nichols, Philippe Bourges, Alexei Bosak, Yu-Sheng Chen, Mark D. Hollingsworth, Bertrand Toudic, Physical Review B 106, 134109 (2022).

> Investigator, conduct the experiment, analyse of the data, support on writing the manuscript.

[3]A. Simonov, P. Rabiller, C. Mariette, L. Guérin, A. Bosak, A. Popov, and B. Toudic, Short-Range Order in the Quasiliquid Phases of Alkane Substructures within Aperiodic Urea Inclusion Crystals, Physical Review B 106, 054206 (2022).

> Conduct the experiment, partial analysis of the data

[4]T. Yoshida, S. Takaishi, L. Guérin, T. Kojima, H. Ohtsu, M. Kawano, T. Miyamoto, H. Okamoto, K. Kato, M. Takata, Y. Hosomi, S. Yoshida, H. Shigekawa, H. Tanaka, S. Kuroda, H. Iguchi, B. K. Breedlove, Z.-Y. Li, and M. Yamashita, Hydrogen Bonding Propagated Phase Separation in Quasi-Epitaxial Single Crystals: A Pd–Br Molecular Insulator, Inorganic Chemistry,61,35,14067 (2022)

> Conduct the experiment, partial analysis of the data. support on writing the manuscript.

[5]L. Guérin*, T. Yoshida*, E. Zatterin, A. Simonov, D. Chernyshov, H. Iguchi, B. Toudic, S. Takaishi, and M. Yamashita, Elucidating 2D Charge-Density-Wave Atomic Structure in an MX–Chain by the 3D-ΔPair Distribution Function Method, ChemPhysChem 23 (2022). VIP + COVER

> Principal investigator, coordination of the project, conduct the experiment, analyse of the data, Complete writing of the manuscript. Supervision of E. Zatterin, T. Yoshida, E. Collet, G. Adam

[6]Gournay, L., Chaban, I., Mevellec, J.-Y., Humbert, B., Janod, E., Guérin, L., Cammarata, M., Daro, N., Chastanet, G., & Collet, E. Shifting photo-stationary light-induced excited spin state trapping equilibrium towards higher temperature by increasing light fluence. In Chemical Physics Letters 791, p. 139395. (2022)

> Supervision of L. Gournay

[7]Céline Mariette, Maciej Lorenc, Hervé Cailleau, Eric Collet, Laurent Guérin, et al.. Strain wave pathway to semiconductor-to-metal transition revealed by time-resolved X-ray powder diffraction. Nature Communications, 12 (1), pp.1239. (2021)

> Conduct the experiment

[8]Céline Mariette*, Laurent Guérin*, Philippe Rabiller, Christophe Odin, Mariana Verezhak, et al.. High spatial resolution studies of phase transitions within organic aperiodic crystals. Physical Review B, American Physical Society, 2020, 101 (18)

> Principal investigator, coordination of the project, conduct the experiment, analyse of the data, writing of the manuscript. Supervision of M. Verezhak.

[9]B. Toudic, Laurent Guérin, C. Mariette, I. Frantsuzov, P. Rabiller, et al.. Comment on Couzi et al. (2018): a phenomenological model for structural transitions in incommensurate alkane/urea inclusion compounds. Royal Society Open Science, The Royal Society, 2019, 6 (8), pp.182073.

> Analyse of the data, Co-writing of the manuscript

[10]Eric Collet, Giovanni Azzolina, Tomoaki Ichii, Laurent Guérin, Roman Bertoni, et al.. Lattice phonon modes of the spin crossover crystal [Fe(phen)2(NCS)2] studied by THz, IR, Raman spectroscopies and DFT calculations. European Physical Journal B: Condensed Matter and Complex Systems, 2019, 92 (1), pp.12

> Conduct the Thz spectroscopy experiment at the University of Kyoto

[11]C. Ecolivet, M. Verezhak, Céline Mariette, Laurent Guérin, P. Rabiller, et al.. Phonons in an aperiodic alkane/urea composite crystal studied by inelastic x-ray scattering. Physical Review B, 2018, 98 (22), pp.224308+.

> Writing of the proposal, conduct the experiment, writing of analysis program, supervision of M. Verezhak.

[12]Céline Mariette, Philippe Rabiller, Laurent Guérin, Bertrand Toudic. Crystallography and dynamics in superspace. EPJ Web of Conferences, 2017, 155

> Review article based on previous work, support on writing the manuscript

[13]T. Yoshida, S. Takaishi, H. Iguchi, H. Okamoto, H. Tanaka, S. Kuroda, Y. Hosomi, S. Yoshida, H. Shigekawa, T. Kojima, H. Ohtsu, M. Kawano, B. K. Breedlove, L. Guérin, and M. Yamashita, Optically Visible Phase Separation between Mott-Hubbard and Charge-Density-Wave Domains in a Pd-Br Chain Complex, ChemistrySelect 1, 259 (2016).

> Coordination of the project, support on writing the manuscript.

[14] E. Trzop, D. Zhang, L. Piñeiro-Lopez, F. J. Valverde-Muñoz, M. Carmen Muñoz, L. Palatinus, L. Guérin, H. Cailleau, J. A. Real, and E. Collet, Inside Back Cover: First Step Towards a Devil’s Staircase in Spin-Crossover Materials, Angewandte Chemie International Edition 55, 1 (2016).

> Structure determination using superspace crystallography, support on writing the manuscript

[15]C. Mariette, Ilya Frantsuzov, Bo Wang, Laurent Guérin, P. Rabiller, et al.. Frustrated pretransitional phenomena in aperiodic composites. Physical Review B, 2016, 94 (18).

> Conduct the experiment, writing of analysis program, support on writing the manuscript.

[16] Kamil K. Kolincio, Ramzy Daou, Olivier Perez, Laurent Guérin, Pierre Fertey, et al.. Giant Nernst effect in the incommensurate charge density wave state of P4W12O44. Physical Review B, 2016, 94 (24), pp.241118

> Participation to the experiment, support on writing the manuscript

[17] K. H. Kim, J. Kim, K. Y. Oang, J. H. Lee, D. Grolimund, C. J. Milne, T. J. Penfold, S. L. Johnson, A. Galler, T. W. Kim, J. G. Kim, D. Suh, J. Moon, J. Kim, K. Hong, L. Guérin, T. K. Kim, M. Wulff, C. Bressler, and H. Ihee, Identifying the Major Intermediate Species by Combining Time-Resolved X-Ray Solution Scattering and X-Ray Absorption Spectroscopy, Phys. Chem. Chem. Phys. 17, 23298 (2015).

> Beamline scientist at ESRF. Preparation of the experiment. Conduct of the experiment.

[18] S. Zerdane, C. Mariette, G. J. McIntyre, M.-H. Lemée-Cailleau, P. Rabiller, L. Guérin, J. C. Ameline, and B. Toudic, Neutron Laue and X-Ray Diffraction Study of a New Crystallographic Superspace Phase Inn-Nonadecane–Urea, Acta Crystallographica Section B, 71, 293 (2015).

> Conduct the experiment of X-ray diffraction using Helium gaz. Supervision of S. Zerdane

[19] Laurent Guérin, Céline Mariette, Philippe Rabiller, Michael Huard, Sylvain Ravy, et al.. Long-range modulation in a five-dimensional crystallographic superspace. Physical Review B , 2015, 91 (18), pp.184101.

> Principal investigator, coordination of the project, conduct the experiment, analyse of the data, Co-writing of the manuscript.

[20] Céline Mariette, Laurent Guérin, Philippe Rabiller, Yu-Sheng Chen, Alexei Bosak, et al.. The creation of modulated monoclinic aperiodic composites in n-alkane/urea compounds. Zeitschrift für Kristallographie, 2015, 230 (1), pp.5--11.

> Analyse of data, support on writing the manuscript

[21]Céline Mariette, Laurent Guérin, Philippe Rabiller, Claude Ecolivet, P. Garcia-Orduna, et al.. Critical phenomena in higher dimensional spaces : The hexagonal-to-orthorhombic phase transition in aperiodic n-nonadecane/urea.. Physical Review B, 2013, 87 (10), pp.104101.

> Principal investigator, coordination of the project, conduct the experiment, development of analyse program, analyse of the data, Co-writing of the manuscript, supervision of C. Mariette

[22] J. H. Lee, M. Wulff, S. Bratos, J. Petersen, L. Guerin, J.-C. Leicknam, M. Cammarata, Q. Kong, J. Kim, K. B. Møller, and H. Ihee, Filming the Birth of Molecules and Accompanying Solvent Rearrangement, J. Am. Chem. Soc. 135, 3255 (2013)

> Beamline scientist at ESRF. Preparation the experiment. Conduct the experiment.

[23] W. Kaszub, M. Buron-Le Cointe, M. Lorenc, M. Boillot, M. Servol, A. Tissot, L. Guérin, H. Cailleau, and E. Collet, Spin-State Photoswitching Dynamics of the (TPA)Fe(TCC)]SbF6 Complex, European Journal of Inorganic Chemistry 2013, 992 (2012).

> Participation to the experiment

[24]Eric Collet, Maciej Lorenc, Marco Cammarata, Laurent Guérin, Marina Servol, et al.. 100 picosecond diffraction catches structural transients of laser-pulse triggered switching in a spin-crossover crystal.. Chemistry - A European Journal, 2012, 18 (7), pp.2051-5.

> Beamline scientist at ESRF. Preparation the experiment. Conduct the experiment, support on writing the manuscript.

[25] Laurent Guérin, Qingyu Kong, Dmitry Khakhulin, Marco Cammarata, Hyotcherl Ihee, et al.. Tracking Atomic Positions in Molecular Reactions by Picosecond X-ray Scattering at the ESRF. Synchrotron Radiation News, 2012, 25 (2), pp.25-31.

> Beamline scientist at ESRF. Principal investigator, coordination of the project, conduct the experiment, analyse of the data, Co-writing of the manuscript.

[26]H. Shimizu, M. Iwamoto, T. Konno, A. Royant, S. Von David, L. Guérin, M. Wulff, and S. Oiki, Laser-Triggered Single Molecular Gating Motions of the KcsA Potassium Channels Recorded in a Sub-Millisecond Time Resolution, Biophysical Journal 102, 37a (2012).

Beamline scientist at ESRF. Preparation the experiment. Conduct the experiment. Development of data analysis program.

[27] K. Haldrup, T. Harlang, M. Christensen, A. Dohn, T. B. van Driel, K. S. Kjær, N. Harrit, J. Vibenholt, L. Guérin, M. Wulff, and M. M. Nielsen, Bond Shortening (1.4 Å) in the Singlet and Triplet Excited States of [Ir2(Dimen)4]2+ in Solution Determined by Time-Resolved X-Ray Scattering, Inorg. Chem. 50, 9329 (2011).

Beamline scientist at ESRF. Preparation the experiment. Conduct the experiment.

[28] M. Huard, Bertrand Toudic, Philippe Rabiller, Claude Ecolivet, Laurent Guérin, et al.. Confined linear molecules inside an aperiodic supramolecular crystal: The sequence of superspace phases in n-hexadecane/urea. Journal of Chemical Physics, 2011, 135 (20), pp.204505.

Data analysis, support on writing the manuscript.

[29] Nüske, A. Jurgilaitis, H. Enquist, S. D. Farahani, J. Gaudin, L. Guérin, M. Harb, C. v. K. Schmising, M. Störmer, M. Wulff, and J. Larsson, Picosecond Time-Resolved x-Ray Refectivity of a Laser-Heated Amorphous Carbon Film, Appl. Phys. Lett. 98, 101909 (2011).

Beamline scientist at ESRF. Preparation the experiment. Conduct the experiment.

[30] J. Gaudin, B. Keitel, A. Jurgilaitis, R. Nüske, L. Guérin, J. Larsson, K. Mann, B. Schäfer, K. Tiedtke, A. Trapp, Th. Tschentscher, F. Yang, M. Wulff, H. Sinn, and B. Flöter, Time-Resolved Investigation of Nanometer Scale Deformations Induced by a High Flux x-Ray Beam, Opt. Express 19, 15516 (2011).

Beamline scientist at ESRF. Preparation the experiment. Conduct the experiment.

[31] Bertrand Toudic, Ronan Lefort, Claude Ecolivet, Laurent Guérin, Roland Currat, et al.. Mixed acoustic phonons and phase modes in an aperiodic composite crystal. Physical Review Letters, 2011, 107 (20), pp.205502.

Data analysis, support on writing the manuscript.

[32] H. Ichikawa, S. Nozawa, T. Sato, A. Tomita, K. Ichiyanagi, M. Chollet, L. Guérin, N. Dean, A. Cavalleri, S. Adachi, T. Arima, H. Sawa, Y. Ogimoto, M. Nakamura, R. Tamaki, K. Miyano, and S. Koshihara, Transient Photoinduced ‘Hidden’ Phase in a Manganite, Nature Material 10, 101 (2011)

Beamline scientist at KEK. Preparation of the experiment. Conduct the experiment, support on writing the manuscript.

[33] Laurent Guérin, Johan Hébert, Marylise Buron-Le Cointe, Shin-Ichi Adachi, Shin-Ya Koshihara, et al.. Capturing One-Dimensional Precursors of a Photoinduced Transformation in a Material. Physical Review Letters, 2010, 105, pp.246101.

Principal investigator, coordination of the project, conduct the experiment, development of analyse program, analyse of the data, Co-writing of the manuscript, supervision of J. Hébert

[34] Hervé Cailleau, Maciej Lorenc, Laurent Guérin, Marina Servol, Eric Collet, et al.. Structural dynamics of photoinduced molecular switching in the solid state.. Acta Crystallographica Section A Foundations of Crystallography, 2010, 66 (Pt 2), pp.189-97.

Review article based on previous work, support on writing the manuscript

[35] O. Mariager, D. Khakhulin, H. T. Lemke, K. S. Kjær, L. Guérin, L. Nuccio, C. B. Sørensen, M. M. Nielsen, and R. Feidenhans'l, Direct Observation of Acoustic Oscillations in InAs Nanowires, Nano Lett. 10, 2461 (2010)

> Beamline scientist at ESRF. Preparation the experiment. Conduct the experiment.

[36] H. Ichikawa, S. Nozawa, T. Sato, A. Tomita, K. Ichiyanagi, M. Chollet, L. Guérin, S. Adachi, K. Miyano, and S. Koshihara, 100ps Time-Resolved X-Ray Diffraction Study on Nd0.5Sr0.5MnO3thin Film, J. Phys.: Conf. Ser. 148, 012020 (2009).

> Beamline scientist at KEK. Preparation of the experiment. Conduct the experiment, support on writing the manuscript.

[37] S. Adachi, S. Nozawa, K. Ichiyanagi, H. Ichikawa, M. Chollet, L. Guérin, R. Tazaki, T. Sato, A. Tomita, H. Sawa, T. Arima, H. Kawata, and S. Koshihara, Pulsed Synchrotron X-Ray as a Tool for Providing Molecular Movies at 100-Picosecond Temporal and Sub-Nanometer Spatial Resolution, J. Phys.: Conf. Ser. 148, 012044 (2009).

> Beamline scientist at KEK. Preparation of the experiment. Conduct the experiment, support on writing the manuscript.

[38] Shunsuke Nozawa, Shin-Ichi Adachi, Jun-Ichi Takahashi, Ryoko Tazaki, Laurent Guérin, et al.. Developing 100 ps-resolved X-ray structural analysis capabilities on beamline NW14A at the Photon Factory Advanced Ring. Journal of Synchrotron Radiation, 2007, 14 (Pt 4), pp.313-9.

> Beamline scientist at KEK. Built a complete beamline from scratch. Support on writing the manuscript.

[39] S. Adachi, S. Nozawa, R. Tazaki, J. Takahashi, J. Itatani, M. Daimon, T. Mori, H. Sawa, H. Kawata, T. Sato, A. Tomita, M. Chollet, L. Guérin, E. Collet, H. Cailleau, and S. Koshihara, Current Status of 50-Picosecond Resolved x-Ray Diffraction at Photon Factory Advanced Ring (PF-AR), J. Phys.: Conf. Ser. 21, 101 (2005).

> Beamline scientist at KEK. Built a complete beamline from scratch. Support on writing the manuscript.

[40] M. Chollet, L. Guérin, N. Uchida, S. Fukaya, H. Shimoda, T. Ishikawa, K. Matsuda, T. Hasegawa, A. Ota, H. Yamochi, G. Saito, R. Tazaki, S. Adachi, and S. Koshihara, Gigantic Photoresponse in ¼-Filled-Band Organic Salt (EDO-TTF)2PF6, Science 307, 86 (2005).

> PhD Student at Tokyo-Institute of technology. Principal investigator, Conduct the experiment, analyse of the data, support on writing the manuscript

[41] L. Guérin, D. Glijer, N. Moisan, M. Lorenc, M. B.-L. Cointe, E. Collet, H. Cailleau, A. Ota, G. Saito, X. Shao, H. Yamochi, M. Chollet, K. Onda, T. Ishikawa, and S. Koshihara, Phase Transition in (EDO-TTF)2PF6: Domain Growth in the Thermal Hysteresis and Ultra-Fast Photoinduced Effects, J. Phys.: Conf. Ser. 21, 149 (2005).

> PhD Student at Tokyo-Institute of Technology. Principal investigator, Conduct the experiment, development of analyse program, analyse of the data, Complete writing of the manuscript

[42] L. Guérin, N. Huby, E. Collet, L. Toupet, H. Cailleau, and K. Tanaka, Structural Investigation of the Photoinduced Spin Transition in the Three States Molecular System [Fe(2-Pic)3]Cl2EtOH, J. Phys.: Conf. Ser. 21, 136 (2005).

> PhD Student at Université de Rennes 1. Principal investigator, Conduct the experiment, analyse of the data, Complete writing of the manuscript

[43] M. Buron-Le Cointe, E. Collet, L. Guérin, M. H. Lemée-Cailleau, H. Cailleau, M. Wulff, T. Luty, S. Koshihara, and K. Tanaka, Time-Resolved X-Ray Diffraction: A Wonderful Tool for Probing Structural Photo-Induced Phase Transitions, Journal of Luminescence 112, 235 (2005).

PhD Student at Université de Rennes 1. Conduct the experiment, analyse of the data

[44] M. Chollet, L. Guérin, N. Uchida, S. Fukaya, T. Ishikawa, S. Koshihara, K. Matsuda, H. Yamochi, A. Ota, and G. Saito, Ultra-Fast and Sensitive Photo-Induced Phase Switching in (EDO-TTF)2PF6, Journal of Luminescence 112, 275 (2005)

PhD Student at Tokyo-Institute of technology. Principal investigator, Conduct the experiment, analyse of the data

[45] M. Chollet, L. Guérin, N. Uchida, S. Fukaya, H. Shimoda, T. Ishikawa, K. Matsuda, T. Hasegawa, A. Ota, H. Yamochi, G. Saito, R. Tazaki, S. Adachi, and S. Koshihara, Ultrafast Photo-Induced Metal–Insulator Transition in 1/4 Filled Organic Crystal (EDO-TTF)2PF6, J. Phys.: Conf. Ser. 21, 130 (2005).

PhD Student at Tokyo-Institute of technology. Principal investigator, Conduct the experiment, analyse of the data, support on the writing of the manuscript

[46] L. Guérin, E. Collet, M. Buron-Le Cointe, M.-H. Lemée-Cailleau, H. Cailleau, M. Wulff, S. Techert, and S.-Y. Koshihara, 100 Ps Time-Resolved Crystallographic Investigation of the Photoinduced Phase Transition in TTF-CA, J. Phys. IV France 114, 99 (2004).

PhD Student at Université de Rennes 1. Principal investigator, Conduct the experiment, analyse of the data, Complete writing of the manuscript

[47] N. Huby, L. Guérin, E. Collet, L. Toupet, J.-C. Ameline, H. Cailleau, T. Roisnel, T. Tayagaki, and K. Tanaka, Photoinduced Spin Transition Probed by X-Ray Diffraction, Phys. Rev. B 69, (2004).

PhD Student at Université de Rennes 1. Conduct the experiment, analyse of the data, support on writing the manuscript. Supervision of N. Huby.

[48] L. Guérin*, E. Collet, M.-H. Lemée-Cailleau, M. Buron-Le Cointe, H. Cailleau, A. Plech, M. Wulff, S.-Y. Koshihara, and T. Luty, Probing Photoinduced Phase Transition in a Charge-Transfer Molecular Crystal by 100 Picosecond X-Ray Diffraction, Chemical Physics 299, 163 (2004).

PhD Student at Université de Rennes 1. Principal investigator, Conduct the experiment, analyse of the data, Co-writing of the manuscript

Supervision

L3/M1 Internship

Cheikh Ndiaye, master student at université de Rennes 1 : determination of the undecane-urea structure using superspace formalism.	2011
Jeremy Rio, master student at université de Rennes 1 : Synthesis of mellitate-based organic crystals. Structure determination using X-ray diffraction.	2012
Nadege Nzone, master student at université de Rennes 1 : Structure determination of TMTTF-Mellitate crystal	2012
Laurent Delcouder, undergraduate student at université de Rennes Machine learning algorithm for radiotherapy	2013
Erwann Lahlou, undergraduate student at université de Rennes 1 : Machine learning algorithm for controlling Xray dose	2013
Mathieu Moalic, undergraduate student at université de Rennes 1 : Building a new intenseThz pulse source at IPR	2016
Yoan Saudrais, undergraduate student at université de Rennes 1 : Online crystallography education	2016
Luc Grasson, undergraduate student at université de Rennes 1 : Structure of Pd-dmit crystal	2016
Mathieu Moalic, master student at université de Rennes 1 : Thz pulse characterisation	2017
Elisa Collet, undergraduate student at université de Rennes 1 : Structure determination of MX crystals	2021
Guillemette Adam, undergraduate student at université de Rennes 1 : Structure determination of MX crystals	2021
Elisa Jarry, undergraduate student at université de Rennes 1 : Structure determination of the low temperature phase of dichlorodurane	2022
Flavie Leray, master student at université de Rennes 1 Structural analysis of the phase transition in dichlorodurane	2022
Alexandre Huguet, ESIR 2 (2022) Diffraction experiment of dichlorodurane crystals	2022

M2 Master Thesis

Kasper Skov Kjaer, master student at Copenhagen university Beamline X-ray optics at ID09B ESRF	2009
Mariana Verezhak, master student at université de Rennes 1 : Inelastic Xray scattering : experiment at ESRF and data analysis	2013
K. Numazawa, master student at Tohoku University : Electron diffraction experiment at ISCR	2014
T. Hara, master student at Tohoku University High resolution Xray diffraction of alloys	2014

Edoardo Zatterin, master student at université de Rennes 1 2015
Diffuse scattering of MX crystals

PhD supervision 2006
Nicolas Moisan, PhD thesis at université de Rennes 1
Time resolved spectroscopy setup at NW14 beamline

Johan Hébert, PhD thesis at université de Rennes 1 2007
Time resolved X-ray scattering of TTF-CA

Alesandro Spilotros, PhD thesis Palerme University 2009
Time resolved WAXS for studying oxygen binding in myoglobin

Celine Mariette, PhD thesis at université de Rennes 1 2010-2013
Structural study of alkane-urea aperiodic crystals

Takefumi Yoshida, PhD thesis at Tohoku University 2016
Diffuse scattering of MX crystals at ESRF

Kazuki Nakamura, PhD thesis at the University of Tokyo 2022-2023
Time resolved spectroscopy of Co-W cyanide bridged bimetallic assembly

PhD Direction 2018-2022
Lucas Gournay, PhD thesis at université de Rennes 1
Structural and electronic response of materials under intense THz radiation.
Defended on February 16th 2022

Maryam Alashoor, PhD thesis at université de Rennes From October 2023
Ultrafast dynamics and non-volatile photoswitching in cyanide bridged Cobalt-Tungsten assemblies

Appendix B

PhD Direction

Lucas Gournay, PhD thesis at université de Rennes 1

Structural and electronic response of materials under intense THz radiation.

Defended on February 16th 2022

The question this thesis aims to answer is as follows: Can THz radiation be used to induce photo-induced phase transitions? The characteristics of THz radiation are presented here :

Frequency	Energy	Wavelength	Wavenumber	Pulse duration
1 THz	4meV	300 mum	33 cm-1	1ps

Intense Terahertz (THz) radiation typically exhibits what is known as a single-cycle electric field. A single-cycle electric field has high intensity in a single direction with a duration on the order of picoseconds. Such electric fields can reach intensities on the order of MV/cm. The temporal profile of the single-cycle electric field allows the use of Terahertz (THz) radiation either to trigger electronic responses in materials or to directly modify the materials' structure, justifying the title of this thesis. THz radiation has already been employed on the molecular crystal known as TTF-CA in both ways to induce different effects, particularly the generation or modulation of Second Harmonic in the material. Hence, the development of an intense THz source is crucial for advancing these studies.

A source based on the optical rectification technique has been developed during this thesis work. Optical rectification is a second-order nonlinear phenomenon that transforms radiation with a duration close to 100 fs into single-cycle radiation lasting 1 ps. The spectrum associated with the generated radiation spans a frequency range from 0.1 to 5 THz. Specifically, for a source radiation with a duration of 100 fs, the expected THz radiation is presented in the following figure :

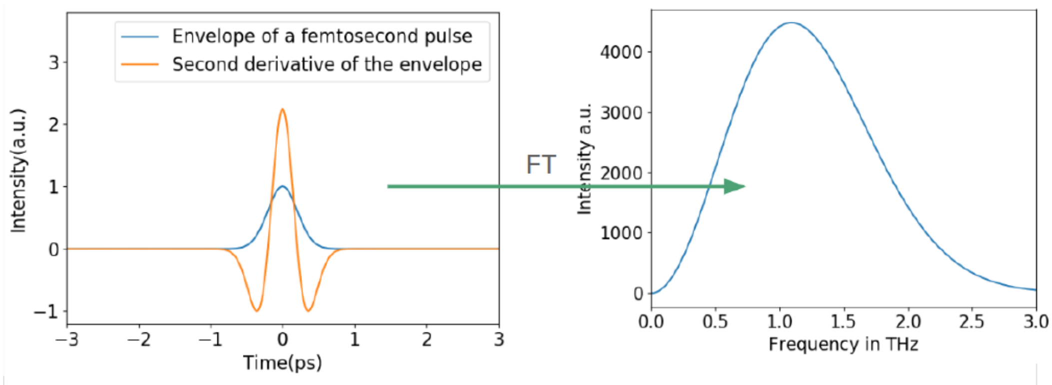

We chose the crystal LiNbO3 as the generation crystal. This crystal exhibits optimal characteristics for THz generation compared to our laser specifications. However, a technique must be employed to achieve phase matching in this crystal. Indeed, THz radiation is not generated collinearly with the source pulse in the crystal, leading to destructive interference. By tilting the wavefront at the same angle as the THz generation, optimal THz radiation can be generated.

To achieve the most intense Terahertz (THz) source possible, excellent focusing must be achieved. A system of three gold parabolic mirrors is used to magnify and then focus the beam. The choice of parabolic mirrors is explained by their very low loss rate in the THz regime. A metal plate, developed in collaboration with the Rennes workshop, was created to facilitate the alignment of the parabolic mirrors.

As the use of THz radiation is relatively recent, standard visualization tools do not yet exist. To image the beam, a pyroelectric camera Pyrocam III was used. An image of the THz beam taken with the Pyrocam III is presented in the following figure. The focusing system has enabled obtaining a focal spot of approximately 800 µm.

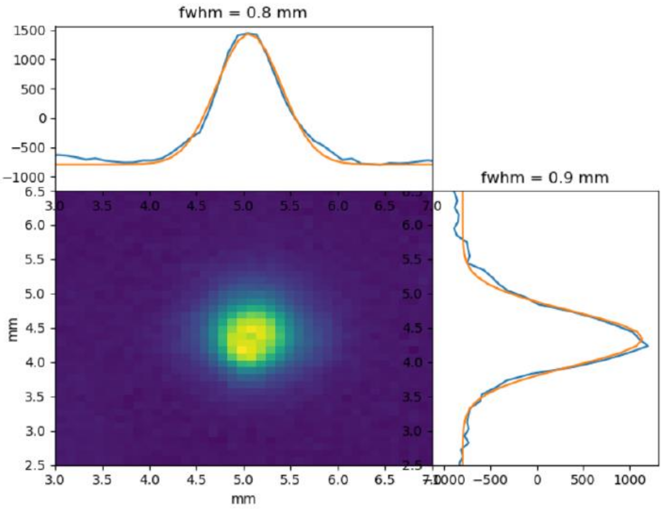

The characterization of the THz electric field obtained was performed using the Electro-Optic Sampling (EOS) technique. This technique relies on the Pockels effect, where certain materials become birefringent under the influence of an electric field. This birefringence causes a polarization change in the incident light, shifting from linear to elliptical. By measuring the degree of ellipticity, for example, using a Wollaston prism, the applied electric field value on the crystal can be deduced. An electric field of a value of 800 kV/cm was thus obtained and is presented in Figure 6. The characteristics of this source rank it among the world's best sources, utilizing optical rectification combined with the tilted wavefront technique in the LiNbO3 crystal.

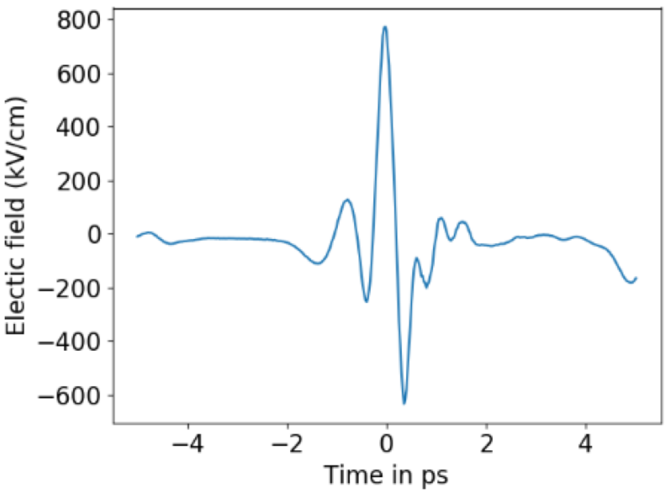

This source was developed for conducting Terahertz (THz) pump-probe optical experiments. The final step for this source to be fully functional is validation through a test experiment. We chose to replicate the experiment by Chen et al. on β-BaB2O4 (BBO). In this experiment, THz radiation is used to modulate the second harmonic generation in the β-BBO crystal. Chen et al.'s experiment was conducted with a maximum electric field of 160 kV/cm, while the experiment carried out in this thesis was performed with a maximum electric field of 300 kV/cm. Comparative results between those of Chen et al. (dotted lines) and those of this work (solid lines) are presented in the following figure. A modulation of the second harmonic similar in both works is observed below 160 kV/cm. At 300 kV/cm, the obtained results remain similar to those obtained at lower electric field values. This similarity allows us to conclude that not only is the source usable, but it also validates Chen et al.'s results for larger electric field values.

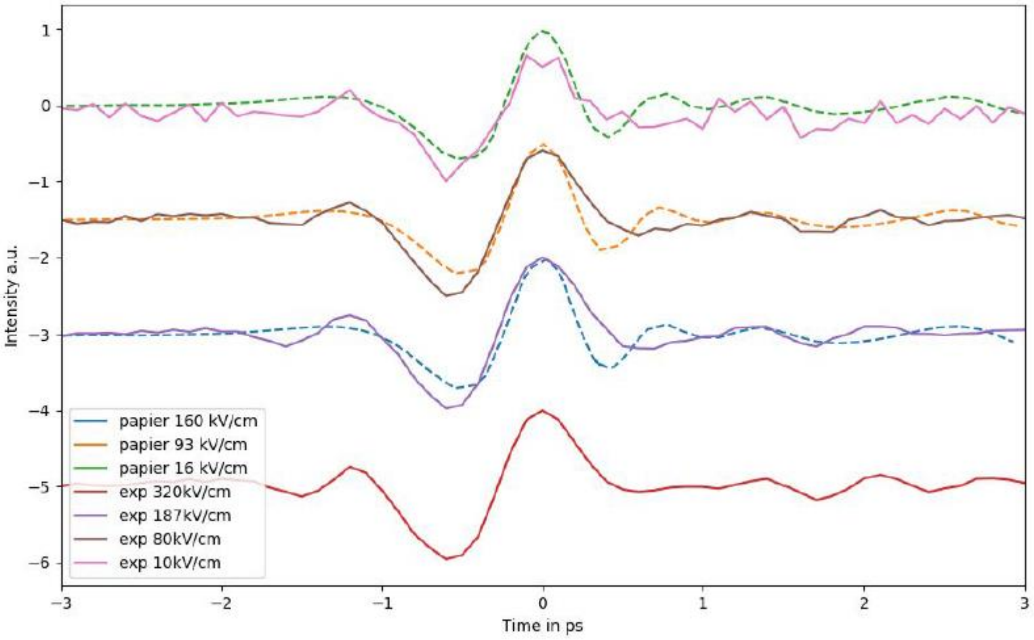

In conclusion, this thesis work facilitated the development of a THz radiation source whose level equals the best sources in the state of the art. This source was validated by reproducing and extending results from existing studies.

CV

CONTACT INFORMATION

Associate professor – CNRS Delegation
IRL2015 Dynamical Control of Materials, CNRS, Department of Chemistry, The University of Tokyo

+81 90 6497 1002
laurent.guerin@univ-rennes.fr

CITIZENSHIP

French

EDUCATION

PhD., Physics — 2005
Université de Rennes 1/ Tokyo Institute of Technology

Master degree of Physics, — 2002
Université de Rennes 1

Engineering diploma in Physics, optoelectronics and matter, — 2002
Institut National des Sciences Appliquées

B.S Mathematics and Physics, — 1999
Université de Bretagne Sud

Baccalauréat série S, — 1996
Lycée Pierre Guéguin, Concarneau

HONOR, GRANT

Laureate of the Lavoisier Grant of The Ministry of Foreign Affairs — 2005

Laureate of the Young researcher Bretagne 2007 — 2007

RESEARCH EXPERIENCE

Delagation CNRS – IRL2015 Dynamical Control of Materials, CNRS, Department of Chemistry, The University of Tokyo — From sept. 2023

Associate Professor - Institut de Physique de Rennes, Université de Rennes 1 — 2010-present
Advanced Crystallography – Aperiodic system – THz pulse to trigger structural response

Visiting Researcher – IMRAM- Tohoku University – Tsai research Group — 2015 (3 months)
Phase transition in quasicrystal approximant using NMR and Xray diffraction

Post-doctoral Fellow at the European Synchrotron Research Facility beamline ID09B — 2008 - 2010
Formation of a chemical bond: vibrational cooling in I2 studied by TR Small Angle X-ray Scattering – multilayer X-ray optics. Laser facility supervisor.

Post-doctoral Fellow at KEK: Exploratory Research for Advanced Technology, Tsukuba, Japan. — 2005 - 2008
Development of time-resolved X-ray diffuse scattering. construction of a new synchrotron beamline, research in material science using synchrotron radiation (EXAFS, Laue and monochromatic diffraction, liquid scattering)

PhD in Physics at the University of Rennes 1 — 2002 - 2005
Advisor : Pr. Herve Cailleau (UR1) and Pr. Shin-ya Koshihara (Tokyo Institute of Technology)

Photoinduced phase transition in molecular solids
1 year at Tokyo Institute of Technology: time-resolved spectroscopy

TECHNICAL SKILLS

Programming languages : Matlab, Python, Labview, html

Technical Knowledge: Alignment and maintenance of ultrafast Ti:Sapphire optical systems (oscillators and regenerative amplifiers); construction and operation of nonlinear crystals based THz generation setups; x-ray time-resolved diffraction experiments; cryogeny. Superspace srystallography, 3D-ΔPDF method, structure determination

PUBLICATIONS

[1]**Laurent Guérin***, Elzbieta Trzop, Tadahiko Ishikawa, Shinya Koshihara ,Takashi Yamamoto, Bertrand Toudic, Reizo Kato*, Frustrated competitive forces in the Et2Me2Sb[Pd(dmit)2]2 molecular conductor, **Physical Review B** 108, 134104 (2023).

[2]Céline Mariette,Philippe Rabiller,**Laurent Guérin**, Claude Ecolivet ,Ilya Frantsuzov, Bo Wang, Shane M. Nichols, Philippe Bourges, Alexei Bosak, Yu-Sheng Chen, Mark D. Hollingsworth, Bertrand Toudic, **Physical Review B** 106, 134109 (2022).

[3]A. Simonov, P. Rabiller, C. Mariette, **L. Guérin**, A. Bosak, A. Popov, and B. Toudic, Short-Range Order in the Quasiliquid Phases of Alkane Substructures within Aperiodic Urea Inclusion Crystals, **Physical Review B** 106, 054206 (2022).

[4]T. Yoshida, S. Takaishi, **L. Guérin**, T. Kojima, H. Ohtsu, M. Kawano, T. Miyamoto, H. Okamoto, K. Kato, M. Takata, Y. Hosomi, S. Yoshida, H. Shigekawa, H. Tanaka, S. Kuroda, H. Iguchi, B. K. Breedlove, Z.-Y. Li, and M. Yamashita, Hydrogen Bonding Propagated Phase Separation in Quasi-Epitaxial Single Crystals: A Pd–Br Molecular Insulator, **Inorganic Chemistry**,61,35,14067 (2022)

[5]**L. Guérin***, T. Yoshida*, E. Zatterin, A. Simonov, D. Chernyshov, H. Iguchi, B. Toudic, S. Takaishi, and M. Yamashita, Elucidating 2D Charge-Density-Wave Atomic Structure in an MX–Chain by the 3D-ΔPair Distribution Function Method, ***ChemPhysChem*** 23 (2022).
VIP + COVER

[6]Gournay, L., Chaban, I., Mevellec, J.-Y., Humbert, B., Janod, E., **Guérin, L.**, Cammarata, M., Daro, N., Chastanet, G., & Collet, E. Shifting photo-stationary light-induced excited spin state trapping equilibrium towards higher temperature by increasing light fluence. In ***Chemical Physics Letters*** 791, p. 139395. (2022)

[7]Céline Mariette, Maciej Lorenc, Hervé Cailleau, Eric Collet, **Laurent Guérin**, et al.. Strain wave pathway to semiconductor-to-metal transition revealed by time-resolved X-ray powder diffraction. ***Nature Communications***, 12 (1), pp.1239. (2021)

[8]Céline Mariette*, **Laurent Guérin***, Philippe Rabiller, Christophe Odin, Mariana Verezhak, et al.. High spatial resolution studies of phase transitions within organic aperiodic crystals. ***Physical Review B***, American Physical Society, 2020, 101 (18)

[9]B. Toudic, **Laurent Guérin**, C. Mariette, I. Frantsuzov, P. Rabiller, et al.. Comment on Couzi et al. (2018): a phenomenological model for structural transitions in incommensurate alkane/urea inclusion compounds. ***Royal Society Open Science***, The Royal Society, 2019, 6 (8), pp.182073.

[10]Eric Collet, Giovanni Azzolina, Tomoaki Ichii, **Laurent Guérin**, Roman Bertoni, et al.. Lattice phonon modes of the spin crossover crystal [Fe(phen)2(NCS)2] studied by THz, IR, Raman spectroscopies and DFT calculations. ***European Physical Journal B: Condensed Matter and Complex Systems***, 2019, 92 (1), pp.12

[11]C. Ecolivet, M. Verezhak, Céline Mariette, **Laurent Guérin**, P. Rabiller, et al.. Phonons in an aperiodic alkane/urea composite crystal studied by inelastic x-ray scattering. ***Physical Review B***, 2018, 98 (22), pp.224308+.

[12]Céline Mariette, Philippe Rabiller, **Laurent Guérin**, Bertrand Toudic. Crystallography and dynamics in superspace. ***EPJ Web of Conferences***, 2017, 155

[13]T. Yoshida, S. Takaishi, H. Iguchi, H. Okamoto, H. Tanaka, S. Kuroda, Y. Hosomi, S. Yoshida, H. Shigekawa, T. Kojima, H. Ohtsu, M. Kawano, B. K. Breedlove, **L. Guérin**, and M. Yamashita, Optically Visible Phase Separation between Mott-Hubbard and Charge-Density-Wave Domains in a Pd-Br Chain Complex, ***ChemistrySelect*** 1, 259 (2016).

[14] E. Trzop, D. Zhang, L. Piñeiro-Lopez, F. J. Valverde-Muñoz, M. Carmen Muñoz, L. Palatinus, **L. Guérin**, H. Cailleau, J. A. Real, and E. Collet, Inside Back Cover: First Step Towards a Devil's Staircase in Spin-Crossover Materials, ***Angewandte Chemie International Edition*** 55, 1 (2016).

[15]C. Mariette, Ilya Frantsuzov, Bo Wang, **Laurent Guérin**, P. Rabiller, et al.. Frustrated pretransitional phenomena in aperiodic composites. ***Physical Review B***, 2016, 94 (18).

[16] Kamil K. Kolincio, Ramzy Daou, Olivier Perez, **Laurent Guérin**, Pierre Fertey, et al.. Giant Nernst effect in the incommensurate charge density wave state of P4W12O44. ***Physical Review B***, 2016, 94 (24), pp.241118

[17] K. H. Kim, J. Kim, K. Y. Oang, J. H. Lee, D. Grolimund, C. J. Milne, T. J. Penfold, S. L. Johnson, A. Galler, T. W. Kim, J. G. Kim, D. Suh, J. Moon, J. Kim, K. Hong, **L. Guérin**, T. K. Kim, M. Wulff, C. Bressler, and H. Ihee, Identifying the Major Intermediate Species by Combining Time-Resolved X-Ray Solution Scattering and X-Ray Absorption Spectroscopy, **Phys. Chem. Chem. Phys.** 17, 23298 (2015).

[18] S. Zerdane, C. Mariette, G. J. McIntyre, M.-H. Lemée-Cailleau, P. Rabiller, **L. Guérin**, J. C. Ameline, and B. Toudic, Neutron Laue and X-Ray Diffraction Study of a New Crystallographic Superspace Phase Inn-Nonadecane–Urea, ***Acta Crystallographica Section B***, 71, 293 (2015).

[19] **Laurent Guérin**, Céline Mariette, Philippe Rabiller, Michael Huard, Sylvain Ravy, et al.. Long-range modulation in a five-

dimensional crystallographic superspace. ***Physical Review B ,*** 2015, 91 (18), pp.184101.

[20] Céline Mariette, **Laurent Guérin**, Philippe Rabiller, Yu-Sheng Chen, Alexei Bosak, et al.. The creation of modulated monoclinic aperiodic composites in n-alkane/urea compounds. ***Zeitschrift für Kristallographie***, 2015, 230 (1), pp.5--11.

[21]Céline Mariette, **Laurent Guérin**, Philippe Rabiller, Claude Ecolivet, P. Garcia-Orduna, et al.. Critical phenomena in higher dimensional spaces : The hexagonal-to-orthorhombic phase transition in aperiodic n-nonadecane/urea.. ***Physical Review B,*** 2013, 87 (10), pp.104101.

[22] J. H. Lee, M. Wulff, S. Bratos, J. Petersen, **L. Guerin**, J.-C. Leicknam, M. Cammarata, Q. Kong, J. Kim, K. B. Møller, and H. Ihee, Filming the Birth of Molecules and Accompanying Solvent Rearrangement, ***J. Am. Chem. Soc.*** 135, 3255 (2013)

[23] W. Kaszub, M. Buron-Le Cointe, M. Lorenc, M. Boillot, M. Servol, A. Tissot, **L. Guérin**, H. Cailleau, and E. Collet, Spin-State Photoswitching Dynamics of the (TPA)Fe(TCC)]SbF_6 Complex, ***European Journal of Inorganic Chemistry*** 2013, 992 (2012).

[24]Eric Collet, Maciej Lorenc, Marco Cammarata, **Laurent Guérin**, Marina Servol, et al.. 100 picosecond diffraction catches structural transients of laser-pulse triggered switching in a spin-crossover crystal.. ***Chemistry - A European Journal***, 2012, 18 (7), pp.2051-5.

[25] **Laurent Guérin**, Qingyu Kong, Dmitry Khakhulin, Marco Cammarata, Hyotcherl Ihee, et al.. Tracking Atomic Positions in Molecular Reactions by Picosecond X-ray Scattering at the ESRF. ***Synchrotron Radiation News***, 2012, 25 (2), pp.25-31.

[26]H. Shimizu, M. Iwamoto, T. Konno, A. Royant, S. Von David, **L. Guérin**, M. Wulff, and S. Oiki, Laser-Triggered Single Molecular Gating Motions of the KcsA Potassium Channels Recorded in a Sub-Millisecond Time Resolution, ***Biophysical Journal*** 102, 37a (2012).

[27] K. Haldrup, T. Harlang, M. Christensen, A. Dohn, T. B. van Driel, K. S. Kjær, N. Harrit, J. Vibenholt, **L. Guérin**, M. Wulff, and M. M. Nielsen, Bond Shortening (1.4 Å) in the Singlet and Triplet Excited States of [Ir2(Dimen)4]2+ in Solution Determined by Time-Resolved X-Ray Scattering, ***Inorg. Chem***. 50, 9329 (2011).

[28] M. Huard, Bertrand Toudic, Philippe Rabiller, Claude Ecolivet, **Laurent Guérin**, et al.. Confined linear molecules inside an aperiodic supramolecular crystal: The sequence of superspace phases in n-hexadecane/urea. ***Journal of Chemical Physics***, 2011, 135 (20), pp.204505.

[29] Nüske, A. Jurgilaitis, H. Enquist, S. D. Farahani, J. Gaudin, **L. Guérin**, M. Harb, C. v. K. Schmising, M. Störmer, M. Wulff, and J. Larsson, Picosecond Time-Resolved x-Ray Refectivity of a Laser-Heated Amorphous Carbon Film, ***Appl. Phys. Lett.*** 98, 101909 (2011).

[30] J. Gaudin, B. Keitel, A. Jurgilaitis, R. Nüske, **L. Guérin**, J. Larsson, K. Mann, B. Schäfer, K. Tiedtke, A. Trapp, Th. Tschentscher, F. Yang, M. Wulff, H. Sinn, and B. Flöter, Time-Resolved Investigation of Nanometer Scale Deformations Induced by a High Flux x-Ray Beam, ***Opt. Express*** 19, 15516 (2011).

[31] Bertrand Toudic, Ronan Lefort, Claude Ecolivet, **Laurent Guérin**, Roland Currat, et al.. Mixed acoustic phonons and phase modes in an aperiodic composite crystal. ***Physical Review Letters***, 2011, 107 (20), pp.205502.

[32] H. Ichikawa, S. Nozawa, T. Sato, A. Tomita, K. Ichiyanagi, M. Chollet, **L. Guérin**, N. Dean, A. Cavalleri, S. Adachi, T. Arima, H. Sawa, Y. Ogimoto, M. Nakamura, R. Tamaki, K. Miyano, and S. Koshihara, Transient Photoinduced 'Hidden' Phase in a Manganite, ***Nature Material*** 10, 101 (2011)

[33] **Laurent Guérin**, Johan Hébert, Marylise Buron-Le Cointe, Shin-Ichi Adachi, Shin-Ya Koshihara, et al.. Capturing One-Dimensional Precursors of a Photoinduced Transformation in a Material. ***Physical Review Letters***, 2010, 105, pp.246101.

[34] Hervé Cailleau, Maciej Lorenc, **Laurent Guérin**, Marina Servol, Eric Collet, et al.. Structural dynamics of photoinduced molecular switching in the solid state.. ***Acta Crystallographica Section A Foundations of Crystallography***, 2010, 66 (Pt 2), pp.189-97.

[35] O. Mariager, D. Khakhulin, H. T. Lemke, K. S. Kjær, **L. Guérin**, L. Nuccio, C. B. Sørensen, M. M. Nielsen, and R. Feidenhans'l, Direct Observation of Acoustic Oscillations in InAs Nanowires, ***Nano Lett.*** 10, 2461 (2010)

[36] H. Ichikawa, S. Nozawa, T. Sato, A. Tomita, K. Ichiyanagi, M. Chollet, **L. Guérin**, S. Adachi, K. Miyano, and S. Koshihara, 100ps Time-Resolved X-Ray Diffraction Study on Nd0.5Sr0.5MnO3thin Film, ***J. Phys.: Conf.*** Ser. 148, 012020 (2009).

[37] S. Adachi, S. Nozawa, K. Ichiyanagi, H. Ichikawa, M. Chollet, **L. Guérin**, R. Tazaki, T. Sato, A. Tomita, H. Sawa, T. Arima, H. Kawata, and S. Koshihara, Pulsed Synchrotron X-Ray as a Tool for Providing Molecular Movies at 100-Picosecond Temporal and Sub-Nanometer Spatial Resolution, **J. Phys.: Conf. Ser**. 148, 012044 (2009).

[38] Shunsuke Nozawa, Shin-Ichi Adachi, Jun-Ichi Takahashi, Ryoko Tazaki, **Laurent Guérin**, et al.. Developing 100 ps-resolved X-ray structural analysis capabilities on beamline NW14A at the Photon Factory Advanced Ring. ***Journal of Synchrotron Radiation***, 2007, 14 (Pt 4), pp.313-9.

[39] S. Adachi, S. Nozawa, R. Tazaki, J. Takahashi, J. Itatani, M. Daimon, T. Mori, H. Sawa, H. Kawata, T. Sato, A. Tomita, M. Chollet, **L. Guérin**, E. Collet, H. Cailleau, and S. Koshihara, Current Status of 50-Picosecond Resolved x-Ray Diffraction at Photon Factory Advanced Ring (PF-AR), ***J. Phys.: Conf. Ser.*** 21, 101 (2005).

[40] M. Chollet, **L. Guérin**, N. Uchida, S. Fukaya, H. Shimoda, T. Ishikawa, K. Matsuda, T. Hasegawa, A. Ota, H. Yamochi, G. Saito, R. Tazaki, S. Adachi, and S. Koshihara, Gigantic Photoresponse in

¼-Filled-Band Organic Salt (EDO-TTF)$_2$PF$_6$, ***Science*** 307, 86 (2005).

[41] **L. Guérin**, D. Glijer, N. Moisan, M. Lorenc, M. B.-L. Cointe, E. Collet, H. Cailleau, A. Ota, G. Saito, X. Shao, H. Yamochi, M. Chollet, K. Onda, T. Ishikawa, and S. Koshihara, Phase Transition in (EDO-TTF)2PF6: Domain Growth in the Thermal Hysteresis and Ultra-Fast Photoinduced Effects, ***J. Phys.: Conf. Ser.*** 21, 149 (2005).

[42] **L. Guérin**, N. Huby, E. Collet, L. Toupet, H. Cailleau, and K. Tanaka, Structural Investigation of the Photoinduced Spin Transition in the Three States Molecular System [Fe(2-Pic)3]Cl2EtOH, ***J. Phys.: Conf. Ser***. 21, 136 (2005).

[43] M. Buron-Le Cointe, E. Collet, **L. Guérin**, M. H. Lemée-Cailleau, H. Cailleau, M. Wulff, T. Luty, S. Koshihara, and K. Tanaka, Time-Resolved X-Ray Diffraction: A Wonderful Tool for Probing Structural Photo-Induced Phase Transitions, ***Journal of Luminescence*** 112, 235 (2005).

[44] M. Chollet, **L. Guérin**, N. Uchida, S. Fukaya, T. Ishikawa, S. Koshihara, K. Matsuda, H. Yamochi, A. Ota, and G. Saito, Ultra-Fast and Sensitive Photo-Induced Phase Switching in (EDO-TTF)2PF6, ***Journal of Luminescence*** 112, 275 (2005)

[45] M. Chollet, **L. Guérin**, N. Uchida, S. Fukaya, H. Shimoda, T. Ishikawa, K. Matsuda, T. Hasegawa, A. Ota, H. Yamochi, G. Saito, R. Tazaki, S. Adachi, and S. Koshihara, Ultrafast Photo-Induced Metal–Insulator Transition in 1/4 Filled Organic Crystal (EDO-TTF)2PF6, ***J. Phys.: Conf. Ser.*** 21, 130 (2005).

[46] **L. Guérin**, E. Collet, M. Buron-Le Cointe, M.-H. Lemée-Cailleau, H. Cailleau, M. Wulff, S. Techert, and S.-Y. Koshihara, 100 Ps Time-Resolved Crystallographic Investigation of the Photoinduced Phase Transition in TTF-CA, ***J. Phys. IV*** France 114, 99 (2004).

[47] Huby, **L. Guérin**, E. Collet, L. Toupet, J.-C. Ameline, H. Cailleau, T. Roisnel, T. Tayagaki, and K. Tanaka, Photoinduced Spin Transition Probed by X-Ray Diffraction, ***Phys. Rev. B*** 69, (2004).

[48] **L. Guérin***, E. Collet, M.-H. Lemée-Cailleau, M. Buron-Le Cointe, H. Cailleau, A. Plech, M. Wulff, S.-Y. Koshihara, and T. Luty, Probing Photoinduced Phase Transition in a Charge-Transfer Molecular Crystal by 100 Picosecond X-Ray Diffraction, ***Chemical Physics*** 299, 163 (2004).

COMMUNICATION

Conference oral presentation (as speaker)

Photoinduced phase transition in TTF-CA
Center of Excellence, University of Rennes 1 –Tokyo institute of Technology bilateral relation, Rennes, France
2003

Functional Organic and Inorganic Materials with Electrical Conductivity, Ferromagnetism and other functions.
2nd Japan-France Bilateral Symposium, Rennes, France
2005

Ultra-fast gigantic metallization in quarter filled organic A2B salts 2005
International Conference on Transient Chemical Structure in Dense Media, Paris, France

Studying in Japan: personal experience 2007
Center of excellence, Tokyo institute of Technology: University of Rennes 1 – Tokyo institute of Technology bilateral relation, Tokyo, Japan

Structural investigation of photoinduced processes in TTF-CA: from precursor phenomena to the macroscopic photoinduced phase. 2007
Japan physical society meeting, Kagoshima, Japan

Looking at structural transformation with spatial and temporal high resolution 2011
Workshop Frontier2011, Tohoku University, Sendai, Japan *[Invited]*

Diffuse scattering in one dimensional liquid like aperiodic composites 2011
International conference of the International Union of Crystallography, Madrid, Spain

Phase transition and critical phenomena in a crystallographic superspace 2012
Symposium of the German Crystallography Society, Munich, Germany

Phase Transition in an aperiodic composite 2012
workshop at NIMS, Tsukuba, Japan

Inelastic diffuse scattering to understand dynamics in aperiodic system 2013
Symposium of the French Crystallography Society, Bordeaux, France

Phase Transition in aperiodic composite
Workshop Frontier 2013, Tohoku University, Sendai, Japan 2013
[Invited]

3D-ΔPDF application
Workshop Frontier 2015, Tohoku University, Sendai, Japan 2015
[Invited]

Analyse 3D-ΔPDF de la transition de phase Mott-ODC dans un compose MX unidimensionnel 2016
Association Française de cristallographie (AFC 2016) – Marseille (France)

3D-ΔPDF investigation of the Mott to CDW phase transition in a MX-chains compound 2016
The 3rd edition of the School and Conference on Analysis of Diffraction Data in real-space (ADD2016) - Grenoble (France)

Incommensurate modulation in Pd(dmit) based conductor 2017

The 12th International Symposium on Crystalline Organic Metals, Superconductors and Magnets (ISCOM2017) - Zao (Japan)

Incommensurate modulation in Pd(dmit) based conductor 2017
New Frontier of Molecular Materials international conference (NFMN) – Sendai (Japan)
[Invited]

Incommensurate modulation of the spin frustration in the triangular lattice of a molecular conductor (invited) 2018
International conference on coordination chemistry ICCC2018 – Sendai (Japan)
[Invited]

Elucidating 2D Charge-Density-Wave Atomic Structure in an MX–Chain by the 3D-ΔPair Distribution Function Method 2022
European Crystallography Meeting 33, Versailles, France

Invited Seminar

Time-resolved X-ray diffraction 2007
Seminar at SOLEIL synchrotron, Orsay, France

NW14 TR Beamline 2008
Seminar at European Synchrotron Research Facility, Grenoble, France

Introduction to Time-resolved Diffraction 2010
Seminar, University of Fukui, Fukui, Japan

Multistable materials 2011
Seminar at Hokkaido University, Sapporo, Japan

Evidence of an incommensurate modulated structure in Pd-dmit base salt. 2013
Seminar ODACE, Caen University, France

100 years of crystallography 2014
Seminar at Vannes University, France

Mosaique Arabes et apériodicité, 2014
Seminar at Conservatoire de Rennes, France

Cristallographie et société 2017
Festival Pint of Science, Rennes, France

Incommensurate modulation in Pd(dmit) based conductor 2018
Seminar at RIKEN, Wako, Japan

Advanced crystallography for PIPT 2023
Seminar at U.Tokyo, Japan

Advances in crystallography 2024
Seminar at U.Tokyo, Japan

Aperiodic tillings and Islamic architecture 2024
Seminar at U.Tokyo, Japan

ORGANISATION OF CONFERENCES	International conference « *Photo-induced Phase Transitions* » Université de Rennes 1	2004
	2nd Japan-France Bilateral Symposium Kyoto University 2005	2005
	Frontier 2012 Workshop, Nantes 2012	2012
	Frontier 2013 Workshop, Tohoku 2013	2013
	X-FEL2013 school and Symposium, Dinan 2013	2013
	Comité Année mondiale de la cristallographie	2014
	Frontier 2015 Workshop, Tohoku 2015	2015
	UCM2018, international school and Symposium on ultrafast control of matter	2018

SUPERVISION

L3/M1 Internship

Cheikh Ndiaye, master student at université de Rennes 1	2011
Jeremy Rio, master student at université de Rennes 1	2012
Nadege Nzone, master student at université de Rennes 1	2012
Laurent Delcouder, undergraduate student at université de Rennes 1	2013
Erwann Lahlou, undergraduate student at université de Rennes 1	2013
Mathieu Moalic, undergraduate student at université de Rennes 1	2016
Yoan Saudrais, undergraduate student at université de Rennes 1	2016
Luc Grasson, undergraduate student at université de Rennes 1	2016
Mathieu Moalic, master student at université de Rennes 1	2017
Elisa Collet, undergraduate student at université de Rennes 1	2021
Guillemette Adam, undergraduate student at université de Rennes 1	2021
Elisa Jarry, undergraduate student at université de Rennes 1	2022
Flavie Leray, master student at université de Rennes 1	2022
Alexandre Huguet, ESIR 2 (2022)	2022

M2 Master Thesis

Kasper Skov Kjaer, master student at Copenhagen university	
Mariana Verezhak, master student at université de Rennes 1	2009
K. Numazawa, master student at Tohoku University	2013
T. Hara, master student at Tohoku University	2014
Edoardo Zatterin, master student at université de Rennes 1	2014
	2015

PhD supervision

Nicolas Moisan, PhD thesis at université de Rennes 1	
Johan Hébert, PhD thesis at université de Rennes 1	2006
Alesandro Spilotros, PhD thesis Palerme University	2007
Celine Mariette, PhD thesis at université de Rennes 1	2009
	2010-2013
Takefumi Yoshida, PhD thesis at Tohoku University	2016
Kazuki Nakamura, PhD thesis at the University of Tokyo	2023

PhD Direction

Lucas Gournay, PhD thesis at université de Rennes 1 *Structural and electronic response of materials under intense THz radiation* Defended on February 16th 2022	2018 - 2022
Maryam Alashoor, PhD thesis at université de Rennes *Ultrafast dynamics and non-volatile photoswitching in cyanide bridged Cobalt-Tungsten assemblies*	From October 2023

TEACHING

Undergraduate :
Mechanics, mathematics, practical in physics, quantum mechanics, electronics, solid state physics, acoustic

Master :
Crystallography, solid state physics, medical physics, numerical methods

Developing a teaching project on my solid state physics course (L3 physique of Rennes1) :
Creating a web site : http://physol.xyz/ (offline since june 2023)
Designing online course : http://physol.xyz/lp-courses/ (offline since june 2023)
Youtube Channel : physique du solide 2021 (21000 vues – 361 subs octobre 2023)
Discord server : 112 members

Advanced crystallography lectures at University of Tokyo 2024

ADMINISTRATIVE TASKS

Manager of Tohoku University – U. Rennes 1 international relation 2010-2016
Organisation of workshops between University of Rennes 1 and Tohoku university
Successful call to ERASMUS MUNDUS + (2016)
Supervising the master student exchange program (David Simone, K. Numazawa, T. Hara)

Supervisor of M1 physique parcours material science 2018-present
M1 MAMASELF
Organisation of the schedule, grading panel, internship administration, internship grading, accreditation panel, day to day running of the class

Coordinator IRL DYNACOM 2023-present
Signature delegation, representation of DYNACOM, management of credits and personnel (grant application, credits, VISA, etc.)

LANGUAGES

French : mother tong
English : Fluent
Japanese : Intermediate

ADVANCES IN
CRYSTALLOGRAPHY

This manuscript presents the forefront of crystallography, exploring novel methodologies and cutting-edge experimental techniques. The integration of advanced techniques, such as ultrafast crystallography and time resolved diffuse scattering, revolutionizes our ability to look at dynamic processes at the atomic level. We investigate a range of materials, from aperiodic systems to correlated disorder systems, pushing the boundaries of crystallographic study. The advancements in data analysis streamline the interpretation of complex crystal structures. Our research unveils key findings in aperiodic disorder, photoinduced phase transitions, and correlated disorder. We discuss the implications of our work in materials science, emphasizing the potential for applications in designing new materials. This manuscript represents a comprehensive exploration of crystallography's latest frontiers, offering insights into materials' structural dynamics and paving the way for future advancements in the field.